UNIVERSIDAD DEL PAÍS VASCO
EUSKAL HERRIKO UNIBERSITATEA

PHD THESIS

Synergistic Study of Surface Science and Electrochemistry: Unraveling the Mechanism of Oxygen Evolution Reaction

Thesis by:

Marina Peña-Díaz

Supervised by:

Dr. Sara Barja

and

Dr. Celia Rogero

July, 2024

Como dijo Edith Wharton, *hay dos formas de difundir la luz: ser la vela o el espejo que la refleja.*
Dedico esta tesis a todes vosotres, aquellas y aquellos que seáis velas en la vida de otros. Especialmente a las velas encendidas que yacen en mi camino: mis padres y mi hermana, para vosotros; para las ya apagadas que siguen estando presentes, mis abuelas.
Y a Paula, por ser faro en esta larga travesía.

Contents

Acknowledgements

Esta etapa llega a su fin después de casi seis años, un periodo que ha sido una auténtica montaña rusa. Así es la ciencia: llena de altibajos inesperados, donde los momentos de euforia se alternan con desafíos y frustraciones que ponen a prueba nuestra paciencia y determinación. Un doctorado, por ello, se podría definir como una verdadera prueba de resiliencia, fortaleza mental y autoestima, donde el doctorando se entrega por completo. Enfrentarse a desafíos personales y profesionales completamente nuevos a menudo nos hace cuestionar si tomamos la decisión correcta. En mi caso, siempre he llegado a la misma conclusión: sí, valió la pena. No solo por la ciencia (aunque también), sino por la oportunidad de conocer a personas increíbles en este camino. Sin duda, vosotres, quienes me habéis acompañado y apoyado incondicionalmente, sois la razón por la que el final de esta tesis ha llegado. Cualquier palabra de agradecimiento que pueda escribir a continuación se quedará corta, seguramente.

En primer lugar, me gustaría agradecer a mis directoras, Sara y Celia, por haberme dado la oportunidad de realizar esta tesis en su grupo, por dirigir nuestro proyecto durante todos estos años con tanto mimo y por haber confiado en mis capacidades para afrontar este desafío.

Gracias, Celia, por tu cercanía, sencillez e inmensa empatía, no solo en el plano personal, sino también en el profesional. Gracias por abrirme las puertas de tu casa para resolver cualquier duda (y también de la soci para momentos más lúdicos jeje). Sin duda, siempre recordaré el final experimental de esta tesis con un buen sabor de boca, disfrutando en PEARL y aprendiendo de los rayos X, además de las infinitas vueltas alrededor del anillo para estirar las piernas. No podría imaginar mejor persona para dirigir el CFM de manera respetuosa y transparente; estoy segura de que tu trayectoria como directora aportará un aire renovador, igualitario y colaborador.

Sara, gracias por haber estado mano a mano conmigo durante este largo camino, especialmente por tu continua disponibilidad sobre todo en esta última etapa de correcciones. Agradezco profundamente todas las discusiones científicas y tu apoyo personal; no hay duda de que he aprendido muchísimo sobre ciencia y academia contigo. Espero que esta tesis haya contribuido a abrir este fascinante mundo de la EC-UHV de la mejor manera posible, estableciendo una base metodológica sólida, aunque estoy segura de que aún queda mucho por mejorar y recorrer.

Max, aunque oficialmente no has sido mi director, yo he sentido como si fueras uno más. Por eso, me gustaría darte las gracias. Agradezco que me hayas enseñado todo lo que implica el ultra alto vacío y la física de superficies en primera línea, desde la construcción de una plataforma metálica para el bakeout en los primeros días de doctorado hasta la búsqueda de explicaciones para los resultados más aleatorios en los últimos tiempos. He aprendido muchísimo gracias a tu visión científica, tu habilidad para resolver cualquier problemilla en el labo y tu gran pasión; ha sido verdaderamente inspirador. También quiero agradecerte el haberme invitado a todos los beamtimes, lo que me ha permitido aprender cosas nuevas, crecer científicamente y salir del laboratorio. Sin tu constante ayuda y ánimos, acompañados de muchas risas incluso en los momentos más críticos, no habría sido lo mismo.

También quiero agradecer a todo el grupo de Nanophysics Lab: a Kike y Fred,

por darme la oportunidad de participar en los beamtimes de MAX IV y ALBA; a Laura, Khadisha, Andrew, Sabine, Alaa, Rodrigo, Dimas, Alejandro, Néstor, Marco, Martina, Andrea y a todos los demás por estar siempre ahí. En especial, a Pablo, compañero de batallas en el laboratorio. Mil gracias por todo el tiempo compartido, por todas las transferencias de muestras y por decorar la campana de una forma divertida, sin perder nunca la alegría. Te deseo lo mejor en tu trayectoria científica. Y a ti, John, muchas gracias por el apoyo durante el año que trabajamos juntos. Sentiste este proyecto como si fuera tuyo y te comprometiste desde el primer momento. Aprecio mucho todos los consejos que me diste a lo largo de esta trayectoria.

I would also like to express my gratitude to all the collaborators who made this thesis possible. I want to give special thanks to Edvin Lundgren and Gary Harlow for initiating the collaboration on the electro-oxidation of Au(111), which became the backbone of this work. Visiting Hamburg to participate in the experiments in PETRA III was a wonderful experience, offering a great opportunity to learn new approaches and surface science techniques. It was truly rewarding. It's a pity that the COVID-19 pandemic prevented us from being together at the PHOENIX beamline. For this last beam time, I want to thank Zbynek Novotny for enabling us to conduct the experiment remotely. And of course, thanks Weronica, Giuseppe, Alfred, Lisa, and Sebastian for making me feel like part of the team. Additionally, thank you, Matthias, for your help and support at PSI during the beamtime.

A continuación, me gustaría agradecer a José Solla por abrirme las puertas de su grupo de manera desinteresada, enseñándome los fundamentos de la electroquímica de superficies y toda la metodología que luego utilicé en esta tesis. Gracias por hacerme sentir como una de tus estudiantes, por tu cercanía y por el tiempo que compartimos en el laboratorio; ese mes fue muy enriquecedor. También quiero agradecer a todos los que formaron parte de mi día a día en Alicante: Pepe, Bea, Eleana, Miguel, Alfonso y Fran.

A Iluminada, mi mentora en electroquímica: gracias por todo lo que me enseñaste durante la carrera y el máster. Espero haber puesto en práctica todo lo aprendido de la mejor manera posible. Sobre todo, quiero agradecerte por tu sabiduría, constancia y apoyo tanto durante mi formación como en estos últimos años. Te deseo lo mejor en tu nueva etapa de jubilación.

Thank you, Miguel, Wen, and Paul, for letting me use the AFM, explaining the technique in detail, and assisting me when I couldn't see anything. I hope I wasn't too much of a bother.

También me gustaría agradecer a todas las personas que forman parte del CFM, especialmente a aquellos que han colaborado recientemente en implementar medidas para garantizar el bienestar profesional y personal de los investigadores predoctorales. Gracias a los miembros del equipo de administración e informática — Ane, Marta, Txema y Ioritz — siempre disponibles para resolver cualquier duda; a Johanes y Aldrin, de recepción, por sus sonrisas y conversaciones matutinas. A Juan, por su incansable trabajo en el laboratorio y su ayuda constante con cualquier cambio necesario. Y, en especial, a Idoia, cuya labor es fundamental para acercar la ciencia al público. Gracias por permitirme participar en estas actividades y disfrutar de la ciencia desde una perspectiva diferente, así como por tu constante apoyo para asegurar el bienestar de todos.

Tras mi etapa en el CFM, me incorporé a Tecnalia, un cambio que me ha permitido madurar tanto profesional como personalmente. Quiero agradecer especialmente a Nerea B. por darme la oportunidad de integrarme en el grupo de Biomat— ¡BEST TEAM EVER! También dar las gracias a los Biosexis, Javi, Vero, Irene y Leire Jr.; a las compañeras del chiringuito, Ainhoa, Andrea, Garbi e Iratxe; y al resto del grupo: Bea, Noelia, Leire, Anetxu, Carol V., Nerea G., Carolina S., Bergoi, Xabi, Unai, Rubén y Jaio. Gracias a todas por vuestras palabras de ánimo y apoyo. I also thank Goran for the inspiring conversations on the rooftop.

Esta etapa me ha brindado la oportunidad de conocer a magníficas personas dentro y fuera del ámbito científico. Compañeros del CFM y amigos con los que he compartido numerosos momentos. Empezando por el NanoPhysics Palace, Fer y Carmen, quienes han sido como familia. Fer, puro corazón y bondad ocultos tras una fachada dura y mucha ironía. Aunque pasen tres meses sin llamarnos (prometo que esto cambiará), siempre te siento cerca. ¡Quérote moito! Carmen, mi siamesa de doctorado, tu infinita alegría y energía han sido el motor de muchos planes y buenos momentos (dentro y fuera del labo). Gracias de verdad. Cris M., gracias por tu constante presencia durante estos años y por aportar un punto de serenidad tan necesario. Migui, tu autenticidad y carisma son únicos; no cambies. Eres un ejemplo de autoestima y resiliencia. Y mil gracias a todos, Adri, Alberto, Álvaro, Antonella, Antton, Auguste, Bruno, Charlie, Cris S., Edudu, Iker, Ion, Jon, Jorge, Jorgito, Joseba, María, Martín (¡SI SE PUEDE! Pronto celebraremos tu tesis), Mikel, Mireia, Raoni, Raulillo, Sofi, Thomas, TxeMikel. He tenido mucha suerte de compartir esta andadura con todos vosotros. Siento que los años que hemos compartido han creado un vínculo que, estoy segura, ninguno olvidará. Gracias a los llamados juegos del hambre, formamos un grupo unido y abierto, que con el tiempo ha integrado nuevos miembros. Creamos un espacio donde desahogarse y reconfortarse sin juicio, y también donde todos hemos crecido a nuestra manera y celebrados logros. Todo ello nos ha llevado a compartir rutas en el monte, pintxopotes cualquier día de la semana (con final o no en el Kaiola), las magníficas casas rurales de los veranos, entre muchos otros. De corazón, ¡gracias por todo ello!

También quiero agradecer y hacer especial mención a mi familia extendida de Donosti. Rosel, entraste como un torbellino de aire fresco en NanoPhysics Palace, y nunca pensé que te convertirías en un pilar tan importante. Gracias por tu infinito apoyo, amiga, incluso cuando yo misma dudaba; siempre has estado ahí animándome. Gracias, Ana, por tu inmensa empatía y corazón. Eres especial y me siento muy afortunada de tenerte en mi vida. Eric, coincidimos por casualidad en los platós de televisión, entre risas, y viniste para quedarte. Tu dulzura es infinita. Alberto, contigo formamos el quinteto de los viernes, pura templanza y energía positiva. Gracias, chicos, en los últimos meses habéis sido el motor de esta tesis. Así que sentidla vuestra.

A más de 500 km de distancia, muchas personas me han acompañado, sintiéndolas siempre cerca, brindándome apoyo y comprensión desde lejos. Gracias a mis amigas de la infancia, Alba e Ivet, porque en cada visita parecía que el tiempo no había pasado. Gracias por llenarme siempre de energía. Alba, tu hiperactividad siempre ha hecho que salga de mi zona de confort en cada visita a Terrassa (incluso yendo a la deriva en un paddle surf...). También gracias a Víctor, Pol y Dani, por

la visita a Donosti en los inicios.

No m'oblido de les meves químiques, Merions y Laieta; quina sort tenir-vos i conservar aquesta amistat tant bonica. Gràcies pels skypes que han fet que us senti tant a prop tot i la distancia. També a la UAB us vaig conèixer, Cris y Anna, y qui ens diria que ens retrobaríem a Donosti totes tres. Gràcies per les birres y els cafès per posar-nos al dia.

Gràcies Mikel per acompanyar-me a La Pasta Boixa en totes les meves visites a Sant Cugat. Tot i que molts cops em treguis de polleguera, et tinc molt de carinyo per tot el que hem compartit a la carrera (no tant per desorganitzar-me els apunts... jajaja).

Equipo de investigación, Carlos y Alex, llegasteis en los últimos años de carrera, donde pasamos muchas horas en el pasillo, y fuisteis un aire fresco y divertido. Ese aire siento que me ha acompañado todo este tiempo. ¡Gracias, chicos!

Paso ahora a agradecer a mi familia, que ha sido el pilar fundamental en mi vida. Gracias por siempre apoyar y respetar mis decisiones, por muy estrambóticas que os parecieran. Gracias Tito, Tete, Vero, Álex y Charlie; por todas las comidas familiares organizadas en mis visitas que me recargaban de energía y amor. A mi hermana Bea, quien ha sido una fuente constante de inspiración y apoyo. Moltíssimes gràcies per haver sigut la millor germana, amiga i mare en una sola persona. Per les teves visites que sempre posaven llum a la foscor, y per recordar-me sempre la importància de la unió. A ti papa, gracias. Tu ejemplo de valentía y constancia me ha motivado a no rendirme, incluso cuando los obstáculos parecían insuperables. Gracias por enseñarme con tu ejemplo la importancia del trabajo duro. Tu dedicación y esfuerzo me han mostrado que los sueños se alcanzan con sacrificio, constancia y determinación. A mi madre, mi refugio y mi guía. Gracias por tu paciencia, tu ternura, y tu amor incondicional. Me enseñaste el valor de la empatía, el respeto por los demás y la importancia de ser humilde. Eres, sin duda, el corazón de esta familia y mi mayor ejemplo de fortaleza. Los cuatro, juntos, ya sea a la distancia o en persona formamos el mejor de los equipos.

Y, por supuesto, a ti Paula. Llegaste a mi vida como dice esa canción de Fuel Fandango, como un *Huracán de flores*. Gracias, por ser aire fresco constante, por aguantarme este tiempo y por ayudarme a encontrar el foco en todo momento. Sin duda, no se me ocurre mejor compañera de vida y risas constantes. Ahora si, llegó nuestra ansiada vida y solo queda que vivirla y bailarla. Gracias también a tu familia que me han acogido como una más; Javier, Begoña, Viole, Ibon y las princesas Lili eta Aia, eskerik asko.

A todos, de corazón, gracias. Un cacho de esta tesis es vuestra.

¡Mila esker!

M.

Resumen

En los últimos años, la sociedad ha experimentado un notable incremento en la demanda energética. Este crecimiento, combinado con el continuo aumento del calentamiento global relacionado con la dependencia de combustibles fósiles, resalta el papel fundamental de la energía renovable en la transición hacia un futuro sostenible. En este contexto, la electrocatálisis combinada con fuentes eléctricas renovables como la eólica y la solar tiene la capacidad de generar productos químicos que, a su vez, son combustibles ricos en energía, reduciendo así la demanda de combustibles fósiles. De esta manera, surgen las células de combustible unificadas (URFCs, por sus siglas en inglés), dispositivos que incorporan de forma regenerativa o bifuncional los procesos de electrólisis y celda de combustible, manifestándose como una prometedora tecnología para la generación de energía limpia y eficiente.

Sin embargo, el pleno potencial de esta tecnología y su desarrollo se ve limitado por diversos factores, entre los cuales destaca la reacción de evolución de oxígeno (OER). La OER presenta un alto potencial de equilibrio (1,23 V vs RHE), contribuyendo a la ineficiencia energética del sistema. Además, la reacción implica múltiples pasos de transferencia de electrones, así como la formación y ruptura de enlaces O-H, lo que resulta en una cinética lenta. Esta baja velocidad de reacción hace aumentar el sobrepotencial y, en consecuencia, la energía necesaria para conducir la reacción. La cinética lenta a su vez contribuye en al desgaste acelerado de los electrodos implicados, limitando la vida útil de las URFCs. Estos hechos en su conjunto subrayan la necesidad de emplear catalizadores más eficientes y estables.

Actualmente, los catalizadores basados en óxidos de metales nobles, como el óxido de iridio y rutenio, son los más eficaces para la OER debido a su alta actividad catalítica y estabilidad. Sin embargo, su alto coste y escasez limitan su viabilidad comercial a largo plazo. Por lo tanto, existe una necesidad crítica de desarrollar nuevos catalizadores basados en óxidos que sean más económicos, abundantes y activos catalíticamente. Los óxidos metálicos, como los de manganeso, han mostrado un potencial significativo como catalizadores alternativos debido a su gran disponibilidad en la tierra y su bajo coste. No obstante, su desempeño actual no es comparable a sus predecesores, óxido de rutenio e iridio, en medio ácido (pH $<$ 7).

La investigación actual se centra en mejorar la actividad catalítica y la estabilidad de estos óxidos mediante el estudio de las relaciones actividad-estructura y estabilidad-estructura. Dado que los procesos electrocatalíticos ocurren en la interfaz electrodo-electrolito, la física de superficies, que estudia las propiedades y procesos en la superficie de materiales sólidos, emerge como una herramienta potencial y esencial para comprender cómo funcionan estos catalizadores y cómo pueden optimizarse para mejorar su eficiencia y actividad.

Teniendo en cuenta la importancia de combinar la física de superficies y la electroquímica para entender la interfaz electroquímica y, por ende, el mecanismo de los catalizadores, esta tesis doctoral se ha centrado en el desarrollo de una metodología experimental para investigar diferentes electrodos modelo (superficies metálicas y óxidos) actuando como electrodos de trabajo en reacciones electroquímicas clave para la generación de energía renovable. Por ello, el primer objetivo fue adaptar y desarrollar un sistema que combinara las capacidades de ultra alto vacío (UHV, por

sus siglas en inglés) con técnicas electroquímicas. Durante el proyecto, se diseñó y puso en marcha un sistema de EC-UHV, combinando una celda electroquímica y un sistema de transferencia limpia que evita la exposición de la superficie al aire. Este desarrollo implicó innovaciones técnicas para asegurar que el sistema pudiera mantener las condiciones de UHV mientras se realizaban estudios electroquímicos a presión atmosférica en una atmósfera de gas inerte, fundamental para obtener datos precisos y reproducibles sobre las reacciones en la interfaz electroquímica. La cámara de UHV está equipada con técnicas de análisis de superficies, como la espectroscopía de fotoelectrones emitidos por rayos X (XPS, por sus siglas en inglés) y la difracción de electrones de baja energía (LEED, por sus siglas en inglés) / microscopía de barrido por efecto túnel (STM, por sus siglas en inglés), que permiten investigar la composición química y la estructura cristalina de la muestra antes y después de las mediciones electroquímicas, así como su dinámica con el potencial aplicado. Esto facilita la correlación entre la respuesta electroquímica y la composición y estructura del catalizador. Además, el sistema cuenta con módulos para sintetizar óxidos binarios con estequiometrías y estructuras controladas, expandiendo la investigación de la actividad catalítica a sistemas con mayor relevancia práctica.

Una vez desarrollado el sistema, se evaluó su capacidad utilizando un electrodo modelo de Au(111). Este electrodo fue seleccionado por sus características bien definidas y su relevancia en estudios electroquímicos. Se estudiaron sus propiedades electroquímicas y se asignaron su composición química y estructural mediante la nueva aproximación desarrollada. El sistema demostró ser efectivo para mantener la interfaz electroquímica, permitiendo una comprensión más profunda del comportamiento del oro bajo condiciones de oxidación electroquímica. En particular, se estudió el mecanismo de electro-oxidación del Au, generalmente considerado como un paso previo a la producción de oxígeno en la OER. Este estudio reveló información crítica sobre el rol de los iones y la dinámica de la electro-oxidación a altos potenciales anódicos, estableciendo cuál es la fase catalizadora real en los ánodos de oro.

El éxito en el estudio del Au(111) proporcionó una base sólida para extender la investigación a sistemas más complejos y relevantes, como los óxidos de manganeso. Gracias al uso de técnicas de UHV integradas en el sistema EC-UHV desarrollado, se logró un crecimiento controlado de óxidos de manganeso con diferentes composiciones químicas y estructurales sobre diferentes sustratos como la plata y el oro. Este enfoque permitió evaluar el efecto que tiene diferentes variables de crecimiento, como la naturaleza del sustrato, la orientación del sustrato, el modo de crecimiento y las condiciones de crecimiento (presión de agente oxidante y naturaleza del agente oxidante), en la estructura cristalina y la composición química de los óxidos obtenidos. Además, dado que el Au se oxida a potenciales muy altos, sirvió como un excelente sustrato para el crecimiento de estos óxidos, y permitió realizar estudios detallados de las propiedades catalíticas de estos sistemas. De esta forma, se estudió la relación entre la estructura en la actividad y estabilidad a potenciales relevantes para la OER. El estudio de los óxidos de manganeso reveló cuál es la fase catalizadora real que facilita la evolución de oxígeno, proporcionando una comprensión más profunda de la relación estructura-actividad-estabilidad en estos materiales.

En conclusión, esta tesis ha demostrado con éxito la viabilidad de un sistema

EC-UHV para el estudio quasi-*in situ* de reacciones electroquímicas mediante técnicas de física de superficie. El sistema desarrollado no solo ha permitido avanzar en la comprensión de la electro-oxidación del Au, sino que también ha abierto nuevas líneas de investigación enfocadas en el estudio del mecanismo de la evolución de oxígeno y la dinámica de los iones a altos potenciales anódicos. El posterior estudio de catalizadores modelos con relevancia en su actividad, como el estudio de óxidos de manganeso, ha proporcionado información valiosa sobre las fases catalizadoras reales en la OER, estableciendo una base para futuras investigaciones y desarrollos en catalizadores más eficientes y duraderos. La capacidad de crecer y evaluar diferentes composiciones químicas y estructurales en condiciones controladas ofrece una herramienta poderosa para el diseño racional de nuevos materiales catalíticos.

El enfoque integrado en esta tesis mediante el estudio sinérgico de EC y UHV proporciona una herramienta poderosa para estudiar y entender los mecanismos fundamentales de catalizadores metálicos y óxidos. El avance en la comprensión de la interfaz electroquímica y el desarrollo de nuevos catalizadores basados en óxidos son cruciales para mejorar la eficiencia y la sostenibilidad de las tecnologías de celdas de combustible y almacenamiento de energía, contribuyendo significativamente a la transición hacia una energía renovable y limpia.

Abstract

In recent years, society has experienced a significant increase in energy demand. This growth, combined with the ongoing rise in global warming related to fossil fuel dependency, underscores the crucial importance of renewable energy in the transition towards a sustainable future. In this context, electrocatalysis, combined with renewable electric sources such as wind and solar, has the potential to generate chemical products that are energy-rich fuels, thereby reducing the demand for fossil fuels. This has led to the development of unitized regenerative fuel cells (URFCs), devices that incorporate both electrolytic and fuel cell processes in a regenerative or bifunctional manner, representing a promising technology for clean and efficient energy generation.

However, the full potential of this technology is limited by various factors, among which the oxygen evolution reaction (OER) stands out. The OER has a high equilibrium potential (1.23 V vs RHE), contributing to the system's energy inefficiency. Moreover, the reaction involves multiple electron transfer steps and the formation and breaking of O-H bonds, resulting in slow kinetics. This slow reaction rate increases the overpotential and, consequently, the energy required to drive the reaction. Slow kinetics also contribute to the accelerated degradation of electrode materials, limiting the lifespan of URFCs. These facts highlight the need for efficient and stable catalysts.

Currently, noble metal-based catalysts, such as iridium and ruthenium, are the most effective for the OER due to their high catalytic activity and stability. However, their high cost and scarcity limit their long-term commercial viability. Therefore, there is a critical need to develop new oxide-based catalysts that are more economical, abundant, and still possess high catalytic activity. Metal oxides, such as those of manganese, have shown significant potential as alternative catalysts due to their availability and lower cost. Nonetheless, their current performance is not comparable to that of noble metals.

Current research focuses on improving the catalytic activity and stability of these oxides by studying the activity-structure and stability-structure relationships. Since electrocatalytic processes occur at the electrode-electrolyte interface, surface physics, which studies the properties and processes on the surface of solid materials, emerges as a potential and essential tool for understanding how these catalysts work and how they can be optimized to improve their efficiency and activity.

Considering the importance of combining surface physics and electrochemistry to understand the electrochemical interface and thus the catalysts, this doctoral thesis has focused on developing an experimental methodology to investigate different model electrodes (metal surfaces and oxides) as working electrodes in key electrochemical reactions. The first objective was to adapt and develop a system that combined the capabilities of UHV with electrochemical techniques. This development involved technical innovations to ensure that the system could maintain UHV conditions while conducting electrochemical studies, which is crucial for obtaining precise and reproducible data on reactions at the electrochemical interface.

During the project, a UHV system compatible with electrochemical measurements was designed and implemented, combining an electrochemical cell and a clean

transfer system that prevents surface exposure to air. The UHV chamber is equipped with surface analysis techniques such as XPS and LEED/STM, allowing investigation of the chemical composition and crystalline structure of the sample before and after electrochemical measurements, as well as its dynamics with the applied potential. This facilitates the correlation between electrochemical response and the catalyst's composition and structure. Additionally, the system includes modules for synthesizing binary oxides with controlled stoichiometries and structures, expanding the investigation of catalytic activity to systems with greater practical relevance.

Once the system was developed, its capability was evaluated using an Au(111) model electrode. This electrode was selected due to its well-defined characteristics and relevance in electrochemical studies. Its electrochemical properties were studied, and its chemical composition and structure were assigned using the newly developed approach. The system proved effective in maintaining the electrochemical interface, enabling a deeper understanding of gold's behavior under electrochemical oxidation conditions. In particular, the mechanism of Au electro-oxidation was studied, generally considered a precursor step to oxygen production in the OER. This study revealed critical information about the role of ions and the dynamics of electro-oxidation at high anodic potentials, establishing the actual catalytic phase in gold anodes.

The success in studying Au(111) provided a solid foundation to extend the research to more complex and relevant systems, such as manganese oxides. Using the UHV-EC system, controlled growth of manganese oxides with different chemical compositions and structures was achieved on a gold substrate. This approach allowed evaluation of the structure's effect on activity and stability at potentials relevant to the OER. The study of manganese oxide revealed the actual catalytic phase that facilitates oxygen evolution, providing a deeper understanding of the structure-activity-stability relationship in these materials. Given that Au oxidizes at very high potentials, it served as an excellent substrate for the growth of other materials, including manganese oxides, enabling detailed studies of the catalytic properties of these systems.

In conclusion, this thesis has successfully demonstrated the feasibility of a UHV-EC system for studying electrochemical reactions using surface physics techniques. The developed system not only advanced the understanding of Au electro-oxidation but also opened new lines of research focused on oxygen evolution and ion dynamics at high anodic potentials. The study of manganese oxides provided valuable information about the actual catalytic phases in the OER, establishing a foundation for future research and development of more efficient and durable catalysts. The ability to grow and evaluate different chemical compositions and structures under controlled conditions offers a powerful tool for the rational design of new catalytic materials.

This integrated approach provides a powerful tool for studying and understanding the fundamental mechanisms of metallic and oxide catalysts. Advances in understanding the electrochemical interface and developing new oxide-based catalysts are crucial for improving the efficiency and sustainability of fuel cell and energy storage technologies, significantly contributing to the transition towards renewable and clean energy.

Abbreviations and terms

AFM Atomic Force Microscopy
BE Binding Energy
CE Counter Electrode
CV Cyclic Voltammetry
CVD Chemical Vapour Deposition
DFT Density Functional Theory
DLC Double Layer Capacitance
E Potential
E_a Activation Energy
E_{ads} Adsorption Energy
E_{ap} Applied Potential
$E_{pa/pc}$ Anodic or Cathodic Peak Potential
$E^0_{Red/Ox}$ Standard potential of a general reaction $Ox + ne^- \rightleftharpoons Red$
EC Electrochemistry/Electrochemical
ECSA Electrochemical Active Area
ET Electron Transfer
HER Hydrogen Evolution Reaction
IHP Inner Helmholtz Plane
LEED Low-Energy Electron Diffraction
LSV Linear Sweep Voltammetry
LT Low Temperature
ML Monolayer
MnOx Manganese Oxide
NAP Near Ambient Pressure
OER Oxygen Evolution Reaction
OHP Outer Helmholtz Plane
RDS Rate-Determining Step
RE Reference Electrode
RHE Reference Hydrogen Electrode
SHE Standard Hydrogen Electrode
STM Scanning Tunneling Microscopy
UHV Ultra-High-Vacuum
URFC Unitized Regenerative Fuel Cell
VB Valence Band
WE Working Electrode
XPS X-Ray Photoemission Spectroscopy
ΔE Spin-orbit splitting
$\Delta E_{\frac{p}{2}}$ Peak width, $\Delta E_{\frac{p}{2}} = \left| E_p - E_{\frac{p}{2}} \right|$
η Overpotential
$*$ Active site

Chapter 1
Introduction

Nowadays fossil fuels are acknowledged as our dominant energy resource. Nevertheless, numerous investigations anticipate that, in the near future, the growing global energy demand will exceed the available reserves of fossil fuels.[1] Furthermore, the adverse effects arising from these fuels, including pollution endangering human health and the emission of greenhouse gases contributing to global warming, underscore the imperative for change.[2] The rapid depletion of these resources, coupled with the worsening environmental repercussions of their extraction and utilization, highlights the urgency of transitioning towards more sustainable energy alternatives. Yet, this shift poses significant challenges, predominantly of political and technical dimensions.

Water splitting, which results in the generation of hydrogen (H_2) and oxygen (O_2) gas, represents an environmentally friendly, sustainable, and fossil-free route for producing hydrogen gas — an exemplary clean energy carrier.[3] To harness the chemical energy encapsulated in hydrogen bonds for electricity generation, fuel cell operation is essential. This process reverses the water splitting reaction, thereby producing energy in the form of electricity from chemical compounds. A promising technology for uninterrupted power supply integrates both processes in the so-called unitized regenerative fuel cell (URFC). URFC systems, depicted in Figure 1.1, are a dual-mode innovative technology that can switch between water electrolysis (to generate H_2) and fuel cell operation (to convert chemical carriers into green electricity).[4] They represent a compelling solution for achieving efficient and sustainable energy storage and generation with minimal environmental impact and in the minimal weight[5].

In the electrolyzer mode, illustrated by yellow arrows in Fig. 1.1, external energy that can be generated from renewable sources such as solar or wind power drives the process. In this process water is supplied to the anode, where it is oxidized to produce O_2, protons (H^+), and electrons (e^-). Protons migrate through the electrolyte membrane to the cathode, while electrons flow through an external circuit to the cathode, where they promotes the reduction of protons to form H_2 gas. This overall reaction (Eq. 1.1) comprises two distinct half-reactions: the oxygen evolution reaction (OER) (Eq. 1.2) at the anode and the hydrogen evolution reaction (HER)

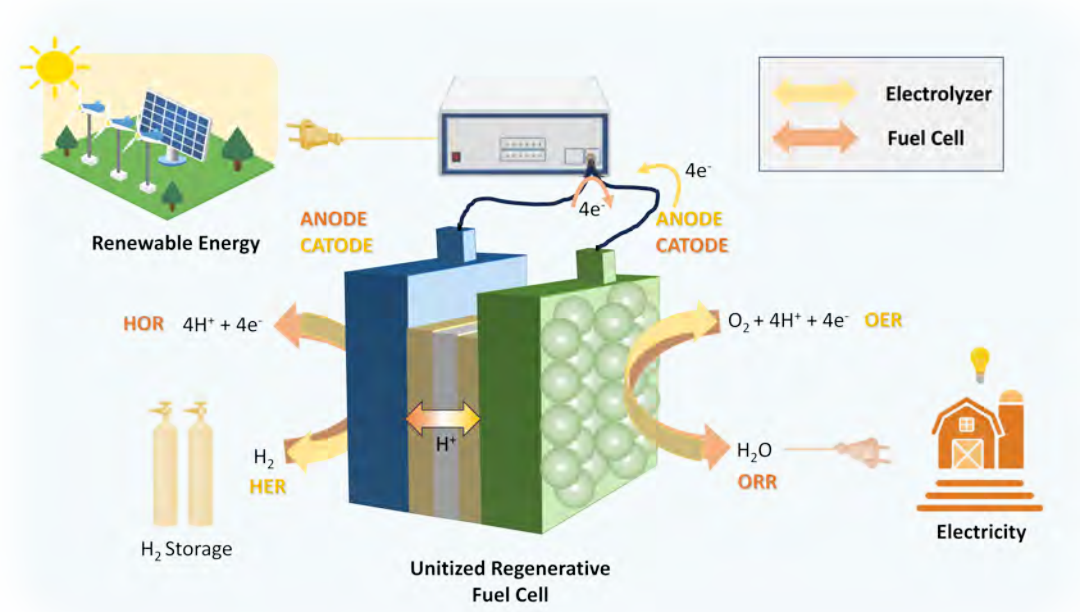

Figure 1.1: Diagram of an Unitized Regenerative Fuel Cell (URFC) system designed for renewable power and hydrogen production in acidic media. The yellow arrows depict the electrolyzer mode, where the system harnesses green energy from wind and solar sources to electrolyze water (H_2O) into hydrogen (H_2), the ultimate clean energy carrier, and oxygen (O_2). Switching to fuel cell mode, illustrated by orange arrows, the system converts hydrogen (H_2) back into water (H_2O), generating clean power in the process. *Created with BioRender.com.*

(Eq. 1.3) at the cathode of the electrolyzer compartment.

$$\text{ORR} \xrightarrow{\text{ELECTROLYZER}} \text{OER}$$

$$2H_2O \rightleftharpoons O_2 + 2H_2 \qquad \Delta E^0 = 1.23V \tag{1.1}$$

$$2H_2O \rightleftharpoons O_2 + 4H^+ + 4e^- \qquad E^0_{H_2O/O_2} = 1.23V \tag{1.2}$$

$$4H^+ + 4e^- \rightleftharpoons 2H_2 \qquad E^0_{H_2/H^+} = 0.00V \tag{1.3}$$

$$\text{HOR} \xleftarrow[\text{FUEL CELL}]{} \text{HER}$$

Conversely, in the fuel cell mode, illustrated by orange arrows in Figure 1.1, the URFC generates clean electricity by utilizing previously produced H_2 and O_2 gases. H_2 is supplied to the anode, where it undergoes oxidation to produce protons and electrons. Protons move through the electrolyte membrane to the cathode, while electrons travel through an external circuit, generating electricity. At the cathode, O_2 gas is reduced by the incoming electrons and protons to form water. The overall process reverses the electrolysis reaction, Eq. 1.1, involving also same two half-reactions: the oxygen reduction reaction (ORR) (Eq. 1.2) at the cathode and the hydrogen oxidation reaction (HOR) (Eq. 1.3) at the anode.

Driving those electrochemical reactions at optimal rates requires specific catalyst materials at the anode and cathode for each process. The electrolyzer's efficiency can be optimized separately from the fuel cell, ensuring that the overall roundtrip energy efficiency of the entire system is also optimized.[6] Focusing on the electrolyzer compartment, the cathode half-reaction, the HER, is defined as a multi-step electrochemical process generating H_2 gas at reasonable currents even with small overpotentials. From a catalyst perspective, overpotential (η) is the extra voltage required beyond the thermodynamic equilibrium potential (E^0) to drive the electrochemical reaction at the desired current rate. The E^0 value for a particular electrochemical reaction is determined under standard conditions, at 298.15 K and a pressure of 1 atm, relative to the standard hydrogen electrode[7]. In an acidic medium with pH=0, this is easily reflected in Eq. 1.3, with $E^0_{H^+/H_2}$ equal to + 0.00 V for the HER process.

In contrast to the HER, the OER on the anode side is recognized as the bottleneck in the overall process. It is stated in Eq. 1.2, that the thermodynamic equilibrium potential is + 1.23 V for the OER process as well as for water splitting reaction (Eq. 1.1). However, in real applications, the actual potential required to drive the reaction is higher than this minimum due to various factors associated with the reaction (i.e. high activation energy, mass transport limitations, high resistance, etc.) producing kinetic barriers. Those barriers that cause slow kinetics of the oxygen-evolution electrochemical reaction result in a substantial overpotential, which constitutes the majority of the energy loss and limits the efficiency of water oxidation, consequently jeopardizing electrolysis and URFC applications.[8] This drawback arises from the chemical process where four electrons must be removed from two water molecules, breaking four O-H bonds to obtain an O-O bond, making it energetically demanding and requiring efficient catalysts for high efficiency.

The pioneering studies of the 20th century have greatly influenced contemporary research on developing new catalyst surfaces for next-generation devices. In this context, minimizing overpotential is key to designing efficient electrochemical systems, as it directly impacts their energy efficiency and performance. In catalysis, lower overpotential indicates a more efficient catalyst, requiring less additional energy to drive the reaction. Therefore, developing ideal OER catalysts and understanding the mechanistic details involved in overpotential formation during the OER process are crucial for optimizing oxygen electrochemistry.

One promising class of catalysts for OER are generally considered the oxides of precious metals[9–11]. Only RuO_2 and IrO_2 are optimal catalyst in acidic media[12–14], although they exhibit instability under high anodic potentials[12]. In alkaline media, many transition metal oxides such us nickel oxides[15, 16], cobalt oxides[15, 17] and manganese oxides[18, 19] have revealed high activity for OER. Their low stability in acidic conditions, however, prevents them from being used in proton exchange membrane (PEM) fuel cells. Thus, developing optimal materials with enhanced catalytic capabilities and stability in acidic media stands as a pivotal task for advancing sustainable energy production. Nonetheless, this long-standing goal presents challenges due to the limited understanding of the mechanisms governing the catalytic activity and stability of these materials. The lack of fundamental insights into the structure-dependent molecular dynamics underlying

catalytic performance on such intricate materials difficulties the rational control over their application. Hence, a comprehension of the macroscopic catalyst mechanism in relation to its surface structure is imperative. Establishing a direct correlation between catalyst performance and its structure, chemical composition, and reactivity is vital for identifying the key prerequisites for designing surfaces with specific catalytic properties.

A direct correlation among catalyst chemical and structural surface properties and its dynamic changes under operation is challenging due to the multitude of parameters that influence the catalyst-electrolyte interaction. A strategic approach to elucidate the structure-dependent mechanism behind catalytic performance involves rationalizing activity or stability trends of catalysts through a single-parameter descriptor. This descriptor could be a microscopic property related to either the catalyst or the catalyst-reactant interaction that governs the catalytic process, such as lattice parameter, bond strength of intermediates[20], or the enthalpy change (ΔH) associated with the transition from a lower oxide to a higher oxide[21], among other possibilities.

Advancements in computational power and the implementation of new methodologies have significantly facilitated the study of catalyst activity and stability trends through single-parameter descriptors. This progress has allowed the explicit description of OER activity using density functional theory (DFT) calculations. By employing a straightforward linear free energy model, researchers have linked overpotential to the binding energies of intermediate species.[10, 22–24] Studies have shown that the binding energies of *OH, *O, and *OOH species on metal and metal oxide surfaces exhibit universal linear scaling relationships, having an associated intrinsic overpotential in each step.[22–24] This linear scaling relationship arises because all potential-induced dynamic processes during OER occurs in the same active site. Therefore, understanding which is the limitant-rate step and the real oxygen-based catalytic phase on the catalyst surface that evolves the oxygen production becomes paramount in crafting catalysts with optimal designs. Consequently, the design of functional active surfaces capable of disrupting these scaling relationships between energies could reduce overpotential, enhancing the activity and stability of surfaces for OER. By revealing the surface-dependent dynamics of OER catalysis, the direct activation of the OER mechanism through the modulation of the chemical and structural properties of the catalyst surface could be achieved, specifically targeting the actual active surface phase formed just before the production of oxygen.

However, there is a limitation in the theoretical scaling relationship to the obtained experimental responses due to the restricted number of parameters that can be evaluated by DFT.[22, 24] To uncover the dynamics of OER catalyst surfaces, a comprehensive experimental understanding at the micro- and nanoscale is essential. Progress in this area necessitates a thorough understanding of the processes occurring at the electrode-electrolyte interface from macroscopic level and both micro- and nanoscale perspectives. This involves delving into the fundamental chemical and catalytic properties of surfaces and their phases, elucidating their relation to macroscopic catalytic performance. However, the complexities of real catalytic systems and the limited availability of experimental techniques capable of probing the electrochemical interface under reaction conditions with sufficient surface sensitivity

pose challenges to acquiring this knowledge.

In electrochemistry, surfaces play a pivotal role in catalyzing reactions and influencing their outcomes. Surfaces typically exhibit various low-coordination sites, such as steps, kinks, and point defects, which are often more reactive than the basal plane. These surface entities are frequently considered active sites during a catalytic reaction, raising a longstanding question in heterogeneous catalysis about their influence on the activity and selectivity of the reaction. Indeed, surface polarization and interaction with the electrolyte (solution) promote dynamic changes on active sites and hence on surface. When an electrode is polarized during electrochemical processes, several surface dynamics come into play. Firstly, polarization may lead to surface rearrangements. This can involve the formation or dissolution of surface oxides, changes in surface roughness, and alterations in the surface electronic structure. For example, during the OER, an electrode surface may undergo restructuring to expose active catalytic sites or to stabilize intermediates involved in the reaction mechanism. Secondly, chemical evolution occurs as a result of the interaction between the electrode surface and the electrolyte. Electrolytes can induce changes in the chemical composition of the electrode surface, leading to the formation of new surface species or the alteration of existing ones. This chemical and structural evolution is crucial in determining the catalytic activity and stability of the electrode during prolonged electrochemical operation. To date, there have been few experimental studies that have attempted to demonstrate a direct correlation between the catalyst's activity and stability and its atomic and molecular surface structure.[25–27] For this reason, historically, scientists predominantly relied on the traditional empirical approach to formulate high-performance catalysts and enhance reaction conditions.[28]

As aforesaid, understanding the potential-induced surface dynamics is essential for the understanding and design of novel catalysts. Here, the utilization of ultra-high vacuum (UHV, base pressure below $1 \cdot 10^{-9}$ mbar) techniques and the evolution of more and more precise surface science methods provided a unique advantage. This enabled the examination of single crystals' surfaces, serving as model catalysts, marking the exploration of surface properties at the atomic level [29, 30]. Many surface science methods have been developed in the last few decades to investigate surface properties [29]. These methods are very different among them and can be classified based on the type of incident excitation probe used: electrons, ions or photons.[31] These fundamental categories encompass a diverse array of techniques utilized for analyzing the structure, composition and electronic properties of surface materials, including spectroscopy, microscopy, and spectrometry, among others. In particular, the use of surface science techniques in molecular studies of catalytic processes yields pertinent data on the adsorption, transport, and reactivity of molecules on metal surfaces[32–34] and oxide surfaces [35–38].

The most important shortcoming of traditional surface science studies conducted under UHV conditions is the limited information they provide about the structure of the catalyst surface under real reaction conditions. By exploiting innovative techniques and cutting-edge instrumentation, the integration of surface science technology with electrochemical reaction-based cell systems can revolutionized the investigation of catalysis on both mesoscopic and nanoscopic scales.[39–42] This integrated

approach can furnishes insights into surface structure, chemical composition, and kinetic data of electrochemical reactions from a surface science perspective unveiling catalyst dynamics, thereby positioning the discipline at the forefront of physics and physical chemistry.

The crucial step to perform synergistic studies of surface sciences and electrochemistry entails transferring the electrode from de EC cell (liquid solution at atmospheric pressure) to the surface analysis chamber under ultra-high vacuum conditions. Ideally, this transfer should occur without inducing alterations in surface structure or composition. The initial analysis of electrode surfaces utilizing UHV characterization techniques traditionally involved a *post-mortem* study with a transfer from liquid to UHV, exposing the electrode to air.[43, 44] This approach was employed to investigate, among other things, the corrosion process of metals through AES and XPS [45]. However, the drawback lies in the lack of control over the surface during air transport, leading to Auger spectra of the samples typically exhibiting atmospheric contaminants such as C, O, and N.[43] As a result, this method often promotes undesirable post-oxidation or adsorption processes, leading to distortions in the post-characterized system as it was extracted from the EC. Therefore, studying aroused non-inert, irreversible, or (meta-)stable phases in surface catalysts due to oxygen evolution reaction dynamics requires a clean and controlled transfer of electrodes between the electrochemical cell and the UHV surface analysis chamber.

Different transfer systems between UHV set up and an electrochemical cell have been developed to address and surmount this challenge creating surface-analysis apparatus that integrates multiple surface science techniques with an electrochemical chamber.[46–50] This approach has significantly advanced the study of emersed electrochemical phases by employing UHV-EC compatible systems that utilize various surface-sensitive techniques, such as: X-ray photo-emission spectroscopy (XPS)[51], scanning tunneling microscopy (STM)[52] and (SXRD)[53]. Despite effectively avoiding uncontrolled chemical and structural changes in catalyst samples, this approach raises several issues such us the alteration in hydrodynamic conditions, that alters surface species only presented at the double-layer electrode-electrolyte interface when voltage is applied. Consequently, pre- and post-electrocatalytic UHV characterization of the catalytic surface aids identifying and evaluating non-reversible dynamic surface changes [54] under electrochemical processes.

In essence, gaining a fundamental understanding of how local properties such as chemical and structural composition of surface catalysts influence their catalytic characteristics is a critical challenge in optimizing catalyst design. Achieving this goal necessitates a comprehensive perspective at the micro- and nanoscale on surface properties and their relationship to macroscopic catalytic performance and dynamics. This endeavor faces obstacles due to the intricate nature of real catalytic systems and the absence of experimental techniques capable of concurrently probing the electrochemical surface interface during catalytic process with chemical and structural surface-sensitive techniques on the same sample. The aim of this thesis is to address these gaps by offering an experimental approach to comprehensively understand the molecular aspects of the electrochemical interface. This involves uncovering the dynamic chemical and structural changes during electrochemical processes such as electro-oxidation and the OER. By revealing the genuine catalytic phases involved,

this research aims to provide a systematic framework for developing more efficient catalysts tailored for enhancing OER performance.

This thesis investigates the compatibility and effectiveness of integrating electrochemical methods with surface-sensitive physics techniques operating in UHV conditions. The newly developed EC-UHV system's capabilities are assessed through model systems relevant to the OER. By employing this synergistic approach, the thesis aims to offer comprehensive insights into the behavior of real electrocatalysts mimicking operating conditions, with a specific focus on revealing surface chemical and structural changes during the OER. The experimental strategy was designed to establish a direct correlation between expected theoretical results, previous studies on surface electrochemistry, molecular characterization, and macroscopic electrochemical measurements with surface characterization. The project involves constructing a modular setup enabling structural, chemical, and electrochemical analysis on the same sample under controlled conditions. Methodological procedures for integrated catalyst surface investigation via synergistic UHV-EC experiments are outlined, emphasizing the development and providing a comprehensive overview. To achieve these objectives the study involves first the construction of the UHV-EC system in conjunction with photoelectron spectroscopy studies and structural imaging of each sample before and after electrocatalytic measurements within a specific UHV chamber. The UHV experimental setup is designed to facilitate sample transfer between UHV conditions and ambient measurements in an electrochemical cell, employing a transfer stage under an inert and controlled atmosphere. Consequently, after electrochemical conditions, the samples can be characterized under surface science techniques, maintaining control over the pressure conditions during the transfer back without exposure to air.

The structure of this manuscript is organized as follows. To begin with, since this thesis integrates two different fields, the first two chapters provide a brief introduction to the most crucial aspects of each — electrochemistry and surface science — necessary for comprehending the discussion of the experimental results presented in this thesis. Chapter 2 introduces the fundamental concepts of electrocatalysis and surface electrochemistry, serving as the foundation for the entire thesis. This chapter also elucidates the primary electrochemical techniques. Chapter 3 provides a surface science perspective, offering brief insights into UHV system. It details the techniques used for sample preparation and characterization before and after electrochemical evaluation. Chapter 4 describes the experimental EC-UHV compatible setup designed as an starting point of this thesis and the process of its implementation. Following, Chapter 5 delves into the system's capability to investigate model anodic surfaces, like Au(111), at high anodic potentials analyzing the electro-oxidation mechanism in acidic media and highlighting the role of anions. This chapter also benchmarks the setup and relates its findings to the broader research community. The final section of the thesis, explored in Chapter 6, focuses on tunable manganese oxide structures and their implications on the OER response, investigating the evolution of surfaces during the OER process. The manuscript concludes with Chapter 7, offering concluding remarks and outlining future prospects

stemming from this project.

Chapter 2

Electrocatalysis and surface electrochemistry

In electrocatalysis, the effects of electrode material properties on the mechanism and rate of electrochemical reactions at the electrode/electrolyte interface are studied in detail. As it was mentioned in the Introduction, this thesis aims to investigate fundamental aspects of electrochemical model processes on catalyst surfaces from a surface physics perspective, integrating electrochemistry and surface science. To this end, this chapter provides a brief introduction to the general background related to electrocatalysis and surface electrochemistry, offering a summary of essential concepts for the surface science community necessary for a correct comprehension of the present research.

This chapter addresses the core of surface electrochemistry, beginning with the definition of a catalyst and the concept of the electrified interface, crucial for facilitating surface(-sensitive) electrochemical reactions. Understanding the catalyst's role and the nature of the electrified interface is paramount to exploring the intricate mechanisms of electrochemical reactions occurring at the catalyst surface, where the interaction between the catalyst material and the electrolyte significantly influences efficiency and stability.

This chapter also includes a section dedicated to the Oxygen Evolution Reaction (OER) mechanism, which is crucial for understanding how catalysts facilitate this pivotal process in energy conversion technologies. It discusses the accepted mechanisms in acidic and alkaline media, which involve electrode oxidation leading to oxygen evolution, and explores the theoretical dependencies on surface properties and overpotential. Various electrochemical prediction tools based on thermodynamic principles are described, including the Pourbaix diagram and Volcano plot, which offer insights into optimal material properties for achieving high stability and performance. The chapter also covers experimental analysis of the kinetics underlying the OER mechanism through Tafel slope analysis, elucidating the kinetics of electrochemical reactions and providing deeper insights into reaction rates and mechanisms.

To achieve a comprehensive macroscopic understanding, various electrochemical

techniques such as cyclic voltammetry and chronoamperometry are explained. Each technique is discussed in terms of basic concepts and principles, emphasizing its relevance in studying electrocatalytic systems.

2.1 Concept of electrocatalysis: what is a catalyst?

Before delving into the area of electrocatalysis and its applications to electrocatalytic reactions, we should first define what a catalyst is.

In 1835, Jöns Jakob Berzelius, a Swedish chemist, introduced the term "catalysis" to describe chemical reactions influenced by a substance that remains unconsumed in the process, seemingly playing no direct role in the reaction.[55] The term and the highlighted phenomenon sparked extensive discussions throughout the 19th century, culminating in the formulation of a widely accepted definition by the German chemist Wilhelm Ostwald: "A catalyst is a substance that speeds up the rate of a chemical reaction without becoming part of its final products".[56] Catalysis plays a crucial role in a wide range of processes since the absence of catalyst typically indicates a negligible reaction rate compared to its presence. The catalyst operates by establishing intermediary compounds with the molecules involved as reactants, presenting an alternative and faster route to the ultimate products. Therefore, the catalytic process requires the existence of a surface where reactants can chemically or physically be adsorbed and participate in reactions, leading to the formation of products characterized by reduced activation energy (E_a).[57, 58] A catalytic process is schematized in Figure 2.1 which depicts the potential energy across the chemical reaction for the conversion of reactants A and B into product C in absence of a catalytic surface. A high energy barrier (represented in red) is observed. When the reactants interact with a suitable catalytic surface, intermediates such as A-B undergo stabilization, facilitating reactions with reduced energy barriers, as illustrated by the blue curve. Thus, in the presence of the catalyst, the reaction occurs with lower free energy.

The catalysis processes are classified as homogeneous or heterogeneous depending on whether the surface is in the same state or a different state as the reactant, respectively. According to this classification, electrochemical processes are considered pure heterogeneous catalysis as the reactions involve a solid surface (the electrode) and a solution in the liquid phase (electrolyte). In the majority of electrochemical applications, the electrode remains chemically unchanged during the process due to its general inertness, except in cases of electrodeposition, dissolution or corrossion processes. Consequently, all electrode could be termed as electrocatalysts. However, in electrocatalysis, a specific interaction between the catalyst's surface and reactive species is mandatory. An electrocatalyst is then defined as a surface that interacts specifically with reactants, creating adsorbed (meta)stable reaction intermediates (generally considered as true active catalyst). These intermediates subsequently undergo the breaking and creation of new bonds until the reaction products are generated, while the catalyst itself remains unaltered after the reaction evolves. In practical terms, a material is considered an electrocatalyst when the formation of these intermediate (meta)stable states significantly enhance the reaction rate com-

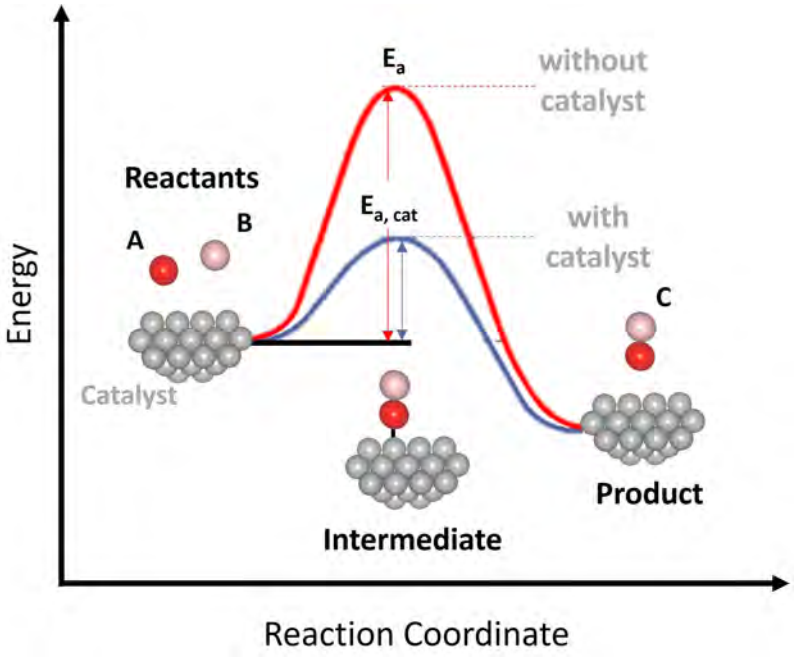

Figure 2.1: Energy diagram of an exemplified (electro)chemical reaction: A + B → C. Depiction of energy variation across the chemical reaction coordination, showcasing the reduction of the activation energy facilitated by the presence of a surface actuating as a catalyst. In this representation the activation energy of the bare (electro)chemical reaction (E_a) is larger than the one occurring on a catalyst's surface ($E_{a,cat}$). The activation energy for the reaction is notably reduced through the existance of an stable intermediate formed on the catalyst surface.

pared to other electrodes.

A distinctive feature of electrochemical reactions and electrocatalysis is that they are surface reactions involving electron transfer (ET), particularly in the case of electrolysis due to the application of a potential. Oxidation-reduction processes, or redox reactions, are the general terms used to describe these ETs. Reduction is the process in which at least one electron is gained, whereas oxidation is the reversed reaction in which one or more electrons are lost. Equations 2.1 and 2.2 present a generalization of these reactions, respectively.

$$Red - ne^- = Ox \tag{2.1}$$

$$Ox + ne^- = Red \tag{2.2}$$

where *Red* represents the reduced species and *Ox* is the oxidized species. Since in electrochemistry (EC) there should be a mechanism for maintaining charge transfer equilibrium, the electrochemical cell should include a minimum of two electrodes to establish a closed circuit. These reactions have the capability to produce energy through spontaneous occurrences, such as in galvanic cells. In an electrolytic cell, primary focus of this thesis, external electrical energy is introduced into the circuit to facilitate a non-spontaneous reaction. In this case, oxidation occurs at the anode, and reduction occurs at the cathode. Figure.2.2 provides an illustration of the

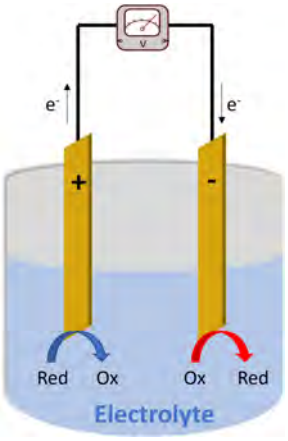

Figure 2.2: Schematized electrochemical cell.

processes. Additionally, these electrodes serve as conduits for the electrons to travel, allowing them to flow from the anode to the cathode via external cell wires. The current, i, which travels through the external circuit is determined as follows:

$$i = A \cdot j \tag{2.3}$$

where A is the electrode area expressed in cm^2 and j is the current density in A/cm^2. By monitoring the current and following Faraday's law equation:

$$q = \int_{t_0}^{t_1} idt = mnF \tag{2.4}$$

where F refers to the Faraday constant 96485 C/mol, m is the number of moles (mol) of the starting reactant, t is the time (s), and n refers to the number of electrons exchanged per reactant molecule[59], the transferred charge, q, can be calculated by monitoring the current.

An applied voltage between the two electrodes is generally required to drive the reaction, and this potential must be bigger than the difference between the standard potentials of the reactions occurring at the cathode and anode, E_a or E_c. Consequently, the following equation can be used to connect the Gibbs free energy of the total reaction occurring within the electrochemical cell to the cell potential:

$$\Delta G = -nFE_{cell} = -nF(E_c - E_a) \tag{2.5}$$

If the reaction occurs under standard conditions, the relationship is as follows:

$$\Delta G^0 = -nFE^0_{cell} = -nF(E^0_c - E^0_a) \tag{2.6}$$

The Nernst equation, $\Delta E = \Delta E^0 + \frac{RT}{nF} ln \frac{a_{ox}}{a_{red}}$ where R is the universal gas constant and T the temperature, arises from the combination of both, Equations 2.5 and 2.6. This equation describes the dependence between the equilibrium potential (E), the standard electrode potential (E^0), and the thermodynamic activities of electroactive species. Under equilibrium conditions, these activities are equivalent to their values in bulk solution.[60]

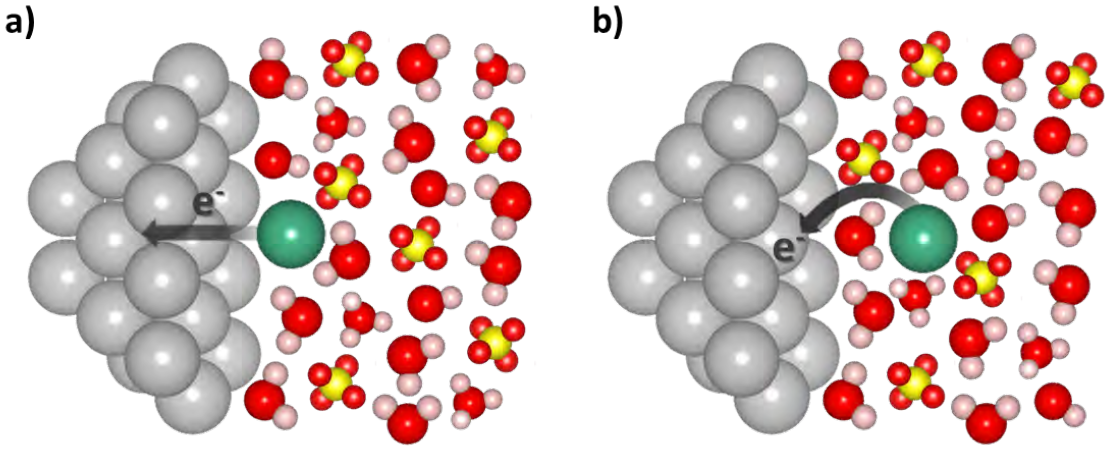

Figure 2.3: Categorization of the two different electrochemical ET reactions on surface electrodes, being a) outer-sphere ET and b) inner-sphere ET.

Electrode reactions often involve multistage processes, with ETs representing just one step in the hole mechanism. Usually, additional steps such as mass transfer and chemical reactions occurring before and/or after ET, also have influence on the electrode reaction. The overall rate of the reaction is governed by the rate constants associated with these processes, and their modulation is controlled by the applied voltage. However, the heart of electrochemical processes is the ET rate.

The electrocatalytic performance (i.e. the ET rate) is governed by the chemical and electrical interactions occurring between the electrode surface and the electrolyte (solution containing electroactive species). Electrical interactions in electrochemical reactions can be categorized as either inner-sphere or outer-sphere ET, based on the character of the interplay between the electrode and electrolyte.[61] The distinction lies in the ability of reactive or ligand species to either overrun the inner layer of adsorbed water on the electrode surface, establishing a direct interaction with surface, or remain outside, resulting in an indirect interaction. Visual examples of both interaction types are illustrated in Figure 2.3a-b. In both scenarios, the electron is transferred across the interface, typically spanning an order of magnitude on the scale of 1 nm.[62]

A distinct classification is based on the overlap of electronic state of reactants and the electrode surface during the transition state[63, 64]. In the context of weak overlap ETs, the transition state remains indifferent to the spatial separation between reactants and the electrode. Conversely, strong overlap ET is significantly influenced by the distance between the electrode and the reactant, exerting a pronounced influence on the energy of the transition state due to the specific interaction between the surface and reactant species. In this scenario, reactant is chemisorbed through a chemical bond to electrode surface.

When considering both interaction classifications, outer-sphere reactions consistently involve weak overlap interactions where species can be physisorbed, making them non-electrocatalytic processes. In such reactions, electrons tunnel between species in the electrode's surroundings, and the reaction rate is determined by varia-

tions in the ion environment. In the second case, inner-sphere reactions can exhibit strong or mild overlap interactions depending on the characteristics of the electrode and reactants. When inner-sphere processes entail strong overlap transfer is when electrocatalytic events are identified. These electrocatalytic processes are influenced by the specific solvation of reactants at the interface or alterations in the structure of the electrified interface, leading to differences in a given catalysis reaction among electrode materials.

2.2 The core of electrochemistry: the interface and the adsorption processes

As I mentioned before, in electrochemical processes, the reaction occurs at the interface that arise when an electrode and an electrolyte are in contact. This type of interface is characteristic due to its chargeability. Upon the polarization of electrode, electromigration of ionic charged molecules occurs onto opposite charge contained in electrified contacts. An electrified interface is the name given to this chargeable interface formed after polarization. The entire electrified interface maintains electroneutrality; and a distinctive electric double layer emerges, featuring inner and outer phases and a specific potential distribution. This formation arises from the non-uniform distribution of charged particles from the electrode to bulk electrolyte. On the inner side of the electrode there exists a specific charge density due to an excess or deficiency of electrons in the surface layer, depending on applied polarity, while the outer side is composed by counterions present in excess in the electrolyte, possessing the opposite charge density. The resulting potential drop within this electric double layer is designated as the interfacial potential. The establishment of this layer implies the creation of potent electrostatic fields at the interface, characterized by a separation of less than 1 nm between the two sides of the electric double layer and potential differences that may extend to several volts.[65]

Over approximately 100 years, a generally accepted model for the electrode / electrolyte interface (electrified interface) has been established [65] and is schematized in Figure 2.4. Various structural models have been proposed during this time to describe the properties of this phenomenon. The initial assumption stated that non-Faradaic processes occur at the interface, implying that no electron transfer takes place and only adsorption processes occur. Following this assumption, Helmholtz defined the interface as two rigid layers formed by the metal surface, with an excess or deficit of charge, and an equivalent quantity of ions with the opposite charge.[39] The interface becomes neutral as a result of the solvation of metal charges with ions present in the electrolyte that have equal and opposite charges [39]. The name Outer Helmholtz Plane (OHP) is given to this solvated ions layer (indicated in Fig. 2.4). In this static model, adsorption is non-specific and purely based on electrostatic forces. This holds true for solvated cations or anions with a strong solvation shells. However, most anions and cations have weaker solvation shells. In such cases, they are specifically adsorbed on the electrode surface through a chemical bond, forming the inner Helmholtz plane (IHP). This chemisorption involves a charge transfer. In the context described by Gouy-Chapman[66], the decrease in potential follows an

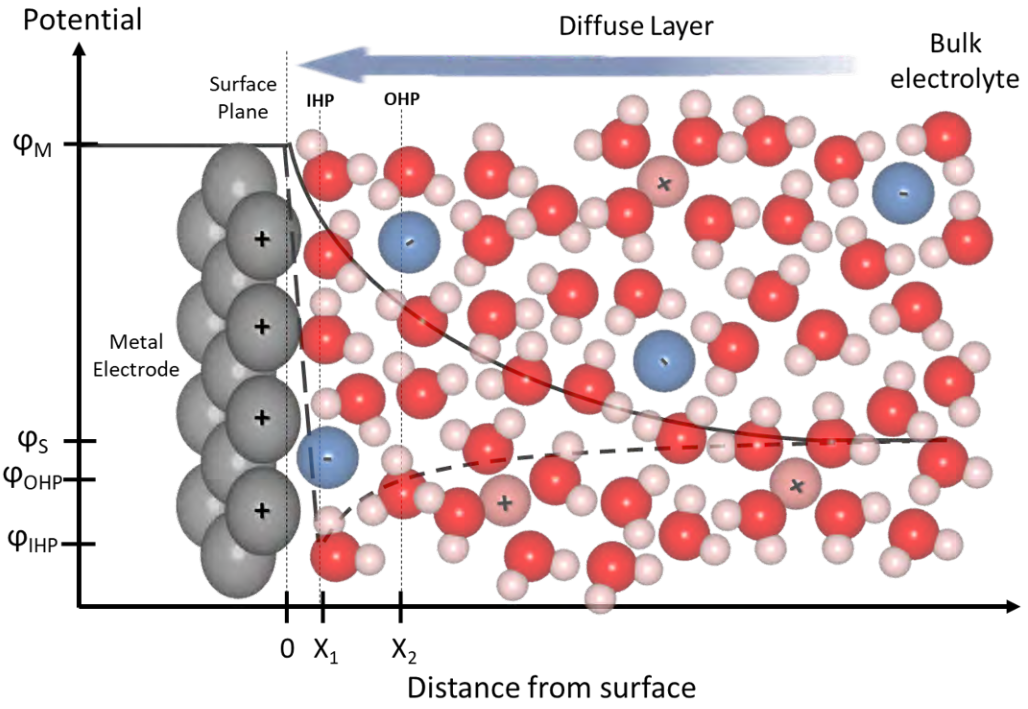

Figure 2.4: Schematic diagram showing the potential decay across the electrochemical interface for a positively charged metal surface considering the accepted double-layer model of the electrode/electrolyte interface.

exponential pattern as it traverses from the OHP to the bulk solution, progressing through the diffusive layer. As a result, the potential variation through the electric double layer depends on the polarity of the metal surface and the adsorption strength of the specifically adsorbed ions.

The widely accepted Gouy-Chapman-Stern-Grahame model[66], which effectively elucidates the majority of experimental findings, is formed by integrating the Helmholtz and Gouy-Chapman models (known collectively as the Stern model) with Grahame's insights on specific adsorption[67].

Additionally, physical water molecules adsorption plays a crucial role in the electrified interface. The applied potential and electrode nature have an impact on the orientation of the water molecules at the contact. The lowest energy configuration for such polar molecule or orientation is the conformation where its dipole moment is aligned parallel to the electric field. Following this assumption, water molecules align with the oxygen atom to face the electrode when it is positively charged. On the other hand, water molecules orient the oxygen atom in the opposite direction when the surface is negatively charged. The water's direction adsorption has a major effect on how quickly electrochemical reactions occur and which typology of reactions are enhanced.

In contrast, within systems characterized by chemisorbed species from electrolytes onto electrode surfaces—an occurrence of paramount importance in electrochemistry—the traditional double-layer theory faces are inadequate in comprehensively elucidating the intricacies of structure and dynamics at the interface. [68]

Factors such as the transformations in solvation shells when ions adhere to a surface and the modifications they undergo during processes like charge transfer or adsorbents intercalation pose significant uncertainties. The challenge arises from the lack of atomic-level characterization of solid/liquid interfaces.[69] In recent years, substantial efforts have been dedicated to provide the specific structures and chemical states undergoing changes within the electrified double-layer, potentially leading to a reevaluation of the generally accepted definition. In this domain, combining electrochemistry with surface science techniques shows potential as a method to unravel these intricacies. Various approaches and complementary probes for studying the electrified interface over different time scales have been investigated. Chapter 4 will extensively analyze the strengths and limitations associated with each approach.

2.3 Surface-sensitive reactions: Well-defined surfaces as simplified cases

The fundamental phenomenon of electrocatalysis is the interaction of reactive species with the electrode surface, leading to the formation of the electrified interface where electrical charge is transferred. Because of that, it is crucial to understand the interface's structure, which includes both the electrode surface and the species in the solution. Commonly utilized catalyst structures, such as nanoparticles (NPs) and polycrystalline surfaces, lack precise surface definition due to their composition of mixed facets, steps, kinks, and defects, each exhibiting distinct crystal orientations and local electronic structures. Consequently, the electrochemical behavior of these catalysts result from the combined contributions of numerous individual sites, rendering them unsuitable for both experimental and theoretical inquiries at the molecular or atomic level. To attain a comprehensive understanding of electrochemical processes, it is preferable to employ atomically well-defined surfaces characterized by an ordered two-dimensional arrangement of atoms, exemplified by single-crystal electrodes. These distinctive surfaces enable a thorough microscopic comprehension of the fundamental chemical and catalytic properties inherent to a surface, in connection with its macroscopic catalytic performance.

A single crystal electrode is defined by its well-oriented surface, characterized by a uniform distribution of active sites and uninterrupted periodicity. Atom positions that are organized to form a periodic lattice can be used to classify the structure of a single crystal.[70] Determining the crystal structure is possible by understanding the repeat unit's structure and the lattice's periodicity. Unitcell is the name of the fundamental repeat unit for the lattice. Face-centered cubic (fcc) lattices are found in the majority of metals (Cu, Pd, Ag, Ir, Pt, Au) that are employed as electrochemical electrodes.[71] This implies that the unit cell, representing the smallest repeating arrangement of atoms within the bulk structure, takes the form of a cube with atoms positioned at both the center and vertices of its faces. The figure illustrating the bulk metal structure and atom distribution within the unit cell of an fcc lattice is presented in Figure 2.5a.

Well-ordered surfaces are obtained by cutting the metal in a specific direction parallel to a crystallographic plane, as shown in Figure 2.5b. Within a crystal

lattice, this plane is characterized by Miller indices consisting in three numbers named '<hkl>'; which indicates the surface's orientation in regard to the crystal axis. The basal planes, or crystal faces with the lowest Miller index, are the most commonly used surfaces in electrochemistry. There are three basal planes noted as (111), (100) and (110) that are obtained by cutting the metals along the planes shown in Figure 2.6.

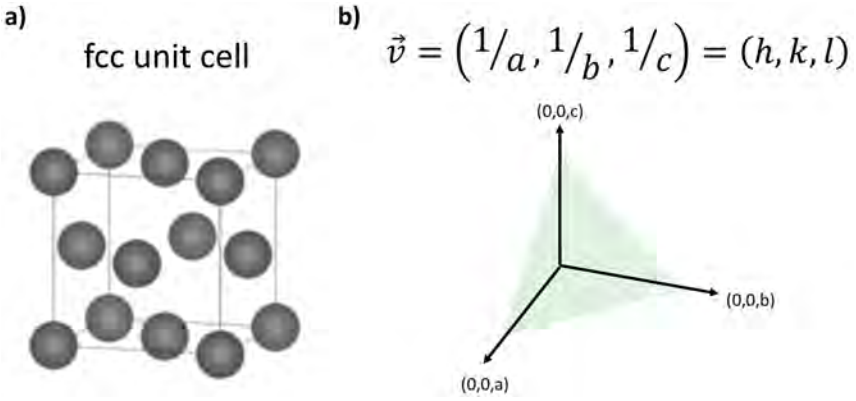

Figure 2.5: a) Depiction of the unit cell in a face-centered cubic (fcc) lattice, emphasizing the positions of atomic centers. b) Visualization of the plane defined by the Miller indices <hkl>.

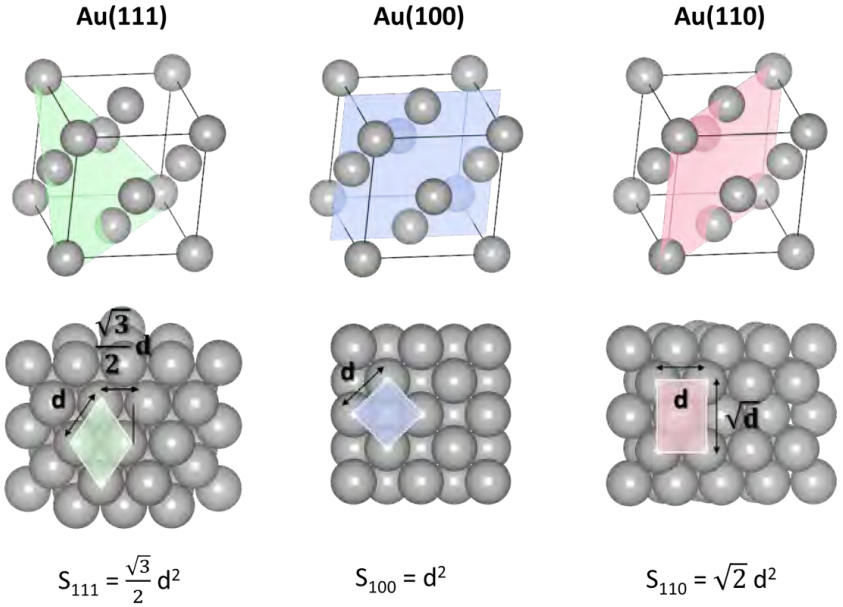

Figure 2.6: The face-centered cubic gold basal planes and the corresponding 2D unit cells scheme. The different site types and each unit cell's surface area (S_{hkl}) value as a function of atomic diameter (d) are indicated for each basal plane.

From an atomistic approach, the atomic arrangement producing different type and number of catalytic sites plays a crucial role in catalysis. For this reason, surface atomic density is an important surface parameter in surface electrochemistry. This parameter refers to the number of atoms per unit area present on the surface. A higher atomic density generally implies more atoms per unit area, potentially leading to an increased number of active sites for catalytic reactions. However, it may also result in increased competition between atoms on the surface, influencing reaction selectivity. In contrast, in some cases, a lower atomic density could promote greater mobility of reactants on the surface, which might be beneficial for certain processes. The following equation can be applied to calculate the surface atomic density on each basal plane:

$$N_{hkl} = \frac{n}{S_{hkl}} \tag{2.7}$$

where n is the number of atoms in the unit cell and S_{hkl} is its area, described in the bottom part of Fig. 2.6 for each basal plane. For instance, in the case of gold, Au, the (111) plane exhibits the highest atomic density, followed by the (110) and (001) planes.

Also, it is possible to calculate the theoretical charge surface density (q_{hkl}) related to any specific orientation for a complete monolayer (ML) of an specific adsorbate (θ=1 ML) by considering the number of transferred electron per one metallic atom applying Faraday's law using the equation 2.8.

$$q_{hkl} = N_{hkl}e = \frac{ne}{S_{hkl}} \tag{2.8}$$

where e is the elementary charge. Table 2.1 summarizes the values of S_{hkl}, N_{hkl} and q_{hkl} (for the adsorption of monovalent ions) in Au basal planes, considering an atomic diameter of 2.95 Å.

In other words, the q_{hkl} parameter refers to the distribution of charge on the surface of a catalytic material due to the adsorption of a monolayer of molecules or atoms. This concept is particularly relevant in understanding the electrochemical processes that occur at the interface between the catalyst and the electrolyte during reactions. In electrocatalysis, the adsorption of species on the surface of the catalyst is a critical factor, helping to facilitate or promote particular reactions. This charge distribution can influence the interactions between the catalyst and the reactants, the energy barriers for electron transfer, and the overall efficiency of the electrochemical reaction. Moreover, it is used to propose possible thickness of adsorbed species as a function of its charge, used to propose dynamic mechanisms.

For example, a higher charge surface density in a specific orientation may enhance the electrocatalyst's ability to adsorb and activate reactant molecules, leading to improved catalytic performance. Predicting and optimizing electrocatalytic processes requires an understanding of the theoretical charge surface density associated with the orientation of an adsorbed monolayer because it sheds light on the electronic structure and electrostatic interactions at the catalyst-electrolyte interface.

It is essential to recall that all discussed in this section up to now concerns nominal structures that could potentially undergo reconstruction depending on their thermal stability. In surface physics, surface reconstruction describes orderly structural

Table 2.1: Calculated values of S_{hkl}, N_{hkl} and q_{hkl} (for the adsorption of monovalent ions) in the case of Au considering an atomic diameter of 2.95 Å.

Basal Plane	$S_{hkl}{\cdot}10^{16}$ (cm^2)	$N_{hkl}{\cdot}10^{15}$ (cm^2)	q_{hkl} $(\mu C{\cdot}cm^{-2})$
Au(100)	8.70	1.15	193
Au(110)	12.30	0.81	137
Au(111)	7.54	1.32 1.26	222

alterations that take place in a material's outermost layer. Because the perfectly terminated bulk surfaces in these situations are unstable, the surface atoms rearrange to form a configuration that is more packed than would be predicted given the fcc crystallographic geometry, which is a structure that is energetically more advantageous.[71] These changes can significantly impact the properties and catalytic activity of the surface. Specifically, surface reconstruction can have several effects on catalysis:

1. Changes in Surface Topography: Reconstruction can alter the arrangement of atoms on the surface, changing the surface topography and roughness. These changes can affect the adsorption of reactant and product molecules, as well as the mobility of surface atoms during catalytic reactions.

2. Modification of Active Sites: Catalysis often occurs at specific active sites on the catalyst's surface. Reconstruction can change the nature and availability of these active sites, directly influencing catalytic activity. There may be a reorganization of atoms that exposes or buries certain active sites, thus altering catalytic efficiency.

3. Alteration of Adsorption Affinity: Reconstruction can also affect the adsorption affinity of reactant molecules on the catalyst's surface. This is crucial since the adsorption of reactant species is often the initial step in many catalytic reactions. A reconstruction that modifies adsorption affinity can influence the kinetics and selectivity of chemical reactions.

4. Effects on Energy Barriers: Reconstruction may alter the energy barrier associated with different steps of a catalytic reaction. This can impact reaction rate and catalyst efficiency by facilitating or hindering certain processes.

This phenomenon happens, among others, in Au basal planes. The thermally stable reconstruction of each Au basal plane is summarized in Figure 2.7.

The Au(111) surface, which is already densely packed, reconstructs into the so-called $(\sqrt{3} \times 22)$ structure (see Fig. 2.7) that consists of a slight lateral compression of the surface atoms in one of the three 110 directions.[72] This causes every 23rd surface atom to be in register with every 22nd atom of the underlying bulk. The surface atomic density in such structure is 23/22 times higher than the one of a Au(111) bulk plane [73]. Thus, the q_{hkl} attributed to $(\sqrt{3} \times 22)$-Au(111) reconstruction is 232 $\mu A \cdot cm^{-2}$. The Au(100) surface reconstructs into a hexagonal close packed (hcp). This 111-like surface is slightly buckled because the top atoms are no

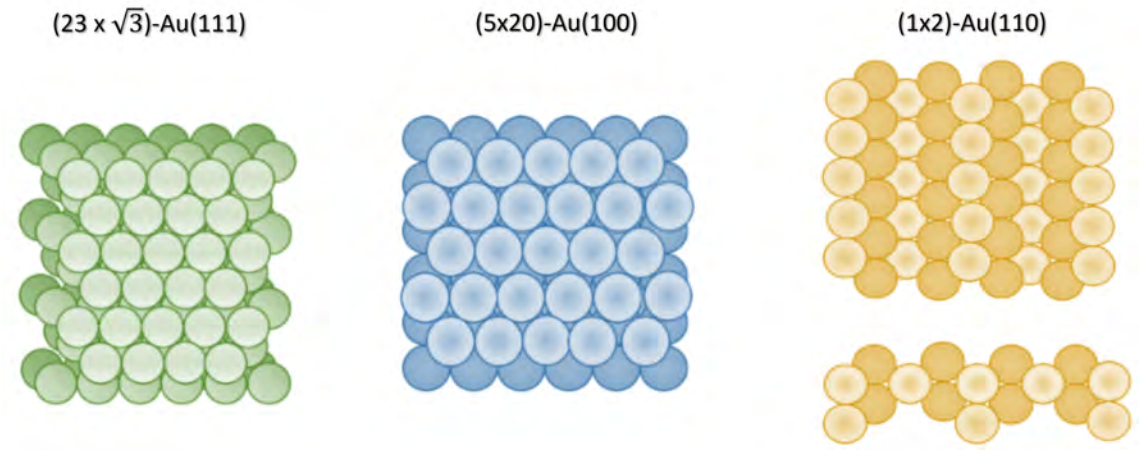

Figure 2.7: Simplified real space models for reconstructed low-index surfaces of gold. From left to right: $(\sqrt{3}\times 22)$-Au(111); $(5\times 20)-Au(100); and (1\times 2)-Au(110)$.

longer in contact with the underlying bulk as schematized in Fig. 2.7. This results in the creation of a surface layer that is denser than the bulk crystal underneath in the Au(111) and Au(001) surfaces.[74, 75] On the other hand, the density of the Au(110) surface reconstruction is 50 % lower than that of the bulk crystal underneath it. The latter case reconstructs into the (1×2)-*missing-row* in which every second row of atoms has been removed to yield narrow 111-microfacets in the 110 direction as clearly seen in the side view represented in the bottom part of Fig. 2.7. Occasionally, a (1×3) or (1×n) with n = 5, 7, etc, reconstruction is observed with correspondingly deeper grooves and larger 111 - microfacets[76].

2.4 Understanding the Electrolyzer Bottleneck: Unraveling Oxygen Evolution Mechanism

As mentioned in the introduction, the oxygen evolution reaction on the anode side is identified as the bottleneck in the overall process taking place in the electrolyzer department of an URFC. According to Eq. 1.2, the standard thermodynamic potential, $E^0_{H_2O/O_2}$, for the OER process is + 1.23 V. However, in practical situations, the actual potential required to drive the reaction is higher since the reaction kinetics is poor, requiring a significant potential difference from the thermodynamic potential. Thus, the development of an active OER catalyst aims to lower the overpotential (η). η can be viewed as the sum of kinetic activation barriers of several intermediate steps involved during OER mechanism. Focusing on the role of oxygen-based intermediates in the mechanism, various theoretical mechanism have been proposed. Our attention will be directed towards the predominant and widely accepted mechanism, which is integrated into free energy models.

For OER in an acidic solution, the mechanism is represented following the formulation provided by Rossmeisl et al.[23] for both metallic and oxide surfaces as follows:

$$H_2O + * \rightarrow {}^*OH + H^+ + e^- \quad \Delta G_1 \tag{2.9}$$

$${}^*OH \rightarrow {}^*O + H^+ + e^- \quad \Delta G_2 \tag{2.10}$$

$$H_2O + 2{}^*O \rightarrow {}^*OOH + H^+ + e^- \quad \Delta G_3 \tag{2.11}$$

$${}^*OOH \rightarrow O_{2(g)} + H^+ + e^- + * \quad \Delta G_4 \tag{2.12}$$

It is important to note that while the reaction mechanism in an alkaline environment exhibits subtle variations, the intermediates involved remain consistent, as described next:

$$OH^- \rightarrow {}^*OH + e^- \quad \Delta G_1 \tag{2.13}$$

$${}^*OH + OH^- \rightarrow {}^*O + H_2O + e^- \quad \Delta G_2 \tag{2.14}$$

$${}^*O + OH^- \rightarrow {}^*OOH + e^- \quad \Delta G_3 \tag{2.15}$$

$${}^*OOH + OH^- \rightarrow O_{2(g)} + H_2O + e^- + * \quad \Delta G_4 \tag{2.16}$$

In both mechanisms, OER proceeds only on an oxidized surface where ${}^*OH$, ${}^*OOH$, and ${}^*O$ are reaction intermediates. Therefore, evaluating a catalyst on this basis must include an assessment of the possible resultant species depending on the pH of the medium, the surface stability, and the acquisition of kinetic data to determine the rate-determining step (RDS), the overpotential and the exchange current density.

2.4.1 Thermodynamics of OER: Pourbaix diagram and Gibbs Free Energy of Intermediates

To effectively deploy water electrolyzers in URFCs technologies, highly stable OER catalysts are essential to withstand metal corrosion and ensure long operational lifetimes. Therefore, a thorough thermodynamic assessment of the most stable phase under operating conditions is imperative.

In this regard, the renowned electrochemist Marcel Pourbaix, made significant contributions in 1945 with his development of the Pourbaix diagram, a pivotal tool in electrochemistry first presented in the *Atlas of Electrochemical Equilibria in Aqueous Solutions*[77]. A Pourbaix diagram, also known as a potential-pH diagram, graphically represents the thermodynamic stability of different surface phases as a function of electrode potential (E) and pH of the environment. It is constructed based on the Nernst equation, detailed in Section 2.1, which correlates the redox potential of an electrochemical reaction to the concentrations of reactants and products.

As an illustrative example, Figure 2.8 presents the Pourbaix diagram for gold. This diagram delineates distinct regions, each denoting a stable phase of gold under varying conditions. Specifically, these phases include metallic gold (Au^0), Au^{+3} ions, and gold (hydro)oxide with stoichiometry $Au(OH)_3$. The black lines dividing these regions indicate equilibrium conditions between both species at the designated conditions, corresponding to specific electrochemical reactions according to the Nernst principle. Additionally, highlighted in red, two crucial lines in every Pourbaix diagram relate to the OER and the HER. These lines are critical because they mark the

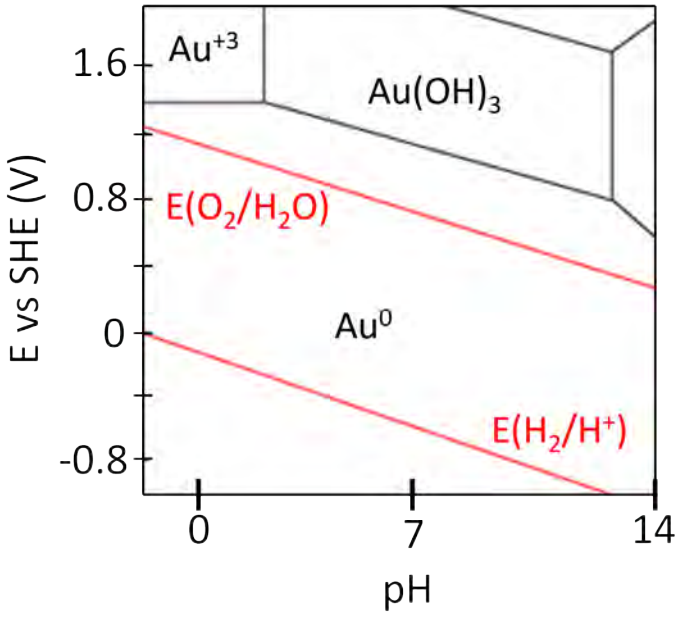

Figure 2.8: Pourbaix diagram of Au electrode, presenting the thermodynamic stable phases as a function of the potential (E) and the pH. Adapted from[77].

potential limits beyond which water either decomposes to form oxygen or hydrogen, defining the electrochemical window of an electrode.

So, this type of diagram is crucial for predicting the stability of catalyst surfaces. By identifying which phases remain stable at potentials near and above OER regimen, researchers can select or design catalysts that retain their activity without degradation from a thermodynamic perspective. However, as we will explore in detail in Chapter 5, this approach only considers ideal scenarios and does not account for the potential influence of ions present in the solution or kinetic factors.

Advancing in the thermodynamics of OER, Density Functional Theory (DFT) methods are employed to compute not only the stability of final phases but also the energies of OER intermediates ($^*OH$, $^*OOH$, and $^*O$) on various catalyst surfaces, encompassing metals and metal oxides. The assessment of binding energies for each step in the reaction mechanism enables the determination of whether a reaction step is thermodynamically feasible in a given catalyst surface, requiring a zero or negative change in free energy, and gives insight into the energy requirements for each step. When all steps exhibit zero or downhill energy trends, the reaction can proceed at "significant" rates. The calculations can be plotted in a free energy diagram, graphical representation used to illustrate the changes in Gibbs free energy (ΔG) that occur during a chemical reaction or process. It provides valuable insights into the identification of the most energy-intensive steps (rate-determining steps).

The binding energies associated with each step of the OER reaction are summarized in Figure 2.9, calculated for both an ideal and a real catalyst. Each reaction step delineated before correlate with the Gibbs reaction energies denoted as ΔG_1, ΔG_2, ΔG_3, and ΔG_4. Koper et al. [22] demonstrated a consistent scaling relation for $\Delta G_(OOH)ads$ - $\Delta G(OH)_{ads}$ independently of the surface nature, being approximately 3.2 eV for a so-called "real catalyst" behaviour. Ideally, an "ideal" catalyst

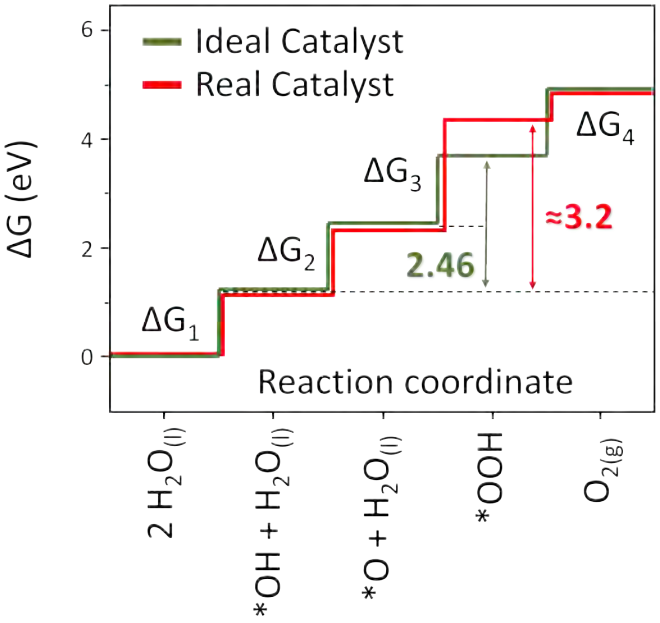

Figure 2.9: Gibbs free energy diagram of the intermediates comparing an optimal and a real catalyst. Adapted from [79].

should exhibit an energy difference of 2.46 eV, corresponding to the transfer of two electrons and protons between steps 1 and 3. This highlights that the rate-limiting step and intrinsic overpotential observed in real catalysts stem from the formation of $^*OOH$.

The Gibbs energy difference between the ideal catalyst and the real catalyst behaviour, following the scaling relations presented in Fig. 2.9, is 0.74 eV. With an optimal distribution of the 0.74 eV offset across two steps, 0.37 eV is equated to each reaction setp. This distribution sets the lowest achievable overpotential as 0.37 eV, which is consistent with the predicted overpotential for RuO_2.[78] Not all catalyst materials match with the performance of RuO_2. Consequently, identifying a straightforward surface with ideal binding energies for all intermediates in OER catalysis appears unattainable. This limitation can be graphically analyzed in a Volcano Plot, a fundamental tool for assessing catalytic activity.

Volcano plots are widely known as the figure of merit for surface- activity relationship benchmarking, illustrating the overpotential in relation to an specific reactivity descriptor such us lattice spacing, bond strength between metal and hydroxide ions (M-OH)[80], or the heat of transition from lower to higher oxide[21]. For example, Figure 2.10 presents a replication of the analyses conducted by Rüetschi[20] (left) and Trasatti[21] (right), demonstrating the correlation between OER overpotential and the energy of M-OH bonds on metal surfaces, and the heat of transition from lower oxides to higher (ΔH_f^0) in transition metal-based oxide surfaces, respectively. These plots typically feature a peak resembling a triangle or an inverted parabola, hence the term "volcano plots" due to their distinctive shape.

Volcano plots are frequently constructed to illustrate Sabatier's principle, which considers optimal surfaces to be those displaying moderate binding energies of reaction intermediates to the catalytic surface.[81] In other words, an efficient catalyst

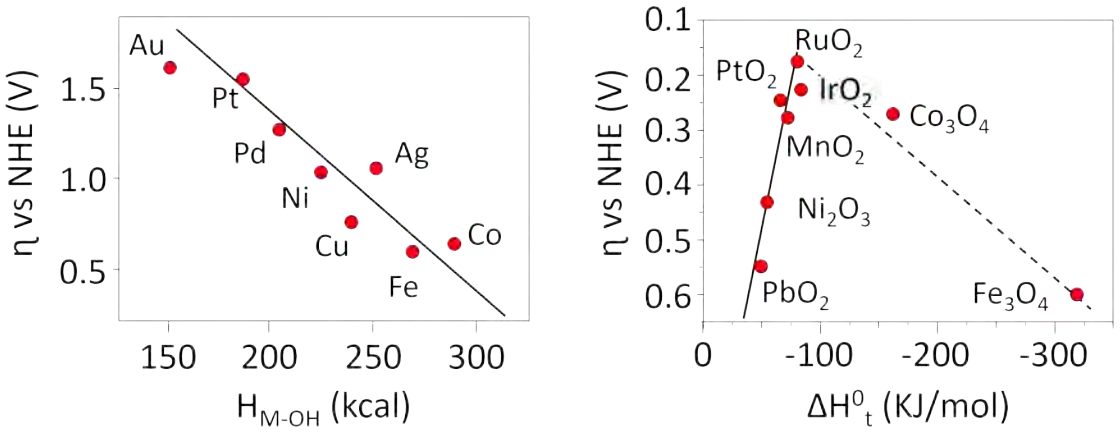

Figure 2.10: Volcano plot showing the overpotential for reaching 1 mA/cm^2 for OER against: (Left) energy of the bond M-OH in 1 M KOH electrolyte and (Right) the heat of oxide transition, ΔH_f^0, in acidic media. The data is digitized from [20] and [21], respectively.

has a surface that interacts strongly with crucial intermediates to facilitate their conversion into products but weakly enough to release them. This characteristic is exemplified by RuO_2, positioned at the peak of the triangular volcano plot depicted in Fig. 2.10, effectively meeting these criteria.

Hence, the computational advancements serve as a potent tool for forecasting the catalytic properties of proposed materials, guiding synthesis design. However, establishing direct connections between the simplified model surfaces and the highly complex real catalytic systems is far from straightforward. The complexity of translating complexity of heterogeneous catalysts from thermodynamic principles to experimental depictions develops in a multifaceted manner, integrating a spectrum of elements including spatial considerations, temporal dynamics, pressure, temperature as well as both the chemistry and structure of the surface.[28, 82] Therefore, it is also important to evaluate catalyst surfaces from a kinetic perspective.

2.4.2 Kinetics of OER: Tafel Slope

At the beginning of the 20th century (1905), Julius Tafel emerged as a pioneering figure in electrochemistry. He revolutionized the understanding of electrode kinetics, which form the basis for electrochemical reaction mechanisms. His discovery of a quantitative method for benchmarking the HER on various electrode materials, and his observation of an exponential relationship between applied current and potential, marked a significant milestone in the field.[83] After his work, the initial attempts to comprehend the OER mechanism experimentally were made in the 1940s and 1950s. Independent research groups conducted experiments using various electrode materials finding similar results to what Tafel had previously found with HER: the activity strongly depends on the material used [84–86]. They highlighted the challenge in comparing the activities of different materials due to significant variations in the current density and measurement procedures.

For a thorough understanding and comparison across various systems, Tafel formulated an empirical principle, referred to as the first law of electrode kinetics. This theoretical framework is based on the fundamental link between η (specific for each catalyst material) and current density j, the primary relation in electrocatalysis, described by the Butler-Volmer equation:

$$j = j_0[exp\frac{(1-\alpha)nF\eta}{RT} - exp\frac{\alpha nF\eta}{RT}] \tag{2.17}$$

where j is the obtained current density, j_0 is the exchanged current density that characterizes the current flowing in both directions when a reaction reaches equilibrium (expressed both in $A \cdot m^{-2}$) and α is a symmetry factor (α=0, 0.5, 1) related with the symmetry among E and E_a of the redox reaction[87].

As indicated by Eq. 2.17, the current exhibits an exponential dependence on the overpotential, η. Here, Tafel introduced a simplification of this relationship expressing it in a logarithmic form, as shown in Eq. 2.18.[88, 89]

$$\eta = \pm \quad b \quad log_{10}\frac{J}{J_0} \tag{2.18}$$

where, in electrochemical terminology, the plus sign denotes an anodic reaction, while the minus sign indicates a cathodic reaction. 'b' denotes the Tafel slope in units of $V \cdot dec^{-1}$. This equation assumes near-equal concentrations at the electrode and in the bulk electrolyte, enabling the current to be exclusively expressed as a function of potential. Stated differently, it is predicated on the idea that the electrode mass transfer rate is substantially higher than the reaction rate and that the slower chemical reaction rate dominates the reaction.

The Tafel slope (b) varies depending on the RDS of the reaction. A step is considered rate-determining if it is at least ten times slower than the other steps in the mechanism [87]. In electrochemical kinetics, a reaction mechanism is described by the types of steps involved: E for electrochemical steps where n electrons are transferred, and C for chemical steps. Reactions involving the transfer of multiple electrons typically occur through multiple sequential steps rather than a single step. While two electrons may sometimes transfer simultaneously (bielectronic step), the transfer of n electrons generally proceeds through n or more sequential steps, forming a mechanism. At least n of these steps are electrochemical (E), while the rest can be chemical (C). Possible sequences of these steps include EE, EEC, ECEC, and so on. Variations among these mechanisms are manifested in different kinetic behaviors, resulting in distinct values of the Tafel slope and hence different RDS.

Determining the electrokinetic mechanism and identifying the RDS of an electrochemical process involves several assumptions, including the symmetry factor and the adsorption isotherm. Table 2.2 summarizes common electrode reaction mechanisms, illustrating the range of Tafel slopes.[90] The numerical values were calculated based on different symmetry factors (α) and adsorption isotherms (θ) and are taken from [87].

In the context of the OER, the Tafel slope is particularly informative for understanding the rate of the OER process under different experimental conditions and revealing its underlying mechanism.[91] To unify the convention, the η_{OER} was

Table 2.2: Reaction mechanisms and Tafel slopes adopted from [87] expressed in mV/decade.

Mechanism	α=0	α=0.5			α=1
		θ=0	θ=0.5	θ=1	
E	60	$\gamma = \alpha \rightarrow 120$	60	120	∞
EC	-	$\gamma = 1 \rightarrow 60$	60	∞	-
ECE $\equiv$ EE	60	$\gamma = 1 + \alpha \rightarrow 40$	60	120	30
ECEC $\equiv$ EEC	-	$\gamma = 2 \rightarrow 30$	60	∞	-

settle to the extra potential needed for a reaction to proceed at a certain rate fixed in 10 mA/cm^2.[92] With this agreement, various literature reports have documented different values of Tafel slopes for the OER mechanism.[93, 94] A theoretical study has identified a Tafel slope of 120 mV/dec when the surface species formed just before the rate-determining step predominates.[95] Conversely, if the surface adsorbed species from the early stages of OER dominate, the Tafel slope decreases.[95] Specifically, when Eq. 2.10 governs the overall rate, a Tafel slope around 30 mV/dec is observed.[95] In some cases, although not extensively documented, the Tafel slope varies with potential.[96, 97] To electrochemically elucidate the rate-determining step and elementary steps, it is crucial to evaluate not only the smallest Tafel slope but also all measured Tafel slopes at lower and higher current densities, respectively.

In summary, the experimental principle established by Tafel (Tafel slope) provided a method to evaluate the sequence of steps that make up an electrochemical mechanism, such as electro-oxidation or OER. This is because the sequence of steps influences the kinetic parameters, enabling the identification of the RDS. However, the specific chemical nature or structure of the species involved cannot be determined. This indicates that electrochemical kinetics are molecularly nonspecific, which is ascribed to the fact that reaction rates in electrochemistry are measured as electron fluxes and energies as electronic energies, regardless of the species involved. Therefore, combining kinetic electrochemical evaluations with surface-sensitive techniques is crucial for revealing the actual chemical and electrochemical phases that emerge due to the application of a potential, particularly when a catalyst is in operation.

2.5 Electrochemical techniques

2.5.1 Cyclic Voltammetry

In electrochemistry, the Cyclic Voltammetry (CV) technique is one of the most extended techniques for electrokinetics study. CV is commonly used to perform the first basic electrochemical characterization because to its simplicity. It provides preliminary information about the kinetics of the redox processes that take place, and it is also sensitive to the presence of contaminants, that allows testing the quality of solutions. To conduct CV measurements, a potentiostat-galvanostat and a

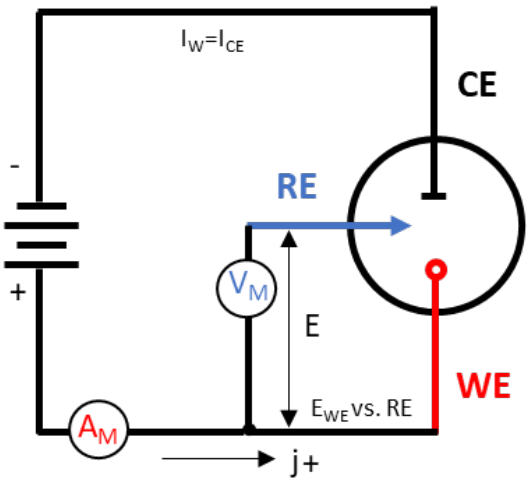

Figure 2.11: Scheme of a three-electrode electrochemical cell connected to a potentiostat. Within the cell, potential and current measurements are divided into a Reference Electrode (blue) loop and a Counter Electrode (black) loop. The working electrode (red) potential is determined by measuring it relative to the reference electrode (RE). The RE input possesses a high-impedance, ensuring that all current is directed through the counter electrode (CE).

three-electrode cell within an electrochemical cell are required alongside the studied solution. Figure 2.11 depicts the electrical circuit for the three-electrode cell configuration. More details about the specific experimental setup and the electrochemical cell employed in this thesis will be given in Chapter 4.

The three electrodes are denoted as the working (WE), counter (CE) and reference electrodes (RE), where the working electrode is, in our case, the single crystal sample of interest. The reference electrode provides a stable and constant potential, as its name implies, against which the potential of the working electrode is referred and measured. Therefore, a potentiostat maintains the working electrode's potential in relation to the reference so that current density flows between the counter and working electrodes.

To be considered a reference electrode, the electrode must have a stable and well-known electrode-potential at fixed conditions. The most commonly used RE are standard hydrogen electrode (SHE) and normal hydrogen electrode (NHE). Both electrodes are redox electrodes that forms the basis of the thermodynamic scale of half-cell oxidation-reduction potentials.[98] The absolute standard electrode potential (E^0) is estimated to be 4.44 ± 0.02 V at 25 °C in both cases. However, to form a basis for comparison with all redox reactions, the potential is declared to be zero at any temperature. Both REs follow the reaction 2.19, but they exhibit differences based on their assumptions regarding solution conditions. The SHE operates under the assumption of ideal thermodynamic solutions, computing activities of redox species, which may not always reflect practical conditions. In contrast, the NHE considers the concentration of redox species, meaning under real solution conditions.

$$H^+_{(aq)} + e^- \rightleftharpoons \frac{1}{2} H_{2(g)} \tag{2.19}$$

As seen before, the Nernst equation serves as the fundamental chemical thermodynamic expression enabling the determination of the half-cell potential for a given chemical reaction. As it is described in Eq. 2.20 and 2.21, the Nernst equation attributed to both REs gives a half-cell potential of 0 V.

$$E_{SHE} = E^o_{H^+/H_2} + \frac{RT}{zF} ln \frac{a_{H^+}}{\sqrt{p_{H_2}/p^0}} = E^o_{H^+/H_2} - \frac{2.303RT}{zF} pH - \frac{RT}{2zF} ln \frac{p_{H_2}}{p^0} \tag{2.20}$$

$$E_{NHE} = E^o_{H^+/H_2} + \frac{RT}{zF} ln \frac{C_{H^+}}{\sqrt{p_{H_2}}} = E^o_{H^+/H_2} - \frac{2.303RT}{zF} pH - \frac{RT}{2zF} ln p_{H_2} \tag{2.21}$$

where $E^o_{H^+/H_2}$ is the standard potential of the half-reaction H^+/H_2 which is 0 V; R is the universal gas constant, 8.314 $J/K \cdot mol$; T is the temperature in K; z is the number of electrons transferred in the half-reaction which is one; F is the Faraday constant, the charge transferred per mol, 964,853 C/mol; a is the activity of the protons present in the solution which is $a_{H^+} = \frac{f_{H^+} C_{H^+}}{C^o} = 1$; C is the concentration of protons in the solution which is 1 M; p_{H_2} is the partial pressure of the hydrogen gas which is 10^5 Pa and p is the standard pressure, 10^5 Pa.

Given that the SHE and NHE both possess a potential of zero, the cell's potential is inherently equivalent to its own. Consequently, employing these electrodes eliminates the need for adjustments to account for their individual potentials. In addition, they can be used over the entire pH range arising the third common electrode called reversible hydrogen electrode (RHE) which follows the same concept exposed before but whose potential depends on the protons concentration being dependent on the pH of the solution and can be used directly in the solution. So, it consists of a pH scale with voltage measurement. The potential expressed in the RHE scale considering Eq. 2.21 and substituting the constant values, can be expressed as follows:

$$E_{RHE} = E^o_{H^+/H_2} - 0.059 \quad pH \tag{2.22}$$

Nevertheless, incorporating such electrodes into the cell introduces certain limitations, primarily stemming from the challenge of obtaining hydrogen gas that is completely pure and dry. Even minute traces of impurities in the hydrogen gas can render the electrode inactive and irreversible. One potential solution involves the use of a Luggin capillary to connect the reference and working electrode compartments. However, achieving electrical contact between these compartments relies on the electrolyte film wetting the stopcock walls, consequently elevating the resistance within our system.

Reference electrodes commonly used in CV experiments include genuine reference electrodes and pseudo-reference electrodes. A fundamental distinction exists between a genuine reference electrode (such as SHE, NHE, and RHE) and a pseudo-reference electrode, which does not have a zero potential but has a well-defined value

relative to NHE. Pseudo-reference electrodes often rely on simple silver/silver chloride (Ag/AgCl) wires. The potential of an Ag/AgCl reference electrode can vary depending on the concentration of the chloride solution. Because of this variability, these electrodes are typically calibrated using a reference redox system, where their potential is measured against either a standard redox system or a conventional reference electrode.

In the scope of this thesis, we have opted for using Ag/AgCl pseudo-reference electrodes, a widely used one. Due to the configuration we used, which will be described in Chapter 4, the implementation of a Lugging in the electrochemical system arises high noise interferences in the measurements and lab-safety protocols prompting us to discard the use of the NHE reference electrode. For the Ag/AgCl pseudo-reference electrode, the potential can be expressed as follows:

$$E_{Ag/AgCl} = E_{SHE} - E^{o}_{Ag/AgCl} = E_{RHE} - 0.059pH - E^{o}_{Ag/AgCl} \tag{2.23}$$

In this thesis, two different Ag/AgCl reference electrodes were utilized. An Ag/AgCl/KCl (3 M) electrode obtained from *Hach* was used to investigate gold single-crystal electrodes in acidic media (Chapter 5), while the leak-less Ag/AgCl/KCl (sat) electrode obtained from *Innovative Instruments* was employed in alkaline media for evaluating manganese oxide catalysts (see Chapter 6). Both electrodes were calibrated against a Pt wire in a 1 M acidic solution bubbling 1 bar of pure H_2 yielding potentials of $+0.285$ V and $+0.318$ V vs RHE, respectively.

After description of electrical circuit and how the potential is referred, we can give insights in CV technique. The CV consists in applying a potential sweep to the WE, which is measured relative to the RE, and register the current density flowing between the CE and WE as a function of time. The starting potential (E_i) is usually set to a potential where negligible current flows, the electrode is stable and no chemical or electrochemical changes affected the electrode prior to measurement. The potential undergoes a linear scan pattern, as illustrated in Fig.2.12a, at a scan rate denoted by ν (in V/s), typically ranging between 1 to 100 mV/s. The scan progresses to the upper potential limit (E_1), after which it reverses direction at the same scan rate until reaching the lower potential limit (E_2). The variant of this technique, where the potential is not reversed and only one scan is conducted in a single direction, is known as linear swept voltammetry (LSV).

The determination of the applied potential for each sweep before the reversal of the scan direction is governed by Equations 2.24 and 2.25:

$$E = E_0 + \nu t \tag{2.24}$$

$$E = E_0 - vt \tag{2.25}$$

where ν, the scan rate, is a critical parameter in CV and the analysis of its effect can reveal valuable information about the nature of electrochemical processes or the mechanism of complex electrochemical reactions.

A cyclic voltammogram is obtained by plotting the applied potential scan versus the measured current, an example of obtained I-E curves is shown in Fig.2.12b. It depicts an example of a reversible monoelectronic process current response in the CV

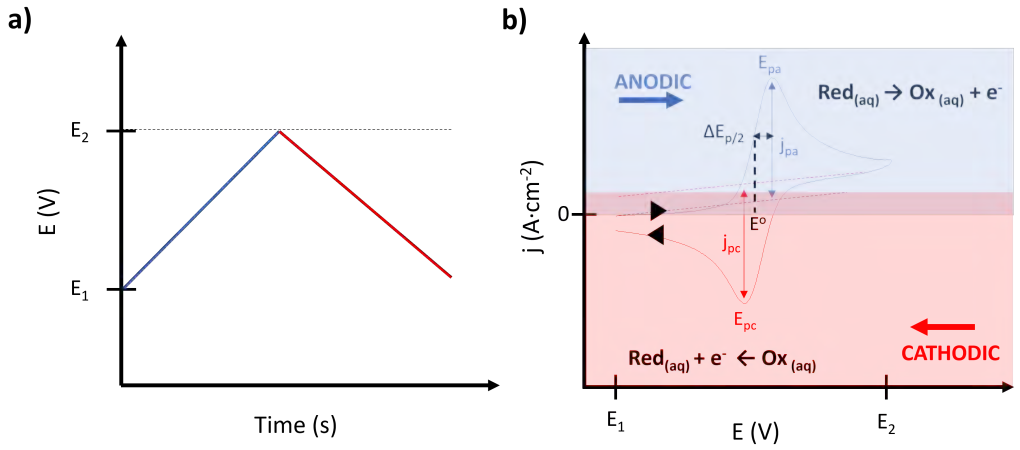

Figure 2.12: Example of a cyclic voltammetry experiment for an electron transfer process: Red $\rightleftharpoons$ Ox $+ e^-$ in static conditions in a solution containing Red specie. a) Potential scan applied to the WE as a function of time. b)Resulting cyclic voltammogram, j vs. E plot, where anodic and cathodic regions of the plot are highlited in blue and red, respectively. It is described how the background of the wave is considered and which are the most important parameters: $E_{pa/pc}$, $j_{pa/pc}$, E^o and $\Delta E_{p/2}$.

for a simple reversible one electron transfer reaction that takes place at a standard potential $E^o_{(Ox/Red)}$, the electrochemical process is described in the next equation:

$$Ox_{(aq)} \pm e^-_{metal} \rightleftharpoons Red_{(aq)}; \qquad E^0(V) \tag{2.26}$$

In the context of a reversible electrochemical reaction, the commencement of the reaction hinges on the application of a sufficiently high potential, rendering the thermodynamics favorable for the oxidation of the reduced species (Red_{aq}). Initially, when the potential is insufficient to trigger a reaction, the cyclic voltammogram (CV) displays no current flow as the potential sweeps from E_1 to E_2. Upon reaching a potential where the oxidation of Red_{aq} becomes feasible, the current rises, attaining a peak at the potential E_{pa} due to the elevated concentration of the species in the diffusion layer. This maximum is reached as more of the Red_{aq} reactant is consumed, necessitating increased diffusion from the bulk solution. At this juncture, all available Red_{aq} at the interface undergoes conversion to Ox_{aq}. Subsequently, the current diminishes and stabilizes at E_2 as diffusion rate dominates. The anodic part of the voltammogram (upper, depicted in blue) encapsulates the oxidation of Red_{aq} to Ox_{aq}. During the reverse potential sweep towards E_1, a similar pattern unfolds. In this scenario, the reactant is Ox_{aq} and the current reaches a maximum at E_{pc} before being governed by the diffusion of Ox_{aq} and returning to zero upon complete conversion of available Ox_{aq} to Red_{aq}. The cathodic segment of the voltammogram (bottom, portrayed in red) corresponds to the reduction of Ox_{aq} to Red_{aq}. Throughout the CV experiment, the concentration of species in proximity to the electrode undergoes temporal variation, aligning with the Nernst equation, as elucidated by Eq. 2.27.

$$E_{Ox/Red} = E^{o}_{Ox/Red} + \frac{RT}{F} ln \frac{C_{Ox}}{C_{Red}} \tag{2.27}$$

The CV of a reversible process is characterized by different electrochemical parameters. When the transformation Ox $\leftrightharpoons$ Red takes place at potentials E_{pa} and E_{pc}, the concentrations of Ox and Red at the electrode surface are equal and following the Nernst equation (equation 3.9), $E = E^{o}_{Ox/Red} = E_{\frac{1}{2}}$. $E_{\frac{1}{2}}$ corresponds to the halfway potential between the two observed peaks. The two peaks are separated due to the diffusion of the analyte to and from the electrode. If the process is chemically and electrochemically reversible, the difference between the anodic and cathodic peak potentials, called peak-to-peak separation (ΔE_p), is 57 mV at 25^{o}C (2.22 $\frac{RT}{F}$, following equation 3.9), and the width at half max ($\Delta E_{\frac{p}{2}}$) on the forward scan of the peak is 59 mV and is independent of scan rate.[99, 100] Under quasi-reversible and irreversible conditions, ΔE_p becomes higher than 57 mV and depends on the scan rate.

For totally reversible systems, the anodic and cathodic peak current (i_{pa} and i_{pc}) for an oxidation/reduction process varies with scan rate according to Randless-Sevick equation:

$$i_p = (2.69x10^5) n^{\frac{3}{2}} \; A \; D^{\frac{1}{2}}_{red} \; C^{bulk}_{Red} \; \nu^{\frac{1}{2}} \tag{2.28}$$

where the initial factor number is calculated at 25 C, n refers to the number of electrons interchanged, A is the area of the electrode in cm^2, D_{Red} or D_{Ox} in reduction and oxidation cases are the diffusion coefficients of the reduced or oxidized species expressed in cm^2/s, C_{Red} or C_{Ox} are the bulk concentrations of the reduced or oxidized species in mol/L and ν is the scan rate in V/s. The same equation with the contrary sign is applied for reduction processes. Therefore, i_p varies proportionally with the square root of the scan rate. In the scope of this thesis, this equation will be used to evaluate electrochemical active area (ECSA) of different manganese oxide grown structures in order to normalize its catalyst performance in Chapter 6.

Furthermore, there exists the potential for one or multiple species to adsorb onto the electrode surface. In scenarios involving the oxidation of an adsorbed Red specie ($Red_{(ads)}$), producing an oxidized specie, Ox_{ads}, (without accounting for any desorption of these species and potential faradaic currents originating from reactions of the dissolved species), the cyclic voltammogram assumes a configuration akin to that depicted in Fig.2.13b. The peak current in this context is determined by the following equation:

$$i_p = \pm \frac{n^2 F^2}{4RT} \nu A \theta_{total} \tag{2.29}$$

where θ_{total} is the total surface coverage. The peak current is proportional to ν in this case and E_{pa} is equal to E_{pc}. Nonetheless, the cyclic voltammogram (CV) profile illustrated in Figure 2.13 corresponds to a reaction that is entirely reversible under Langmuir isotherm conditions. The extent of irreversibility in the reaction and potential lateral interactions among adsorbates can introduce variations in the observed shapes.

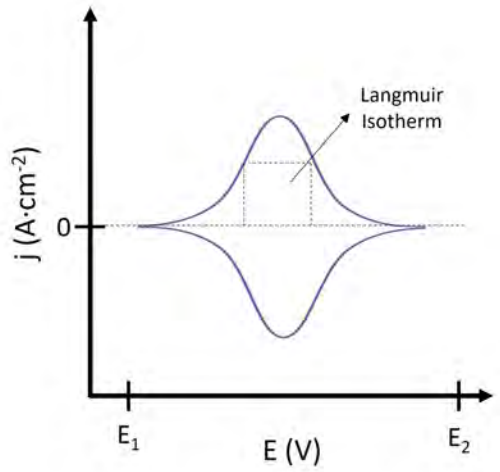

Figure 2.13: Cyclic voltammetry profile for the oxidation and reduction of surface adsorbed R. The square indicated the width potential value related with Langmuir isotherm.

Moreover, numerous complexes exhibit multiple reversible redox processes involving two electrochemical steps, as highlighted by Bard and Faulkner[101]. The appearance of the voltammogram is contingent upon the disparity in the formal potential of these two electrochemical steps. When the second electrochemical step is more thermodynamically favorable than the first, the voltammogram mimics a Nernstian two-electron transfer, resulting in a peak-to-peak separation (ΔE_p) of 28.5 mV, distinct from the 57 mV anticipated for a one-electron process. As the thermodynamic favorability of the second electron transfer diminishes, ΔE_p expands until it peaks at slightly over 140 mV. At this juncture, the waveform bifurcates into two distinguishable waves, each exhibiting $\Delta E_p = 57$ mV.

The concepts outlined in this section pertain to model cases that address ideal situations. Nevertheless, in practical scenarios, mechanisms may involve various combinations of electrochemical stages (reversible, quasi-reversible, or irreversible), homogeneous reactions, and adsorption stages. In such cases, the interpretation of i-E curves becomes more intricate.

2.5.2 Chronoamperometry

Chronoamperometry, CA, is a potential step method that utilizes the same equipment as the CV technique, described in the previous section. In this technique a perturbation known as potential step is applied to the WE in reference to the RE, and the change in the WE current density over time after the polarization is recorded. The applied potential program is depicted in Figure 2.14a. The working electrode's potential swiftly transitions from an initial potential E_1—where no faradaic processes take place—to a subsequent potential E_2, where the intended electrochemical reaction initiates. In this case, the current flowing between CE and WE is measured over time polarization. The typical response obtained in a CA is schematized in Fig.2.14b and c. Generally, along the first 50 μs *approx.* the faradaic current den-

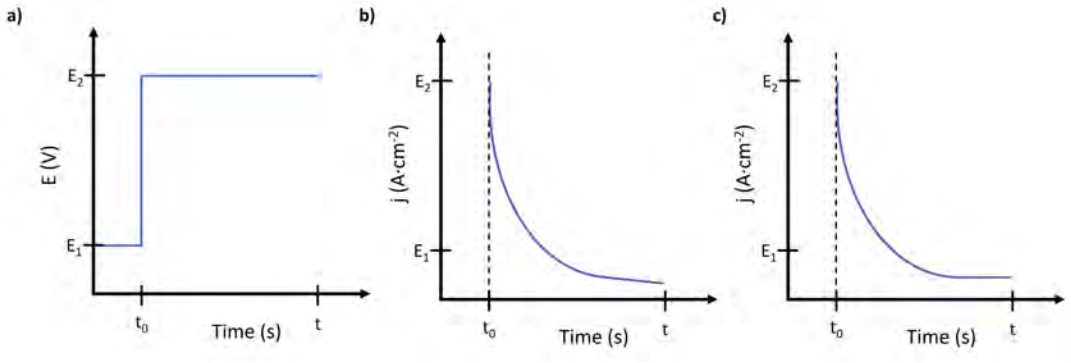

Figure 2.14: a) The potential program outlines a chronoamperometry experiment wherein the redox species is non-electroactive at E_1 but undergoes reduction at a diffusion-limited rate at E_2. b) The graphical representation of current versus time results from the chronoamperometry experiment, indicating that the redox process is entirely governed by mass transport. c) The current versus time plot is generated on a planar electrode, adhering to the Cottrell equation.

sity obtained throughout coincides with the double layer charging at the start of the test, but its influence decays quickly being negligible.

Chronoamperometric transients can exhibit various profiles, depending on the nature of the redox process, electrochemical configuration, and the applied potential. Considering a reaction, such as the example in Equation 2.26 where a specie called Red is oxidized to Ox at a given E^o, different profiles may emerge in the j-t plot. In cases where the kinetics for oxidizing Red are so fast that the concentration of Red at the electrode surface is nearly zero at applied potential (E_2), the process is totally governed by mass transport. This scenario is shown in Fig.2.14b. As the current read-out is proportionate to the concentration gradient, a continuously decay in the chronoamperometric current response is observed. In this situation any applied potential higher than E_1 will yield the same i vs. t plot. For a planar electrode in this case, the electrode current response follows the Cottrell equation:

$$i_d(t) = \pm \frac{n\ F\ A\ C_{Red}^{bulk}\ D_{Red}^{\frac{1}{2}}}{\pi^{\frac{1}{2}} t^{\frac{1}{2}}} \tag{2.30}$$

In a contrary scenario, when the applied potential (E_2) is at a value where the oxidation of Red is less efficient, Red remains largely unaltered and a relatively constant current value is measured over time as it is depicted in Figure 2.14c. In this situation, the process is not under pure diffusion control and the current-time dependency differs deviating from the Cottrell equation. For numerous electrocatalytic reactions, achieving diffusion control requires a significantly large overpotential. Under these conditions, other electrochemical or chemical processes may occur before reaching these overpotentials.

Chapter 3
Surface Science Techniques

After providing insights into the fundamental aspects of electrocatalysis and surface electrochemistry, Chapter 2, we will now delve into the surface science perspective. For those unfamiliar with surface science and UHV-based systems, it is important to briefly explain what UHV systems are. Ultra-High Vacuum systems are specialized environments where the pressure is extremely low, typically below $1 \cdot 10^{-9}$ mbar, meaning there are virtually no molecules in the gas atmosphere. These systems are essential for conducting precise and uncontaminated measurements and processes because they keep surfaces clean and free of contaminants over time-scales of the experiment. UHV prevents surface oxidation from contact with water molecules in the air and contamination from hydrocarbons. This is particularly important in surface science, where even tiny amounts of air can interfere with sensitive processes. Achieving and maintaining UHV involves stages of rough pumping, high vacuum pumping, and specialized UHV pumping, along with constant monitoring and contamination control. Despite their complexity and cost, UHV systems are crucial for advanced scientific and technological applications.

By bridging the pressure gap between ambient pressure electrochemistry and UHV conditions, we employ highly surface-sensitive techniques. This chapter offers a concise overview of the methodology, describing the working principles and functionalities of the main surface science experimental techniques employed, with a specific focus on aspects relevant to this study. First, we describe the cleaning of single crystal samples through UHV means and the growth of model catalysts by chemical vapor deposition (CVD) in an oxidative environment. This is followed by the UHV characterization techniques, being our primary technique, X-Ray Photoemission Spectroscopy (XPS), complemented together with surface structural characterization techniques at the *meso*- and *nano*scale, namely Low Electron Energy Diffraction (LEED) and Scanning Tunneling Microscopy (STM) as well as ambient-Atomic Force Microscopy (AFM), respectively.

These techniques have played a pivotal role in this thesis elucidating the chemical, electrical, and surface structural properties of as-grown or potential-induced metal (oxides) structures both preceding and after electrochemical tests. This capability is crucial for examining the relationship between macroscopic, mesoscopic,

and nanoscopic properties, thereby unraveling the structure-activity and structure-stability of electrodes in electrochemical processes.

3.1 Preparation and Growth of materials

In surface electrochemistry the electrode surface quality and cleanliness are critical factors that directly impacts the success of the investigations. The presence of uncontrollable defects or impurities on the surface can significantly alter measurements, including electrochemical characteristics. Hence, a well-defined cleaning protocol is necessary prior to conducting any experiments. In this thesis all samples were prepared under extremely clean and controlled conditions in UHV and the main surfaces investigated are single crystals, properties described in section 2.3.

To prepare the samples, the procedure entails a series of cycles involving both sputtering and annealing:

- Ion sputtering: A noble gas, typically Ar, is used in a pressure around 10^{-6} mbar through a sputter gun. Ar is ionized with a focused ion beam at an energy of 0.5 to 2 keV directed against the sample that is placed in front. Such an inert gas is chosen because it avoids additional sources of contamination being impossible its binding to the surface. In this process, the surface is bombarded with argon ions, removing atoms layer by layer from the surface. Thus, a large number of defects are created on the surface. In the case of samples that are only used for UHV characterization a 1 keV is enough, while for oxides coming from EC experiments up to 2 keV is needed when high anodic potentials are applied.

- Annealing: A thermal heating process is required to reconstruct the surface. The annealing process consists in increase thermal energy in the sample using a tungsten filament heater situated behind the sample and a cooling system to avoid possible manipulator desorption. For Au(111) case, the samples were heated up to 1,000 - 1,100 K; whereas for Ag(001) sample 700 - 750 K were reached. This process were done for 10 - 15 minutes reaching final pressures below 10^{-9} mbar and avoiding high pressures during the process.

The growth of functional metal-based materials, for instance like the case of Mn, are usually accomplished by evaporation in a preparation chamber using an electron beam (e-beam) evaporator. It is an standard UHV technique used for growing well-ordered thin films in controllable conditions.[102] In the scope of this thesis, a FOCUS FEM 3s evaporator was employed for the growth of manganese oxides, described in Chapter 6. The evaporator consists in a crucible surrounded by a filament. The crucible is constructed using a material that does not chemically interact with the metal to be deposited and has a higher sublimation temperature compared to the metal, in this case tungsten or W is used. During the experimental deployment, an electric bias is applied to the filament, imposing a high voltage $\sim$ 2 kV. This voltage is applied between a tungsten filament and the material source, which in this case is a high purity Mn pellet (99.95%) housed in a crucible. The electron beam

retrieved from the filament is undergoes acceleration and is directed towards the crucible by the high voltage, supplying the necessary energy to rise temperatures up to $2,773.15K$. This heating up promotes atoms sublimation and evaporation into the chamber. A water cooling system is integrated and configured to refrigerate the evaporators so that the heating of the crucible is optimally localized, avoiding overheating of the system.[103] As a result of this configuration, the surroundings are kept at a low temperature, ensuring high purity evaporation.

Another key feature of these evaporators is the inclusion of an ion suppression mechanism which purpose is to remove ions from the beam and ensure that the atoms that arrives at the substrate are neutral. It is achieved by the application of an extra voltage at the suppressor electrode. On this way defects can be minimized. The growth rate was calibrated before and after each evaporation process using a quartz microbalance. Throughout the growth process, the growth rate was continuously monitored using the embedded flux monitor.

Throughout the execution of this thesis, different surfaces have been prepared and investigated. Specifically Au(111) and Ag(001) single crystals, along with grown manganese oxide (MnOx) structures. Au(111) was chosen to test the capability of the compatible ambient pressure-UHV setup to unveil model electrochemical reaction dynamics, such us electro-oxidation and the OER (see Chapter 5). The selection of Au(111) as a model system is due to its extensive study in both surface science and electrochemical fields. Furthermore, due to its inertness and high resistance to dissolution, Au(111) serves as an ideal substrate for growing metal oxide model catalyst structures, particularly MnOx. Since the growth of MnOx in Au(111) surface is complex, we selected Ag(001) as an alternative model surface for this purpose. Thus, the growth of MnOx on Ag(001) and Au(111) will be explored in Chapter 6 in conjunction with testing MnOx as a potential anode in electrolyzer compartments catalyzing the OER.

Apart from the samples presented in this manuscript, various metallic samples have been studied in the context of this thesis, but for consistency, those results will not be included in the present manuscript. For example, the Pt(111) surface was tested as a benchmark sample between ambient and UHV electrochemistry because, alongside gold, it is one of the most studied electrochemical systems. Following a PhD stay at Alicante University with Prof. José Solla, these samples were used to adapt the surface electrochemistry methodology learned there to the methodology developed in this thesis, aligning with the proposed objectives.

Additionally, attempts were made to grow ruthenium oxide by UHV means to serve as a model catalyst for OER, in conjunction with Pt evaporation for HER, forming a bi-catalyst system. However, no potential ruthenium oxides were obtained using direct Ru(0001) oxidation with either molecular or atomic oxygen. Consequently, this data will not be included in this manuscript.

3.2 X-Ray Photoemission spectroscopy (XPS)

Originally known as electron spectroscopy for chemical analysis (ESCA), X-ray photoemission spectroscopy (XPS) is a surface-sensitive analytical method widely used in surface science to investigate the electronic state and elemental composition of materials. The photoelectric effect, which Hertz first identified in 1887, is the basis for XPS [104]. Later the principle was explained by Einstein in 1905 [105]. However, it was not until the 50s and 60s that Kai Siegbahn truly propelled the development of an XPS into its current form[106] leading some years later to his well-deserved recognition with the Nobel Prize in 1981.

As illustrated in Figure 3.1a, the photoelectric effect occurs when photons (light) with sufficient energy interacts with a material and cause the release of electrons to vacuum. This fact is only realized when the energy of the photon beam ($h\nu$) exceeds the sample work function (Φ_s), which is the minimal energy needed to remove an electron from a given material. According to Figure 3.1b, ejected electrons have a certain kinetic energy (E_K) and move in the vacuum in the direction of the electron energy analyzer. Electrons within the analyzer will acquire energy, precisely equivalent to the material's work function (Φ_A), and will subsequently be identified. The emitted photoelectrons are analyzed based on their kinetic energy carrying information about the energy levels and chemical environment of the atoms near the surface, providing valuable insights into the surface properties. Thus, the essence of X-ray photoelectron spectroscopy lies in capturing the intensity of emitted electrons as a function of their kinetic energy (E_K), as described by the following equation:

$$E_K = h\nu - E_{BE} - \Phi_M - \Phi_A \tag{3.1}$$

being $h\nu$ the energy of the photon beam, E_{BE} the binding energy (BE) of the electron core-level and ϕ_M and ϕ_A the work function of the explored surface and analyzer material, respectively. As far as sample and analyzer are electronically connected, their Fermi levels are aligned leading to $E_K = h\nu$ - E_{BE} - Φ. From this formula the E_{BE} can be obtained. E_{BE} is specific for each element, each core level, and each chemical and electric environment since the BE of an electron depends on the nucleus potential well. The E_{BE} is usually referred to the Fermi level (E_F) in metallic surfaces which is the highest occupied orbital at 0 K.[107]

BE versus intensity, where intensity represents the number of photoelectrons, is typically used in XPS plots for comparing chemical structures due to its specificity. This is illustrated in Fig. 3.2a, which shows the overview XPS spectrum of Mn_3O_4 grown on an Ag substrate. In the energy spectra sharp peaks are observed corresponding to the core-level photoelectrons. Peaks at energies corresponding to Ag (gray), Mn (blue) and O (green) are visible. By analyzing the shape, intensity, and position of these peaks, it is possible to determine the elemental composition and chemical states of the sample. A high resolution spectra at a given core level can also be acquired (Fig. 3.2b) being possible its deconvolution, giving valuable information about the species. Several features needs to be taken into account. Here it is summarized the more relevant features observed in XPS analysis and utilized for the scope of this work:

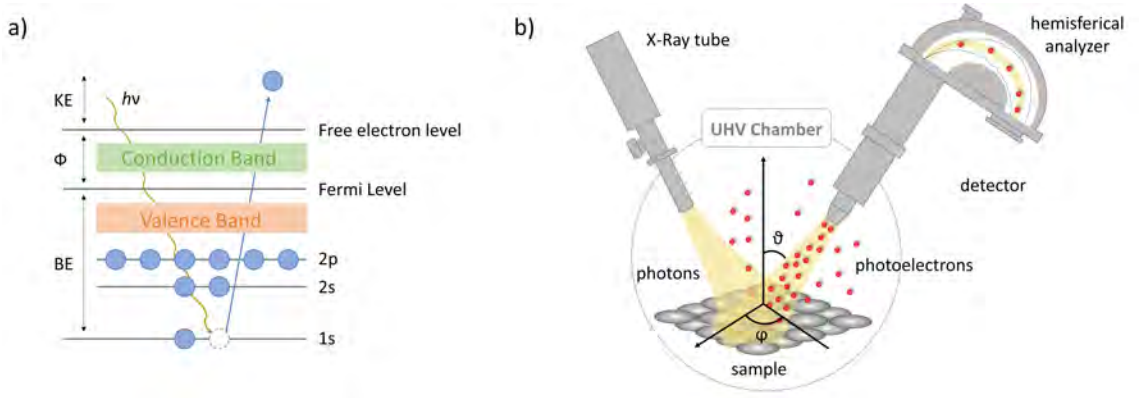

Figure 3.1: a)Schematic model of the photoelectric effect, the basic principle of the x-ray photoelectron spectroscopy technique. b) Depiction of the XPS set up configuration, comprising a source of X-ray photons, a manipulator to hold and move the sample, an analyzer and an electron detector.

- Background: In addition to the visible lines there is an extra intensity in the spectrum, indicated with dashed black line in O 1s spectra in Figure 3.2b. This additional intensity arises from inelastic scattering interactions between the escaping photoelectrons and the sample. As a result of this scattering, photoelectrons lose some of their initial energy and momentum information. [108] Consequently, they are detected at higher binding energies compared to the main peak, being this effect more notable in the left side of the spectra. These scattered electrons, known as secondary electrons, contribute to the distinctive shape of the background. Different backgrounds are proposed in the literature. The choice of background subtraction method depends on the specific characteristics of the spectrum and the desired analysis goals. In the present work, the shape of the so-called Shirley background is used in all explored cases for each component.[109] The Shirley method fits a smooth curve to the low-energy side (higher binding energy) of the XPS peaks and subtracts it from the spectrum. It is widely used due to its simplicity and effectiveness in removing the smoothly varying background signal effect from the peak intensity.

- Shape of the peaks: In the scope of this thesis, different line shapes are observed. As it can be observed in Figure 3.2, Mn 2p and O 1s lines present remarkably differences. On the one hand, the O 1s core-level presents a symmetric bell-shaped distribution with respect to the peak center. It represents a symmetrical function, and its breadth is dictated by the peak's width. In this case, the peak follows a Voigt profile, a linear convolution of Lorentzian and Gaussian functions, allowing the incorporation of peak broadening considerations.[108] This peak characteristics are typically observed when the electrons from a particular element are in a relatively uniform chemical environment and have similar binding energies. Symmetric peaks indicate that the electronic transitions leading to the emission of photoelectrons occur with a well-defined energy. On the other hand, Mn 2p presents a characteristic tail positioned

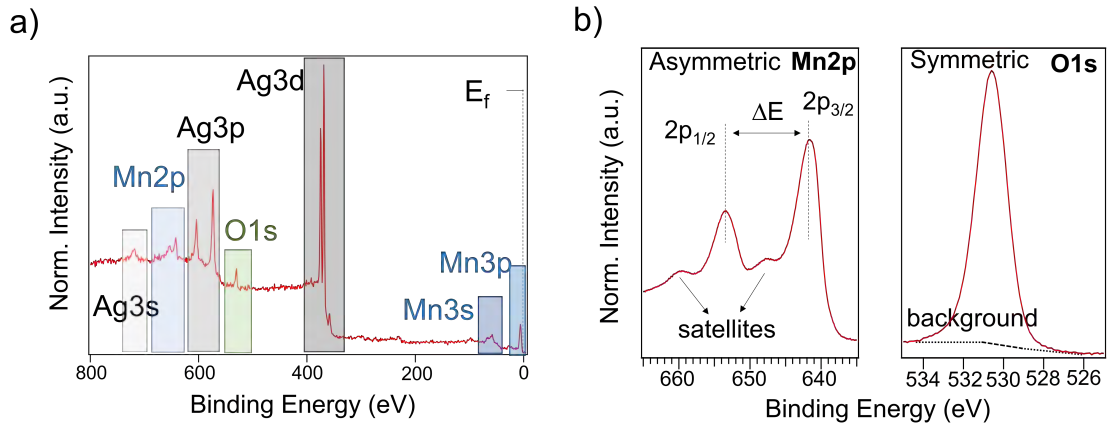

Figure 3.2: General features of photoemission spectra. a)Overview XPS spectrum of as grown manganese oxide on top of Ag(001) with labels of the main core level transitions. b)High resolution spectras on the Mn 2p and O 1s core levels. Mn 2p with two different components arising due to the spin-orbit coupling of the 2p levels and O1s symmetric peak.

at lower kinetic energy in an asymmetric shape. These peaks can arise due to various factors, including chemical interactions between electron-hole pairs produced in the material. The interaction with electron-hole pairs leads to the energy loss of photoelectrons enhanced, resulting in an enhanced intensity at higher binding energies. As the interaction energy increases, the intensity of these peaks diminishes, primarily because electrons strongly attached to the hole face difficulty leaving the sample. They are typical line-shaped metals.

- Spin-orbit splitting: It applies to all electron levels with orbital quantum number $l \leq 1$ (p, d, f). In those cases the spectrum appears as exhibits doublets due to the magnetic interaction of the photoionized spin with the angular momentum of the incompletely filled valence levels. This interaction results in the detection of two distinct orbital levels manifested as separate photoemission peaks, a phenomenon elucidated by Fadley in the context of the XPS principles.[110] The degree of splitting can vary by being several electron volts and is contingent upon the specific element and orbital in question. The stability of the anti-parallel spin configuration dictates that the peak associated with the lower angular momentum (j) invariably possesses a higher binding energy. The intensity of the individual components is determined by the degeneracy factor, represented by $2j + 1$. Comprehensive tabulations detailing the intensity ratio and energy disparity between the orbitals are available[111].

- Exchange splitting effect: The exchange splitting effect refers to the splitting of core-level peaks into multiple sub-peaks due to the exchange interaction between electrons with the same spin. This effect is particularly observed for elements with partially filled inner electron shells, such as transition metals. Its origin stems from the Pauli exclusion principle, a fundamental tenet asserting the impossibility of two electrons occupying identical quantum states simulta-

neously. When an electron is ejected from a core level during XPS, it leaves behind a hole. The remaining electrons in the atom rearrange themselves due to the repulsion caused by the presence of the hole. In the presence of strong electron-electron interactions, the exchange interaction can cause the energy levels of electrons with the same spin to split. This exchange splitting effect results in the observation of multiple sub-peaks in the XPS spectrum corresponding to the same core level. By analyzing the energy separation between the parallel and anti-parallel spin configurations of both implied shells, one can determine the strength of the exchange interaction and gain insights into the spin configurations and spin-dependent interactions within the material as well as oxidative state information.

- Satellite peak: The interaction between the emitted photoelectron and the remaining electrons in the material results in the formation of new energy states. These additional peaks, known as satellite peaks, offer valuable insights into the electronic structure of the material. Among these satellite peaks, an important category is shake-up peaks. In shake-up processes, the outgoing photoelectron induces the promotion of another electron to an excited state, leaving a hole in a lower energy level. The energy required for this electron promotion causes a decrease in the kinetic energy of the photoelectron, giving rise to a distinct peak in the XPS spectrum. These shake-up peaks appear at higher binding energies compared to the main peak and provide valuable information about the excited states and electronic transitions occurring within the material.

The XPS measurements in this thesis were carried out using a Phoibos-100 electron analyzer (SPECS GmbH), using a non monochromatic Al Kα photon source of 1486.6 eV. In the present work, XPS is used as the principle technique to study chemical and electrical properties of catalysts before and after reactions as well as to discern different catalytic manganese-oxide-based phases.

Across this thesis, we also carried out further photoemission measurements at synchrotron radiation facilities. More specially in Swiss Light Source (SLS) at the Paul Scherrer Institut (Villigen, Switzerland), where some of the data shown in Chapter 6 were obtained at the PEARL beamline.

The significance of synchrotron light in material exploration lies in the combination of extremly high intensity, high collimation and tunability providing a continuous energy spectrum along with enhanced resolution featuring components that are unreachable on a laboratory set up. It is of paramount importance to acquired surface chemical sensitivity of, for example, metal oxides. To properly visualize the differences in the XPS measurements when using lab photon source or synchrotron radiation, in the table 3.1, it has been collected the specification of both systems.

Indeed, this light source offers a continuous and broad spectrum, allowing for the adjustment of photon energy in a wide spectrum range to match the resonance of specific elements within the material, coupled with well-defined polarization.

Table 3.1: Characteristics comparison between lab light and synchtron source

Characteristic	Lab Source	Synchrotron Source
Energy Resolution (meV)	1000	50
Beam Size (mm)	> 1	< 0.150
Beam Energy	Fixed	Tunnable
Photon flux (ph/s)	Order of magnitudes lower	$2x10^{11}$ at 1 keV

3.3 Low Energy Electron diffraction (LEED)

Low-energy electron diffraction (LEED) is a technique that provides valuable insights into the crystal structure and surface morphology of solid materials, offering surface sensitivity.[112] Its origins trace back to the early 1930s, when Clinton Davisson and Lester Germer made a groundbreaking observation: the diffraction of electrons by a nickel crystal, confirming the wave-particle duality of electrons. This remarkable discovery earned them the Nobel Prize in 1937.

This technique consists of the perpendicular bombardment of a surface with a collimated electron beam with low kinetic energy (20 – 400 eV). The elastically back-scattered electrons are measured as spots on a fluorescent screen, as depicted in Fig. 3.3a. The observed pattern in LEED arises from the resemblance between the wavelength of the incident electrons and the inter-atomic distances within the material under study, typically on the order of magnitude of Ångstroms (Å).[113] According to the principles of wave-particle duality proposed by Louis de Broglie, the electron beam can be conceptualized as a sequence of electron waves with a wavelength (λ) determined by the momentum (p) of the electrons, which is connected to the Planck constant as follows:

$$\lambda = \frac{h}{p} \tag{3.2}$$

Low-energy electrons exhibit a susceptibility to significant back-scattering interactions with the electronic cloud of the target material, constraining their elastic penetration to a range typically between 10 and 50 Å. This characteristic renders LEED technique inherently surface-sensitive. Furthermore, for LEED to yield a discernible electron diffraction pattern through backscattering, the sample must possess a well-organized surface structure. The elucidation of the diffraction pattern is conventionally conducted in reciprocal space ($\overrightarrow{g_i}$) rather than in the real space ($\overrightarrow{g_a}$). The reciprocal surface lattice vector is defined as:

$$\overrightarrow{g_i} = \frac{2\pi(\overrightarrow{a_j} \; x \; \overrightarrow{n})}{|\overrightarrow{a_i} \; x \; \overrightarrow{a_j}|}; \qquad i, j = 1, 2 \tag{3.3}$$

To acquire a diffraction pattern in a two-dimensional system, it is imperative to fulfill the Laue conditions, articulating the necessary prerequisites for diffraction to take place. These conditions are succinctly expressed as:

$$\left(\overrightarrow{k_i} \; x \; \overrightarrow{k_f}\right) \overrightarrow{a_i} = 2\pi k; \qquad i = 1, 2 \tag{3.4}$$

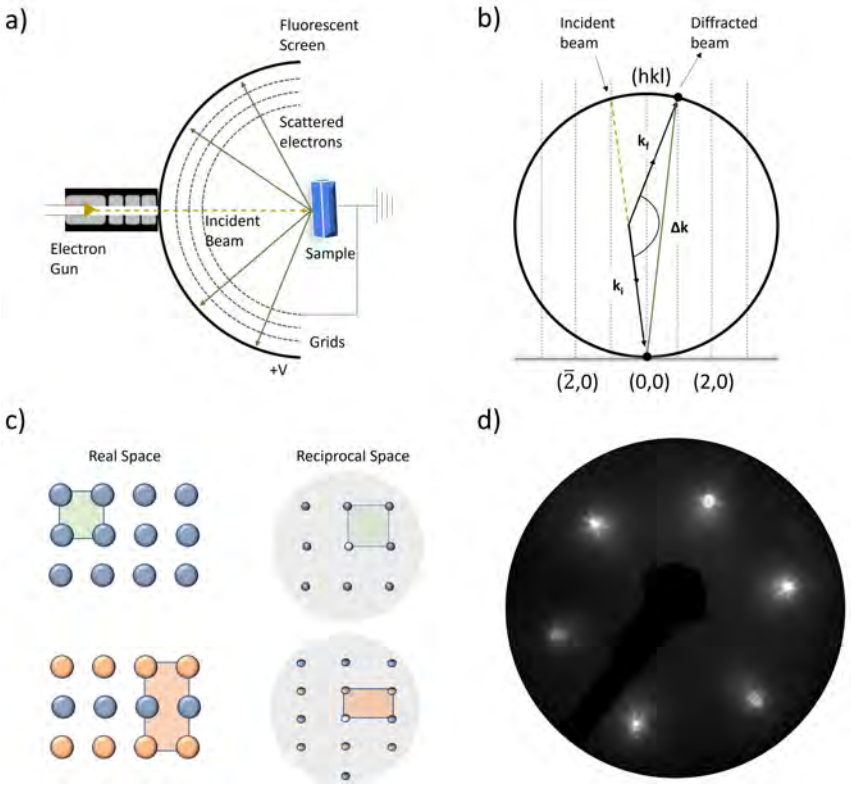

Figure 3.3: LEED schematics explanation: a) Experimental representation of the LEED set-up, b) Representation of the Ewald sphere with the Laue condition for the existence of a diffracted beam. c) Visualization of a 2×2 (top) and 2×1 (bottom) lattices in both real and reciprocal space. In the left panel, the real space lattice is depicted, showing a regular arrangement of atoms or unit cells in a 2×2 and 2×1 grid. In the right panel, the reciprocal space lattice is illustrated, representing the Fourier transform of the real space lattice, and d) LEED pattern of clean Au (111) sample, acquired at 125 eV.

On the other hand, energy conservation requires that:

$$|\overrightarrow{k_f}| = |\overrightarrow{k_i}| \tag{3.5}$$

The fulfillment of both conditions is visually depicted in the Ewald construction, illustrated in Fig. 3.3b. In this representation, the reciprocal lattice of the two-dimensional surface is symbolized by rods. Therefore, a sphere with a radius of $|\overrightarrow{k_i}|$ contains all the possible $|\overrightarrow{k_f}|$ momentum vectors that fullfil with the conservation of the energy law. The intersection between rods and the Ewald sphere satisfies the Laue condition, achieving the maximum diffraction. Consequently, the resulting diffraction pattern (represented in Fig. 3.3c and d), provides insights into the dimensions, symmetry, and rotational positioning of the adsorbate unit cell in relation to the substrate unit cell. This information is instrumental in deducing the unit cell of the superstructure in real space.

In this thesis, LEED is utilized to assess the cleanliness of Au(111) and Ag(001) surfaces. This technique is also employed to gather structural information regarding

the symmetry and superlattice of crystal surfaces, as well as as-prepared oxide films and changes induced by potential on electrode surfaces.

3.4 Scanning Tunneling Microscopy (STM)

Scanning tunneling microscopy, STM, stands out as a versatile tool in the field of nanoscience thanks to its capability for imaging with atomic-scale resolution. Since its invention in 1981 by Binning and Roher [114], leading to a Nobel laureate recognition in physics in 1986, STM has brought about a transformative impact on surface science by enabling the visualization of individual atoms on conductive surfaces.

The underlying principle of this technique hinges on the quantum mechanical phenomenon of electron tunneling. In STM, a sharp pointed metallic tip (typically composed of W, PtIr, or Au) terminated by a single atom scans over a conductive surface in such close proximity (3 - 10 Å) that the wave functions of both entities overlap, exponentially decaying into the junction gap. By applying a bias voltage between tip and sample, the electron wave functions of the tip and the sample partially overlap, facilitating quantum mechanical tunneling and the generation of a tunneling current on the order of nA. A scheme of the STM operation is sketched in Figure 3.4.

The tunneling current (I_T) is influenced by the local density of states (LDOS) of the sample, as demonstrated by theoretical studies on electron tunneling across the vacuum barrier[115]. When applying a low bias voltage (V_S), the tunneling current (I_T) can be expressed in terms of the sample's LDOS (D_S), the distance (d) between the tip and sample, and the respective work functions (Φ_s) and (Φ_t) of the sample and the tip as follows:

$$I_T \propto D_S(E_F) exp\left(-2d\sqrt{\frac{2m}{\hbar}\frac{\Phi_s + \Phi_t}{2}}\right) \tag{3.6}$$

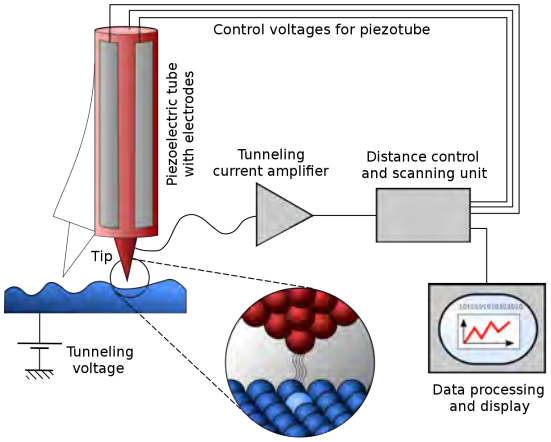

Figure 3.4: Schematic representation of the working principle of scanning tunneling microscopy (STM) obtained from [116].

The polarity of V_S serves as a decisive factor in dictating whether the STM probes the filled states ($V_S < 0$V) or empty states ($V_S > 0$V), facilitating the tunneling of current either into the tip or into the sample, respectively. The exponential correlation between tunneling current and the separation distance, denoted as 'd,' empowers the capability to discern the topographic features of a surface. The operational modalities hinge on the feedback control of the tip-sample interaction, manifesting as constant current mode and constant height mode. Within the constant current mode, the z-position of the tip dynamically adjusts in a feedback loop throughout the scanning process to uphold a predetermined tunneling current. The ensuing variations in tip height are then systematically recorded as a function of lateral coordinates. In the latter scenario, the tunneling current is recorded while the z-position is fixed since the feedback loop is turned off in constant height mode.

The STM technique was used to delve atomic structure of manganese oxide and the influence of the substrate in its growth. The images presented in this Thesis were acquired in a LT-STM (4 K) mainly at PEARL beamline in Paul Scherrer Institute.

3.5 Atomic Force Microscopy (AFM)

Atomic Force Microscopy (AFM) stands as a pivotal scanning probe technique in the realm of surface structure imaging, offering distinct advantages over STM. While STM relies on measuring current, requiring conductive materials for measurement, AFM uses forces (friction, adhesion, magnetic interactions,etc.), enabling measurements on insulating samples.

At its core, AFM operates on the principle of a sharp tip affixed to a flexible cantilever. During surface scanning, the tip encounters features of differing heights, inducing deflection in the cantilever. This deflection is meticulously recorded through the reflection of a laser beam from the cantilever's rear side. AFM operates primarily in two modes: contact and tapping mode. In the former, the tip maintains constant contact with the surface throughout scanning, while in the latter, the AFM cantilever oscillates around its resonance frequency, with the tip intermittently touching the surface at its lowest vertical position. Figure 3.5 illustrates tapping operational mode.

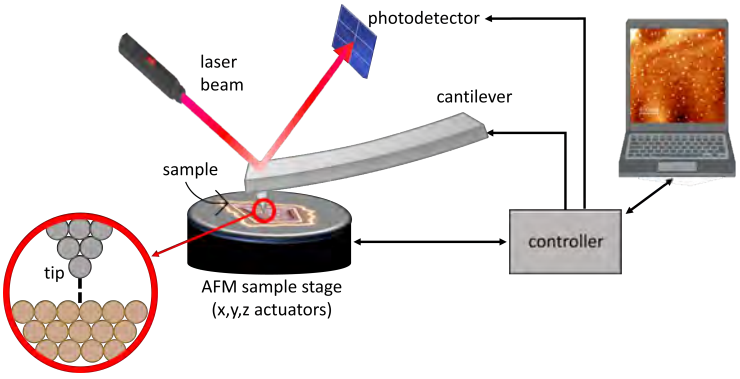

Figure 3.5: Schematic representation of an atomic force microscope and its operation mechanism in tapping mode.

The AFM technique was used to delve into the surface morphology of thick manganese oxide layers. The images presented in this Thesis were acquired in tappingmode using tips with 5 Nm cantilever's elastic constant.

Chapter 4

Novel UHV-ambient pressure compatible set-up

The combination of ultra-high vacuum and electrochemistry (UHV-EC) has gained significant attention within the surface physics community. This innovative approach enables the fundamental investigation of the catalyst surface-electrolyte interface by employing traditional UHV techniques on more realistic systems than those achievable solely under standard UHV conditions. However, the inherent incompatibility of UHV and electrochemical environments necessitates the development of advanced instrumentation. As a result, designing a specific experimental setup became essential and has been a central focus of this thesis and the primary aim of this chapter.

To do so, we begin this chapter by providing a state-of-the-art analysis of the experimental approaches available to probe electrified interfaces, categorized by the type of probe used, the information obtained, and their spatiotemporal resolution. This review will form the basis for our experimental setup selection. After a detailed review and balancing the requirements of this thesis in terms of instrumental complexity and the desired level of control over experimental conditions, we designed and developed a new EC-UHV system based on a quasi-*in situ* approach.

Here, we describe the new UHV-EC transfer chamber and its adaptation to an existing UHV system at the Nanophysics Lab, CFM facilities, which includes highly sensitive surface techniques such as XPS for chemical characterization and LEED for structural analysis. Furthermore, additional equipment was installed to fulfill another objective of this thesis: the study of relevant OER catalysts based on oxides. Specifically, a new oxidation chamber equipped with an integrated oxygen plasma source was installed to produce metal oxide samples, which will be described in detail. Finally, this chapter aims to explain the intricacies of our setup configuration and the methodology employed in this research.

4.1 EC-UHV Compatible Instrumentation: Cutting-Edge Developments

To fully elucidate electrochemical processes and unveil the mechanistic details of electrochemical processes (e.g. surface electro-oxidation or OER catalysis operation) in the electrified interface, EC-UHV synergistic studies, either simultaneous or sequential, are necessary.

In the late 1970s, the integration of UHV and EC methods emerged with a dual objective. The primary aim was to apply UHV analysis techniques to samples originating from a liquid environment. Simultaneously, it sought to investigate the electrochemical behavior of prepared UHV samples. However, this combination presents significant challenges, as UHV and EC environments are inherently incompatible. As introduced in Chapter 3, UHV operates at extremely low pressures around 10^{-9} mbar, in the absence of gas molecules. In contrast, electrochemical methods require the presence of aqueous electrolytes (e.g., H_2O) and operates at ambient pressures, approximately 1 bar. In UHV conditions, liquids like H_2O exist in their gaseous state and can be easily removed through various pumping stages or system bakeouts. Due to the incompatibility of both environments, initial efforts to allow synergistic EC-UHV studies of potential-induced surface chemical and structural changes during electrode operation have spurred the development of new laboratory-based methodologies that present significant experimental challenges.

Here, we will briefly explain different instrumental methodologies and approaches developed by the community to study the electrochemical interface from a surface science perspective. In this thesis, the classification of existing approaches will be based on the criteria agreed upon in the recently published review by Pastor et al. [42].

4.1.1 *Ex situ* EC-UHV approach

The simplest method for EC-UHV transfer is the *ex situ* approach, depicted in Fig. 4.1. This method involves moving the sample electrode through the air, making it easy to implement without the need for specialized equipment.[117–121] Placing the electrochemical cell in air allows for the utilization of standard electrochemical components and a wider range of materials. This setup also enables compatibility with various electrochemical techniques, providing flexibility in exploring different catalytic processes. Despite yielding valuable insights, this method suffer from several drawbacks stemming from the potentially misleading influence of uncontrolled environments. This transfer should occur without introducing any modifications to the surface structure or composition to avoid uncontrolled altered experimental results. Because of that, this approach is only feasible when the surface is inert or covered with a protective film that can be removed through evacuation within the UHV chamber or subsequent annealing without altering its properties.[43, 44]

In conclusion, the *ex situ* methodology is beneficial only for studying inert, stable, and non-reversible changes in electrodes that do not undergo potential oxidation or hydrocarbon-based contamination in the air.

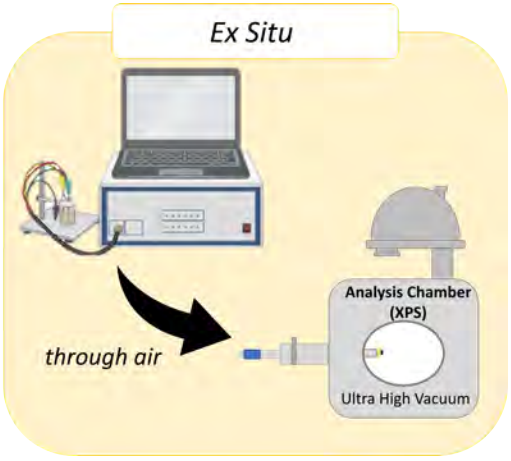

Figure 4.1: Schematic of the *ex situ* approach with sample transfer in ambient air.

4.1.2 Compatible EC-UHV multistage approaches

To prevent uncontrollable surface alterations, one very successful method used for EC-UHV studies of single-crystal electrodes prepared in UHV involves building a multi-technique surface analysis system with an attached electrochemical chamber, either inside or outside the UHV chamber.[43] These approaches aims to prevent unintended changes observed in *ex situ* approaches, like contamination or oxidation of catalyst surfaces, ensuring a clean and controlled ambient like the UHV. This method guarantees:

- Preventing the adsorption of air contained chemical species like CO_2, CO, N_2, O_2, that can induce uncontrolled oxidation of the electrode surface.
- Preserving the original structure and composition obtained and characterized in UHV when immersed in a liquid environment, such as the herringbone reconstruction on the Au(111) surface discussed in section 2.3.

To seamlessly integrate UHV and EC environments, two different approaches can be followed: inserting an electrochemical cell into a UHV chamber or placing a transfer chamber between the UHV and EC conditions, creating two connected compartments. The differences among both approximations will be exposed in following sections.

EC cell into an UHV chamber: *In situ* and operando approach

Placing the electrochemical cell inside the UHV chamber is known as *in situ* or operando analysis. As depicted in Figure 4.2, both methods involve implementing an electrochemical cell inside a UHV chamber where surface science techniques like XPS are applied under electrochemical conditions, maintaining the electrolyte and potential control. Placing the electrochemical cell inside the UHV chamber maintaining UHV conditions allows for better control over experimental parameters, enhancing reproducibility and cleanliness. It facilitates *in situ* surface analysis through integration with UHV techniques, providing real-time insights into dynamic

surface composition, oxidation states, and electronic structures during electrochemical reactions.

The primary distinction between *in situ* and operando analysis lies in the electrochemical conditions applied simultaneously to the XPS analysis. In *in situ* measurements, the conditions represent a simplified version of the actual catalytic reaction, differing from those in real-world applications, such us studying OER catalyst activity at 2 mA/cm^2. Conversely, operando analysis is conducted under actual electrolyzer operating conditions, like 10 mA/cm^2 closely, matching those of the final device and generating oxygen bubbles. These approaches present challenges, including the complexity of integrating an electrochemical cell within a UHV environment, limitations on certain electrochemical techniques, a higher probability of chamber contamination from electrolyte vapors, and the need for a new EC cell prototype with much lower volumes than conventional electrochemistry.

The instrumental development of XPS capable of operating under more realistic pressure conditions (up to 20 mbars) - Near Ambient Pressure - XPS (NAP-XPS) - has revolutionized the analysis of catalyst surfaces and interfaces, mitigating the main drawbacks around vapors and gases. However, due to the high instrumental complexity, *in situ* or operando EC-UHV experiments, such as NAP-XPS in aqueous electrolyte solutions, are primarily conducted at synchrotron facilities: ALS[122], BESSY II[123–125], Elettra[126], MAX IV[127] and SLS[128]. Two prominent approaches in NAP-XPS instrumentation and methodology are observed among presented literature: the so-called dip-and-pull technique and the membrane cell technique.[124]

The dip-and-pull technique involves immersing a sample in a liquid or exposing it to a gas environment, followed by a controlled retraction into the analysis chamber. Thus, it is possible to investigate electrodes within a thin electrolyte meniscus using this retirement technique.[122, 129] This method is particularly useful for studying dynamic processes in the electrode/electrolyte interface by capturing real-time changes. The ability to use monochromatic light and control the exposure time and retraction speed provides high surface sensitivity, crucial for studying thin films and surface reactions. However, in this approach, the experimental setup is complex, requiring precise synchronization between the dipping mechanism and the XPS analysis in conjunction with a precise mechanical stability of the dip-and-pull mechanism to maintain the integrity of the sample and ensure reproducible results. Up to now, this method is available at several synchrotrons: ALS[122], BESSY II[125], SLS[128] and Max IV[127].

Another technique entails the use of a thin membrane cell. In this case, thin Si- or graphene-based membranes are used for separating the liquid from the vacuum side where the analyzer is placed.[130] The sample is placed on one side of the membrane, while X-rays and photoelectrons pass through the membrane for analysis. This method is highly effective for studying samples under continuous high-pressure gas flow, making it ideal for catalytic studies. The membrane acts as a barrier, reducing the risk of sample contamination from ambient conditions during analysis. The sample remains in a stable high-pressure environment, allowing for prolonged measurements and improved data consistency. However, the choice of membrane material is critical and will limit the assayed sample. Also, the membrane can

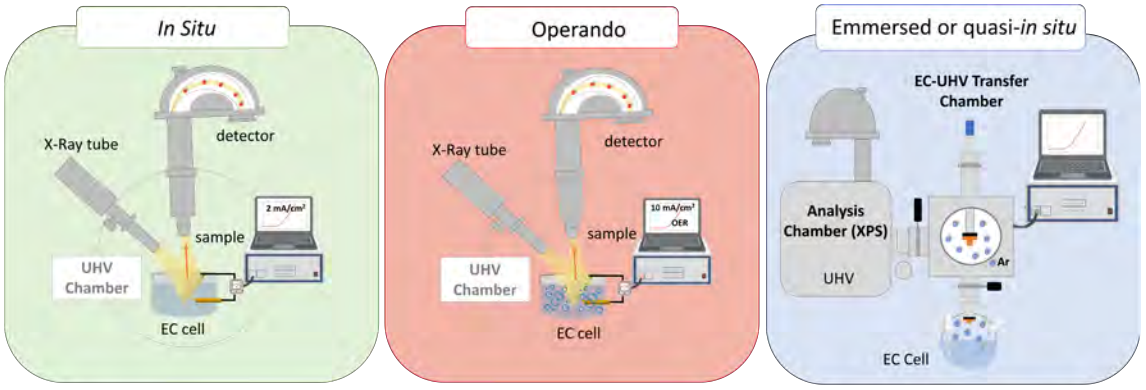

Figure 4.2: Schematic representation of, from left to right, *in situ*, operando, and emersed or quasi-*in situ* approaches.

attenuate the X-ray and photoelectron signals, potentially reducing the sensitivity and resolution of the analysis.

Each approach has distinct advantages and challenges, and their selection depends on the specific requirements of the instrument and the experiment. It should be noted that, as aforesaid, this powerful technique is typically available only at synchrotron facilities, where beamtime is limited. Thus, enabling such investigations in a laboratory environment is crucial to advancing understanding of fundamental processes at the solid/liquid interface. At the time of writing, laboratory NAP-XPS-based instrumentation has increased its presence among different research groups [131–133], demonstrating similar capabilities to synchrotron-based instrumentation in tracking the dynamics of electrochemical reactions *in situ*. However, this equipment is expensive and requires continuous adjustments to address various experimental challenges. Also, it is important to note that NAP-XPS operates at partial pressures up to few millibars. At these low pressures, aqueous electrolytes cannot be utilized in the experimental chamber. Only specific liquid electrolytes with low vapor pressures, such as ionic liquids, can be placed directly in the chamber and used in electrochemical experiments.[134]

EC-UHV Transfer Chamber: quasi-*In situ* or *Emersed* Approach

A second option to integrate UHV and EC environments relies on the implementation of a transfer chamber between both environments. This approach, illustrated in Fig. 4.2, allows for the transfer of samples prepared in UHV to liquid environments under controlled conditions using an inert-atmosphere avoiding potential contamination from exposition to air. Thereby, maintaining the vacuum integrity of the primary chamber and overcoming the main drawbacks of *ex situ* transfer. It can be accomplished, by using an inert-atmosphere glove box connected to the surface analysis apparatus[135] or with a UHV compartment enclosed with main UHV system [47–50, 136–145]. In existing literature, a common aspect of all examined approximations is that EC-UHV compartments are only connected after pressurizing to ambient levels using ultra-high purity inert gas.

This methodology is known as the "emersed" or "quasi-*in situ*" approach, positioned between *ex situ* and *in situ* conditions. It involves the emersion of sample from the electrolyte under potential control to maintain the electrochemical interface intact.[42] However, several questions must be addressed. A fundamental concern is whether the electrode surface and its interface with the electrolyte maintain their original characteristics during electrochemical operations. Ideally, the emersed electrode should exhibit an interfacial layer with the same composition and structure as when it was in the solution. However, emersed electrodes, subjects of study in a UHV transfer experiment, will undergo changes during the transfer process when the potential is lost, forming the so-called "emersed layer". The emersed layer can be experimentally controlled and understood by considering two fundamental factors: (i) the interfacial changes upon emersion, and (ii) the effect of electrolyte evacuation in UHV.[43, 44]

- Interfacial changes upon electrode emersion

  In the emersion approach, the withdrawal of the electrode induces changes in the double-layer (explained in Section 2.2 and depicted in Fig. 2.4) in terms of thickness and total interface charge.

  Firstly, the thickness must be sufficiently thick to incorporate the intact electrochemical double layer but thin enough to exclude residual bulk electrolyte that could alter results. The thickness of emersed layer can be tuned by electrolyte concentration, considering whether the emersion is hydrophobic or hydrophilic.[43, 44] For hydrophilic emersion, the concentration should not surpass much more than 10^{-3} M to prevent the inclusion of bulk electrolyte.[43, 44] For hydrophobic emersion, the concentration should not be much lower than 10^{-3} M to avoid double-layer discharge.[43, 44] In situations where the immersion mode is unknown, an electrolyte concentration of 10^{-3} M would be a logical choice.[43, 44] Thus, under appropriate electrolyte concentrations, the electrochemical double layer can be retained intact when the electrode is withdrawn from the solution.

  In terms of electrochemical interface charge, the interface polarization is lost, and the unbroken double layer retains contact with the surface electrode but loses electrical contact with the bulk electrolyte upon emersion. Consequently, the interface's total charge must remain neutral. However, this neutrality criterion does not prevent spontaneous faradaic reactions within the emerging layer. These reactions, which may involve material loss, can occur spontaneously as long as they do not disrupt the charge balance within the layer.

- Interfacial changes upon electrolyte evacuation

  An expected outcome of evacuation is the alteration of the composition within the electrochemical double layer due to UHV-induced desorption. The degree of these compositional changes will be influenced by the heats of vaporization (ΔH_{vap}) or sublimation (ΔH_{sub}) of the unbound species present within the emersed layer. It is evident that excess water, adsorbed gases, liquids, and substances capable of sublimation will be effectively eliminated in UHV. However, water retained as part of the hydration sphere of the counter ions may

persist despite the evacuation process, especially when hydration enthalpies (ΔH_{hyd}) are significant. For instance, chemisorbed species like sulfate anions, type of anions that strongly adsorbs on gold electrodes, are anticipated to form stable, well-ordered adlattices in solution that retain stability even under vacuum conditions.[43, 146, 147].

By controlling the factors that influence emersed layer using the quasi-*in situ* approach, this methodology allows for studying catalyst in a quasi-*in situ* manner utilizing common electrolytes. Previous works dealing with the preservation of potential-dependent surface resistance[148], changes in work function[149], and the retention of accumulated excess counter ions in the double layer observed on emersed electrodes[46], suggest the feasibility of removing an intact double layer from electrolytes. This preservation, particularly the maintenance of potential-induced work function changes under UHV conditions[149, 150], underscores the stability of electrode potentials even after emersion. So, this approach facilitates the monitoring of stable and irreversible potential-dependent chemical and structural surface changes during electrochemical processes using UHV techniques. The simplicity of the experimental setup enables the use of standard electrochemical components and a wider range of materials, making tasks such as electrode replacement, adjustments, and cell cleaning more feasible and accessible. Consequently, this approach has become widely adopted in laboratory conditions.

In conclusion, the decision to position the electrochemical cell inside or outside the UHV chamber in catalysis-focused UHV-EC experiments involves balancing factors such as experimental complexity, flexibility, and technical implications. Each approach grants access to different sets of surface catalyst properties but provides only partial insights, summarized in Table 4.1. The choice among them depends on specific study requirements, equipment availability, and the desired degree of control over experimental conditions. Researchers must carefully weigh these considerations to design experiments that yield meaningful insights into the electrochemical process desired to study at the electrochemical interface.

Table 4.1: Classification of EC-UHV approaches adapted from [42].

Characteristic	***Ex situ***	**Quasi-*in situ***	***In situ***	**Operando**
Potential Control	×	≈	√	√
Environment Controlled	×	inert gas transfer	electrolyte	electrolyte

4.2 Implementation of an EC-UHV compatible system

Building on the previously discussed EC-UHV approaches and balancing factors like instrumental availability in our laboratory facilities and electrochemical information we can obtain, a quasi-*in situ* or emersed approach is selected for the purpose of the present thesis. To implement this methodology, a UHV system is adapted

and an EC-UHV transfer system is designed and constructed. The design of the EC-UHV system is inspired by previously reported equipment[151, 152] and will be described in following sections.

4.2.1 Experimental Ultra High Vacuum chamber

As stated previously, this PhD project began in 2018 by adapting a UHV chamber of Nanophysics Lab Group to meet the requirements of my thesis. The system consisted of two different UHV chambers: a main XPS chamber with a preparation chamber and a second chamber with a RT-STM.

The first step was the replacement of the RT-STM by a LEED given its capacity to furnish insights into the overall structure on a mesoscopic scale, aligning with a pragmatic approach for macroscopic understanding.

The next step was to design and connect two additional chambers specifically designed to separate preparation from characterization. One was designed as a preparation chamber for growing different materials based on electron beam evaporation and a second preparation chamber with an incorporated plasma source for the growth of oxides at high pressure range. The resulting system, presented in Figure 4.3, consists of four UHV chambers interconnected by valves. It is equipped with all the necessary tools for the preparation and characterization of atomically well-defined single crystal-based systems.

The newly added preparation chamber, depicted in the right inset of Fig. 4.3 and installed in the beginning of 2019, contains several ports where evaporators can be placed. Those evaporators point to the center of the chamber, making it the best configuration for growth of metal-based structures. A quartz microbalance (QMB) is incorporated to measure the metal deposition rate before and after evaporation. Additionally, leak valves facilitate the controlled dosing of gases like O_2 during sample growth. For surface cleaning, the chamber is equipped with an Ar^+ sputter gun with a gas inlet. Also, a new manipulator was designed and installed at the beginning of this Thesis. This manipulator introduces a novel feature with three vertical slots designed for mask insertion, facilitating the precise growth of thin wires in UHV conditions using the shadow mask technique. This manipulator presents a heating filament to perform annealing or degassing of the samples up to 1,473.15 K by resistive or sputter heating.

The second plasma-based preparation chamber, located on the left side of Fig. 4.3, was installed in the latter part of 2020. It was designed to grow oxides using either molecular O_2 or atomic oxygen via an installed plasma source at high pressures (up to 10^{-3} mbar). To facilitate this, it is equipped with an atomic plasma source (SPECS PCS-ECR-AO) positioned in the main port, along with additional free ports for evaporator installation. This chamber is connected to the rest of the UHV system, allowing high-pressure conditions without compromising the vacuum integrity of the primary chamber. It was also designed to function as an antechamber for the UHV-EC transfer chamber, as you will see in the next section.

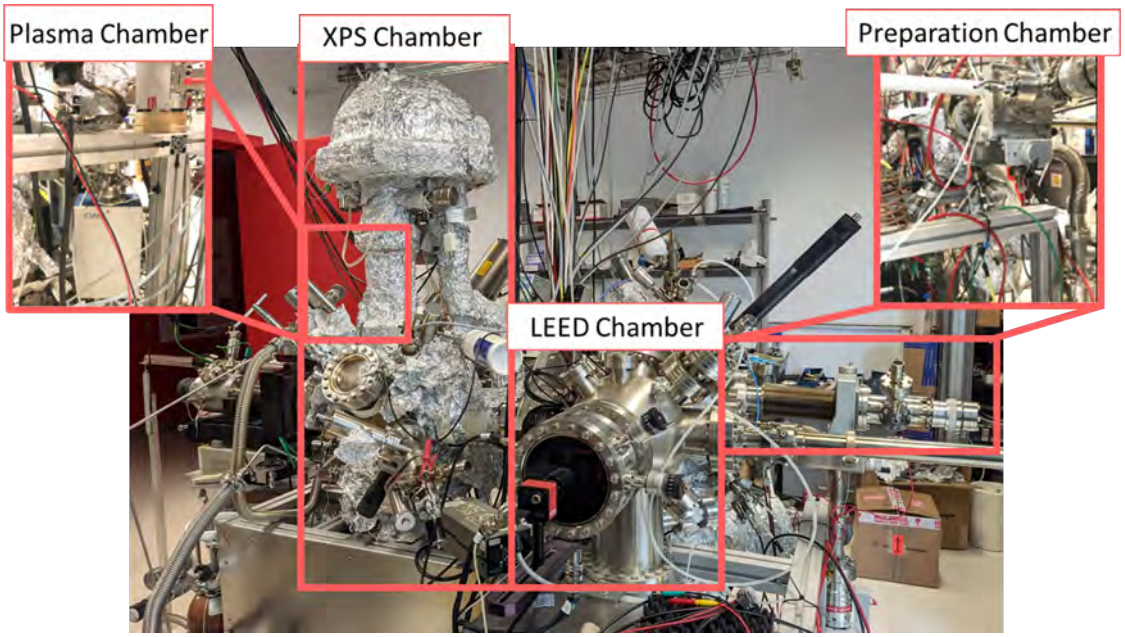

Figure 4.3: Ultra High Vacuum (UHV) system before the connection to the EC-UHV system. It is equipped for the preparation and characterization of surface catalysts. The photograph was captured in 2020.

4.2.2 EC-UHV transfer system: clean and controlled atmosphere

As aforesaid, after adapting the UHV system, we have designed a customized UHV-EC sample transfer system that facilitates the controlled transfer of samples in an Ar-based inert atmosphere between the UHV and the EC cell. It is illustrated in Figure 4.4.

The newly designed EC-UHV chamber features independent pumping capability, enabled by a small turbomolecular pump positioned on the left side, as shown in Figure 4.4. It includes a gas dosing system driven by a metal leak valve connected to a high-purity Ar bottle (99.999%) via Swagelok connections. This setup, combined with a compact full-range gauge (Pfeiffer Vacuum PKR 361), ensures precise control of the inert ultra-pure argon atmosphere. The chamber can be filled with ultra-pure argon gas to atmospheric pressure without compromising cleanliness during sample immersion or pumped down to UHV for post-characterization of the emersed sample.

The strategic placement of the chamber, adjacent to the high-pressure preparation chamber described previously, allows it to function as a pre-chamber from the EC to the primary UHV analysis chamber. This configuration provides three autonomously pumped modules, ensuring atmospheric control of the sample environment at each experimental stage. It also maintains low pressures in each stage during sample transfer, preventing surface contamination or uncontrolled reactions on prepared surfaces before the electrochemical test. Additionally, it facilitates the sample's return transfer to the UHV analysis chamber for post-characterization using general surface science tools.

The position of the EC cell is critical. Various authors have explored different

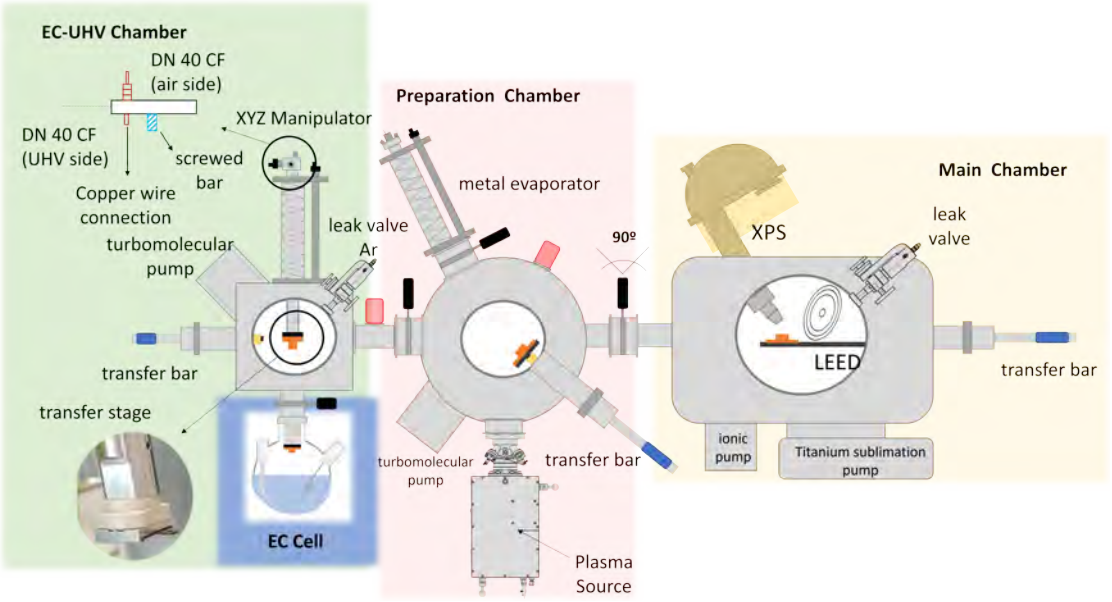

Figure 4.4: Schematic design of the in-house experimental setup designed for the porpoise of this thesis. The EC cell, EC-UHV transfer chamber, preparation and main chambers are highlighted with different colors to clarify the position of each one. Also, it is depicted all the tools used along the thesis.

configurations for electrochemical cells.[42, 47–50, 136–142, 152] Taking previous works into account, we selected the external configuration placing the electrochemical cell behind the UHV chamber. This configuration presents several advantages:

- It allows for conventional electrochemistry with typical liquid volumes in a well-established setup, making it an ideal choice from an electrochemical perspective.
- It provides greater flexibility, as the cell's design can be modified for various experiments, as long as the main connecting flange remains consistent and can adapt to the transfer chamber.
- It facilitates easy visual monitoring of the hanging meniscus and the liquid-solid interface since the glass cell is located outside the UHV chamber.
- Although we did not explored in this thesis, it offers potential benefits for using optical techniques coupled with the cell, such as Infrared Reflection-Absorption Spectroscopy (IRAS), Surface-Enhanced Raman Spectroscopy (SERS), or Ultraviolet (UV) spectroscopy, as the cell remains outside the vacuum chamber during measurements.
- As one of the primary objectives of transfer systems is to prevent contamination, the external cell setup enables straightforward removal of the cell for thorough cleaning following standard electrochemistry procedures.

In this case the EC cell is independent connected to the EC-UHV chamber through a CF/KF adaptation and isolated from this by a VAT valve.

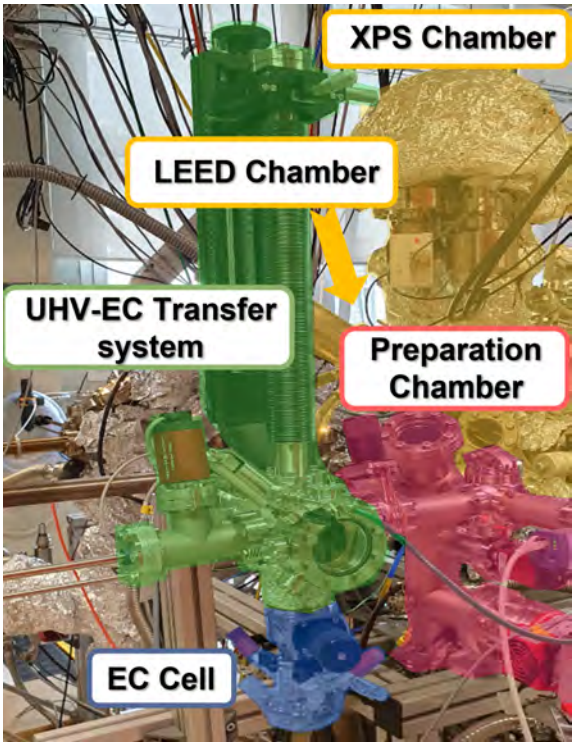

Figure 4.5: Photograph of the experimental setup with false color highlighting analysis chamber (green), preparation chamber (red), EC or transfer chamber (green) and EC cell (blue). It was taken in 2020.

Given the EC cell's position, the designed EC-UHV stage includes a transfer bar that allows the sample to be picked up from the preceding stage (the plasma chamber) and placed into the vertical xyz-manipulator installed in the EC chamber. The manipulator integrates an adapted and isolated commercial sample holder (RECOM from Ferrovac) connected to the manipulator through a threaded bar. It terminates with a modified DN40CF fitted with a BNC connection, establishing the external electrical contact to the sample holder and sample (working electrode). The bottom part of the chamber is sealed from UHV and ambient atmosphere via a gate valve (VAT Germany) with an incorporated CF to KF adaptation for the insertion of the EC cell. The EC cell is positioned below the EC chamber in the KF flange and is sealed by an O'ring and an adapter that ensures the isolation to air, enabling a protected transfer of the sample to the liquid or electrochemical environment without exposure to air in a controlled atmosphere. In this configuration, the EC-UHV chamber is designed to be the transfer chamber between the UHV-EC environments.

A photograph of the final system is shown in Figure 4.5. The UHV-EC system operates at a base pressure in the range of $1 \cdot 10^{-9}$ mbar (after backeout) - $1 \cdot 10^{-8}$ mbar (after EC-UHV experiments).

To summarize, the described and implemented setup allows samples to be prepared in UHV and then transferred from UHV to ambient pressures through a controlled, clean atmosphere based on an inert gas like Ar. The EC-UHV transfer mechanism will be exposed later. For a proper comprehension of the transference

methodology followed, first I need to introduce additional specialized instrumentation for this process. The following subsections will provide a brief description of the special design of the EC cell and the sample geometry used.

Electrochemical cell and operational configuration

The EC cell used in this thesis is a conventional three-electrode-based cell, originally developed by Grumelli et al.[151, 152], with the studied sample serving as the working electrode being immersed vertically. The cell was designed at the Nanoscale Science Department at Max Planck Insitute for Solid State Research (MPI-FKF-Stuttgart) using pyrex glass. It is imperative to avoid glasses containing arsenic, a common component in many Pyrex varieties. Pyrex 7740 minimizes the use of arsenic. A schematic illustration of the EC cell is presented in Figure 4.6a.

The design incorporates four ground joints: two for the reference and counter electrode, one for introducing gases into the solution or maintaining a gas flow above it, and an additional one for potential oxygen sensitivity monitoring or electrolyte filling.

To establish a controlled atmosphere within the cell Schlenck techniques are needed. The EC cell needs to connect different tube-based systems connecting it to vacuum, as described in the preceding section, and to Ar gas. Consequently, the cell includes Schlenck-based ports for argon gas entry. As depicted in Fig. 4.6a, there are two ports featuring two Teflon taps: one for filling the cell with inert Ar atmosphere (Ar in) and a second one for evacuating (Ar out), used to sustain a clean and controlled atmosphere over the hole cell. Two analogous ports to RE and CE ones are placed beside them, facilitating the Ar solution bubbling for removal of dissolved oxygen from the electrolyte. An additional port is positioned in the upper part of the cell, specifically designed for the use of a drop-maker as indicated in Fig. 4.6a, enabling the placement of a drop on the sample facing downward for the hanging meniscus configuration. Further details will be provided in the next section.

A real photograph of the cell, along with the drop-maker, is depicted in Figure 4.6b.

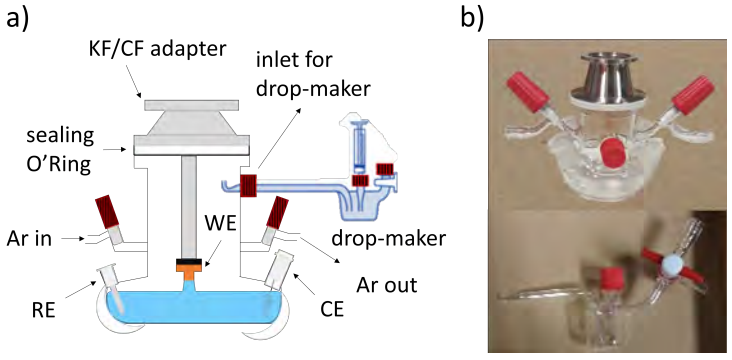

Figure 4.6: Schematic drawing of the EC cell adapted from [151]. Two additional ground joints are omitted for simplification. b) Real photographs of (top) the EC cell and (bottom) the drop-maker device.

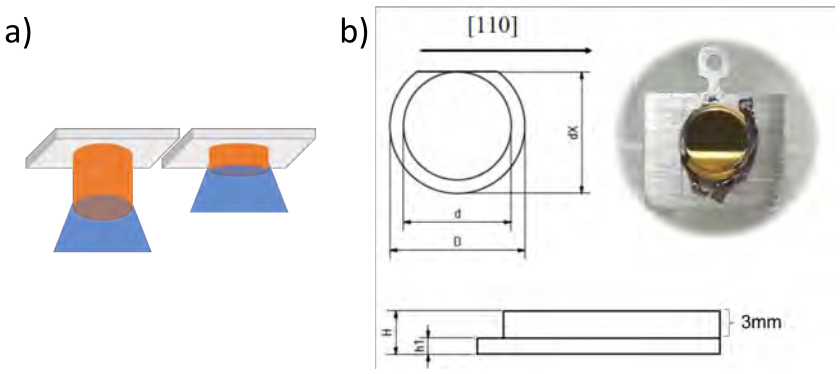

Figure 4.7: a) Schematic drawing of the meniscus configuration in the hat-shaped samples utilized in this thesis. b) Design and actual photograph of an Au(111) single-crystal hat-shaped sample.

Sample geometry: meniscus configuration

The electrochemical studies are performed using the meniscus configuration, a method commonly employed in surface electrochemistry.[153, 154] In this configuration, only the surface plane of the single crystal working electrode makes contact with the electrolyte solution. The electrode is then gently lifted just above the liquid level, creating a meniscus suspended from the crystal face. The arrangement of the resulted configuration is schematized in Figure 4.7a. Utilizing this configuration helps minimizing electrochemical reactions along the sides of the electrode, allowing a focused study on the well-ordered surface plane of the crystal.

Moreover, operating within this geometric configuration facilitates the correlation of electrochemical data with specific crystallographic planes, thereby establishing structure-function relationships at the electrolyte interface. However, a significant challenge associated with this approach is the potential for surface and electrolyte cross-contamination during reactions. This risk arises from inadvertent contact with the sample plate, either during the formation of the meniscus configuration or due to capillary action resulting from electrolyte vapor condensation following prolonged electrochemical tests.

To address this issue, the sample surface is initially wetted with a hanging droplet of purged electrolyte before contacting the electrolyte surface. This procedure minimizes the likelihood of wetting other parts of the sample or the sample holder. A device called a drop-maker (presented in Fig. 4.6) which includes a specially shaped pipette, is employed to create a droplet on the crystal surface, ensuring controlled wetting and preventing splashing. Alternatively, chemically inert sample holders can be used.

In our method, single crystals are configured in a hat-shaped geometry and attached to a standard flag-shaped sample holder using mechanical fasteners such as metal wires or strips made from stainless steel, molybdenum, or tantalum, as depicted in Fig. 4.7b. The height of the crystal is adjusted to maintain a minimum separation of 3 mm between the base of the sample plate and the upper crystal surface (see Fig. 4.6). This straightforward approach effectively prevents accidental contact between the electrolyte and the sample holder, thereby minimizing unin-

tended interactions beyond the crystal surface components.

4.3 Synergistic methodology followed in this Thesis

By mid-2020, after the COVID-19 lockdown, the EC-UHV segment of the system was operational following the adaptation and installation of the full setup. Consequently, a comprehensive methodology for EC-UHV experiments is warranted. This section will offer an overview of the synergistic study of electrocatalysts, demonstrating how surface science and electrochemistry are applied to the same sample without uncontrolled alterations during the transfer between both environments within the established setup.

4.3.1 Preparation of electrochemical tools and reagents

Routinely UHV-EC experiments on the same sample involve more than just transferring from UHV to an EC environment. Additional steps include ensuring ultra-clean conditions using high-purity chemicals. Ultrapure water (18.2 M·Ωcm, total carbon $<$ 5 ppb) is provided by a Smart2Pure3 water purification system (Thermo Fisher Scientific). Before measurements, all glass and components in contact with the electrolyte must be meticulously cleaned, following a protocol from Feliu's research group [155], methodology acquired during the stay in Alicante University. Glass is immersed for at least 12 hours in a 2 g/L $KMnO_4$ solution in diluted H_2SO_4, followed by rinsing in 1 H_2O_2 + 0.1 M H_2SO_4 to remove residuals, then rinsed with ultrapure water and boiled for 15 minutes. This cycle is repeated three times for H_2SO_4 electrolytes and once more for non-specific adsorption solutions like NaOH.

Prior to initiating the experiment, the Ar inlet system to the EC cell is evacuated by opening the valve to an external pumping station. The EC cell is prepared before sample transfer: initially filled with the chosen electrolyte, followed by Ar filling to displace air content while simultaneously bubbling with Ar to eliminate dissolved O_2 in the solution. A stable and controlled atmosphere is maintained for 1 hour before experiment, allowing electrochemistry to commence directly after the transfer.

4.3.2 EC-UHV Transfer stage

We have implemented a design where the EC cell is situated beneath the EC-UHV chamber, offering convenient visual monitoring of the hanging meniscus. The immersed transfer UHV-EC mechanism follows next steps:

1. The process begins with the plasma chamber, where sample is placed, and the EC-UHV transfer chamber both at their base pressure being $< 1 \cdot 10^{-9}$ and $5 \cdot 10^{-9}$ mbar, respectively. All valves are closed.

2. The valve VAT is opened and both chambers are connected, stabilizing the pressure at $1 \cdot 10^{-9}$ mbar.The sample is picked with the transfer bar and transferred into the EC chamber.

3. The gate valve is promptly closed again. The time duration during which this valve is open is brief, minimizing the impact on the vacuum in the preparation chamber during the transfer. The vertical manipulator holding the sample holder is maneuvered into the chamber, and the sample is positioned facing downward.

4. The turbomolecular pump is turned off, and the bottom part is sealed to prevent air insertion. The Ar line is gradually opened while the turbomolecular pump is slowing down, ensuring a controlled process.

5. When the pump speed is below 500 rev/min, the needle valve is fully opened to augment the Ar flux. This entire process takes approximately 15 - 20 minutes until the pump is completely turned off, and the chamber reaches atmospheric pressure with Ar gas.

6. Now that the EC-UHV chamber is at atmospheric pressure of Ar gas and the cell has been at this pressure, both parts have equal pressure and the gate valve can be opened. The gate valve to the EC cell is opened and the sample is lowered into it. Note that the EC-UHV chamber and the EC cell remain connected over the hole EC experiment. To prevent air insertion, a slight Ar overpressure is applied to both the transfer chamber and the EC cell.

7. An overpressure is generated in the cell via the Ar inlet port, while the port for inserting the drop-maker is opened. This step allows one to verify the release of the overpressure, confirming its proper operation and ensuring no air is introduced. The drop-maker is then inserted, and using a syringe, a droplet is carefully created and placed onto the sample surface. Subsequently, the port is closed, and the overpressure is ceased.

8. The sample is slowly moved back, ensuring it makes contact safely with the solution to prevent splashing. Upon contact, the surface is retracted by 3 mm, measured on the vertical manipulator, to minimize edge effects.

While the process of transferring a sample from UHV to the EC cell is intricate, careful adherence to the correct order and attention to gas flow ensures complete control over the process, guaranteeing a clean transfer. The entire procedure, from the sample being in UHV to the commencement of the EC experiment, takes approximately 30 minutes, which aligns with our requirements. The longest stage is the chamber filling when the pump is turned off, constrained by the maximum flow via the needle valve. The chamber's intentional small size expedites the filling process.

After the EC experiment, the chronological steps in the emersed transfer is as follows:

1. The sample is removed just seconds before finishing the EC test with potential control.

2. The sample surface is rinsed with purged Milli-Q water using the drop-maker while applying an overpressure of Ar to the cell. This procedure serves two

purposes: (i) to remove any residual bulk electrolyte that may have been adsorbed onto the surface due to improper concentration selection (if applicable), thus eliminating its presence, and (ii) to leave only stable chemisorbed species on the surface.

3. The manipulator is retracted, and the valve connecting the EC cell and the EC-UHV chamber is closed.

4. The Ar leak valve is closed, and the bottom valve in the turbomolecular pump is opened slowly. At a first instance the membrane pump makes noise removing the Ar atmospheric pressure, after some seconds it works in silence as intended.

5. When the pressure is below 10^{-2} mbar, reaching the 10^{-3} mbar range, the small turbo molecular pump is switched on. If you do not wait to this pressure, the final pressure of the chamber is worst.

6. The EC-UHV chamber reaches pressures $1 \cdot 10^{-8}$ to $5 \cdot 10^{-9}$ mbar after approximately 2 h. To reduce the exposition of the surface to high pressure, the transfer is made at $1 \cdot 10^{-6}$ mbar after 1h.

7. The VAT valve between EC-UHV chamber and plasma chamber is carefully opened, stabilizing the pressure at $1 \cdot 10^{-8}$ mbar, and the sample is transferred to UHV system. The gate valve to the preparation chamber is opened for the shortest time possible. Immediately after the transfer, the pressure is slightly higher in the preparation chamber but recovers within 5–10 minutes, having minimal impact on the pressure in the preparation chamber.

This system is time expensive due to the gradual recovery pressure. This fact is attributed to the incapacity to close the gate valve between the transfer chamber and the EC cell during electrochemical experiments. In our design, the gate valve must remain open due to the manipulator blocking its closure. This configuration results in water vapor from the electrolyte entering the transfer chamber and adsorbing on the inside walls, desorbing slowly during pump-down. Baking the bellows could address this issue. In addition, an ongoing system upgrade involves the addition of a gate valve between the turbomolecular pump and the entire UHV-EC transfer chamber, allowing prolonged pumping for enhanced cleanliness. This modification also could facilitated a quicker pump shutdown during Ar gas introduction, preventing operational issues. Additionally, the pump may be safeguarded against corrosion from electrolyte fumes, and an extra bypass valve could further reduce the chamber-filling time.

The synergistic methodology routine outlined and followed in this thesis is schematized in Figure 4.8. Here, routine EC-UHV experiments involve XPS and LEED characterizations of clean or as-grown samples both before and after EC experiments for unavailing surface dynamics on electrochemical processes like electro-oxidation and OER catalysis. In some cases, as we will see in the next chapters, additional EC characterization is performed after post-EC XPS analysis, making this synergistic study a complete cycle, as depicted. It should be noted that during sample

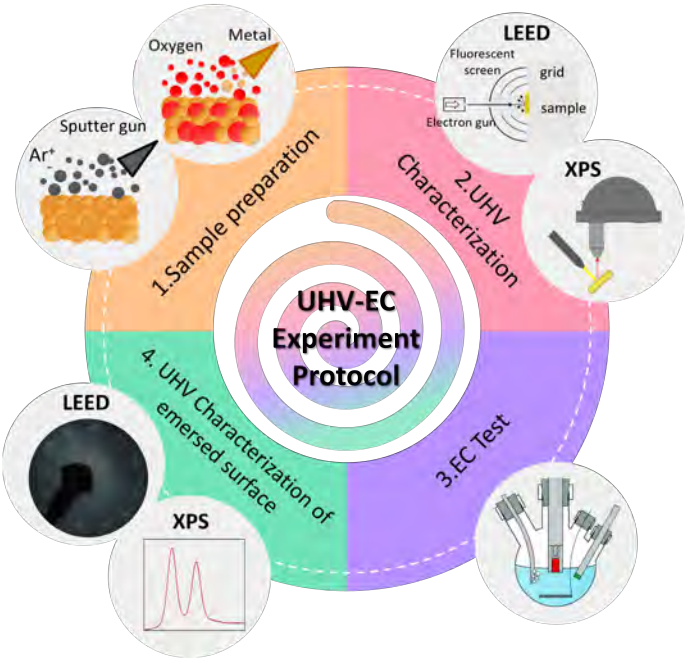

Figure 4.8: Diagram illustrating the synergistic UHV-EC experiment, beginning with the preparation of the sample through UHV cleaning and/or CVD oxide growth (1), followed by surface characterization (2), electrochemical tests (3), and characterization of the emersed layer (4). This cycle can then be repeated.

preparation, the transfer chamber is under UHV conditions, and this time is utilized for all preparation steps, including sample preparation as well as the preparation of glassware and electrochemical reagents, before the actual transfer.

4.4 Summary

In summary, this chapter has outlined various instrumental approaches for studying electrode surfaces by integrating electrochemistry with surface physics characterization techniques. The literature review has examined the strengths and limitations of each approach, emphasizing the significant advantages of the emersed or quasi-in situ method over other methodologies. These benefits include its compatibility with existing UHV equipment, such as the use of standard electrochemical cells with conventional volumes and geometries, the versatility in employing multiple techniques, and the ease of maintenance and daily operation without compromising the vacuum integrity of the main chamber. This approach is particularly advantageous for tracking stable and irreversible potential-dependent chemical and structural surface changes due to the controlled removal of samples from the electrolyte under potential control for surface characterization in a clean atmosphere, aligning with the primary objectives of this thesis.

Consequently, an operational UHV system has been customized to incorporate sample preparation chambers essential for this thesis and to integrate a transfer chamber tailored for EC-UHV experiments. This development has culminated in

the establishment of a modular system comprising a UHV chamber coupled with an EC-UHV transfer chamber, facilitating sample transfers under controlled environmental conditions. Detailed descriptions have been provided regarding the electrode configuration, including the electrochemical cell utilized and the use of the so-called meniscus configuration,

Furthermore, the methodology employed for each experiment in this thesis has been comprehensively explained. This encompasses the preparation of materials for electrochemistry and the step-by-step procedures involved in sample immersion and emersion, ensuring clarity and reproducibility in experimental protocols. With this design, the time required for one complete experiment is a minimum of 8 hours. This includes cleaning the sample, growing selected structures (if needed), transferring the sample, performing EC experiments, and post-characterizing it. Despite this duration, the sample remains under UHV for the majority of the time.

Chapter 5

Unveiling Au(111) surface species during its electrochemical oxidation

In the previous chapter, Chapter 4, we detailed the design and implementation of a customized EC-UHV compatible setup installed during this thesis. By bridging the material gap within the same sample and experimental setup under controlled conditions allows for a fundamental understanding of the reaction processes at the electrode-electrolyte interface in a quasi-*in situ* EC-UHV approach. Consequently, the primary objective of this chapter is to give insights into the applicability of the experimental methodology developed to investigate the electrode/electrolyte interface.

To this end, we have used the well-ordered surface electrode, Au(111), as a model system. The choice of gold (Au) and its (111) facet as the model system is due to its widespread use in scientific research, especially in electrochemistry and surface science. This choice facilitates a better understanding of general surface processes, including surface reconstruction, adsorption, and electrocatalytic reactions, which have been extensively studied in the literature with ambient pressure EC (AP-EC), as well as *ex situ* and emersed electrode approaches.

Although Au(111) is well-known in the electrochemical community, it also holds significant relevance in the electrocatalysis field. Gold, Au(111), exhibits an extended stable potential window, remaining stable at high anodic potentials where OER evolves. This stability allows Au(111) to be used as an OER catalyst at high anodic potentials, albeit with low rate performance. Thus, this surface serves as an ideal substrate for supporting highly active catalysts. However, there are still fundamental questions that need to be resolved before this model surface can be fully utilized for this purpose. Consequently, the applicability of the quasi-*in situ* experimental approach will be tested investigating potential-induced changes at the Au(111) electrode/electrolyte interface under realistic reaction conditions in particular in its electro-oxidation and subsequent OER evolution, establishing a direct correlation between local catalyst surface properties at the meso/nano-scale (surface composition and structure) and its macroscopic catalytic response (reaction mechanism, catalyst activity, and stability). To accomplish this, it is crucial to maintain a

clean environment where surfaces remain unaltered and free of contaminants or particles sticking on the surface during all the processes to not alter the potential-induced phase. Therefore, we will use the previously designed EC-UHV system to unify the controlled study of these electrochemical processes through surface-sensitive physics techniques on the same electrode (sample).

Specifically, we have examined the electrochemical features along with the chemical and structural evolution of the Au(111) surface in relation to applied potential and electrolyte media, ranging from acidic (in H_2SO_4 and $HClO_4$, letter data not presented in this manuscript) to alkaline (NaOH, discussed in the subsequent chapter in section 6.4.1) pH conditions. In this chapter, we will explore the electro-oxidation mechanism of the Au(111) surface under high anodic potentials preceding and under the OER in diluted H_2SO_4 focusing on the role of electrolyte anion-adsorbed species. To this end, we will begin by describing the electrochemistry of Au(111), highlighting voltammogram features and previously established chemical and structural attributes from the literature to set the context for our findings. We will then present the electrochemical features of Au(111) obtained with our setup and compare them with literature data. Following this, we will examine the mechanistic aspects of electrochemical oxidation and subsequent OER on gold. This investigation will focus particularly on different potentials within the surface electrochemical window, spanning both non-faradaic and faradaic regions, and extending beyond the OER onset in diluted H_2SO_4 solution. Next, we will discuss the impact of time-dependent high anodic potentials within the OER regime on the chemical and structural composition of Au(111). All this will include a synergic study combining UHV-based techniques for chemical analysis using XPS and structural characterization via LEED before and after electrochemical tests (cyclic or linear voltammetry and chronoamperometry) on the same Au(111) sample. Finally, we will partially corroborate our findings with DFT calculations.

Through this interdisciplinary study, we aim to evaluate the effectiveness of our instrumental approach in studying model anode surfaces and address fundamental electrochemical questions. Particularly, our aim is to offer novel insights into the commonly accepted electro-oxidation mechanisms preceding the Oxygen Evolution Reaction (OER). This will be achieved by uncovering: (i) the reaction mechanism through the surface composition, (ii) the role of electrolyte ions and (iii) the actual OER active phase. Validating these opened questions in the model Au(111) system with the newly developed EC-UHV set-up allows to establish the approach and its applicability to more complex systems, such us manganese oxides catalysts (presented in next chapter, Chapter 6).

5.1 The electrochemistry of Au(111) surface in H_2SO_4: General aspects

Gold surface orientations, in general, exhibit very weak chemisorbing properties compared to other metals like Pt, resulting in an extensive double-layer region where non-Faradaic processes are observed.[156] This property makes gold a suit-

able substrate for studying electrochemically active materials within relatively high potential ranges, as will be seen in Chapter 6. Among all basal planes, the (111) facet is considered the most reactive, presenting stronger interactions with adsorbates than other facets. With the highest atomic density compared to the (110) and (001) plane, it provides numerous sites for physisorption and chemisorption. In this regard, as exposed in Chapter 2, the only processes that can be observed in the non-Faradaic range are adsorption and desorption, which is influenced by the electrolyte concentration. Additional electrochemical features, specifically Faradaic processes where electrons are transferred across catalyst/electrolyte solution interface, emerge at very high anodic potentials where the oxidation of the gold surface precedes the OER.

In electrochemistry, the oxidation of noble metals like Au in acidic media has been extensively studied, focusing on both the initial stages of oxidation and the growth of thicker oxides. The combination of various surface techniques, such as *ex situ* XPS[117–120] and STM[119] (with air-based transfers between EC and UHV environments) and *in situ* or operando ambient pressure EC-STM[121, 157], -SXS [158, 159], -HESXRD combined with 2D-SOR [160], -SERS[161–163], and -SEIRAS[121]; together with electrochemical techniques, such as CV[164–168] and CA, offer insights into the electro-oxidation mechanism of the gold surface in acidic media. The sequential electro-oxidation mechanism, considering the general agreement in the cited literature and considering the role of electrolyte anions (e.g. HSO_4^- and SO_4^{-2}), unfolds as follows:

1. Adsorption of interfacial water and anions from the electrolyte in a single form, either HSO_4^- or SO_4^{-2}. The anion adlayer determines the actual onset potential for oxidation because of its competition with the initial stages of OH electrosorption.

$$AuX^- \cdot nH_2O \leftrightharpoons AuX^- \cdot OH^{(1-\delta)-} \cdot (n-1)H_2O + H^+_{(aq)} + \delta e^- \tag{5.1}$$

   where X^- refers to either HSO_4^- or SO_4^{-2} and $0 \leqslant \delta \leqslant 2$.

2. Two-dimensional formation of OH/O species with simultaneous anion desorption, caused by adsorbed OH^- species discharge.

$$AuX^- \cdot mOH^{(1-\delta)-} + (m-1)Au \rightarrow mAuOH + X^- + m(1-\delta)e^- \tag{5.2}$$

$$AuOH \rightarrow AuO + H^+ + e^- \tag{5.3}$$

3. Place exchange process ("turnover process"- RTO) between OH/O species and the metal surface atoms leads to the formation of "(hydrous)oxide" in a quasi-2D compact layer (called β-oxide) as the coverage of OH/O species increases with potential, from less than 1 ML up to 3 ML. It is accepted that the repulsive interactions between the AuOH/AuO dipoles eventually cause the RTO.[168]

$$AuOH \rightarrow OHAu/AuO \rightarrow OAu \tag{5.4}$$

   At least one of the described RTO processes occurs, either forming OHAu or OAu. The aroused species from this process stem from the type and position of the oxygen bond: transformed from AuO(H), in which the oxygen is

chemisorbed on the gold surface while in O(H)Au the oxygen is incorporated into the gold surface.

4. The progressive thicker oxide growing gives a three-dimensional "(hydrous)oxide" (called α-oxide), occurring by a high-field type mechanism proposed by Mott and Cabrera [169].

This mechanistic model aligns with the general model accepted for the electro-oxidation of noble metals[164]. This model assumes a combination of anion effects with a place-exchange process, converting a two-dimensional oxygen-based layer into a three-dimensional layer as the film extends. The electrochemical oxidation of noble metals is typically recognized as the preceding step to the OER reaction.[161]

The primary pathways proposed and extensively accepted for OER reaction on metal surfaces in acidic media are detailed in section 2.4. In the introductory chapters, the function of oxygen-based intermediates in the oxygen-evolving mechanism was described without surface consideration. For a proper understanding focused on the present case of Au(111), considering equations 2.9-2.12 and involving a gold metallic surface, the dynamic reaction for the reorganization of oxygen atoms on the surface to form O_2 can be described as follows:

$$M + H_2O \leftrightharpoons M - OH + H^+ + e^- \tag{5.5}$$

$$M - OH \leftrightharpoons M - O + H^+ + e^- \tag{5.6}$$

$$M - O + H_2O \leftrightharpoons M - OOH + H^+ + e^- \tag{5.7}$$

$$M - OOH \leftrightharpoons M + O_2 + H^+ + e^- \tag{5.8}$$

It should be highlighted that the steps 5.5-5.6 detailed in the mechanism for the OER agree with steps 5.1-5.3 specifically outlined for gold electro-oxidation in an acidic medium. This mechanism assumes that the oxidized metal acts as the actual OER active phase. However, it does not account for the influence of ions on oxygen evolution or the RTO process. Therefore, it is essential to study both processes — electro-oxidation and OER — simultaneously and with the same methodology to elucidate the role of anions and the OER active phase in the evolution of oxygen gas, giving comprehension on its behaviour acting as anode in an electrolyzer.

Both electro-oxidation and the OER reaction involve oxygen-based species, which depend on the applied potential and the time scale. Disparities among the analyzed literature arise in this context due to the use of different experimental methodologies and characterization techniques, as well as electrochemical configurations to determine the surface chemical composition at each step of the Au(111) electro-oxidation mechanism. Initially it was believed that the oxide or hydroxide phases formed consisted of either Au^+[170] or Au^{+2}[171, 172] states. However, following Pourbaix prediction, it should be noted that oxidation states Au^+ and Au^{+2} are not characteristic of gold oxygen compounds [77]. More recently, papers claimed that the adlayers contain gold in the Au^{+3} oxidation state [118, 173, 174].

The exact nature of the adsorbed oxygen species, whether they are OH- or O-based species, and the changes in the OH/O ratio with applied potential and time

remain unresolved. This has led also to different theories proposing various compositions of oxygen-based gold layers raised due to the RTO process: AuO[170] and $Au(OH)_2$[171, 172] in earlier works, and $Au(OH)_3$[117, 118, 161], Au_2O_3 or $Au_2O_3 \cdot 3H_2O$[175], and $AuOOH$ in more recently studies. The same occurs with the unveiling of the actual OER active phase in Au(111) anode attributing $Au(OH)_3$[118], Au_2O_3 or $Au_2O_3 \cdot 3H_2O$[161], and $AuOOH$[117, 162] chemical stochiometries. Understanding these attributions underscores the necessity to thoroughly explore how different authors have arrived at their conclusions.

In the early stages of oxidation, it is widely proposed that chemisorbed hydroxyl radicals ($^*OH_{(ads)}$) are derived from water molecules present in solution. Supporting this theory, *in situ* STM studies show the appearance of rough patches on the surface at potentials below anodic features, which grow significantly in the potential range of the RTO, where the anodic feature appears [157]. This is consistent with the presence of a precursor layer, likely involving OH adsorption, which later transforms into oxide.[117, 118, 161] Indeed, Peuckert et al.[117] conducting *ex situ* XPS studies on thin oxide layers on polycrystalline gold revealed the formation of an initial $Au(OH)_3$ layer. New insights into the chemical composition transition upon further increase in potential are provided in their work. This layer is thought to deprotonate or break down into gold oxyhydroxide, $AuOOH$, at potentials above 2.0 V vs. RHE, where OER occurs, as indicated by a new component observed in the CV reduction feature. This conclusion is also supported by *in situ* SERS[161, 162] and theoretical DFT calculations[23, 24], which show that OOH species form on Au only at potentials above which a surface oxide layer has been formed, thus entering the OER regime. Conversely, another theory postulates that chemisorbed OH forming an $Au(OH)_3$ precursor adlayer undergoes further oxidation to Au_2O_3, as indicated by the anodic ET peak observed in a CV, confirmed by the analysis of integrated peak charge from voltammetric techniques. Similarly, Juodkazis et. al.[118], by *ex situ* XPS, suggested that at 2.1 V vs. RHE, gold anodic polarization produces Au^{3+} and O_2^{2-} oxidation states, indicating $Au(OH)_3$ or Au_2O_3 structures, with a preference for $Au(OH)_3$ based on a thermodynamic perspective. Although none of the mentioned works identified an unified chemical specie until now, they agree that high anodic potentials or extended time scales are needed to observe oxide emergence.

In terms of electrolyte ions role in, Rodriguez et. al.[119] investigated the initial stages of Au(111) electro-oxidation combining surface science techniques and CV, with samples transferred through air and protected with a water drop. This work revealed a sulfate or bisulfate adlayer prior to surface oxidation using surface science techniques, but it could not fully elucidate the electro-oxidation mechanism due to carbonaceous residues from air transfer passivating the surface and avoiding the oxidation of the surface. More recently, Zhumaev et al. proposed that (hydrogen)-sulfate ions adsorbed on the Au(111) surface form a precursor phase to the oxide layer (AuO) without observing OH presence, based on SIRAS measurements [121]. Shi et al. suggested that the layer consists of sulfate based on chronocoulometric data [176].

Despite extensive efforts to determine the sequence of potential-dependent surface changes and the chemical composition of gold oxide, the structure and composition of the emergent structures remain controversial. It is crucial to note that all

previous assignments were conducted using *ex situ* surface-sensitive techniques like XPS, where samples transferred through air are susceptible to inevitable contamination. Furthermore, *in situ* experimental investigations utilize ambient-pressure electrochemical techniques, preparing samples through air flame-annealing instead of UHV methods, and assessing cleanliness via CV rather than surface science techniques, which may not comprehensively evaluate sample cleanliness. Therefore, a comprehensive study employing quasi-*in situ* surface-sensitive techniques with controlled and inert transfers on the same sample is necessary to preserve oxygen-related species and address unresolved previously proposed questions.

In summary, drawing on existing research, the complex process of anodic surface electro-oxidation of Au(111) in acidic media involves competitive adsorption of species like OH^-, SO_4^{-2}, or HSO_4^-, as well as OH or O exchanging places with metal surface atoms, forming compounds such as $Au(OH)_3$, Au_2O_3, and $AuOOH$. Correlating CV features in H_2SO_4 media with potential- and time-dependent species at high anodic potentials and their impact on surface structure and chemical composition is essential for understanding electrode dynamics.

For that porpoise, in the following section, we will detail different published studies involving the electrochemical analysis of the Au(111) surface in H_2SO_4 using CV. The goal is to identify and correlate widely accepted electrochemical features associated with each step of the described electrochemical oxidation mechanism, linking the chemical and structural attributes of each step with the corresponding electrochemical features as a function of the applied potential. This analysis is intended to provide a foundational understanding to facilitate easier comprehension of the experiments conducted and results obtained in our investigation.

5.2 Au(111) electrochemical features in H_2SO_4 media

The entire potential range of Au(111) encompasses three distinct regions, as illustrated in Figure 5.1: the blue region represents the double-layer region, characterized by potentials below 1.15 V, where mere adsorption processes occur[67, 69]; the yellow region has been related to the Au oxide formation; and the red region is where the OER region starts. It should be highlighted that although the following discussion draws extensively from the literature the presented voltammogram, depicting all relevant processes, has been obtained using our described experimental setup and serves as mere fingerprint for the subsequent explanation. It will be additionally presented in next section where our obtained results will be discussed. Notice that the potential in the figure is referred to Ag/AgCl/KCl (3 M) instead of RHE.

5.2.1 Au(111) double-layer region

Au is a polarizable electrode, though it is not a highly effective HER catalytic surface[177]. The absence of a hydrogen adsorption region is evident in the initial

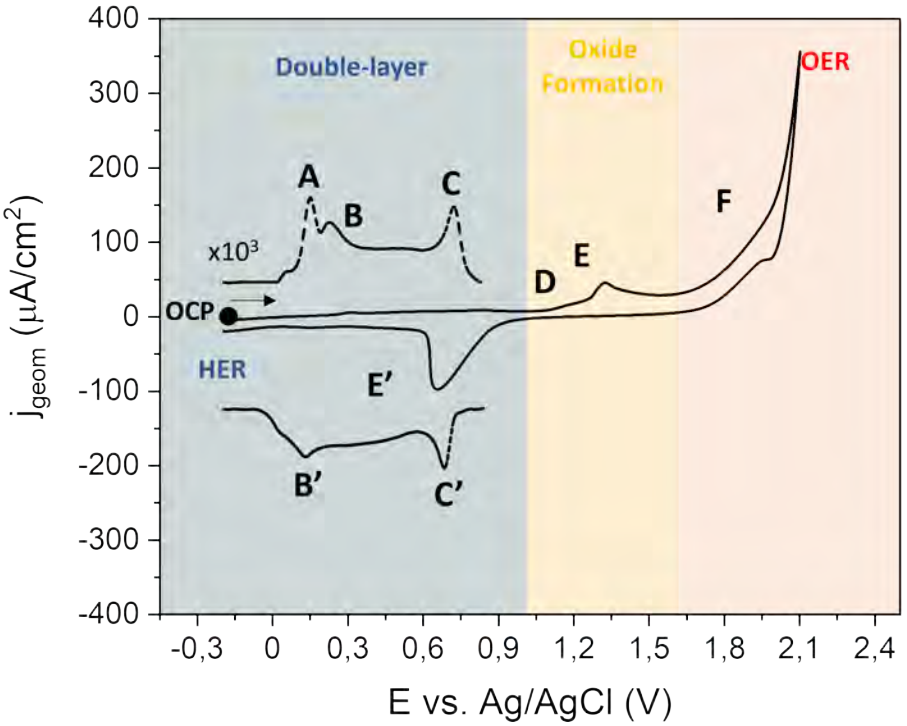

Figure 5.1: Cyclic voltammogram of Au(111) acquired in the EC-UHV set up in deaerated 0.05 M H_2SO_4 , scan rate 50 mV/s used as model resembling the ones found in literature.

segment of the voltammetric window, as depicted in Figure 5.1, which would show a broader capacitive double-layer with a current onset at the end of the cathodic brunch. Instead, an extended capacitive double-layer region predominates at the onset of the CV, highlighted in blue, allowing to distinguish adsorption processes of anions. It reveals anion adsorption (peaks A and B) and emphasizes surface sensitivity due to the lack of hydrogen occupying available metal sites. Peaks A and B have been attributed to the adsorption of sulfate/bisulfate anions and the subsequent lifting of the herringbone reconstruction, respectively.[158, 159, 178, 179] This observation underscores the significant influence of surface reconstructions and anion adsorption layers on the electrochemical behavior of Au(111).[179]

Indeed, as the potential increases from the open circuit potential (OCP) — which represents the electrode's equilibrium potential when no net current flows and no chemical or electrochemical reactions occur — a distinct peak appears around 0.44 V vs RHE (corresponding to Peak A at 0.298 V vs Ag/AgCl). This peak is linked to the anion-induced lifting of the $(\sqrt{3} \times 22) - Au(111)$ surface reconstruction.[180] After A, a broad peak at 0.50 V vs RHE arises (Peak B at 0.376 V vs Ag/AgCl in Figure 5.1), attributed to (hydrogen)sulfate (SO_4^{-2}/HSO_4^-) adsorption in a disordered manner, resulting in an unreconstructed (1×1)-phase.[181] This lifting of reconstruction followed by anion adsorption, transitioning to a rough $(1\times1) - Au(111)$ surface structure, is induced by the sulfur-composed layer formed by anion adsorption as was reflected *in situ* by the combination of IR reflection-absorption spectroscopy (IRAS), atomically resolved STM in conjunction with electrochemical measurements.[182,

183]. In those works it was established that the anions supply charge density, compelling atom rearrangement to accommodate the new energetic surface state, eliminating the reconstructed form. Sulfate-based species contained in the electorlyte, proposed to be adsorbed trigonally on Au(111) surface, involve 10 % SO_4^{-2} and 90 % HSO_4^-, both having three O atoms to interact with the gold surface. To mitigate possible coulombic repulsions between adjacent sulfate/bisulfate ions, hydronium ions (H_3O^+) are coadsorbed.[182] Additionally, water molecules interacting through hydrogen-bridge bonding with oxygen atoms from sulfate/bisulfate anions have been detected.[183]

Between 0.6 and 0.9 V vs RHE, sulfate coverage increases, and hydronium ions (H_3O^+) coadsorb with potential scans until 1.05 V. This coadsorption aims to diminish possible coulombic repulsion between adjacent sulfate/bisulfate ions.[182] IR experiments also confirm the presence of water molecules interacting through hydrogen-bridge bonding with oxygen atoms from sulfate/bisulfate anions.[183] At this point, sulfate coverage becomes substantial enough to initiate a transition in anion structuration from disorder to an ordered phase, marked by a sharp peak (labeled C) at 0.842 V vs Ag/AgCl in Fig. 5.1. This peak's current density serves as an indicator for surface quality, decreasing with an increase in surface defects or step density.[157] Sulfate is known to form a $(\sqrt{3} \times \sqrt{7})R19.1^o - (1 \times 1) - Au(111)$ reconstruction at potentials higher than the sharp peak [180, 183–185]. STM characterization of this layer reveals two kinds of maxima, with the principal one corresponding to adsorbed sulfate and the second one assigned to either coadsorbed water or hydronium.[182] The higher anodic potential in this double-layer window, 1 V vs Ag/AgCl, is considered the initial stage of oxidation, determining the onset of surface oxidation as it competes with the initial stages of OH electroadsorption at higher potentials [186].

The reverse potential scan demonstrates the reversibility of the ordered/disordered sulfate phase (Peak C' at 0.796 V vs Ag/AgCl in 5.1) and anion desorption in the peak labeled B' at 0.269 V vs Ag/AgCl. Below 0.30 V vs RHE, it is considered that the surface starts to reconstruct the $(\sqrt{3} \times 22)$ surface, although the process is slow at room temperature. For this reason, repetitive CV cycles in the double-layer region disrupt the long-range order of the surface, leading to the disappearance of the spike produced by the sulfate disorder/order phase [154].

5.2.2 Au(111) electrochemical window

In the region marked in yellow starts the transition from non-Faradaic region to Faradaic one where Au(111) surface oxidation is proposed to occur. The preceding sulfate $(\sqrt{3} \times \sqrt{7})R19.1^o - (1x1) - Au(111)$ adlayer contends with the co-adsorption of H_3O^+/H_2O. As it was stated, the anion adlayer determines the onset potential for electro-oxidation due to its competition with OH electrosorption. In this regard, Kondo et al. gave insights on the role of co-adsorbed anions prior to OH/O electrosorption by the use of *in situ* SXS reporting that the SO_4^{2-}/HSO_4^- adlayer blocks the surface, and their findings suggest that at higher potentials, around 1 V vs RHE, the sulfate adlayer gives away allowing the adsorption of a monolayer of hydroxyl and water at an atop site of the Au(111)-(1 × 1) surface [159]. This

process was unraveled using *in situ* SXS [159] combined with CV where a minimal anodic current is produced at 1.05 V vs RHE, as indicated by the pre-peak shape labeled D in Figure 5.1. The adsorption of hydroxyl precedes the electron transfer process that produces the oxide formation after a sufficient overvoltage is reached. Simultaneous anion desorption is also evident by CV at slow sweep rates [157]. This step involves the two-dimensional electrodeposition of OH/O species followed by a place exchange (RTO) process between OH and/or O species and the metal surface. Peak E in Figure 5.1, appearing at 1.31 V vs Ag/AgCl, has been attributed to this process.[118, 156, 157, 164] The formed oxide is subsequently reduced in the reversed scan (peak E'), and anions re-adhere at lower potentials until the reconstruction at the end of the voltammogram.

The marked asymmetry observed in the anodic and cathodic peaks strongly indicates the quasi-reversible nature inherent in this process. Even with the initiation of surface reconstruction, a complete restoration to the initial state is never achieved. This well-documented phenomenon in the literature [156] elucidates how surface oxidation followed by reduction leads to the creation of pits and islands, resulting in a surface characterized by defects.[181] This postulation is supported by considering the presence of a place exchange mechanism, where oxygen atoms infiltrate subsurface positions. Subsequent extraction during the reduction process displaces Au atoms from their equilibrium sites, enriching the gold (111) surface with defects.

5.2.3 OER Regimen in Au(111)

Above the anodic peak E, in the Au(111) redox-active window, when the potential is significantly increased, a continuous current trend precedes the OER as it is depicted in the red region, indicating complex sequential chemical changes probably involving oxygen species. At large time-scales[118] or higher overpotentials[117], it is proposed that the oxide formed during peak E undergoes progressive growth, transitioning into a three-dimensional (hydrous)oxide structure. This phenomenon is explained by the high-field mechanism proposed by Mott and Cabrera [169], which retarded the OER to occur.

Around 2.0 V vs NHE the electrocatalytic evolution of oxygen gas begins. Notably, the OER process on the Au surface exhibits inefficiency, characterized by a significant overpotential relative to the theoretical value of + 1.23 V. It is widely accepted that the oxygen coupling steps produce hydroperoxide species (M-OOH) as previously detailed in the OER mechanism (see reactions 5.6-5.8). The formation of the gold oxide layer marks the commencement of molecular oxygen evolution.

The position of the cathodic reduction/desorption peak (peak E') provides insights into the reactions occurring at specific potentials that precede OER. The cathodic peak shifts towards lower potentials in correspondence with the anodic peak, demonstrating the transformation of the oxide layer into a quasi three-dimensional or bulk oxide structure.[157, 164] As the oxide layer thickness increases, the reduction peak also shifts due to the potential drop across the adsorbed layers[117].

The study of the OER regime on Au(111) is challenging due to the absence of distinct electrochemical transfer-based peaks. The mechanism can only be elucidated through Tafel slope analysis (for theoretical insights, revisit Section 2.4.2). The Tafel

slope for OER on Au(111) in sulfuric acid offers crucial insights into the reaction mechanism. Different values have been postulated in the literature, ranging from 45 mV/dec, which suggests a dual potential barrier consisting of a film (not identified) and the double layer at the film/solution interface [187]. However, considering the widely accepted mechanism and the reported values for different RDS in Table 2.2, a range from 60 to 120 mV/decade, indicating the involvement of multiple steps and intermediates, would be expected.

5.3 Potential induced changes in Au(111) surface

Following the previously stated motivation, emphasizing the need to reach a consensus on the electro-oxidation mechanism of the Au(111) surface in H_2SO_4 prior to OER, in this section we will present a synergistic study combining the chemical and structural investigation of the surface along with the electrochemical features obtained from CV using the quasi-*in situ* EC-UHV methodology (described in section 4.3). Here we will demonstrate the effectiveness of our EC-UHV compatible setup for probing electrochemical interfaces. Moreover, we provide a detailed chemical and structural analysis of the Au(111) electrode surface across potential ranges previously described in section 5.2. By employing quasi-*in situ* surface-sensitive techniques such as XPS and LEED alongside electrochemical CV analysis, we investigate the potential-induced surface changes.

We begin by investigating a flat Au(111) sample. Achieving a flat and clean Au(111) surface typically involves a preparation process comprising three cycles of Ar^+ sputtering and annealing. This process includes sputtering at 0.5 - 2 keV, followed by sample annealing to 800 K. Figure 5.2a-b shows XPS spectra for four different core levels, Au 4f, O 1s, C 1s and S 2p, and a LEED image depicting a clean Au(111) surface. The Au 4f spectrum displays the primary peak, Au $4f_{7/2}$, located at 84.1 eV with well-separated spin-orbit components Au $4f_{5/2}$ (Δ=3.67 eV). No O 1s and S 2p signals are detected on the surface, while a faint peak is observed in the C 1s spectrum at 284.4 eV attributed to residual crystalline graphitic carbon, C=C bond[188, 189], a contaminant present with a thickness $<$ 0.15 ML (more accurately between 0.13 - 0.03 ML). The carbon contaminant thickness is calculated employing the very popular method for measuring the thickness of films by XPS developed by Hill et al.[190], using the area of the Au 4f and C 1s peaks in conjunction with atomic sensitivity factor of them, being 6.250 and 0.296, respectively; and an attenuation length $\approx$ 28Å[191].

The LEED image at 125 eV exhibits the characteristic hexagonal diffraction pattern corresponding to the (111) fcc terraces. The $(\sqrt{3} \times 22)$-Au(111) surface reconstruction is evidenced by the additional hexagonal points (see inset Figure 5.2b) surrounding the principal ones, assessing the proper cleaning and the thermal reconstruction of the surface. Afterwards, the clean Au(111) surface was electrochemically characterized at various potential regions in a diluted H_2SO_4 solution.

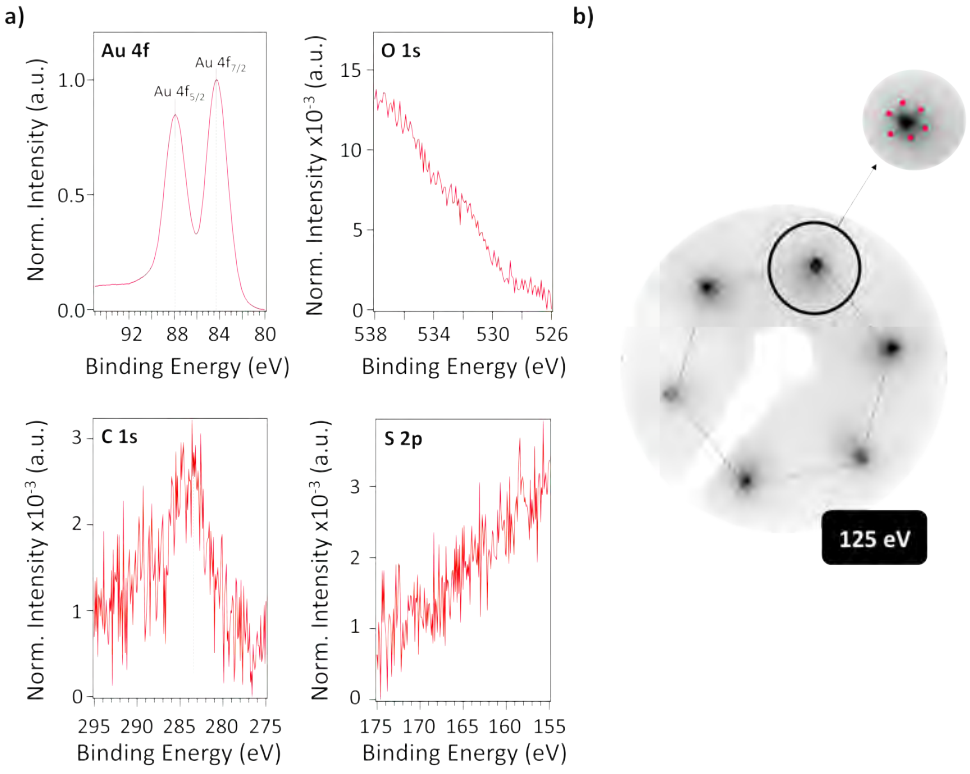

Figure 5.2: XPS (a) and LEED (b) characterization for a model clean Au(111) surface.

5.3.1 Electrochemical window

Figure 5.3 shows the CV acquired in the double-layer potential region of Au(111) in an Ar-purged 0.05 M H_2SO_4 solution within the potential window spanning from the OCP, -0.15 V, to 1 V vs Ag/AgCl/KCl (3 M). The scan rate for this experiment is set at 50 mVs^{-1}. Immersing the single-crystal electrode under OCP allows to assess the stability of the electrode surface, thereby mitigating the risk of unexpected (electro)chemical reactions and induced reconstructions that may occur under the influence of an applied potential.

This CV serves as "fingerprint" of a clean Au(111) surface, just like the $(\sqrt{3} \times 22) - Au(111)$ surface reconstruction in LEED for surface science investigations. In the present case, the CV exhibits sensitivity to contamination, evident in a minor peak at 0.22 V attributed to the adsorption of Cl^- onto the gold surface, expected at 0.15 V[152] and before sulphate adsorption in peak A[153], coming from the liquid-junction reference electrode. Despite the presence of Cl^-, it does not disturb the overall CV shape considering that this effect will not influence our investigations. The inertness of Cl^- adsorption in regard to the analysis we made was corroborated by the use of the commercial $Ag/AgCl/KCl_{(sat)}$ leak-less reference electrode.

Following electrochemical assessment via CV, we evaluated potential-induced surface structural changes at various potential values (denoted by blue points in Fig. 5.3) within the designated range. Each data point was obtained using a freshly prepared Au(111) surface.

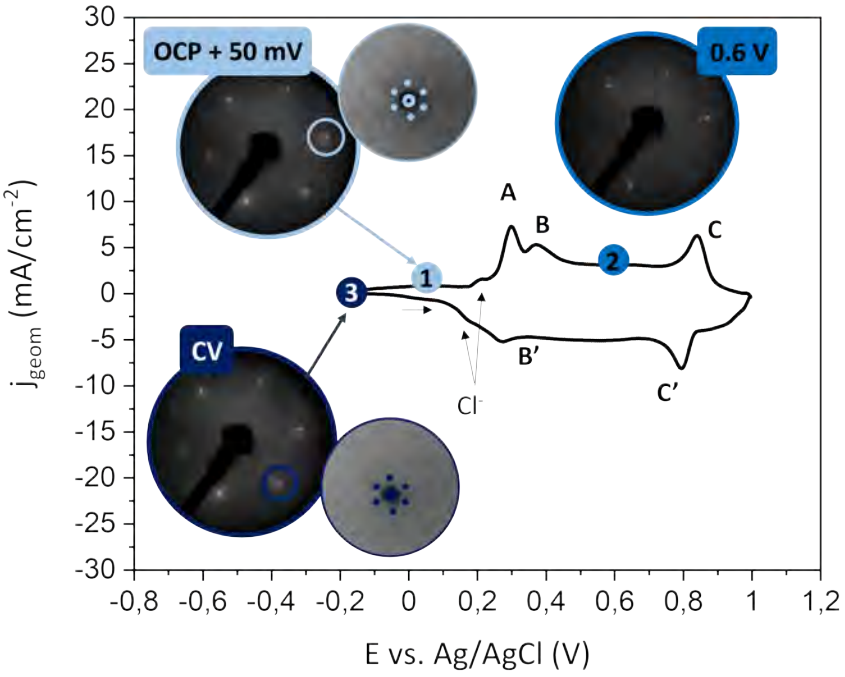

Figure 5.3: Cyclic voltammogram of Au(111) in the double-layer potential region recorded in deaerated 0.05 M H_2SO_4 at a scan rate of 50 mV/s. The discernible peaks observed between 0.2 – 0.4 V signify the lifting/recovery of the surface reconstruction, while the transition between 0.7 – 0.9 V denotes a disorder-to-order transition within the layer of adsorbed (hydrogen)sulfate ions. Supplementary insights are provided by LEED images taken at 125 eV, presented in the inset for samples emersed at 1) OCP + 50mV, 2) 0.6 V, and 3) after completing a full CV scan.

Observations revealed that after emersion at OCP plus 50 mV (sample 1), the surface reconstruction of $(\sqrt{3} \times 22)$-Au(111) persists, as shown in the LEED pattern in Figure 5.3, confirming the surface stability at OCP. The LEED image captured at a potential ascribed to the lifting of the reconstruction and the sulfur-based ordered layer formation processes (between peaks B and C, sample 2) corroborates the transition of $(\sqrt{3} \times 22)$-Au(111) reconstruction to a (1×1)-Au(111), indicating the possibility of a new sulfur-based surface layer as previously reported. During the cathodic scan, previous studies claimed the recovery of the reconstruction at potentials below 0.2 V after B' and A'. It has been established that surface reconstruction initiates as electron density increases. In this context, the LEED pattern obtained after a complete CV (sample 3) depicted in Figure 5.3 reveals a diffusive $(\sqrt{3}\times22)$-Au(111) reconstruction, consistent with the previous state. This potential-induced reconstruction differs from the initial thermally induced one and is referred to as electrochemically induced reconstruction, which remains incomplete due to its sluggish nature at room temperature.[154]

Up to this point, the surface structural changes induced by potential, previously reported, have been confirmed through our pre- and post-electrochemical characterization using a quasi-*in situ* methodology. The next inquiry is whether potential-

induced chemical changes occur on the Au(111) surface within the double-layer potential range, as previously suggested, and if these changes remain stable upon emersion of the electrode from the electrolyte with the subsequent loss of potential. To investigate this, XPS analysis was performed on the mentioned samples. The results are shown in Fig. 5.4. All spectra have been normalized to Au 4f and are presented without subtracting a Shirley background.

The Au 4f core level of the sample emersed at OCP plus 50 mV and the sample emersed after a complete CV maintains its metallic character, showing the same primary peak position (Au $4f_{7/2}$ = 84.1 eV) and spin-orbit splitting (Δ=3.67 eV) as the clean Au(111) surface. These findings, along with previous LEED observations, suggest the chemical and surface stability of the samples as well as the chemical recovery of the surface when the CV is completed without undergoing chemical changes. Cycling surface electrode samples within their electrochemical window is widely used in literature as a preconditioning method for single-crystal-based electrodes in AP-EC, following flame annealing and prior to conducting electrochemical tests.

This process ensures the chemical reversibility of any oxidative processes or the reduction of any oxide layers present on the surface. However, our results show that the thermally induced reconstruction obtained in UHV is not fully recovered, resulting in surface roughness and the formation of pits.

For the sample taken out at 0.6 V (curve highlighted in light violet), a faint shoulder appears, as indicated by an orange box. To gain a deeper understanding of these observations, Fig. 5.4b-c present the O 1s, S 2p, and C 1s core levels acquired for all the samples.

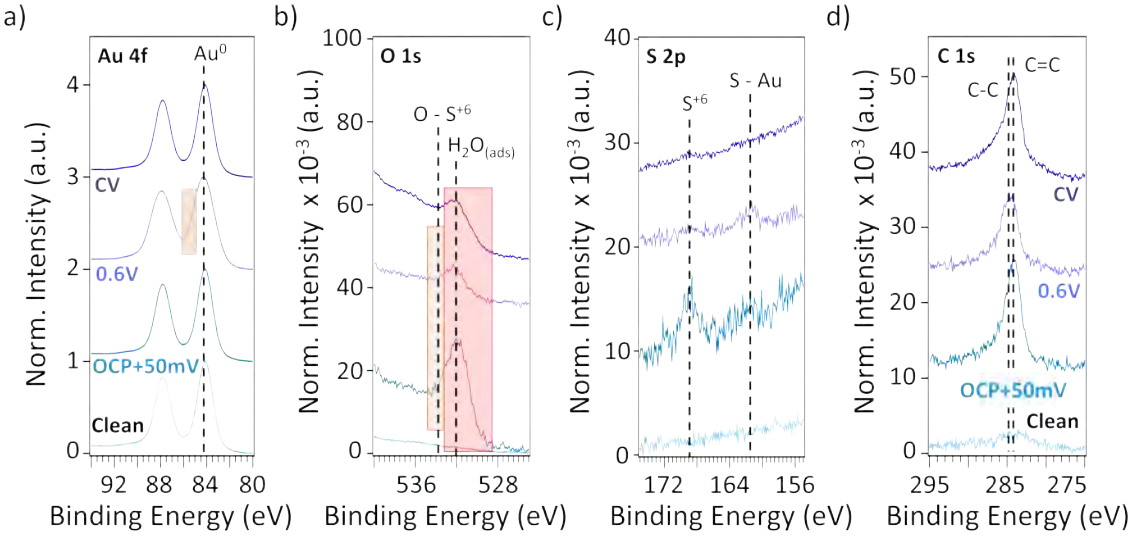

Figure 5.4: XPS spectra at Au 4f (a), O 1s (b), S 2p (c) and C 1s (d) core levels of Au(111) surface under different CV potential stopping: clean (light blue), OCP + 50 mV (dark blue), 0.6 V (light violet) and complete CV (dark violet).

In the O 1s spectra (Fig. 5.4b) of all points, two distinct components are discernible, highlighted by orange and red squares. The red component, located at

531.7 eV, is common to all three studied cases and is also observed when the sample is transferred to the EC cell, immersed, and emersed in the electrolyte solution without applied potential (as will be discussed later). This component is attributed to adsorbed water, retained as part of the hydration sphere of the emersed layer. The orange component at 532.7 eV is only observable in the anodically scanned samples (OCP + 50 mV and 0.6 V). This is accompanied by the appearance of an S 2p peak at 168.8 eV, attributed to S^{+6}[192, 193], along with a secondary peak at 161.5 eV, indicative of metal sulfide bond formation[194]. Consequently, the orange component of O 1s is assigned to oxygen bound to sulfur, forming either SO_4^{-2} or HSO_4^-, which interacts with gold via an S - Au chemical bond. While both anions, SO_4^{-2} and HSO_4^-, cannot be distinguished by XPS, given the dissociation of sulfuric acid in water, 90 % is likely HSO_4^- (with $pKa_1 = -3$, $pKa_2 = 1.92$) making it the most probable specie. Henceforth, we will consider this species, which as you will see later, is the predominant one present demonstrated by DFT calculations (see section 5.4.3). This finding confirms the adsorption of HSO_4^- anions, stabilized by H_2O molecules, previously reported in the same potential range between A and C electrochemical peaks.[180–183] Moreover, this state corroborates that sulfate/bisulfate anion present in the Au(111)/H_2SO_4 interface is retained during transfer to the UHV and remains stable under those conditions[43, 146, 147], thereby indicating our EC-UHV system's capability to unveil the dynamics of Au(111) surface reactions upon potential. It should be noted that the S^{+6} component becomes almost negligible after a complete CV (dark violet curve). This change is further confirmed in the S 2p core level, corroborating the recovery of the surface and the reversibility of anion adsorption.

Examining the C 1s spectra reveals that, after polarization, the C 1s content rises by an average of approximately 8 % compared to the clean sample, while maintaining BE positions indicative of graphitic carbon, either in sp^2 (284.0 eV) or sp^3 (284.4 eV) configurations. We speculate that the increase in carbon content may result from residual graphitic carbon after UHV cleaning and sample polarization, potentially causing reorganization in the bulk crystal and leading to carbon emerging on the surface. Alternatively, it could stem from the EC-UHV transfer process or even the electrochemical cell itself. This phenomenon has been previously observed in the literature and attributed to similar causes [48, 195]. Nevertheless, it should be noted that the presence of carbon on the surface in our case does not affect the electrochemical response or the electro-oxidation mechanism, neither does it hinder the surface compound analysis.

The results obtained so far on the Au(111) surface indicate that the newly implemented experimental approach involving a quasi-*in situ* synergistic EC-UHV methodology can unveil the chemical and structural changes in the electrified interface. To further confirm this, we performed an additional experiment to ensure that the observed chemical changes in the double-layer region were caused by the applied potential and not by the presence of bulk electrolyte (which would suggest an incorrect electrolyte concentration), possible crystallization of the electrolyte, or inadequate rinsing. To do so, we compared the XPS spectra obtained for samples emersed after applying potential with those obtained by performing the EC transfer

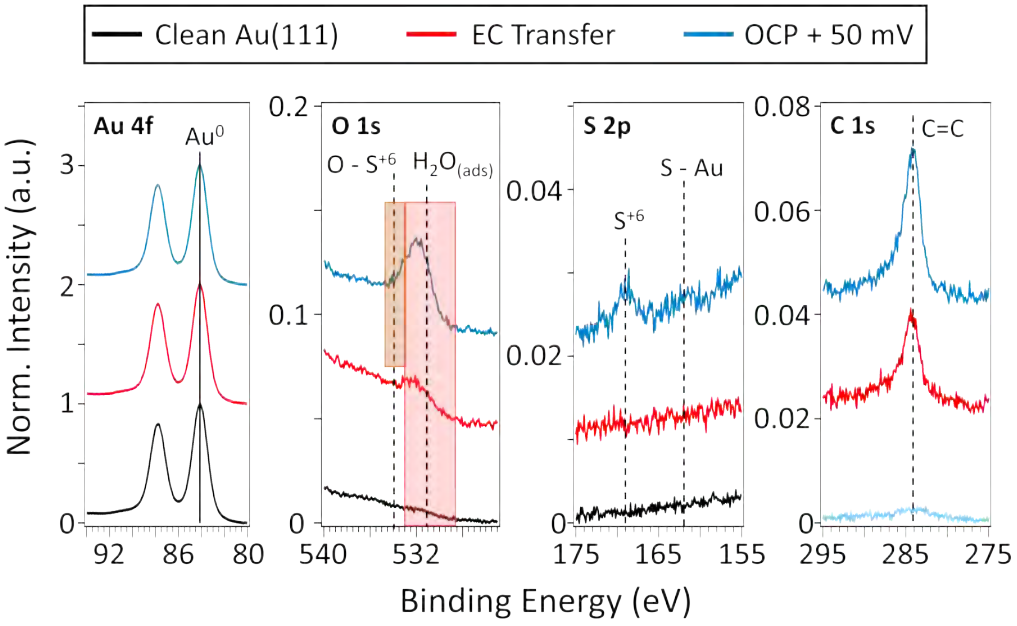

Figure 5.5: XPS spectra at Au 4f, O 1s, S 2p and C 1s core levels of a clean Au(111) surface (black) and immersed/emersed samples without applying a potential (red) and at OCP + 50 mV (blue).

with immersion and emersion of the electrode without potential in both processes. Figure 5.5 illustrates this comparison, showing the Au 4f, O 1s, and S 2p core levels for a sample immersed and emersed without potential (red) alongside a sample emersed at OCP plus 50 mV (blue), previously discussed, and a freshly prepared Au(111) surface.

Notably, both the sample without potential and the sample emersed under potential at OCP plus 50 mV demonstrate the chemical preservation of Au surface in its metallic state. However, distinctions emerge in the O 1s and S 2p spectra. The EC transferred sample without potential shows a unique contribution in the O 1s spectrum from H_2O adsorbed on the surface, along with the absence of sulfur. In contrast, Sample 1 exhibits different behavior, with stabilization and preservation of anion adsorption during the emersion process. This is evident from the presence of two components in the O 1s spectrum, previously attributed to the HSO_4^- component and adsorbed $H_2O_{(ads)}$, and a significant peak in the S 2p core levels at the binding energy of S^{+6} assigned to the S - Au bond.

These findings confirm the capability of the implemented emersed or quasi-*in situ* approach to study the electrochemical interface. The potential-induced chemical and structural changes observed under the studied conditions align with Helmholtz's theory of the double-layer, where ions adsorb onto the surface (sulfate/bisulfate in this case) in the double-layer region, facilitating charge transfer through electrostatic adsorption (electrochemical features A and B observed) without chemically altering the Au substrate. Furthermore, the electrode-withdrawal process with potential control preserves key chemical and structural characteristics of the expected interfacial layer after emersion process and potential removal, retaining the contact between the sur-

face and the unbroken double-layer. This confirms that the thickness of the emersed layer is sufficiently thick to incorporate the intact electrochemical double-layer but thin enough to exclude residual bulk electrolyte or ensure proper cleaning by rinsing.

In summary, the surface chemical and structural characterization conducted here supports a key objective of this thesis: demonstrating the capability of the EC-UHV system and the quasi-*in situ* or emersed approach to maintain the electrified interface necessary to study the dynamics of surface catalysts under applied potential. We demonstrate no significant chemical changes on the Au(111) surface in the double-layer region. Only minor physical species (HSO_4^-/SO_4^{-2}, most probably HSO_4^-) adsorption changes are evident at 0.6 V (between Peaks A/B and C), along with the lifting of the $(\sqrt{3}\times 22)-Au(111)$ reconstruction to $(1\times 1)-Au(111)$. The observance of the Au(111)/H_2SO_4 electrochemical characteristics, in addition to the LEED analysis and subsequent XPS, serves as a fingerprint for validating the cleanness and crystallinity of the electrode's Au(111) surface and ensures the reproducibility and compatibility of the results obtained from EC-UHV analysis.

5.3.2 Electrochemical oxide formation

Anticipated chemical changes induced by the applied potential are expected to occur at higher anodic potential between sulphur-based components adsorption and OER starting. After corroborating the suitability of the established approach to unveil electrode surface dynamics and with the purpose of identifying potential-dependent species that may emerge, the surface is examined using the same approach as in the previous section but over an extended potential range from the OCP (-0.15 V) to 1.5 V at a scan rate of 50 mVs^{-1}.

Figure 5.6 depicts the characteristic CV measured for the Au(111) surface. This profile includes a pre-peak (D), generally attributed to OH^- adsorption, followed by a pseudo-reversible redox feature at 1.31 V (peak ε) previously associated with the RTO (reversible transition oxide) process, where O/OH pre-adsorbed films lead to the formation of a quasi two-dimensional compact oxide layer in conjunction with sulfate/bisulfate desorption. The reduction around 0.85 V (peak E') and the ε/E' transition are associated with surface oxidation/reduction processes [157, 159, 167, 168, 181].

The electrochemical parameters of this oxidation/reduction processes in the Au(111) electrochemical window are evaluated to acquire insights on the possible mechanism and the kinetics of redox processes.

The anodic peak ε exhibits a $\Delta E_{\frac{p}{2}}$ of approximately 117 mV, indicative of a two-electron transfer process. Considering the widely accepted mechanism for electrochemical oxide formation, detailed in section 5.1, along with the thermodynamic behavior of gold-based species in its Pourbaix diagram (presented in Fig. 2.8) and the interaction of anions with the surface in the electrochemical interface, different two-electron transfer-based reactions could be involved in this process:

$$Au - OH_{(ads)} \leftrightharpoons Au(OH)_3 + 2H^+ + 2e^- \tag{5.9}$$

$$Au(OH)_3 \leftrightharpoons Au_2O_3 + 2H^+ + 2e^- \tag{5.10}$$

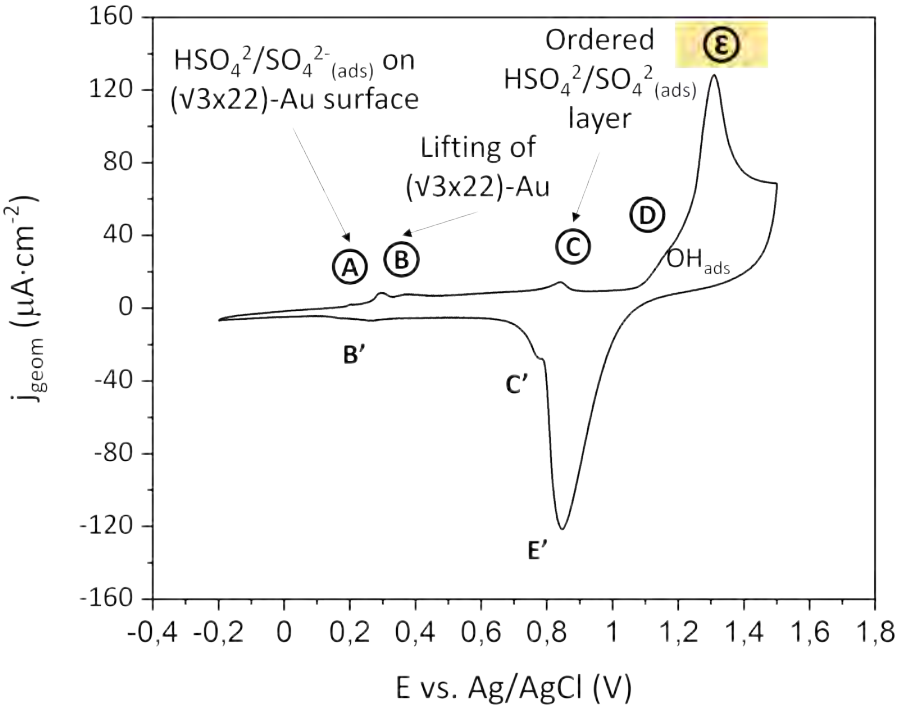

Figure 5.6: In the context of degassed 0.05 M H_2SO_4, a cyclic voltammogram of Au(111) is depicted, capturing the oxidation/reduction dynamics of the surface at a scan rate of 50 mVs^{-1}. The data presented correspond to the fifth cycle.

$$2SO_4^{-2} \leftrightharpoons S_2O_8^{-2} + 2e^- \tag{5.11}$$

$$2HSO_4^- \leftrightharpoons S_2O_8^{-2} + 2H^+ + 2e^- \tag{5.12}$$

The area integrated under a CV peak, obtained following the depiction of Fig. 2.12, can be related to the amount of the electrochemical product released, as mentioned in section 2.5.1. So, the thickness of the potential adsorbed layer generated during the electron transfer at peak ε can be calculated. The charge under peak ε, calculated from the integrated area, is approximately 227.95 $\mu C \cdot cm^{-2}$. This charge could correspond to about 1.02 ML of states with a -1 charge (such as OH^- or HSO_4^-) or approximately 0.51 ML for species with a -2 charge (such as O_2^{-2} or SO_4^{-2}). These calculations consider exposed structures as potential candidates, utilizing Faraday's Law (Eq. 2.4) and assuming a planar density of $1.39 \cdot 10^{15}$ atoms/cm^2.

The distance value between E_{pa} and E_{pc}, electrochemical characteristics defined in Fig. 2.12, exceeds the anticipated value for a fast, reversible electron transfer (100 mV). A common characteristic in the formation/reduction behavior of metal oxides, especially for noble metals, is the hysteresis — a difference in the potential range for oxide formation compared to reduction. This hysteresis is ascribed to post-electrochemical processes. In this case, the product potentially formed undergoes a change after the electron transfer at peak ε, leading to differences in the species, energies, and potential ranges involved in the subsequent reduction. [156, 159] Indeed, the charge under peak E' is roughly 253.50 $\mu C \cdot cm^{-2}$, exceeding anodic Q_ε, confirming the evolution of species in the hysteresis. Under the same assump-

tions, the thickness of any suggested specie would increase by approximately 10 % of a ML. Nevertheless, the formed layer can be fully reduced, as indicated by the electrochemical transient B', attributed to the recovery of the $(1 \times 1) - Au(111)$ reconstruction previously demonstrated.

To unveil the potential-induced chemical species and its structure after the EC experiment, the sample was emersed from the EC cell at the end of the anodic branch (1.5 V), both with and without holding the applied potential for 5 minutes, and after completing a CV cycle. Subsequent post-EC XPS (Fig. 5.7a) and LEED (Fig. 5.7b) analysis were carried out to reveal the chemical and structural changes on the Au(111) surface.

Figure 5.7a collects the photoemission spectra acquired at the Au 4f, O 1s and S 2p core levels. As in the previous section, the intensity of all the spectra has been normalized to Au 4f. XPS spectres exhibit no significant changes upon potential scan, except for a residual O 1s peak at 531.7 eV, previously attributed to water retained as part of the hydration sphere of counter ions on emersed layer at potentials contained in double-layer range. In this case, since no anions are detected in the S 2p and literature suggests the presence of OH, this feature position could be attributed to either adsorbed H_2O or OH^- species.[196]

Following the possible phases suggested in Eq. 5.9-5.12, based on thermodynamic assignment and CV measurements, different sulfur-based and oxide-based phases were proposed. However, no prominent O 1s and S 2p phases were detected. The absence of sulfur-based species suggests that sulfur does not participate in the chemical composition of the emersed layer at 1.5 V, which contrasts with previous findings on the double layer. While literature suggests that sulfur desorbs with the appearance of the oxide [157, 158], we know that at higher potentials and polarization times (discussed in the next section, Section 5.4), S 2p features will be detected. The absence of sulfur in this case could be due to two factors: (i) slow reaction kinetics necessitating high overpotentials for detection, or (ii) the formation of a sulfur-based precursor from the one that is detected later, which could be metastable and only detectable under potential (because, for instance, it is evacuated or decomposed during the UHV transfer).

In any case, what our XPS analysis ruled out is the formation of any kind of gold oxides ($Au_2(OH)_3$ neither Au_2O_3) which were previously suggested as an explanation for the peak ε[117, 157–159]. In fact, we know in advance that when the surface is oxidized forming the so-called "bulk oxide", the resulting oxide phase remains stable during the emersion process to UHV and represents an irreversible (electro)chemical step, as will be discussed later. This oxide can be measured for overnight without showing any differences, proving its stability and irreversibility.

To examine possible structure differences, LEED patterns were compared at 125 eV (Fig 5.7b). This comparison aimed to confirm the reversibility after CV recovering the reconstruction. As illustrated in Figure 5.7b, both cases exhibit the same hexagonal pattern, with a very attenuated $(\sqrt{3} \times 22)$-Au(111) reconstruction visible after CV in the zoomed area. As in the double-layer potential region, the elctrochemical processes are reversible but the thermally induced reconstruction it neither fully recovered. In fact, cycling the sample in this extended potential range results in a defective surface [181].

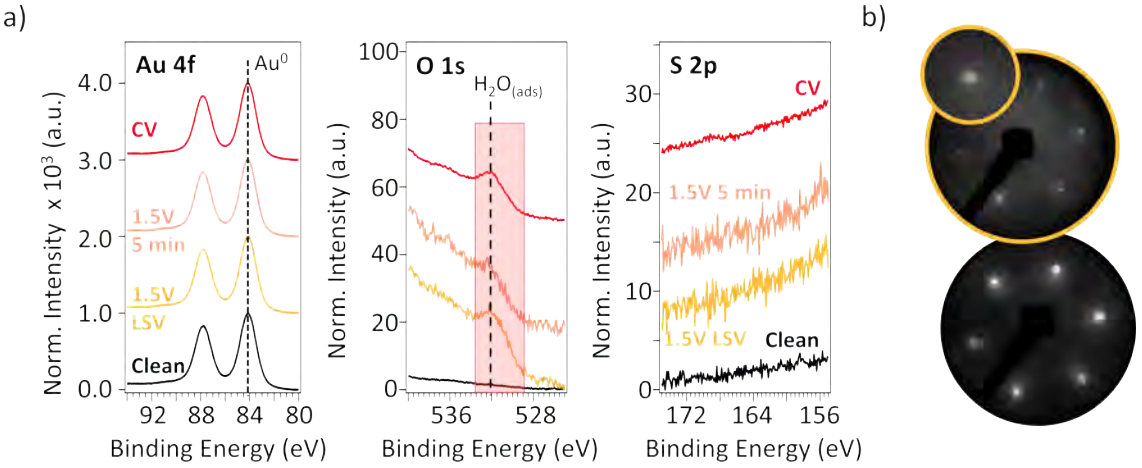

Figure 5.7: a) XPS spectra at Au 4f, O 1s and S 2p core levels of Au(111) surface under different CV potential stopping: clean (light yellow), 1.5 V (dark yellow) and complete CV (orange). b) LEED images taken at 125 eV for (bottom part) clean Au(111) surface and (upper part) same surface after a complete CV cycle with an inset in one spot.

5.3.3 Electrochemical study within OER regimen

The onset of a continuous anodic current starts at 1.5 V, precluding the OER region. Extending the upper potential limit increases the overpotential from ϵ CV feature and prolongs the time spent at oxidizing potentials. This could chemically evolve the Au(111) surface towards forming an oxide-based structure due to the possible adsorption of OH- and O-based species at E > 1.5 V, as supported by literature. For example, when performing a CV at a scan rate of 50 mV/s, increasing the upper potential limit from 1.5 V to 1.6 V results in an additional 4 seconds spent at potentials above 1.5 V. This change can overcome kinetic barriers or increase the thickness of the deposited layer until it can be quantified by XPS. Therefore, we chose to analyze the Au(111) surface using CV within an extended potential range.

To elucidate potential electrochemical hydro(oxide) species beyond 1.5 V, we incrementally raised the upper potential limit (Φ) from 1.5 to 2.1 V, the onset of OER, and examined the corresponding CV characteristics. Figure 5.8 illustrates consecutive I-E curves obtained in the same surface at each applied Φ where at each potential step the anodic ramp is preceded by a cathodic reduction.

The observed peaks in Fig.5.8a are the characteristic ones belonging to Au(111) surface. Minor variations in the anodic peak height ϵ are evident, as highlighted in the zoomed graph in Fig.5.8b-Peak 1. The ϵ peak current increases by approximately 0.5 % to 8 % with the upper potential limit. These changes are likely due to increased roughness during successive oxidation/reduction cycles, which enhance pit density and thereby increase the electrochemically active area. This underscores the chemical reproducibility of the Au(111) surface across each cycle where the upper potential limit varies, despite structural differences arising from each anodic run following a cathodic reduction.

In contrast to the anodic findings, the reduction peak in the cathodic branch

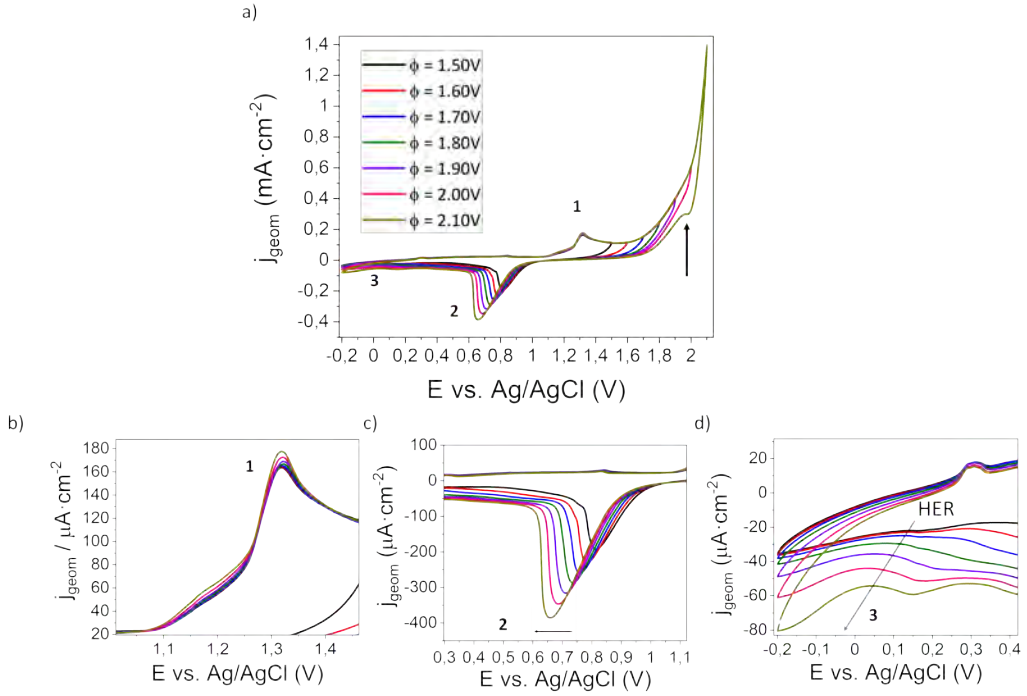

Figure 5.8: Subsequent cyclic voltammograms for Au(111) surface in 0.05 M H_2SO_4, at 50 mV/s from OCP, -0.15V to different upper potential limits (Φ). Distinguishable stages in oxide formation and reduction are identified by lettering. Three different insets in regions 1, 2 and 3 are depicted.

is displaced towards a lower E_{pc} as Φ increases (Fig.5.8c-Peak 2), manifesting an increased difficulty in reducing the formed layer. This trend suggests the emergence of a new phase with a composition influenced by the applied overpotential or the duration spent at E > 1.5 V. Differences in cathodic peak shapes are also detected as potential increases, indicating the presence of different components on the surface. Additionally, the HER activity is enhanced with the upper potential limit, as indicated by an arrow in Fig.5.8c-Peak 3. HER is highly sensitive to surface structure, and its activity is enhanced in potential-induced Au(111) reconstructions compared to thermally induced ones. Despite having identical unit cells for each surface, the presence of smaller domains and domain boundaries in potential-induced reconstructions increases HER activity [197].

Furthermore, a small perturbation is detected in the cathodic phase of the sample cycled up to 2.1 V, as indicated by an arrow in Fig. 5.8a. This process is reproducible in a different sample scanned at a lower scan rate (10 mV/s, data not shown) and could be attributed to the formation of O_2 bubbles, clearly seen in the crystal surface.

Hence, the increased potentials from 1.5 to 2.1 V suggest a complex dynamic process likely involving oxygen-based phases until oxygen evolution occurs. Despite this, the surface undergoes "recovery" in electrochemical terms during the reversed scan upon reaching the OCP, making the anodic branch reproducible for consecutive cycles.

Quantitative descriptions of the thickness of adsorbed precursor phases or subsequent chemical transformations can be derived from the comparison of the integrated

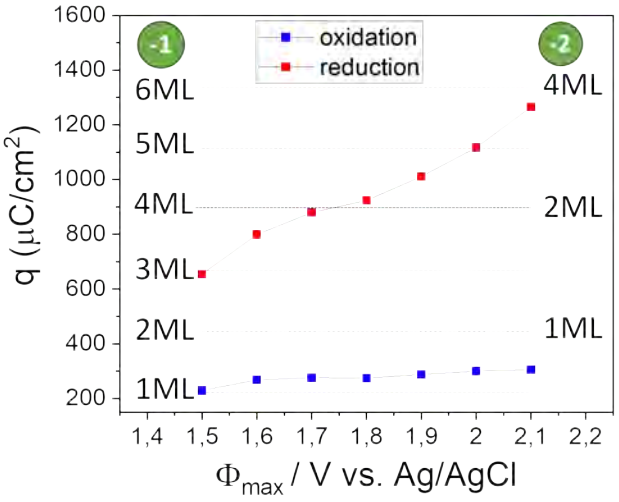

Figure 5.9: Integrated charge flows from anodic and cathodic peak on voltammograms, fig. 5.8, of oxidation and reduction processed of oxygenated species as a function of upper scan potential. Broken lines indicate charge densities for different numbers of ML of OH^- adsorbate (left), O adsorbate (righ).

anodic and cathodic areas in Fig. 5.8. As previously outlined, on a Au(111) surface with a planar density of $1.39 \cdot 10^{15} atoms/cm^2$ and following Faraday's law, Eq. 2.4; the equivalent charge density for 1 ML of adsorbate can be calculated. It is approximately 222 $\mu A/cm^2$ or 444 $\mu A/cm^2$ for a monovalent adsorbate like OH^-/HSO_4^- or a divalent one such as O_2^{-2}/SO_4^{-2}, respectively. Following this principle, the obtained charge density is plotted versus the maximum upper potential, and the resulting plot in Fig. 5.9 quantitatively describes the degree of surface oxidation under the theoretical assumption. Figure 5.9 shows that the charge obtained in the anodic peak ε remains almost constant, as expected, demonstrating a consistent thickness of same adsorbed precursor phase. This thickness is estimated to be between 1.05 - 1.3 ML of monovalent species or 0.5 - 0.7 ML of divalent species.

The reduction layer thickness is in all cases bigger than the pre-adsorbed one, confirming the influence of overpotential and the time scale dependence of oxidation. If we consider a monovalent phase as the initial adsorbed specie, (left side on Fig. 5.9) at 1.5 V, the adlayer thickness increases from 1 ML to 3 ML along the reverse scan, attributed to the hysteresis between oxidation and reduction peaks where deposited species evolve. As the time spent to reach the cathodic peak is 2.5 times longer than the time spent to reach the plateau in the anodic peak, the reduced oxygen-rich phase thickness is expected to be 2.5 times larger.

Moreover, between 1.5 and 2.1 V, the cathodic area exponentially increases with the upper potential limit until the onset of OER, with a subtle inflection point observed at 1.8 V, indicating the transformation of the formed phase with the overpotential. Even in this region, studying its mechanism remains challenging due to the absence of distinct electrochemical transfer-based peaks. To address this, Tafel slope analysis becomes an indispensable tool, providing insights into the underlying reaction steps and possible intermediates. Therefore, we will evaluate the Tafel slope after CV measurements and compute the thickness of the electrochemical films

formed. By correlating the Tafel slope values with the film thickness, we aim to elucidate the reaction mechanism and identify key parameters influencing the OER on Au(111) through solely macroscopic characterization.

Figure 5.10 presents the Tafel slop representation resulted from the anodic branch obteined in the CV from OCP to 2.1 V (presented in Fig. 5.8). Note that the overpotential is calculated from the difference with the thermodinamic +1.23 V value for the OER.

The investigation of the rate-determining step (RDS) has been conducted at low overpotentials (blue region in Fig. 5.10), where electro-oxidation is expected, and at high overpotentials where the oxygen evolution reaction (OER) commences (red region in Fig. 5.10). The two analyzed regions exhibit different slopes of approximately 60 mV/dec and 30 mV/dec under varying conditions, suggesting distinct electrochemical mechanisms governing each potential range.

At low overpotentials, the slope of 52.9 mV/dec indicates a reaction mechanism where the rate-determining step involves an electrochemical process, confirming our previous attributions. This steep slope suggests a slower reaction rate per tenfold change in current density, likely due to processes such as charge transfer across an interface or surface restructuring involving significant energy barriers. For instance, a steep slope like 60 mV/dec could correspond to a mechanism involving a complex surface reaction or the electrochemical desorption of species.

At overpotentials where OER is expected to start, the slope of approximately 30 mV/dec suggests a mechanism where the rate-determining step involves multiple steps or intermediate species with lower activation energies. This shallower slope implies a more rapid increase in current density per decade, indicating a faster electrochemical reaction compared to the scenario with the steeper slope. As previously discussed, values around 30 mV/dec are associated with the transformation of M-OH to M-O species.

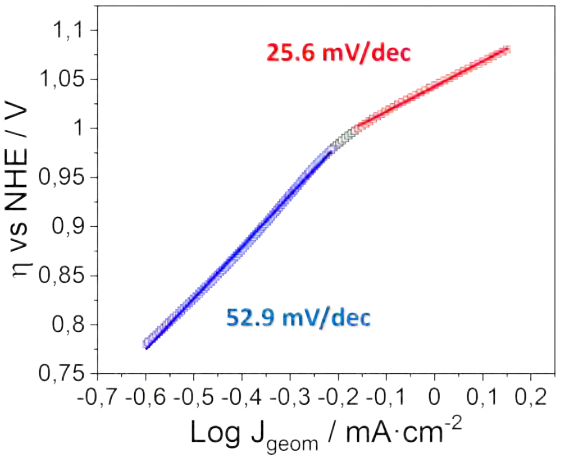

Figure 5.10: Tafel plot for Au(111) in 0.05 M H_2SO_4, illustrating the relationship between overpotential and current density precluding the OER. The data provides insights into the kinetics of electro-oxidation process at low overpotentials (blue) and in the OER onset (red).

While thickness information can be extracted from j-E curves and kinetic mechanisms can be predicted using Tafel slopes, only speculative predictions regarding changes in chemical composition can be made from observed electrochemical features. This underscores the importance of complementing electrochemical studies with surface-sensitive techniques to explore anode electro-oxidation mechanisms and the species involved, particularly in relation to OER.

5.4 Chemical and structural composition of emerged species near OER

In an effort to elucidate the chemical changes on the Au(111) surface and to investigate the oxygen-rich species expected, polarizations at higher potentials (E_{ap} > 1.5 V) were conducted. This study is pursued since samples polarized within the Au electrochemical window did not reveal substantial chemical changes in XPS (results presented in section 5.3). Therefore, we opted for the chronoamperometry (CA) technique at various potentials (between 1.5 to 2.1 V, where OER commences) and different time scales (30 seconds and 5 minutes).

As a first approach, we followed the experimental EC-UHV methodology described in section 4.3. In the present case we conducted each electrochemical polarization on a UHV-cleaned Au(111) surface after cycling the surface between OCP (-0.15V) to 1.5 V to ensure the consistency on the starting surface for each case through the analysis of the electrochemical features.

5.4.1 Short time range: 30s polarization

XPS studies conducted on samples emersed after specific potential CAs at values delineated by colored circles in Figure 5.11a are illustrated in Figure 5.11b. The photoemission spectra acquired at the Au 4f, O 1s, S 2p and C1s core levels are summarized for comparison.

For samples polarized at potentials between 1.8 and 2.0 V, Au 4f maintains its metallic character without chemical changes, with Au $4f_{7/2}$ and Au $4f_{5/2}$ centered at 84.1 eV and 87.8 eV, respectively. At a relatively high potential, at 2.1 V above the OER onset, a significant contribution at 1.6 eV higher binding energy, around 85.7 eV, indicates the formation of an oxidized Au(111) surface. Its position suggests Au^{+3} oxidation state, consistent with previous reports on Au^{+3}-based gold oxide. [117, 118, 198]. The Au^{+3} state in gold oxide can be manifested with different stoichiometries: $Au(OH)_3$, AuOOH or Au_2O_3. For a comprehensive understanding of the electro-oxidation mechanism and the resulting compound; O 1s, S 2p and C 1s core levels will be analyzed.

In the O 1s spectra, at potentials below 2.1 V in the OER onset, the shape spectra are similar for the three explored potentials. They all consist of a peak centered at around 531.4 eV, with an intensity that increases as the potential rises. This peak consists of two main components: a predominant one at approximately 531.7 eV and a smaller contribution at 532.7 eV. These components match those observed in emersed samples at potentials within the double-layer region and the oxide formation

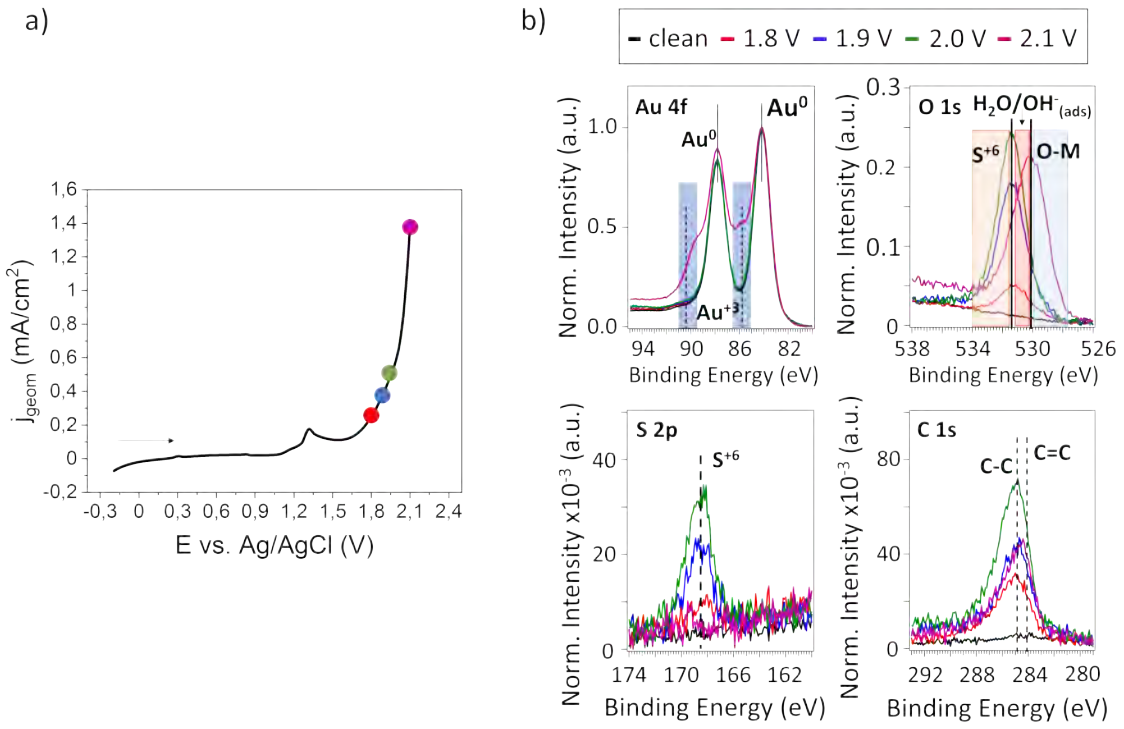

Figure 5.11: XPS spectra at Au 4f, O 1s, S 2p and C 1s core levels of Au(111) surface after polarizations at: (black) clean surface, (red) 1.8 V, (blue) 1.9 V, (green) 2.0 V and (violet) 2.1 V, for 30 s in a deaerated 0.05 M H_2SO_4 solution.

potential region (see Fig. 5.4 and 5.7), attributed to adsorbed H_2O/OH^- species and sulfate/bisulfate components, respectively, thereby precluding the emergence of oxide species.

In the S 2p spectra, at potentials between 1.8 and 2.0 V, sulfur exhibits the same chemical state observed before, with a peak centered at 168.4 eV, which is attributed to the S^{+6} state. The intensity of the S 2p peak significantly increases along with the oxygen content as the potential increases. This indicates that sulfur is bonded to oxygen in the S^{+6} state, forming either HSO_4^- or SO_4^{-2} species[192, 193, 199], the quantity of which depends on the applied potential. This observation represents a novel finding, as previous literature consensus suggested the desorption of anions during the electrochemical transition (ϵ) where oxide is thought to be formed. Specifically, this finding may be associated with the previously proposed two-electron transfer process (see Eq. 5.11 - 5.12), where sulfate or bisulfate anions (HSO_4^- or SO_4^{-2}) present at the electrochemical interface, as detected in the double-layer emersed phases, undergo electrochemical oxidation on the Au(111) surface to form peroxydisulfate or persulfate ($S_2O_8^{-2}$) at $E^0 = 2.01$ V vs NHE (1.72 V vs Ag/AgCl) or $E^0 = 2.123$ V vs NHE (1.83 V vs Ag/AgCl), respectively. It is true that the prominent anion is HSO_4^-, as stated before. However it is most likely the ET reaction $S_2O_8^{-2}/SO_4^{-2}$ since a lower overpotential is needed. Also, as we will see later in section 5.4.3, by DFT calculations it was demonstrated that HSO_4^- converts into SO_4^{-2} due to the interaction with H_2O at potentials between peak B (sulfate

adsorption) and peak ε; most probably in peak C.

As the potential and overpotential increase, a thicker $S_2O_8^{-2}$ based layer accumulates until reaching 2.1 V, where oxide formation likely occurs due to oxygen insertion into the surface lattice and subsequent desorption of sulfur-based species or inability to adsorb due to fully active sites occupied by oxide phases. It is noteworthy that $S_2O_8^{-2}$ functions as a relatively stable oxidizing agent whose production rate varies with applied potential[200], and its composition decomposes with temperature or photon energy $h\upsilon$ into SO_4^{-2*}[201]. These facts in conjunction with previous findings suggest a new electro-oxidation mechanism indicating that the ϵ transient stems from the transformation of sulfate into peroxydisulfate instead of hydroxyl adsorption and subsequent RTO, as generally agreed by literature up to now.

At 2.1 V, O 1s and S 2p core levels suddenly change. There is a shift in the O 1s peak. The characteristic oxide peak appears centered at 530.1 eV, composed of a large contribution around 531.7 eV and a new one (highlighted in blue) at 529.3 eV approximately. This chemical interaction happens in conjunction with the disappearance of S 2p and the growth of a shoulder in Au 4f core level, reflecting the vanishing of adsorbed anions leading to the formation of gold oxide. The latter either blocks or catalyzes the surface, influencing its oxidation. However, the exact composition of aroused structure can not be evaluated just by peaks positions or suggested components, it is crucial to resolve the real composition through XPS fitting.

The Au 4f, O 1s and C 1 s spectra were deconvoluted, and a Shirley background was subtracted. As seen in Fig. 5.12, the Au 4f core level of the as-grown oxide at 2.1 V exhibits a dual-component fitting, corresponding to Au^0 and Au^{+3} chemical states, as previously discussed. This dual-component observation is consistent across both Au 4f contributions, each displaying a spin-orbit splitting of 3.67 eV for the 4f core level. Furthermore, an oxidic component is also detected in the O 1s core level, which is fitted using three components: one at 531.3 eV, attributed to the physical adsorption of either OH^- or H_2O to the Au(111) surface; a second at 530.2 eV associated with chemisorbed OH^- not bonded to the gold surface; and a third at the lowest BE around 529.3 eV, linked to oxygen chemisorbed on the Au(111) surface forming the oxide.

A minor peak detected in the C 1s core level is fitted with a single component at 284.4 eV, commonly associated with the C=C bond [188]. This finding suggests that carbon does not participate in the oxide formation or the preceding adsorption steps, as previously exposed. This assertion is further supported by the absence of carbon features in the O 1s spectra. Additionally, C 1s peak position differs from the typical positions expected for components originating from C-O-C/C-OH, O-C=O, and C=O bonds (around 286.0 eV, 288.5 eV, and 288.0 - 290.0 eV, respectively) [202–205] confirming the absence of a significant carbon contribution to the oxide formation process.

The main fitting parameters for chemical composition analysis of each assigned contribution are summarized in Table 5.1. For a more precise chemical assignment to the emerged layer, the O:Au ratio was calculated for Au - O attributed components

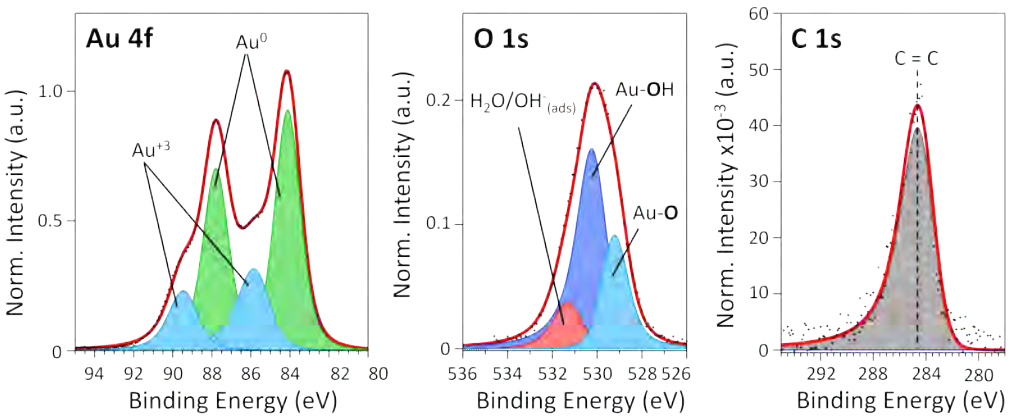

Figure 5.12: XPS spectra and fitting components at the energies of a) Au 4f core level, b) O 1s core level and c) C 1s core level, after 30s of polarization at 2.1V in deaerated 0.05 M H_2SO_4 solution

using Eq. 5.13:

$$Ratio(O:Au) = \frac{\frac{A}{SF}(O1s)}{\frac{A}{SF}(Au4f)} \tag{5.13}$$

In this equation, the peak areas are normalized to the sensitivity factor (SF), a coefficient dependent on the angle between the X-Ray gun and the detector, as well as the cross-section and inelastic mean free path (IMFP) of electrons for a specific element at a defined energy level. Hence, for the given angle between the X-ray gun and the detector, this sensitivity factor is unique for each element and transition. In this instance, the sensitivity factors are 0.711 for O 1s and 6.25 for Au 4f [206]. Utilizing Equation 5.13 in conjunction with the area values detailed in Table 5.1 for all Au-O related components within both Au 4f and O 1s spectra, the O:Au ratio can be calculated. The resulting O:Au ratio approximates 1.40, closely aligning with the expected value for a stoichiometry of Au_2O_3, with an error margin of 6.7 %. Anticipated ratios for other gold-based stoichiometries such as $Au(OH)_3$ and $AuOOH$ would be 3 and 2, respectively. Therefore, it is inferred that under the applied conditions, Au_2O_3 is formed. However, due to XPS resolution limitations (non monochromatic light), it is not possible to differentiate between the hydrous or anhydrous state, representing either Au_2O_3 or $Au_2O_3 \cdot 3H_2O$.

Based on previous attributions, it has been revealed for the first time that the so-called bulk oxide does not form through a RTO process. Instead, we have uncovered a precursor phase involving a peroxydisulfate adlayer at higher potentials, 1.8 < E < 2.0 V. Importantly, the oxide layer does not emerge until the potential reaches 2.1 V for 30 seconds, precluding OER, with a proposed stoichiometry of Au_2O_3, facilitated by the removal of the sulfur-based precursor, which likely catalyzes surface oxidation. The discrepancy between the observed mechanism and the generally agreed one (exposed in section 5.1) could arise from the S-Au bond formed by the interaction of electrolyte anions with the Au(111) surface, HSO_4^-, which may inhibit surface oxidation (by inhibiting OH adsorption and subsequent transformation into O) until a reorganization in the adlayer facilitates the formation of the true pre-oxidation

Table 5.1: Binding energy and total area of the analysis of the XPS spectra at Au 4f and O 1s core level, for Au(111) sample polarized during 30 s at 2.1V in deaerated 0.05 M H_2SO_4 solution.

Au 4f XPS spectra			O 1s XPS spectra		
Comp.	B.E. (eV)	Area (a.u.)	Comp.	B.E. (eV)	Area (a.u.)
$Au^0_{7/2}$	84.1	17,448	$OH^-/H_2O_{(ads)}$	531.3	999
$Au^0_{5/2}$	87.8	14,120	M - OH	530.2	2,760
$Au^{+3}_{7/2}$	85.8	8,340	M - O	529.3	2,115
$Au^{+3}_{5/2}$	89.4	5,238			

catalytic phase: the persulfate or peroxodysulfate, $S_2O_8^{-2}$.

Having demonstrated the formation of an oxidized surface, compatible with a stoichiometric Au_2O_3 phase, at high anodic potentials precluding the OER, it is crucial to investigate the influence of time scale on the electro-oxidation mechanism. Given that 30s long polarization leads to abrupt changes, extending the polarization time could offer insights into different mechanistic steps at lower potentials, excluding OER, and providing a comprehensive understanding of the electro-oxidation mechanism on the Au(111) surface.

5.4.2 Large time range: 300s polarization

Following the same work methodology as in the previous 30s polarizations, larger timely consumed chronoamperometry (5 minutes) at anodic potentials ranging from 1.5 to 2.1 V was conducted. The XPS spectra at the Au 4f, O 1s, S 2p and C 1s core levels were acquired after the electro-oxidation and presented in Fig. 5.13a-d. In this representation, XPS spectres have been deconvoluted and a Shirley background has been subtracted for quantitative analysis.

The Au 4f core level of the Au(111) surface polarized at 1.5 V can be fitted using two components corresponding to the two spin-orbit splitting components of the Au 4f core level for metallic gold (Au^0) centered at 84.1 eV and 87.8 eV for Au $4f_{7/2}$ and Au $4f_{5/2}$, respectively. A new component highlighted in orange appears for samples polarized at 1.6 and 1.7 V, situated around 84.7 eV. This component is attributed to sulfur-based species adsorbed on the surface. In contrast to 30s polarizations, anion adsorbed species can be detected at a lower potential, specifically at 1.6 V. At 1.8 V, the orange component disappears, and a higher-binding-energy contribution at 85.7 eV emerges, attributed to Au_2O_3 formation, similar to the observations at 2.1 V for 30s. Thus, in both time-scaled evaluated scenarios (30 seconds and 5 minutes), the release of adsorbed sulfur-based anions, $M-SO_x$ with S^{+6} oxidation state, from the surface precludes the formation of metal oxide. With a further increase in potential from 1.9 to 2.0 V, the metallic component decreases, while two components associated with oxides (the Au_2O_3 and a new one in lilac) grow. At 1.9 V, the new component appears in the Au 4f core level at 86.1 eV, 2 eV higher BE than the metallic component, associated also to Au^{+3} chemical state. Below, the stoichiometry of the oxidized surface will be analyzed. The new oxide-related

species becomes predominant when the potential is increased to 2.0 V, continuing until the decomposition of the as-deposited layers above 2.1 V, where O_2 bubbles are observed in the electrode surface. At this potential, the metallic component contribution is recovered with the emergence of the orange component.

At 1.6 V, a S 2p peak centered at 168.4 eV appears, assigned to the S^{+6} state, in conjunction with the appearance of the $M-SO_x$ component in the Au 4f core level. The S 2p peak presents an unresolved doublet with closely spaced spin-orbit components ($\Delta = 1.16eV$). Simultaneously, a prominent O 1s contribution is detected, consisting of two different components: a large one at around 531.7 eV, combined with a smaller component at 532.7 eV. As previously stated, the red component is attributed to physically retained H_2O/OH^- species on Au(111), while the orange one is attributed to O bonded with S^{+6} state, forming either HSO_4^- or SO_4^{-2} chemisorbed on the gold surface. Notice that in these emersed layers, the metallic sulfide component previously detected in S 2p core level (S-Au) is not observed, suggesting a rearrangement in the sulfur-based species present in the electrified layer from the double-layer potential range (see section 5.3.1) to the polarized samples at potentials precluding OER range.

In the present case, the sulfur-based phase is bonded to the Au surface through the O atom, which will later lead to the formation of oxide phases. As the potential increases to 1.7 V, the sulfur component in Au 4f decreases, along with O 1s and S 2p, indicating the desorption of the anion layer. This is attributed to the place-exchange mechanism between Au atoms on the surface and the oxygen present in the adsorbed sulfur-based anions. Above 1.8 V, the S 2p contribution disappears, confirming anion desorption. Based on the previous analysis of the electrochemical feature ε (in section 5.3.2) assigned to the reaction described in Eq. 5.11, and the emersed layers after short-time polarizations of 30 seconds, the insertion of the oxygen atom occurs through the species $S_2O_8^{-2}$, which desorbs from the surface afterwards.

Sulfur-based anion desorption aligns with a shift of around 2.0 eV across the entire O 1s region caused by the formation of new components at 1.8 V. In this case, the O 1s core level is fitted using same components previously ascribed to the sample polarized at 2.1 V for 30s, evolving same oxide phase and confirming the effect of polarization time on the evolution of surface species. The observation of same oxide at different potentials and time scales — 1.8 V for 5 minutes and 2.1 V for 30 seconds — can be understood by examining the kinetics and thermodynamics of the electrochemical reactions involved.

From a thermodynamic perspective, the formation of the oxide is determined by the E^0 or E, which indicates the voltage at which the oxide phase starts to form and forms at a considerable rate being stable. Both 1.8 V and 2.1 V are within the potential range where oxides formed by EC are thermodynamically expected and stable. However, the rate at which the oxide forms is governed by the kinetics of the reaction. Kinetics involves the speed of the electrochemical processes, which is influenced by factors such as the applied overpotential, reaction pathways, and activation energy barriers. At 1.8 V, the overpotential is lower, meaning that the driving force for the reaction is less, and thus the reaction proceeds more slowly, requiring a longer time (5 minutes) to achieve the formation of the oxide. Conversely,

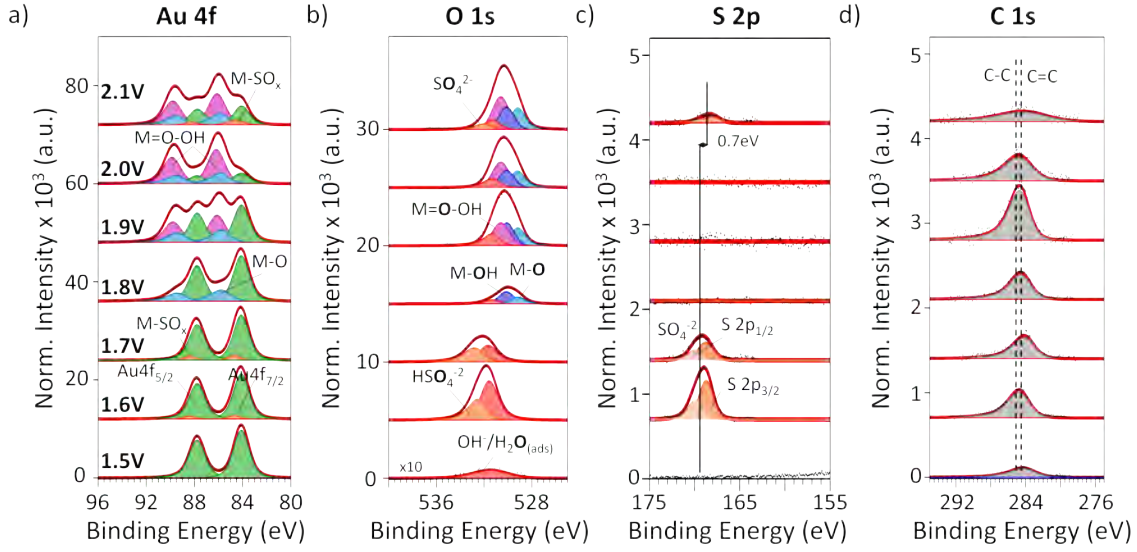

Figure 5.13: a) XPS spectra and fitting components at the energies of Au 4f, O 1s, S 2p and C 1s core levels after 5 minutes of polarization at different potentials ranged from 1.5 to 2.1V in deaerated 0.05 M H_2SO_4 solution.

at 2.1 V, the higher overpotential provides a greater driving force, lowering the activation energy barrier and accelerating the reaction rate, so the oxide forms more quickly (in 30 seconds). This difference highlights the interplay between kinetics and thermodynamics in electrochemical systems.

Upon further potential increase from 1.9 to 2.0 V, a new component appears in the O 1s peak at around 530.6 eV. As this new component appears in conjunction with the new one at 86.1 eV in Au 4f XPS spectra, it is assigned to the formation of gold hydroxide oxide (AuOOH), following the proposed oxide transformation mechanism at high anodic potentials preceding OER: M-O oxide is in contact with the media, which incorporates oxygen into the structure. To confirm this assumption, the proportion between O and Au was calculated for this new species using the SF values and Eq. 5.13. The O:Au ratio gives 2.3, which falls within the error range of approximately 15 % for AuOOH.

The AuOOH species becomes predominant when the potential is increased from 1.9 V to 2.0 V precluding the evolution of O_2 molecules which, indeed, oxygen is formed from the decomposition of AuOOH at 2.1 V. The decomposition of AuOOH surface layer is suggested with the reappearance of the component assigned to O-S bond in conjunction with an increase in the metallic Au one. At this potential, a prominent S 2p peak appears shifted by 0.7 eV with respect to the previously detected state. Both peak positions are attributed to S^{+6} state but with different chemical formulas. This difference indicates that the first species detected on the surface is the decomposition of persulfate giving $SO_4^{-2}*$, and just after the different oxide-based layers formation, new available Au sites are occupied by the chemisorption of the bisulfate anion, HSO_4^-. [207–209]

It is noteworthy to emphasize that the findings elucidating the mechanism of Au(111) electro-oxidation are consistent and reproducible across multiple experimen-

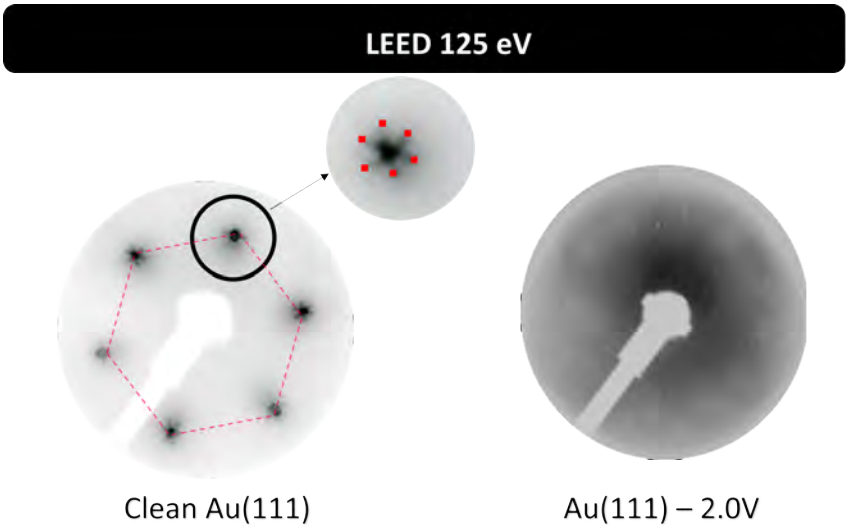

Figure 5.14: LEED images taken at 125 eV for (left) clean Au(111) surface and (right) surface obtained after 5 minutes polarization at 2.0 V.

tal iterations. While minor deviations in the identified components may manifest, the overarching trend delineated within this section remains steadfastly reproducible.

To study the structural differences in the polarized Au(111) surface, LEED experiments were carried out. Fig. 5.14 contains patterns of a clean Au (111) surface and an emersed sample after after applying 2.1 V for 5 minutes. After polarization no pattern is obtained, coinciding with the newly emerged oxide layers confirming the formation of a non-ordered new layer. In this case, both Au_2O_3 and AuOOH presents disordered structures. Thanks to XPS characterization we have detected that Au_2O_3 is formed as precursor of AuOOH, which finally gives the OER to occur.

In summary, thanks to the analysis by XPS and LEED of emersed layers to study the electro-oxidation mechanism of Au(111) preceding the OER a new mechanism has been unveiled and is depicted in Figure X.

Following UHV characterization, by XPS and LEED, the resulting samples were analyzed electrochemically by CV. These samples were then immersed in the same acidic solution, and CV is performed at a scan rate of 50 mV/s within the same potential range (OCP to 1.5 V). Figure 5.15 summarizes the potential fingerprints of all the emerged species.

The peak attributed to sulfate adsorption around 0.4 V is predominant and broader in the emersed layers formed from 1.6 V (red curve) up to 1.8 V (blue curve), diminishing and almost disappearing at higher potentials. This behavior is consistent with the presence of a sulfate layer acting as a precursor to the oxide, previously characterized by XPS and attributed to the decomposition of persulfate. Once the oxide is formed, the sample no longer presents available adsorption sites, causing the peak to almost disappear. The increase in the charge under the peak at low potential indicates an augmentation in sulfur-based component thickness.

The transition from a disordered to an ordered phase, ascribed in the literature as a transition from HSO_4^- to SO_4^{-2}, at 0.8 V is slightly observed at potentials

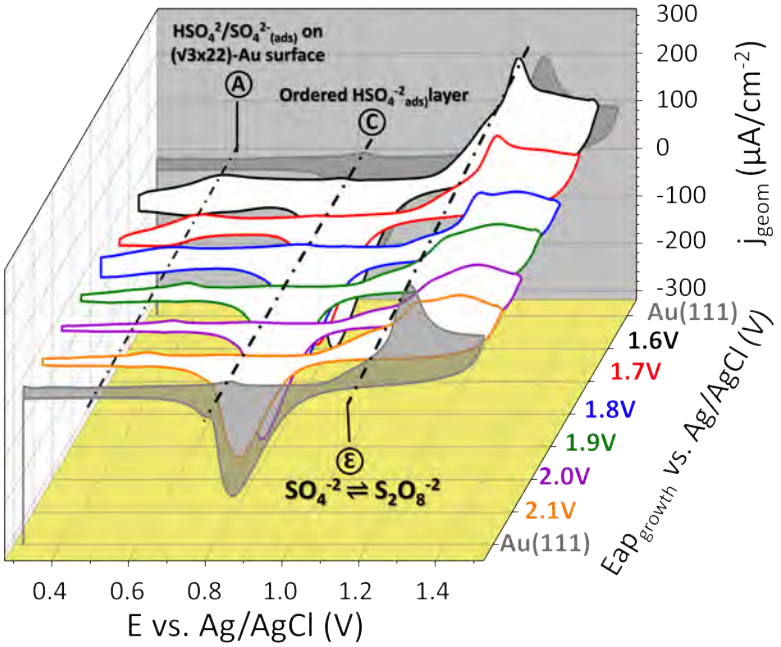

Figure 5.15: Cyclic voltammogram of Au(111) surfaces after polarization for 5 min in deaerated 0.05 M H_2SO_4 electrolyte from 0.3 to 1.5V at a scan rate of 50 mVs^{-1} . It is the 1^{st} cycle.

below 1.8 V and disappears at E >1.8 V, confirming its absence on the surface when oxide is present. The oxidation peak around 1.3 V also becomes attenuated with the same tendency as peaks A and C, aligning with previous assumptions pointing to the emergence of a sulfur-based species. The structure emerging at potentials higher than 1.8 V exhibits a new broad peak at 1.4 V, attributed to O_2^{-2} species, which persists until 2.1 V, where oxide decomposition occurs and the peak disappears. This further demonstrates that the plateau achieved at 1.3 V is attributed to the transformation of SO_4^{-2} to $S_2O_6^{-2}$, releasing two electrons, consistent with the 120 mV peak-to-peak width.

The post j-E curves align with previous electrochemical and XPS assumptions, demonstrating the capability of the EC-UHV system to immerse and emerse electrodes, revealing surface chemical and structural properties.

5.4.3 DFT Calculations employing Extended Surface Pourbaix Diagram

The mechanism of Au(111) oxidation surface based on the experimental data obtained has been recently confirmed by DFT calculations using Extended Surface Pourbaix Diagram (ESPD). ESPD is a method developed and used by Stefano Americo from DTU which served to predict the status of a material surface in electrochemical environments in terms of coverage by water dissociation products. By including surface vacancies in the list of explored configurations, the method is able to explicitly model the material chemical and structural changes, giving insights in the atomic arrangement. Alongside with the collaboration occurring during his stay

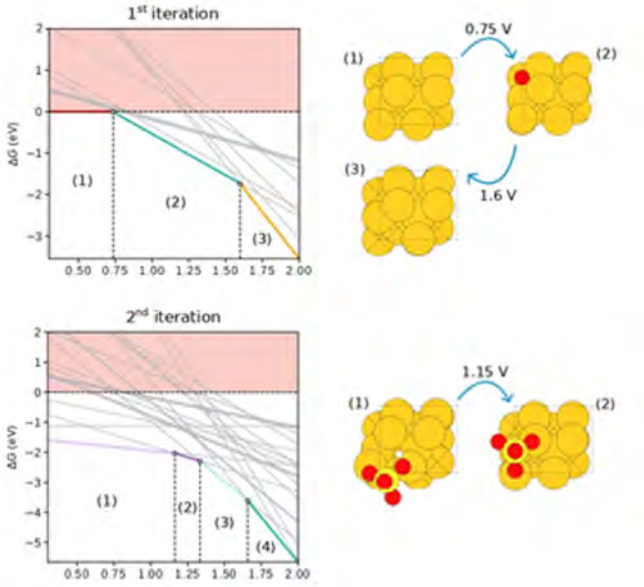

Figure 5.16: ESPD slice depicting the pH 1.3 on a gold surface. The panels unveil slices obtained through two distinct methodological iterations, each advancing the depiction of surface configurations. Accompanying each iteration are the atomic arrangement associated with various stability domains.

in our team, ESPD was applied to experimental results exposed before, measured in 2020 in Nanophysics Lab facilities, and served as a benchmark for assessing the accuracy of the developed ESPD method. For further information on it, check [210].

Americo has simulated the clean Au(111) surface in presence of 0.05 M H_2SO_4 electrolyte. The different aroused electrochemical features in the oxide electrochemical window and in the OER regimen, commented before in Section 5.3 (see Fig. 5.6 and 5.8) have been investigated by DFT.

Along different iterations, illustrated in Figure 5.16, calculations revealed that the surface is stable until 0.75 V, thereafter succumbing to spontaneous O adsorption. Around 1.6 V, vacancy formation emerges as the preferred degradation pathway suggesting vacancy formation as a prerequisite for irreversible oxidation process. When augmenting the number of adsorption configurations in the calculation, second iteration in Fig. 5.16 and considering sulfur-based species, its adherence finds favor at relatively modest potentials, aligning harmoniously with empirical observations. Moreover electrochemical transformation of HSO_4^- (confirming the first sulphur-specie in adsorbs) into SO_4^{-2} dominates at 1.15 V (Fig. 5.16-second iteration).[211] This finding corroborates the transition exposed before where HSO_4^- is thought to transform into SO_4^{-2} at $0.6 < \text{E} < 1.31$ V (see Fig. 5.13). Additionally, two further delineations emerge at 1.3 V and 1.65 V, correlating it in his study with OH and O adsorption, respectively.

Although collectively, ESPD prognostications could mirror the experimental CV's features shown on 5.6, though with slight differences in their positions, furthes analysys should be made to include the peroxodysulfate formation instead of OH and O. Even though, what this calculations served is to confirm that bisulfat is the

rpeferred form in be adosrbed on the surface being transformed to bisulfate in peak C.

5.5 Summary

In summary, the studies conducted in this chapter have evaluated and validated the capabilities of the new EC-UHV approach implemented in this thesis to study fundamental electrochemical processes, such as the electro-oxidation leading to the OER, on a model surface like the Au(111). Using a quasi-in situ methodology for structural, chemical, and electrochemical characterization of the same sample, with an innovative transfer method in a controlled, clean environment with an inert Ar atmosphere, we have obtained the following key findings:

- **Electrochemical Features of Au(111)**: The characteristic electrochemical features of the Au(111) surface in diluted H_2SO_4 solution were successfully obtained. This was confirmed both in the double-layer potential region and within the electrochemical window, obtaining comparable results to previously reported ones. The ability to distinguish the potential-induced chemical and structural changes corresponding to these electrochemical processes was also verified.

- **Validity of the Emersed or Quasi-*in Situ* Approach**: The study confirmed that the quasi-*in situ* approach preserves the electrochemical interface composition. The composition observed in the double-layer potential region was consistent with the theory of the electrified interface, exposed in section 2.2, where presumably HSO_4^- ions chemically adsorb to the surface via an Au-S bond without chemically altering it. This phase, despite losing potential, retains contact between the surface and the double-layer, forming the emersed layer in conjunction with retained water as part of the hydration sphere.

- **Role of Anions in Electro-Oxidation**: The study highlighted the crucial role of anions present in the electrolyte. Bisulfate adsorption at potentials within the double-layer region (Peak A and B) lifts the herringbone reconstruction to form (1×1)-Au(111), as previously reported. At higher potentials (1.6 - 2.1 V), new chemical species appear on the surface, not identified before, presumably with sulfate (assuming that the transition from HSO_4^-/SO_4^{-2} occurs in Peak C) transforming into peroxydisulfate ($S_2O_6^{-2}$), which binds to the surface via an Au-O bond. This finding suggests a prior phase, either metastable or not detectable by the emersion approach, in which bisulfate bound via an Au-S bond transitions to an Au-O bond, likely facilitated by the interaction of the anion with H_2O/OH molecules. This process substitutes the widely accepted RTO mechanism in the literature, being also a two-electron transfer reaction and occurring in the anodic peak ε below OER potentials. The peroxydisulfate phase increases with potential and time, eventually leading to the formation of bulk oxide. This means that the peroxydisulfate intermediate inserts oxygen into the surface before desorbing, acting as a promoter of

oxidation. This suggests that strongly bound species ($HSO_4^-/SO_4^{-2}/S_2O_8^{-2}$) desorb, leading abruptly to the formation of the so-called bulk oxide.

- **Oxidized Phases**: The results indicate an Au^{+3} oxidation state, aligning with previous studies and following Pourbaix diagram phase. Intermediate oxide phases detected include Au_2O_3, which transforms into AuOOH as the potential increases, ultimately decomposing to produce oxygen, confirming that AuOOH is the catalytically active phase in the OER. This finding supports the previously reported formation of Au_2O_3 as an electro-oxidation product and its transformation to AuOOH precluding OER and its decomposition during the OER.

Therefore, the methodology described effectively addresses key questions in electrochemical processes, such as the role of adsorbed electrolytes and the identification of the active phase in the OER. The study emphasizes the importance of complementing different techniques and scales—meso-/atomic scale using surface physics techniques like XPS and LEED, and macroscopic scale using electrochemical tests—to gain a comprehensive understanding of electrochemical processes and surface catalyst changes. This integrated approach provides a more complete and nuanced insight into electro-oxidation and the OER on Au(111).

Chapter 6

Model manganese-oxide based catalyst structures for OER

As aforementioned, this thesis implemented an experimental methodology to study potential-induced chemical and structural changes at the electrode/electrolyte interface using the new quasi-*in situ* experimental EC-UHV setup and methodology (further insights were given in Chapter 4). After validating the approach and its applicability in the model Au(111) system (reported in Chapter 5), we have extended its applicability to a more relevant and complex system. In this chapter, manganese oxide (MnOx), a promising active catalyst for the OER developed employing UHV methods, has been investigated.

MnOx, a group of transition metal oxides, emerge as a compelling alternative to precious metal-based catalysts due to their abundance [212] , cost-effectiveness [213], non-toxicity [214], and demonstrated efficiency in catalyizing various chemical reactions [215, 216], holding promising properties as bi-functional catalyst for oxygen reduction and water oxidation [217, 218].

Inspired by the redox-active site Mn^{+2} in the manganese-calcium-oxo cluster ($CaMn_4O_5$) complex, responsible for oxygen turnover in biological photosystem II enzyme (PS-II) [219–221], there is a growing interest in developing MnOx-based catalysts that mimic the optimized natural catalyst. This pursuit aims to provide a cost-effective alternative to materials like Ir and Ru for OER. However, the challenge lies in the low surface stability causing sluggish kinetics of oxygen-based electrochemical reactions, attributed to a significant deviation from $E^0_{H_2O/O_2}$ (resulting in a a high η_{H_2O/O_2}). This limitation is influenced by adsorbed species and formed intermediates on the catalyst surface, affected by the electronic structure and surface chemistry. Thus, the necessity for a comprehensive investigation of OER catalyst design extends beyond the manipulation of bulk variables, considering the impact of the surface on reactivity.

Manipulating surface structure and its composition offers the potential to optimize the electronic structure and surface chemistry within distinct yet interconnected atomic layers, thereby enhancing their overall appeal. Progress in alternative catalysts attests to the potential benefits of such an approach. [222–224] It

is well known that the stability, composition and properties of catalytic materials depend primarily on the synthesis conditions. Therefore, controlling growth conditions allows tuning structural, chemical and electrical properties of catalyst surfaces, thereby affecting catalytic properties. On this regard, studying model catalytic film systems constructed within UHV environments and analyzed through surface science methodologies presents a unique avenue for unraveling intricate surface reaction mechanisms.

The accelerated development of manganese oxide catalysts with improved stability and performance against the oxygen evolving reaction is of paramount importance. To achieve this long-standing goal, a comprehensive study on the same sample regarding the surface chemical state and structure of MnOx catalyst prior, operando, and after exposure to OER relevant potentials is essential. This involves delving into the OER mechanism on this surface and evolving the real active phase. In this direction, the characterization of MnOx surface state under reaction conditions is still very limited [225–228]. Thus, this chapter focuses on identifying the real MnOx catalyst phase towards OER in alkaline media, employing a combined surface science and electrochemical approach facilitated by our handmade UHV-EC system.

In this chapter, a detailed study utilizing various surface science techniques such as XPS, LEED, STM, and AFM was employed to elucidate the parameters controlling the chemical composition and, consequently, the OER performance of MnOx thin layers grown on different substrates. In contrast to the previous chapter were I discussed the effect of electrochemistry on surface oxidation, in this chapter we aim to determine whether different film oxidation states affect the electrochemical response. Accordingly, we will evaluate the role of substrate crystal orientation on the nature and crystalline structure of the oxide layers grown on top and relate these structural and chemical properties to the electrochemical response under reaction conditions in alkaline media. Furthermore, the stability of these catalytic layers will be assessed after the OER reaction. This systematic study allows the interrogation of the composition/structure–activity relation of a highly active earth-abundant catalyst at or after exposure to relevant OER potentials, evolving the real catalyst surface.

6.1 Properties of Manganese Oxides

Before delving into the growth and characterization of various manganese oxide structures and their application in the oxygen-evolving reaction, it is essential to provide a brief introduction to the general properties of these materials. As highlighted earlier, the distinction between bulk and thin film structures results in varying electronic structures and surface's chemistry, influencing overall performance. This section will offer an in-depth exploration of the structural variability and chemical composition of Mn oxides/hydroxides across the entire range of manganese oxidation states, whether in bulk or film structures.

Table 6.1: Oxidation states and phases of most common manganese oxides (MnOx) found in nature.

Mineral	Composition	Valance	Structure	Lattice Param. (Å)	Ref.
Manganosite	MnO	+2	Rock salt	a=b=c=4.44	[229]
Hausmannite	Mn_3O_4	+2,+3	Spinel	a=b=8.14, c=9.42	[230]
Bixbyte	Mn_2O_3	+3	Corundum	a=9.41, b=9.42, c=9.40	[231]
Pyrolusite	$\beta - MnO_2$	+4	Rutile	a=4.40, b=2.87	[232]

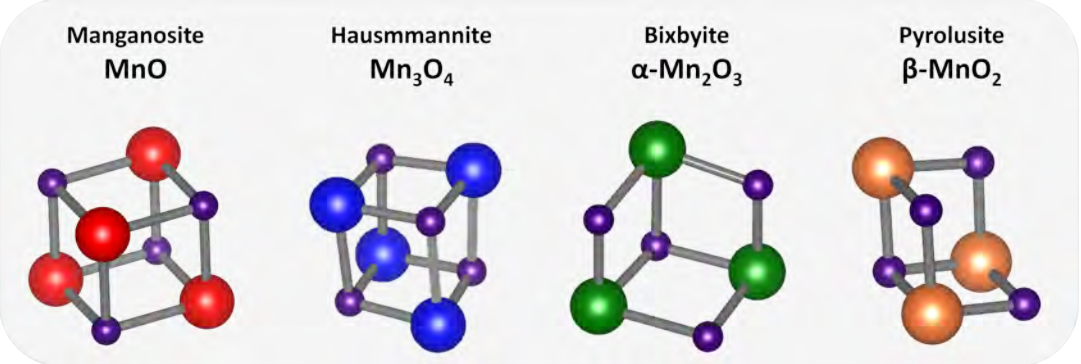

Figure 6.1: Representations of crystal structure of most common manganese oxides: manganosite, hausmannite, bixbyte and pyrolusite.

6.1.1 Bulk materials

It is known that transition metals (TM) typically exhibit multiple stable oxidation state. In comparison to other TMs, manganese stands out for its large number of oxidation states spanning from +2 to +7. This distinctive characteristic confers a significant richness to the chemistry of manganese-containing compounds. The interaction between manganese and oxygen generates an array of oxides, distinguished by their varied chemical compositions and multiple crystalline phases. This diversity offers a rich prospect for developing a wide range of catalysts based on MnOx. The structural versatility encompasses over 30 distinct crystal structures for Mn oxides/hydroxides across various oxidation states of manganese. The predominant phases of MnOx found in nature are encapsulated in Table 6.1, with their corresponding crystal structures depicted in Figure 6.1.

The majority of MnOx compounds are assembled through octahedra $[MnO_6]$ structure bonds, resulting in the formation of distinct nanostructure types.[233] These crystal structures, characterized by highly densely packed structures, exhibit three-dimensional connectivity, growing uniformly in all three dimensions. Examples of this configuration include MnO (magnesite), Mn_3O_4 (hausmannite), and Mn_2O_3 (bixbyte). The second type, represented by $\beta - MnO_2$ (pyrolusite), features edge- and corner-linked $[MnO_6]$ chains, creating tunnel structures with varying channel dimensions. The third group encompasses less common morphologies, wherein each layer shares $[MnO_6]$ edges with cations such as Li^+, Na^+, and K^+, as well as other alkali metals and water molecules occupying the interlayer space. Moreover, these MnOx compounds display a diverse array of polymorphic structures.[234]

Consequently, among other low-cost transition metals, manganese and its potential MnOx derivatives emerge as compelling candidates due to their rich variety of crystallographic phases, enabling the exploration of chemical and structural catalytic relationships.

The tunability of structures and composition in MnOx results in unique physical and chemical properties for each morphology. These characteristics make MnOx structures ideal materials for various applications, including novel electronic device technology [235, 236] and heterogeneous catalysis[237], among others. For instance, magnetic oxides in the rock salt structure like MnO are well-known for exhibiting antiferromagnetic properties where the magnetic moments of adjacent ions are opposite arising from the arrangement of spins in the crystal structure. This material possess a broad band gap, typically ranging from 3.6 to 3.8 eV, arising from the localized band structure inherent to the cubic $3d$ transition metal monoxides in their later stages[238]. This property makes MnO suitable for novel electronic device technology and spintronic-based devices if spontaneous magnetization is achieved in it. Simiarly, Mn_2O_3 also displays antiferromagnetic properties which is attributed to the arrangement of spins in the crystal lattice and the magnetic moments of Mn^{+3} ions.[239] In contrast, Mn_3O_4 can display ferromagnetic properties since exhibits a mixed valance state of Mn^{+2} and Mn^{+3} contributing to a spinel structure.[240] On the other hand, MnO_2 is typically non-magnetic in its bulk form owing to the d^0 configuration of Mn^{+4} ions. In different applications like catalysis, as a TM oxide, all MnOx show potential-pH responsive behaviours. The configuration of the electric potential and the acidity level of the electrolyte play pivotal roles in shaping the structure and makeup of oxides, consequently impacting their effectiveness in catalyzing the water oxidation reaction.[241] A conventional Pourbaix diagram offers insights into the thermodynamically favorable domains of various MnOx phases across anodic potential gradients and a broad pH spectrum, elucidated in Figure 6.2.

Observing the stability trends in bulky phases represented in Fig. 6.2, Mn^{2+} emerges as the most stable phase in the acidic and neutral regimes. In the basic regime, stable manganese oxides include MnO_2, Mn_2O_3, Mn_3O_4 and $Mn(OH)_2$. Notably, alkaline media is the preferred environment for MnOx structures, as it encompasses the thermodynamically stable majority of possible structures. This media evolves as the perfect one to evaluate real MnOx-based catalytic phase precluding and after OER.

With the increasing emphasis on harnessing MnOx for catalyzing water oxidation, alongside its applications in energy-related fields such as supercapacitors [242] and batteries [243], a multitude of techniques have emerged and been fine-tuned for the preparation of MnOx crystals. Several approaches exist for synthesizing manganese oxide crystals, including chemical precipitation, hydrothermal synthesis, solid-state reaction, sol-gel synthesis, and template-assisted synthesis. The choice of the method significantly influences the crystal structure and chemical composition of the as-synthesized MnOx, thereby altering its properties.

In the realm of experimental setups, fabricating bulk oxide single crystals presents a formidable challenge in achieving surfaces that are both stoichiometric and structurally well-ordered, while maintaining low defect densities. This challenge is par-

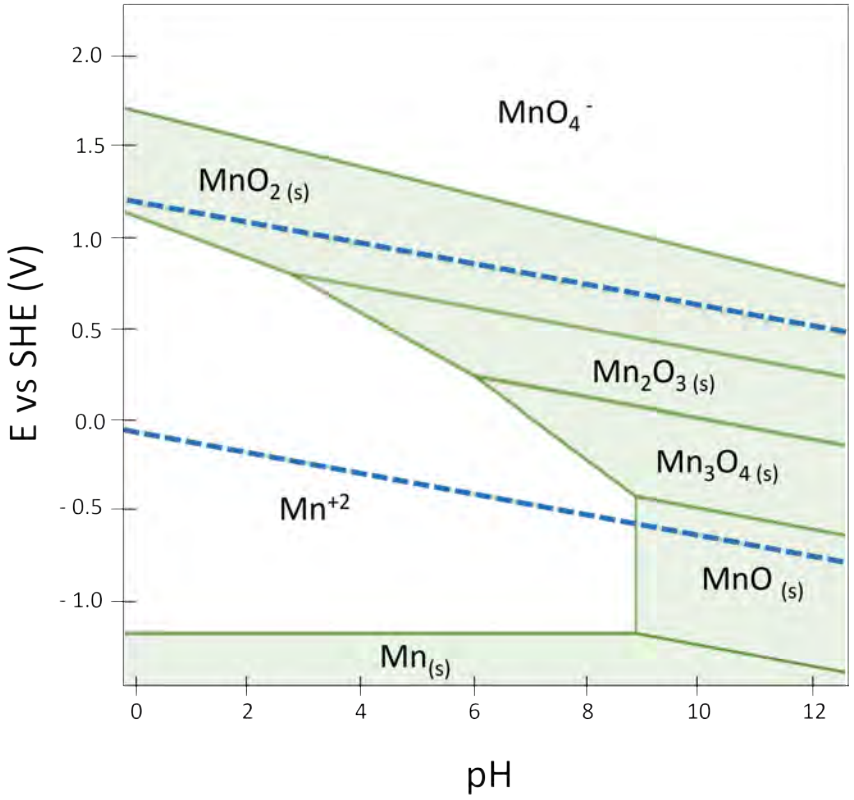

Figure 6.2: Thermodynamic stable phases as a function of the potential and the pH displayed as Pourbaix diagram. Adapted from [77].

ticularly pronounced in manganese oxides, which consist of stacked layers of Mn-O and Mn, where surfaces exposing metal atoms are susceptible to altering their oxidation states under specific conditions, yielding complex surface configurations. The identification and examination of these phases encounter substantial obstacles, as many samples consist of brittle, poorly crystallized materials, often comprising mixtures of multiple oxides. Moreover, in the case of MnO oxide, the surface structural integrity is compromised. For example, cleaving a MnO single crystal along the (001) plane typically yields a surface composed of pyramids with (111) octahedral faces. Furthermore, subjecting the crystal to annealing temperatures of up to 1000 K results in (2×2) and (6×6) reconstructions without altering the surface stoichiometry.[244] These arbitrary irregularities can introduce unpredictable alterations in surface properties. Consequently, even in bulk-synthesized crystal structures, the surface may diverge from the bulk material, exerting an influence on properties such as catalysis. Given the critical role of parameters like surface morphology, chemical composition, and electronic structure in oxygen evolution reaction (OER) performance, effective synthesis strategies are indispensable for producing controlled catalysts with minimal over-potential and heightened activity.[245]

Over the past few years, strides in nanotechnology have paved the way for a controlled fabrication of well-defined nanostructured catalysts, such as nanoparticles and thin films, offering heightened control even at the atomic level. This technological breakthrough plays a pivotal role in circumventing uncontrolled modifications

in the bulk crystal structure. Furthermore, nanostructured catalysts demonstrate a considerable surface area-to-volume ratio, thereby creating a more extensive interface between the electrolyte and the catalyst. This, in turn, enhances catalytic efficiency [246]. By localizing the majority of active sites on their surface, nanostructured catalysts prove to be more efficient compared to bulk materials [247]. Given that the Oxygen Evolution Reaction's performance is significantly influenced by the catalysts' surface area, the implementation of thin film growth methods becomes crucial for achieving efficient catalysts.

6.1.2 MnOx thin films

Physical vapor deposition (PVD) emerges as the predominant technique for the fabrication of thin films under UHV. This methodology entails the vaporization of a metal source material followed by its condensation within an oxidative atmosphere. [248] Common PVD methods for the growth of manganese oxide films encompass thermal evaporation [249], reactive electron beam evaporation in an oxidizing ambient [250–252], and magnetron sputtering [253]. The resultant films exhibit elevated purity levels and well-ordered crystalline structures, rendering them highly suitable for the envisaged applications. Moreover, molecular beam epitaxy stands out as the optimal experimental technique for growing these materials with the utmost crystallinity and minimal defect density. This process is controlled, affording the ability to fine-tune the composition and thickness of the film by manipulating parameters such as the substrate temperature, oxidizing agent, or evaporation rate. Additionally, the symmetry and lattice constant of the substrate surface wield a pivotal influence in the epitaxial growth of oxide thin films.

In recent years, an increasing interest has been observed in the fabrication of Mn-oxide thin films, particularly under UHV conditions, employing PVD-based methodologies. Nevertheless, the successful growth of such films remains limited, with only MnO and Mn_3O_4 structures affordable realized through reactive electron beam evaporation in an oxidizing ambient.[250–252] These exposed structures, MnO and Mn_3O_4, have been grown on various metal single crystal substrates, including Pd [254–256], Ag [250, 252, 257–260], Rh [261, 262], Au [215, 263, 264] and Pt [265–267], among others. Ag(001) stands out as the preferred substrate due to its crystal structure, facilitating MnOx growth with minimal lattice mismatch, and its relatively low reactivity with oxygen, mitigating undesired substrate oxidation. Given the limited success in achieving these structures, it becomes imperative to scrutinize the influence of growth conditions on the resultant structures' properties, as established in the existing literature, to serve as a valuable reference.

On one hand, ultra-thin (1×1)-MnO reconstructed films, supported on Ag(100), have been systematically prepared under oxygen pressure ranged from 10^{-8} to 10^{-7} mbar at RT [257, 259]. For MnO, an in-plane lattice match is observed, as corroborated by the LEED pattern. Nevertheless, as mentioned before, MnO crystals exhibit multiple associated reconstructions, and subsequent investigations unveil a dependence of the in-plane lattice constant on the thickness of the epitaxially grown MnO film. Chassé and colleagues observed a shift in the LEED pattern from (1×1) to p(2×2) as the thickness of MnO increases from 3 to 7 ML[258]. This transition

can also be attributed to the growth of $Mn_3O_4(001)$ layers along the $< 110 >$ direction of Ag(001), with a lattice parameter nearly twice that of the Ag(001) surface lattice parameter ($a_{Ag} = 2.89$ Å) [252, 257].

Interestingly, Mn_3O_4 oxide exhibits polar bulk terminations in the (001)-plane, making it suitable for layer-by-layer film investigations. The bulk structure of $Mn_3O_4(001)$ comprises two distinct sublayers, each with a square (a x a) unit cell: one layer is a mixed O/Mn layer with Mn_2O_4 composition, while the other layer consists solely of Mn. In thin-film growth, both layers must be considered to control the thickness effect. These layers are stacked alternately, with consecutive layers of the same type laterally displaced by a/2 and rotated by 90^o. A complete unit cell comprises eight layers with an overall height of $c = 9.47$ Å. Depending on film thickness, a p(2×1) or apparent (2×2) superstructure composed of p(2×1) and c(2×2) domains may develop [251]. Furthermore, electron diffraction indicated that the $Mn_3O_4(001)$ film can grow parallel to the $<110>$ direction of the underlying MnO(001) surface, with the Mn_3O_4 unit mesh rotated by 45^o with respect to the MnO(001), resulting in a (2×2) LEED pattern due to the conjunction of both oxides [268]. Increasing oxygen pressure and annealing induce c(4×4) and p(4×4) reconstructions originating from the oxygen-terminated Mn_2O_4 surface and oxygen vacancy ordering on the Mn_2O_4-terminated surface, respectively [252].

It is widely-known that not only oxygen pressure and substrate surface lattice constant but also substrate symmetry are critical parameters for the epitaxial growth of oxide thin films. In this context, square oxide overlayers have been previously obtained on Ag(001) substrate, exemplified by the rock salt MnO(001) [257, 260] and the spinel $Mn_3O_4(001)$ [251]. Conversely, on hexagonal substrates, hexagonal oxides have been reported, such us hexagonal MnO(111) on Pt(111) [266] or distorted $Mn_3O_4(110)$ on Cu(111) [269].

Thin films of Mn-based oxides have been characterized not only by their lattice structure but also by their electronic and chemical properties. The analysis of electronic and chemical composition holds paramount importance in elucidating the characteristics of grown thin oxide layers. The community employs meticulous XPS analysis to establish the chemical composition and oxide stoichiometry of Mn oxides. Typically, oxide stoichiometry can be discerned for most metals by analyzing peak shifts. However, determining Mn oxidation states based on energy positions is challenging due to the small separation between the peak maxima of different oxidation states. The peak maxima of Mn^{+2}, Mn^{+3}, and Mn^{+4} are all contained within a width of $\approx$ 2 eV.[270][271] Instead, researchers used signatures, such as the characteristics $Mn2p$ satellites as well as the distances between maxims for the Mn 3s multiplet splitting [19, 250, 272]. The 3s orbitals are spherical and no spin splitting occurs, being single XPS peak. However, in the case of manganese, the 3s splitting emerges from the interplay between the spin of the remaining Mn 3s electron post-photoemission and the resulting Mn 3d spin. This energy discrepancy between parallel and anti-parallel spin alignments of both shells, as dictated by the van Vleck theorem (Eq. 6.1) [273], is directly proportional to the 3d spin.

$$\Delta E \approx E(3d \uparrow\uparrow\uparrow\uparrow\uparrow 3s \uparrow) - E(3d \uparrow\uparrow\uparrow\uparrow\uparrow 3s \downarrow) \approx A(2S_{3d} + 1) \tag{6.1}$$

As a result, the extent of the $3s$ splitting is expected to be most significant in

Table 6.2: Reference values of $Mn2p_{1/2}$ satellite distances ($\Delta E2p_{1/2}$) and Mn 3s splitting for metallic Mn and for various Mn-based oxides taken from literature.

Structure	$\Delta E2p_{1/2}$ **(eV)**	$\Delta E3s$ **(eV)**	**Ref.**
Mn	-	4.1	[274]
MnO	6.0	4.5	[19]
	5.4	4.5	[272]
Mn_3O_4	10.0	5.1	[19]
	10.5	5.4	[272]
Mn_2O_3	11.8	6.0	[19]
	11.9	6.1	[272]
MnO_2	10.5	6.0	[19]
	11.3	5.3	[272]

MnO, owing to the $3d^5$ high spin configuration of the Mn $2p$ ion with $S_{3d} = 5/2$, gradually diminishing with higher oxidation states.

In summary, both the $Mn2p_{1/2}$ satellite distance and the Mn 3s multiplet energy difference represent attributes contingent upon the stoichiometry. Table 6.2 provides a summary of diverse reference values encompassing $Mn2p_{1/2}$ satellite distances and the strength of the 3s splitting across various Mn-oxides.

The presence of diverse surface Mn oxides has prompted investigations into the impact of the initial oxide on OER activity, giving rise to studies on structure-activity relations [225, 234, 275–277]. Despite the documented controlled growth of MnO and Mn_3O_4 nanoislands and thin films in Ultra-High Vacuum (UHV) on various metal substrates, the OER performance of these grown samples has not been systematically assessed. Consequently, the structure-activity/stability relationship of Mn-based catalysts in the context of OER emerges as a key inquiry within the UHV-EC framework. Despite considerable efforts by the electrochemical community to explore MnOx structures as OER catalysts, an exhaustive evaluation of the OER performance of MnO and Mn_3O_4 nanostructures grown in UHV has yet to be undertaken.

6.1.3 Electrocatalytic properties of MnOx against OER

The use of manganese oxides as electrocatalysts for water oxidation dates back to the 1970s, when Morita and colleagues [278] identified mixed oxides, comprising $\beta - MnO_2$ (pyrolusite) and $\alpha - Mn_2O_3$ (bixbyite), as exhibiting the highest catalytic activity for the Oxygen Evolution Reaction (OER). This phase combination demonstrated efficient water oxidation in both acidic and basic electrolytes. Notably, the MnOx electrode in basic electrolytes sustained water oxidation for an extended duration without a proportional increase in overpotential, while in acidic electrolytes, a 150 mV overpotential increase was necessary. Morita et al. proposed that the Mn^{+3} sites on the oxide surface served as active sites for oxygen evolution. Subsequent research by Nakamura's group indicated the instability of Mn^{+3} species in neutral and acidic pH electrolytes, undergoing disproportionation to form Mn^{+2} and Mn^{+4}, thereby compromising catalytic activity [279, 280].

Su et al. conducted a comprehensive study on the surface stability of Mn oxides and their binding energies to OER intermediates, utilizing a combination of Density Functional Theory (DFT) and electrochemical measurements [217]. DFT calculations suggested that, at OER-relevant potentials, the MnO_2 phase exhibited the highest stability, consistent with the bulk stability regions outlined in the Pourbaix diagram [77]. Therefore, the persistence of a +3 state of Mn at the electrode surface at highly anodic potentials seemed improbable. Instead, the study highlighted the potential influence of the preparation method and resultant catalyst roughness or conductivity in establishing an activity hierarchy.

Since these seminal works limited exploration of the anodic characteristics of manganese oxides has appeared, especially those prepared using UHV-grown films. Robinson et al. investigated eight different polymorph manganese oxide structures containing Mn^{+3} and Mn^{+4} for photochemical water oxidation [234]. Among them, $\beta - MnO_2$, $\gamma - MnO_2$, $\alpha - MnO_2$, $\delta - MnO_2$, and $LiMn_2O_4$ exhibited no OER activity under experimental conditions. The most efficient catalysts were identified as Mn_2O_3, followed by Mn_3O_4 and $\lambda - MnO_2$. Frey et al. examined 13 different manganese oxides as OER catalysts and concluded that the order of catalytic activity from most to least active was: Ca-birnessite $> Mn_2O_3 > MnO_2$.[281]. Ramírez et al. compared the OER activity of amorphous MnOx, Mn_2O_3, and Mn_3O_4, finding that Mn_2O_3 exhibited the best catalytic activity, while Mn_3O_4 showed the least activity [276].

Several other reports have explored the OER activity of individual manganese oxide structures, including MnO_2 nanorod arrays (NRAs), $\beta - MnO_2$, mixed-valent MnOx, marokite $CaMn_2O_4 \cdot xH_2O$, birnessite-type MnO_2 ($\delta - MnO_2$), and amorphous manganese oxides. Additionally, Gorlin et al. monitored, through *ex situ* XPS, the oxidation state changes of the catalyst, identified as $\alpha - Mn_2O_3$ in its initial state, as a function of applied potential, demonstrating the oxidation of Mn (III) oxide to MnO_2 at 1 V [282]. However, to unravel the dependence on oxidation state, *in situ* techniques are imperative, allowing the characterization of both the pre-OER surface and the surface formed after OER operation conditions. Unfortunately, such comprehensive studies are currently lacking for Mn-based OER catalysts.

In summary, this section has elucidated the properties of both bulk and thin MnOx structures, alongside their electrocatalytic behavior. Within the context of this thesis, MnOx structures are employed as catalysts in the form of thin film structures. The inherent properties of these structures are significantly influenced by growth conditions such as oxygen pressure, oxidizing agent, substrate temperature and orientation, as well as thickness. These factors collectively impact the composition and structure of the MnOx thin films, and their precise control is dictated by the film deposition process.

Following this introductory section, the subsequent sections will be dedicated to a focused exploration of the growth of diverse MnOx thin film structures. The emphasis will be on how the preparation process leads to substantial variations in chemical composition and structure. Identification of different phases will pave the way for quasi-*in situ* chemical and structural characterizations on the same sample. This approach aims to unveil the evolving MnOx phases, both preceding

and resulting from the OER, offering a comprehensive understanding of the catalytic processes involved.

6.2 Manganese oxide growth on Ag(001) substrate

The recent surge in interest on investigating the epitaxial growth of MnOx thin films, has prompted exploration into various substrates for this purpose. Among these substrates, Ag(001) emerges as the preferred substrate. As detailed in Section 6.1.2, with proper tuning of preparation parameters such us reactive oxygen pressure atmosphere and substrate temperature, well-ordered films of both MnO and Mn_3O_4 can be grown on the Ag(001) surface in UHV.[250, 252, 257–260] It is well-known that in the $MnO/Ag(001)$ system the lattice mismatch stands at approximately 9 % (a_{Ag}=4.09 Å; a_{MnO}=4.44 Å) [283], which is a moderate value, being able its epitaxial growth. In the case of $Mn_3O_4/Ag(001)$, a 45 rotated growth is anticipated with a 0.3 % misfit following the "roles of lattice fitting in epitaxy" [284], given the ratio $a_{Ag} : a_{Mn_3O_4}$ approaches to $\sqrt{2}$ $a_{Mn_3O_4}$=5.76 Å)[283].

In light of these findings, Ag(001) was selected as the substrate for the epitaxial growth of different MnOx phases in this work, as a first instance. This choice facilitates benchmarking against previously reported structures, with the overarching goal of attaining higher degrees of oxidation in our UHV system.

6.2.1 Manganese evaporation and oxidation: on-surface or in-flight?

Generally, ultra-thin metal oxides are crafted by vapor depositing the metal onto a suitable single-crystalline substrate and subsequently oxidizing the resulting layer after deposition. Following this idea, we first explored the fabrication of ultra-thin metal oxide films by depositing high-purity Mn powder onto an Ag(001) substrate via an e-beam evaporator.

The Ag(001) single crystal was prepared under UHV conditions by subjecting it to standard cycles of Ar^+ ion sputtering, ranging between 0.5 - 1 keV for 15 minutes, followed by subsequent UHV annealing at 530 K for 30 minutes until a distinct sharp (1 × 1) LEED pattern emerged (Fig. 6.3b). Once the substrate was thoroughly cleaned, high-purity Mn powder (99.95 %) was evaporated from a degassed, water-cooled e-beam evaporator, within UHV conditions (maintained at 10^{-9} mbar). The evaporation was conducted at a constant rate of approximately 0.08 ML/min Mn/Ag(001) (equivalent to 0.26 Å/min), while the substrate was maintained at room temperature.The rate of Mn-deposition was calibrated with an air-cooled quartz microbalance prior and after deposition and controlled by monitoring the flux of Mn ions.

A thin layer of about 2.5 ML of Mn was deposited on Ag(001) at RT. Figure 6.3a and b presents the XPS and LEED characterization, respectively, of cleaned Ag(001) substrate surface as well as as-deposited Mn/Ag(001) layer.

The Ag 3d XPS spectrum of the cleaned substrate, shown on the right hand panel in Figure 6.3a, is composed by two main peaks associated to the spin orbit

components, Ag $3d_{5/2}$ and Ag $3d_{3/2}$, centered at 368.5 eV and 374.5 eV, respectively, ΔE=6.0 eV is between them as documented for Ag^0[285]. When Mn is on top, an apparent shift of $\approx$ 0.1 eV is visible, due to the contribution of a small shoulder at higher BE attributed to MnAg alloy. Mn forms an alloy with Ag, even at RT, as reported before [286].

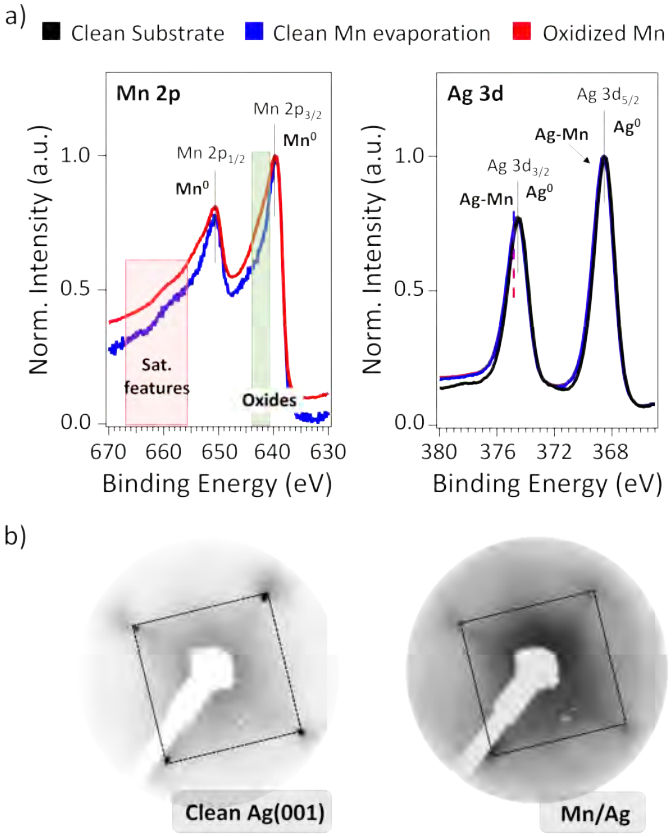

Figure 6.3: a) XPS measurements for as-grown manganese layers on Ag(001) in fresh load crucible (blue) and after several preparations in oxidizing atmospheres (red) in Mn 2p, O 1s and Ag 3d core levels. b) LEED images taken at 65 eV for a clean Ag(001) substrate and Mn/Ag(001) layer.

The Mn 2p core level of as deposited layer is composed by two main peaks associated to the spin-orbit splitting components: Mn $2p_{3/2}$ and Mn $2p_{1/2}$ centered at 639.4 eV and 650.6 eV, respectively, corresponding to Mn^0.[287] In this section, I would like to emphasize that even with careful attention to sublimating pure and non-oxidized Mn, oxidation of Mn in the evaporator's crisol occurs over time due to subsequent exposition to the backfilling oxygen atmosphere during MnOx thin films preparation. This process can be monitored, as shown by the red curve in Fig. 6.3a, where a shoulder appears between the spin-orbit split Mn 2p components. During subsequent MnOx preparations, we observed that the peak shape broadens, indicating partial oxidation of the Mn powder in the crucible. Therefore, we take special care to ensure pure metallic sublimation. To this end, it is estimated that the evaporator is typically removed and refilled every six preparations under oxygen atmosphere to prevent oxidized Mn evaporation, even under UHV conditions.

Nonetheless, as I will demonstrate later, this oxidation is negligible compared to the oxidation formed intentionally.

The LEED patterns of both, clean Ag(001) and Mn/Ag(001) surfaces, taken at 65 eV were collected and presented in Fig. 6.3b. On the left side of the panel, the LEED pattern of the pristine Ag(001) substrate is depicted, showing the characteristic fourfold symmetry indicative of the (001) surface. The pattern displays intense and well-defined spots with a measured surface parameter of $a_{Ag} = 4.09$ Å. After manganese evaporation, a 1×1 reconstruction is visible with exactly the same lattice parameter than Ag. Nonetheless, the LEED spots show attenuation and diffusion, accompanied by a higher background, indicating a lack of long-range structural order. This observation is consistent with prior findings by Shieffer *et al.*., who similarly identified a diffuse Mn/Ag(100) interface at room temperature [286, 288]. Beyond a thickness of 1.5 ML, as in this case, manganese and silver intermix, forming a two-layer interfacial film. Within this film, both manganese and silver atoms adopt face-centered cubic positions within the Ag lattice, a consequence of manganese's limited mobility during room temperature deposition. While this issue can be mitigated by maintaining the substrate at moderate temperatures during the growth process or through post-annealing, increasing the substrate temperature promotes alloy formation. This has been previously discussed and evidenced in the Ag 3d XPS spectra, even at room temperature. Therefore, this option is currently not feasible.

This study demonstrates that the evaporation of Mn is clean and occurs in a metallic state, ensuring that future oxide structures will form when an oxidizing atmosphere is used. To grow MnOx phases, two different approaches were compared: oxidation of deposited metallic Mn on an Ag(001) substrate and oxidation during the Mn deposition process. The objective was to identify the most effective method for achieving well-defined and highly oxidized structures, thereby establishing a correlation between oxidation state and methodology.

At the same time, to achieve higher degrees of oxidation in our UHV system, atomic oxygen plasma was utilized as an alternative approach. This method enhances oxide growth by eliminating the need to dissociate O_2 molecules, resulting in more stoichiometric and higher-oxidation oxides. Microwave atom plasma source, which generates atomic oxygen plasma, was chosen for this purpose. Although atomic oxygen synthesis and control present challenges compared to molecular oxygen, its implementation introduces significant advancements in growth processes. The high reactivity of atomic oxygen radicals facilitates faster growth rates, and the resulting films exhibit enhanced stoichiometry and crystallinity due to increased reaction efficiency. Consequently, microwave plasma oxidation was adopted as the primary method to determine the most efficient growth methodology.

Traditionally, deposited metals are exposed directly to oxidizing agents, either at room or elevated temperatures.[289] Following this approach, the previously deposited Mn layer was subjected to plasma oxygen pressure of $5 \cdot 10^{-5}$ mbar for 5 minutes at room temperature. XPS spectra of Mn 2p, O 1s, and Ag 3d core levels were acquired and are presented in Figure 6.4-blue curve. The intensities of the Ag 3d and Mn 2p spectra were adjusted to ensure uniform height, while the O 1s

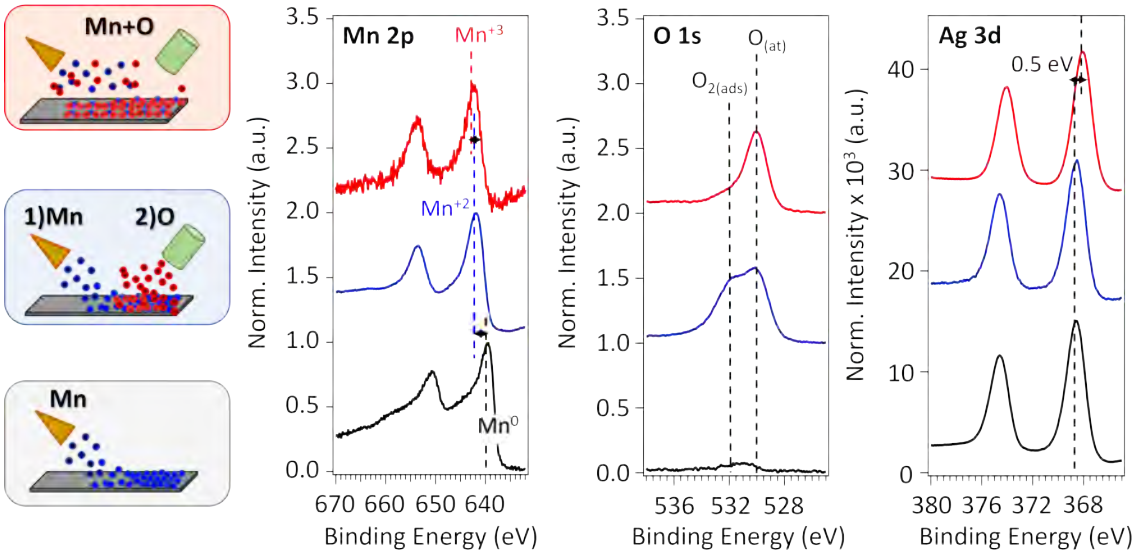

Figure 6.4: XPS spectra acquired for different manganese samples grown in UHV, post-oxidized with atomic oxygen and under oxidizing atmosphere at Ag 3d, Mn 2p and O 1s core levels. It is supported with an schematic representation of the methodology tested with a stacking disposition, from bottom to upper part: manganese evaporation in UHV conditions, manganese evaporation previously to oxidation and manganese evaporation under reactive atomic oxygen environment.

spectra were normalized to the Mn 2p contribution.

In the Mn 2p spectra, the Mn $2p_{3/2}$ peak initially observed at 639.4 eV in the Mn/Ag(001) sample shifted by approximately 2.4 eV to 641.8 eV, suggesting the formation of the first MnOx structure. The O 1s spectra exhibited two components: one around 529.5 eV, attributed to the oxide, and another at higher BE around 532.1 eV, likely due to chemisorbed oxygen on Mn or Ag, or unreacted O. The Ag 3d peak retained its characteristic metallic doublet, indicating no oxidation of Ag. This finding suggests the presence of oxygen species not participating in the oxide formation.

Decoupling metal deposition and oxidation mitigated the risk of unintended reactions or impurity incorporation during film growth. However, unreacted oxygen on the surface indicated a bottleneck in oxygen atom penetration, which step culminates in subsurface oxide formation that grows into a "bulk structure".[290] An increasingly popular alternative is reactive deposition in an oxidized atmosphere. Here, the metal is evaporated and simultaneously oxidized in an oxygen-rich environment during e-beam deposition, as schematized in the red box of Fig. 6.4. Metal atoms react with oxygen molecules either in-flight or upon reaching the substrate surface, resulting in the direct deposition or formation of metal oxides.

Using this alternative approach, the chemical composition of the MnOx structure obtained by oxidizing manganese during deposition in an atomic oxygen plasma atmosphere was explored in the same way via XPS. The same anticipated Mn layer thickness was evaporated under the same plasma pressure atmosphere at room temperature. XPS spectra of Mn 2p, O 1s, and Ag 3d core levels were acquired and presented in Figure 6.4-red curve. The Ag 3d spectra shows a notable shift of the

entire core level of approximately 0.5 eV, also observable in the Mn 2p and O 1s core levels. This shift likely arises due to an electronic effect related to the growth of a highly oxidized structure atop the Ag(001) substrate, affecting its work function. At this point, it should be highlighted that the MnAg alloy component was only observable in the Mn/Ag(001) sample.

For a comprehensive comparison of oxidation levels, the Mn 2p and O 1s peaks were rigidly shifted by 0.5 eV to maintain true peak positions among the samples, aligning the Ag 3d line. In the Mn 2p spectra, the Mn $2p_{3/2}$ peak shifted further from previous prepared sample (oxidation of deposited Mn) by 0.6 eV to 642.4 eV, indicating the formation of a more highly oxidized structure when manganese is deposited in an oxidized atmosphere. The O 1s spectra exhibits the same two components, but the higher BE component was reduced, suggesting more efficient oxidation.

In conclusion, employing an oxidizing atmosphere during Mn evaporation facilitates the creation of higher oxidized layers, with MnOx structures directly deposited. This method proves that Mn is further oxidized in-flight and subsequently deposited on the substrate surface. The methodology for oxide growth is thus standardized, with Mn deposition performed under a reactive oxidative atmosphere.

6.2.2 Manganese oxides composition: MnO, Mn_3O_4 and Mn_2O_3

As mentioned earlier in this section, the partial pressure and the nature of the oxidizing agent (O_2 or atomic O) will influence the final chemical composition and structure. Therefore, having established the methodology for oxide growth, we first proceed to investigate the evolution of the MnOx composition as a function of oxygen pressure and oxidizing agent atmosphere through XPS characterization

O_2 pressure role

We began by employing different partial pressures of molecular oxygen, ranged from $1 \cdot 10^{-8}$ to $1 \cdot 10^{-4}$ mbar, while sublimating the Mn atoms and compared the results with exposition to other oxidizing agent such as atomic oxygen in a pressure of $5 \cdot 10^{-5}$ mbar. To do so, we estimated a 2.5 ML thickness of Mn under each applied oxidizing atmosphere conditions using an evaporation rate of 0.26 Å/min and $\approx$ 130 nA of Mn flux during 30 minutes. The substrate temperature was kept at room-temperature during the process.

Figure 6.5 shows the Mn 2p, O 1s and Mn 3s core levels of layers grown in the absence of O_2 (black) and under a partial pressure of $1 \cdot 10^{-8}$ (red), $1 \cdot 10^{-6}$ (blue), and $1 \cdot 10^{-4}$ mbars (green) of O_2, as well as under $5 \cdot 10^{-5}$ mbars of atomic oxygen pressure (violet). In order to resolve all possible species, we performed a consistent peak fitting procedure. The intensity of all the spectra have been resized to make all the Mn 2p same height while O 1s and Mn 3s are resized respect to Mn 2p peak. All spectres are presented after subtracting a Shirley background.

For the sample grown in UHV conditions in the absence of O_2, as mentioned before, the Mn $2p_{3/2}$ region reveals the metallic Mn phase centered at 639.4 eV. For

the sample prepared under $1 \cdot 10^{-8}$ mbar O_2 pressure, a shift of 1.8 eV towards higher BE of the full peak takes place. The metallic component disappears completely proving the first MnOx structure. The deconvolution of the Mn 2p peak show a main contribution located at 640.6 eV which is attributed to Mn^{+2} oxidation state.[291] The core level position aligns well with the Mn 2p core level spectra documented in existing literature for MnO(001)[250, 257]. In addition, satellite features are notably detectable at 6.0 eV from main peaks, which is also in agreement with values reported for MnO. [19] Finally, to properly fit the entire Mn $2p_{3/2}$ region, it is necessary to include a second component at 642.5 eV, that can be ascribed to Mn^{+3} oxidation state. [292]

For samples prepared at $1 \cdot 10^{-6}$ mbar and $1 \cdot 10^{-4}$ mbar, the intensity of the Mn^{3+} component becomes prominent and, as a consequence, there is an apparent shift of the entire core level of around 0.4 eV. This suggests that increasing the partial pressure of molecular oxygen leads to the formation of a higher oxidized structures. However, no further oxidation is achieved at pressures higher than $1 \cdot 10^{-6}$ mbar. In this latter case, the satellite appears at 10.0 eV matching well with values reported for Mn_3O_4 and MnO_2 phases.[19, 272] In fact, because of the +2 and +3 mixed valances, it is Mn_3O_4 structure and not MnO_2 (+4 valence).

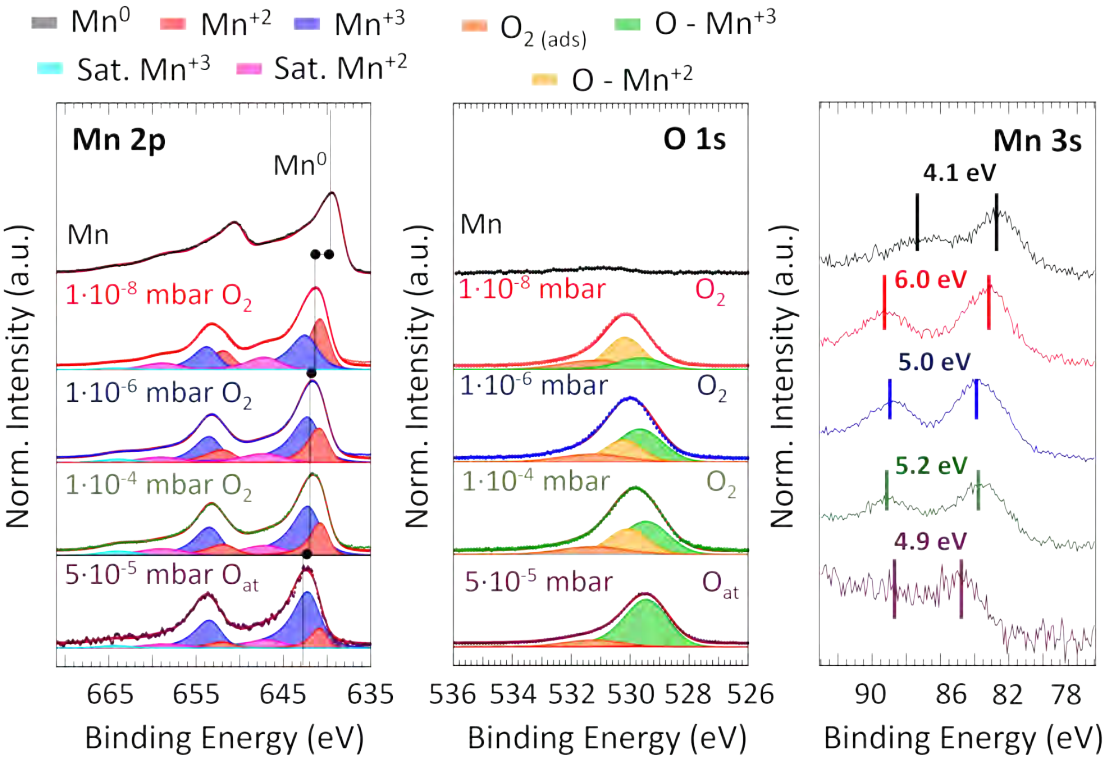

Figure 6.5: XPS spectra and fitting components at the energies of, from left to right, Mn 2p, O 1s and Mn 3s core levels for different manganese-based oxides grown at room temperature under different oxygen partial pressure as well as oxidizing agent.

Although higher oxidative states on MnOx have been identified in nature, like

fully +3 and +4 states, obtaining those states with molecular oxygen in UHV is challenging due to insufficient oxygen pressure and thermodynamic stability. It is well established that the thermodynamic stability of MnO_2 relative to other manganese oxides may be lower under UHV conditions. For instance, MnO and Mn_3O_4 are more thermodynamically stable at lower oxygen chemical potentials, which are characteristic of UHV environments. In cotnrast, MnO_2 formation is favored at higher oxygen potentials. To solve this, using atomic oxygen plasma could enhance the oxidation process. To further confirm this assumption we have used atomic oxygen for the growth of MnOx. On this regard, when atomic oxygen is used as oxidizing agent, violet spectra in Fig. 6.5, a further oxidized structure is obtained based on the apparent full core level shift of ≈ 0.4 eV. In this latter case the Mn^{+2} component influence almost disappears in the Mn 2p region and Mn^{+3} component becomes predominant. Indeed, the Mn^{+3} satellite appears 10.6 eV apart from the main peak (shifting 0.6 eV in comparison with previous structures). It suggests a rather higher oxidized structure like Mn_2O_3 based on previous assignments.[293]

Figure 6.5 presents the O 1s spectra acquired for the described samples. The manganese evaporation (without O_2 pressure, black spectra) shows a really small contribution in the O 1s core level centered at 531.1 eV, in agreement with the main metallic manganese component measured in the Mn 2p core level. Once the pressure increases to $1 \cdot 10^{-8}$ mbar, in the red spectra, first oxygen signal peak is detected centered at 530.2 eV. The photoemission peak is fitted using three components: one located at 529.5 eV that corresponds to the oxygen bonded to Mn^{+3}[276, 294]; one centered at 530.1 eV, compatible with compounds of oxygen bonded to Mn^{+2}[276, 294]; and a last one at higher BE, 531.1 eV, associated to chemisorbed oxygen which does not bond to manganese, being attributed to surface species such us OH^- or O_2^{2-}.[226] The intensity ratio between the two components at lower BE follows the same evolution observed on Mn 2p when pressure increases: the $O - Mn^{+3}$ component increases with oxygen pressure. Moreover, when the oxygen pressure is increased up to $1 \cdot 10^{-4}$ (green spectra and blue spectra at $1 \cdot 10^{-6}$ mbar) the same Mn2p relative shift is observed in O 1s, shifting ≈ 0.2 eV towards lower BE, demonstrating the developing of an oxidized structure respect to the one obtained in the lower oxygen pressure regimen, $1 \cdot 10^{-8}$ mbars. In both cases, the components proportion changes being more prominent the one positioned at lower binding energy, 529.5 eV, corresponding to $Mn^{+3} - O$ phase. For sample grown in atomic oxygen atmosphere, the full O 1s spectra shifts around 0.4 eV towards lower BE, in fully agreement with Mn 2p previously observed one. The component attributed to $O - Mn^{+2}$ disappears, in concordance with previously Mn 2p analysis, and the one assigned to $O - Mn^{+3}$ state becomes prominent.

The assessment of oxide nature is further confirmed by the analysis of the Mn 3s core level. In Figure 6.5, the corresponding Mn 3s core levels are explored. While the s core level typically lacks spin splitting, Mn 3s exhibits two peaks, as evident in the figure. As mentioned in the introduction to this chapter, the exchange splitting of Mn 3s arises from its interaction with the Mn 3d spin after photoemission, differing for each electronic configuration. Indeed, the magnitude of the multiplet splitting (ΔE) relates to the oxidation state where a higher splitting corresponds to a lower oxidation state in the Mn-based phase. The measured value for Mn/Ag(001) is

4.1 eV, as indicated in the black spectra, consistent with previous reported values assigned to metallic Mn.[274] For the sample prepared under $1 \cdot 10^{-8}$ mbar, presented in red, the obtained value is 6.0 eV, aligning with both calculated[250] and measured [257, 272] values for MnO 3s splitting, all falling within the range of 5.8 - 6.15 eV. This value is regarded as the highest among MnOx phases due to the high spin configuration of the Mn^{+2} ion with $S_{3d} = 5/2$. With an increase in pressure and a higher contribution of Mn^{+3} state relative to Mn^{+2}, a reduction in splitting strength is expected due to the higher oxidation states. Accordingly, the exchange splitting decreases to 5.0 and 5.2 eV for layers grown at oxygen pressures of $1 \cdot 10^{-6}$ (blue) and $1 \cdot 10^{-4}$ (green) mbar, respectively. These values suggest the formation of either Mn_3O_4 or Mn_2O_3 structures[250, 257, 272]. Since the prior analysis of Mn 2p indicates a higher probability of the Mn_3O_4 phase, we assign it as such. The calculated Mn 3s orbital splitting for the sample grown in an atomic oxygen atmosphere, violet spectra, is 4.9 eV, consistent with previous assignments to the Mn_2O_3 structure.[295]

In summary, the chemical composition of MnOx phases exhibits a strong dependency on oxygen pressure, revealing a clear trend towards increased oxidation states with higher oxygen pressures. Under applied methodology in UHV, MnO (+2) phase results in the low pressure range, $1 \cdot 10^{-8}$ mbar, while Mn_3O_4 (+2, +3) emerges as the most oxidized structure using molecular oxygen which leads to saturation of this phase at or above pressures of $1 \cdot 10^{-6}$ mbar. To attain even higher degrees of oxidation, employing a more potent oxidizing agent, such as a microwave plasma atomic oxygen source, becomes necessary. This latter approach facilitates the formation of Mn_2O_3 (+3). So, XPS characterization underscores the significance of fine-tuning either the pressure or nature of the oxidizing agent, as it dictates the growth of distinct MnOx layers on a clean, ordered, and flat Ag(001) surface at room temperature.

Film thickness role

Another interesting phenomenon to be studied is the influence of oxide thickness. It is well known that the properties of metal oxides are significantly dependent on the thickness of the as-deposited layer, resulting in alterations to its chemical composition and structure.[258] By tracking chemical composition with layer thickness, our primary objective is to elucidate the underlying growth mechanisms that govern the formation of the two attained structures: MnO and Mn_3O_4.

In this study, we replicate the previously described growth conditions, utilizing molecular oxygen as the sole oxidizing agent, to investigate the effects of varying layer thicknesses within two distinct pressure ranges ($1 \cdot 10^{-8}$ and $1 \cdot 10^{-6}$ mbar). The thickness of the deposited layers has been controlled by the evaporation duration. By prolonging the evaporation time, each duration has been ascribed and assigned to the corresponding thickness range. The samples are renamed as sub-monolayer (subML), monolayer (ML), multilayer (MultiL), and thick layer (ThickL) regimes.

The investigation into the chemical composition of the grown oxides was conducted utilizing non monochromatic Al kX Ray source as well as synchrotron radia-

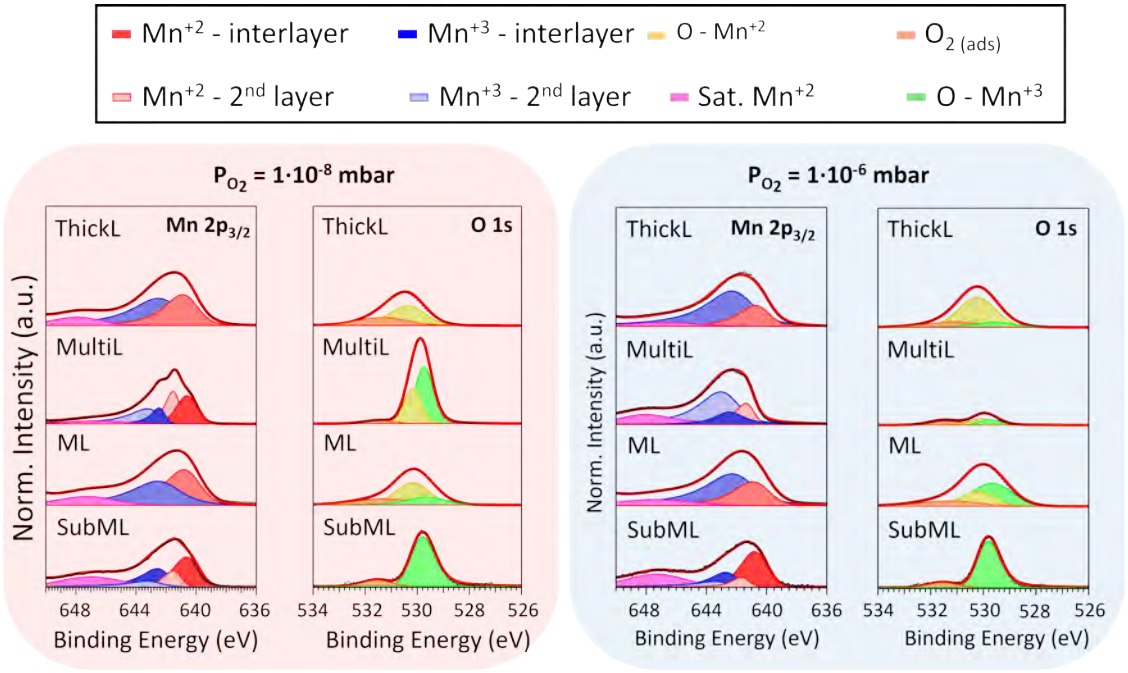

Figure 6.6: XPS study of the chemical composition of manganese oxide layers deposited with variable molecular oxygen partial pressure of (left) 10^{-8} mbar and (right) 10^{-6} mbar with variable thickness from sub-monolayer to thick layers regimen. XPS deconvoluted spectres at $Mn2p_{3/2}$ and O 1s core levels of manganese oxides.

tion at the Swiss Light Source Synchrotron facilities (at the PEARL beamline) with a photon energy $h\nu$=840 eV. Figure 6.6 provides a summary of the photoemission spectra obtained for the $Mn2p_{3/2}$ (left) and O 1s (right) core levels, acquired for the samples grown under $1{\cdot}10^{-8}$ mbar (Figure 6.6a) and $1{\cdot}10^{-6}$ mbar (Figure 6.6b). The shape of the deconvoluted peaks for Mn $2p_{3/2}$ and O 1s remains largely unchanged, except for spectra acquired using synchrotron radiation. As outlined in Section 3, synchrotron X-Ray source allows for tuneable and high energy resolution in the photoelectron spectrum. Consequently, each metallic component can be resolved into two different components, allowing for the distinction between surface and bulk influences. As depicted in Figure 6.6, all Mn $2p_{3/2}$ core level spectra exhibit the same normalized height to 1 for improved comparison, alongside the normalization of O 1s spectra with respect to Mn 2p. Both peaks are presented subsequent to subtracting a Shirley background.

The Mn $2p_{3/2}$ and O 1s spectra exhibit intriguing similarities in the sub-monolayer (subML) regime, bottom row of Figure 6.6a and b, for both structures obtained in different pressure regimens, at $1{\cdot}10^{-8}$ mbar and at $1{\cdot}10^{-6}$ mbar, respectively. These spectra present a prominent peak at 640.5 eV and a smaller peak at 642.4 eV, differing by 1.9 eV in binding energy. These peaks correspond to distinct manganese oxidation states of Mn^{+2} and Mn^{+3}, respectively, as previously determined. Indeed, employing synchrotron radiation for characterization enables the detection of components with remarkable surface resolution. Within this framework, two additional components (light blue and red colors) emerge around 641.4 and 643.1 eV, albeit no-

tably smaller than their predecessors (dark blue and red colors). Following the idea of a layer-by-layer growth model, surface species in the Ag-oxide interlayer would predominate in the subML regime compared to second layer formation. Accordingly, the dark red and blue components are ascribed to Mn^{+2} and Mn^{+3} states in the Ag-oxide buffer layer, while the lighter components correspond to the subsequent formed layer. Remarkably, both layers exhibit identical Mn^{2+} and Mn^{3+} ratios.

The O 1s peak comprises same three components previously analyzed: the one at higher BE, 531.6 eV, and two additional ones linked to oxygen atoms in different coordination environments with manganese ($O - Mn^{+2}$ and $O - Mn^{+3}$). The dominant influence in both cases is the $O - Mn^{2+}$. However the influence of $O - Mn^{+2}$ in the layer increase with the oxygen pressure applied, being increased in the structure grown at $1 \cdot 10^{-6}$ mbar. The deconvolution of both peaks, Mn $2p_{3/2}$ and O 1s, confirm that the chemical composition of both structures in the subML regime is the same.

Analyzing low oxygen pressure regimen, $1 \cdot 10^{-8}$ mbar in Fig. 6.6, reveals that as thickness transitions from subML to MultiL, the Mn^{2+}/Mn^{+3} ratio remains consistent. In the MultiL regimen, the components attributed to the second layer (light red and blue components) increases being predominant and corroborating a layer-by-layer growth mode. Conversely, when a thicker layer is grown, the peak exhibits an equal proportion of Mn^{+2} and Mn^{+3}, suggesting a higher oxidized structure attributed to Mn_3O_4, as depicted in the ML raw. If we pay attention to O 1s profile, the same 3 components ($O_{2(ads)}$, $O - Mn^{+2}$ and $O - Mn^{+3}$) discussed before are present in all cases with similar component influence.

In the case of growing MnOx structures in a higher oxygen pressure regimen, $1 \cdot 10^{-6}$ mbar in Fig. 6.6, an enrichment in the Mn^{+3} state is observed as thickness transitions from subML to MultiL. This transition underscores the significant interplay between molecular oxygen pressure and thickness in the growth mechanism. As thickness progresses to MultiL and ThickL, the component ratios remain unaltered. In the MultiL spectra, where surface sensitivity is attained, the Mn^{+2} Ag-MnOx interlayer component disappears, concomitant with an increase in second layer components (light red and blue components). This fact together with previous assignments in the SubML phases, suggests the existence of an MnO structure as a wetting layer in the Ag-MnOx interface, which with the pressure and time gap evolves in a higher oxidized structure. Concerning O 1s spectra, no significant differences are observed related to the layer's thickness.

In conclusion, the chemical composition of MnOx structures is not only influenced by the oxidizing agent but also strongly correlates with the thickness of the sample. The investigation reveals that in the initial stage of oxide deposition, a consistent inter-layer is observed across two distinct pressure ranges, indicating the presence of a phase enriched in MnO as the wetting layer. This observation aligns with the structural properties of bulk Mn_3O_4, which features a unit cell height of 942 pm consisting of 8 sublayers compared to the MnO structure with a unit cell height of 444 pm. As the sample thickness increases from single-layer to thicker layers, additional layers of atoms contribute to the XPS and denotes a layer-by-layer growth mode. This increase in thickness provides more opportunities for interlayer

interactions, diffusion processes, and nucleation events, thereby influencing the evolution of the oxide structure. It is noteworthy that under the same oxygen pressure, thicker films tend to exhibit higher oxidative states due to the accumulation of oxygen atoms within the film's bulk. Hence, both oxygen pressure and film thickness emerge as critical parameters that must be meticulously controlled to dictate the resulting oxide structure. This underscores the intricate interplay between growth conditions and material properties, highlighting the necessity for precise control over experimental parameters in oxide thin film deposition processes.

6.2.3 Surface structure of manganese oxides phases

In this section, we shift our focus on investigating the surface structure of the as-grown manganese-based phases. The surface structure of the oxides has been analyzed using LEED and various scanning probe microscopy techniques, including LT-STM and AFM. The primary aim of these investigations is to identify correlations between the surface structure and the chemical stoichiometry elucidated in the preceding section.

Initial LEED investigations of the as-prepared film samples revealed a lack of crystalline order, indicated by the absence of LEED reconstruction. These results demonstrated that, at room temperature, the manganese oxides grow without a well-defined crystal structure. Since temperature can facilitate surface atomic ion diffusion and oxygen dissociation, we explored a new growth parameter: the influence of temperature on crystal structure order. By maintaining the substrate temperature at 100^oC or 200^oC during the deposition of Mn in an oxygen atmosphere, we obtained diffusive LEED structures.

An alternative approach involves performing a post-annealing step. Although Mn and Ag tend to form an alloy upon surface annealing in UHV, the prior formation of MnOx prevents further alloying with Ag, even at annealing temperatures up to 700 K[257]. However, post-annealing in UHV can provoke the reduction of oxides, as observed in the case of TiO_2[296]. The decomposition of the oxide depends on its thermal stability and atomic restructuring. Therefore, before conducting surface structure characterization, the chemical composition was verified using XPS. Obtained spectres confirmed that temperature does not induce significant changes in the chemical composition of the oxide layers. No notable differences were observed in the Mn 2p, O 1s, and Mn 3s spectra of samples before and after annealing, corroborating the same chemical composition presented in the preceding section. This ruled out the reduction and decomposition of oxides. Next, we will use LEED characterization to determine if atomic restructuring occurs after annealing samples at 200^oC.

Figure 6.7 showcases LEED patterns obtained at 65 eV for pristine Ag(001) substrate (a), and for the post-annealed oxides surfaces (prepared at $1 \cdot 10^{-8}$, $1 \cdot 10^{-6}$ and $1 \cdot 10^{-4}$ mbar O_2 atmosphere and $5 \cdot 10^{-5}$ mbar atomic oxygen). Figure 6.7b illustrates the LEED image of the MnO/Ag(001) phase grown under an oxygen molecular pressure of $1 \cdot 10^{-8}$ mbar. Here, a (1×1) pattern is observed with a comparable background intensity but less defined spots compared to clean Ag(001), suggesting smaller domains of long-range ordering. Nonetheless, the fourfold symmetry remains

intact, indicating in-plane lattice-matched growth with a slightly different calculated lattice parameter, a_{MnO}=4.42 Å, as indicated by the red square. This result aligns with the lattice mismatch of approximately 9 % in the MnO/Ag(001) structure, supporting the growth of a commensurate MnO(001) structure [260, 297].

For the Mn_3O_4/Ag(001) phase grown under higher oxygen pressures, $1 \cdot 10^{-6}$ and $1 \cdot 10^{-4}$ mbar) (Figures 6.7c and d, respectively) exhibits a p(2×1) superstructure, with a surface lattice parameter of 5.75 Å, nearly double than that of the Ag(001) surface lattice. The film main directions align along the $<$ 110 $>$ and $<$ 1-10 $>$ substrate directions, presenting two domains, indicated by blue and yellow rectangles, rotated by 90º due to the fourfold symmetry of the Ag(001) substrate. This structure is consistent with the sub-layer model of Mn_3O_4(001) on Ag(001), where a mixed manganese-oxygen island forms at the interface with the substrate[251, 257].

Finally, the structure achieved under the atomic oxygen atmosphere (Fig. 6.7f) exhibits symmetric LEED pattern spots arranged in two hexagonal domains rotated by 25 ºC, forming concentric rings with measured surface parameters of a = 9.6 Å, b = 9.6 Å, and c = 9.7 Å. The hexagonal structure aligns along the $<$ 110 $>$ and $<1-10>$ directions of the substrate, whose lattice vectors are rotated by 45º relative to the Ag(001) substrate. This structure is attributed to α-Mn_2O_3 since it possess a rhombohedral crystal structure with similar lattice parameters.

Therefore, a post-annealing step is necessary to achieve high crystalline order in MnOx phases with varying chemical compositions.In conclusion, based on the cumulative evidence gathered thus far, we have successfully achieved the primary objective of this chapter: the development of a model catalytic system, MnOx, whose chemical and structural properties can be precisely controlled through the deliberate adjustment of various growth parameters, including oxidizing atmosphere pressure and nature, thickness and time, and temperature (either substrate temperature and post-annealing treatment). This tailored MnOx system is an ideal candidate for investigating structure-function relationships.

Atomic structure of thin-film manganese oxides

Through LEED characterization, the resulting pattern emerges as the incoherent sum of the diffraction patterns associated with individual domains, effectively yielding an average pattern over a large mesoscale area. To overcome this limitation, a technique with atomic resolution, such as LT-STM, is employed to resolve the existence of different domains and reveal the distribution of various oxide phases previously hypothesized through high-resolution surface analysis by XPS. Furthermore, in this case, STM is utilized to determine the growth mode and the size of oxide islands formed on the Ag(001) substrate.

Thus, complementary low-temperature STM images of MnO (Figure **??**) and Mn_3O_4 (Figure 6.9) structures on Ag(001), with thicknesses within the subML regime, were measured. The dataset presented below was acquired at the PEARL beamline of the Paul Scherrer Institute and corresponds to samples grown in the subML regimen (XPS characterization shown in Fig. 6.6)

Figure 6.8a shows a representative image of the MnO phase. The contour plot reveals that MnO growth occurs through two distinct typology of layers, the one

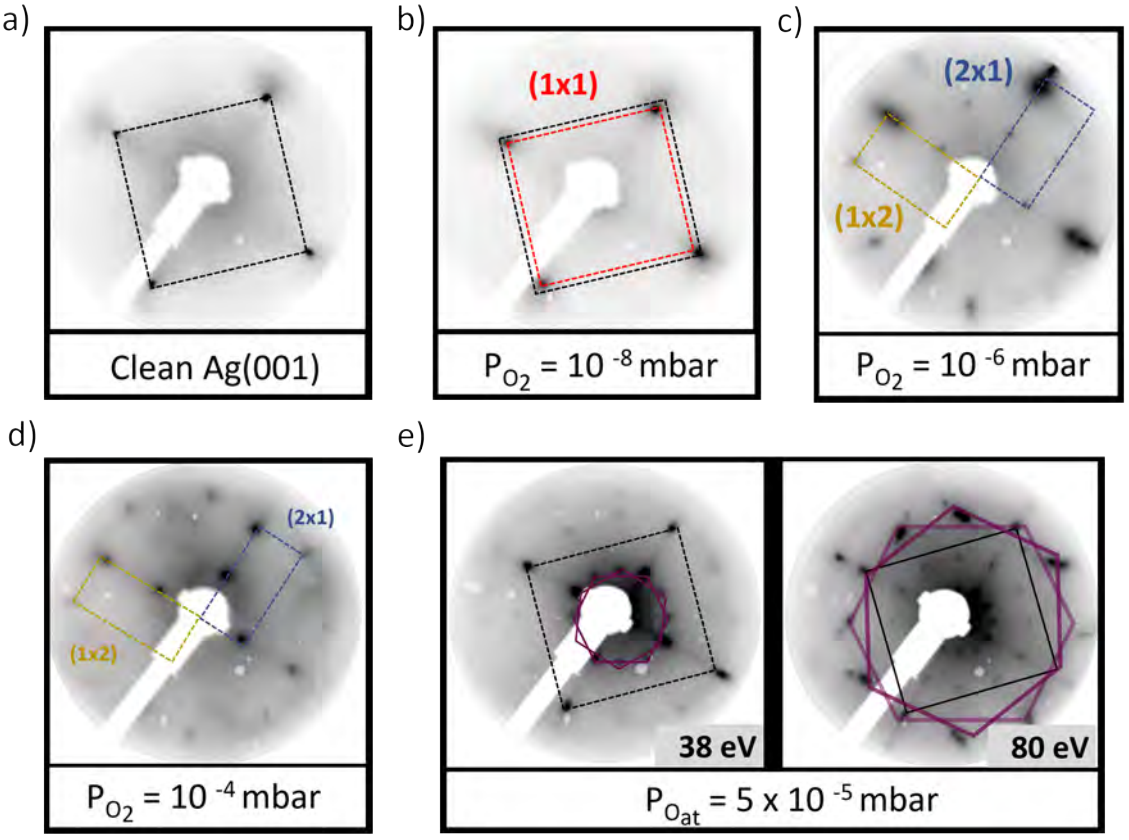

Figure 6.7: LEED patterns measured at 65 eV of a) pristine Ag(001), post-annealed manganese oxide structures grown at room temperature in a molecular oxygen partial pressure of b)10^{-8} mbar, c)10^{-6} mbar, d)10^{-4} mbar. And (e) LEED images taken at 38 and 80 eV of manganese oxide structure grown at room temperature in an atomic oxygen partial pressure of $5x10^{-5}$ mbar.

highlighted in black and the three-dimensional islands, corroborating the earlier statement made through high-resolution XPS analysis of samples with varying thickness where layer by layer growth was pointed out. By analyzing the number of items, it can be extracted that the average height of the different islands observed is $\approx$ 4 Å(see Fig. 6.8d). This value matches with the expected height value for bulk MnO crystal structure, with its crystallographic parameter $a_{MnO} = 4.445$ Å.

To analyze the wetting layer mode of growth, as well as the size and shape of the islands, a close-up image around the island highlighted in green (Fig. 6.8a) is presented in Figure 6.8b. Here, it is observed that the majority of islands (around 90 % of substrate surface), highlighted in pink, adopt a three-dimensional cubic shape. The second type of island, like the one highlighted in green, is observed beneath the three-dimensional ones, acting as a wetting layer characterized by elongation and smoothness borders without a defined shape. These bi-dimensional MnO islands appear in about a 10 % of the surface and presents a height of $\approx$ 2 Å and a length of around 35 nm as shows the profile image in Fig. 6.8e. Computing bi-dimensional island length over the sample it is estimated an average length comprised from 20 to 40 nm.

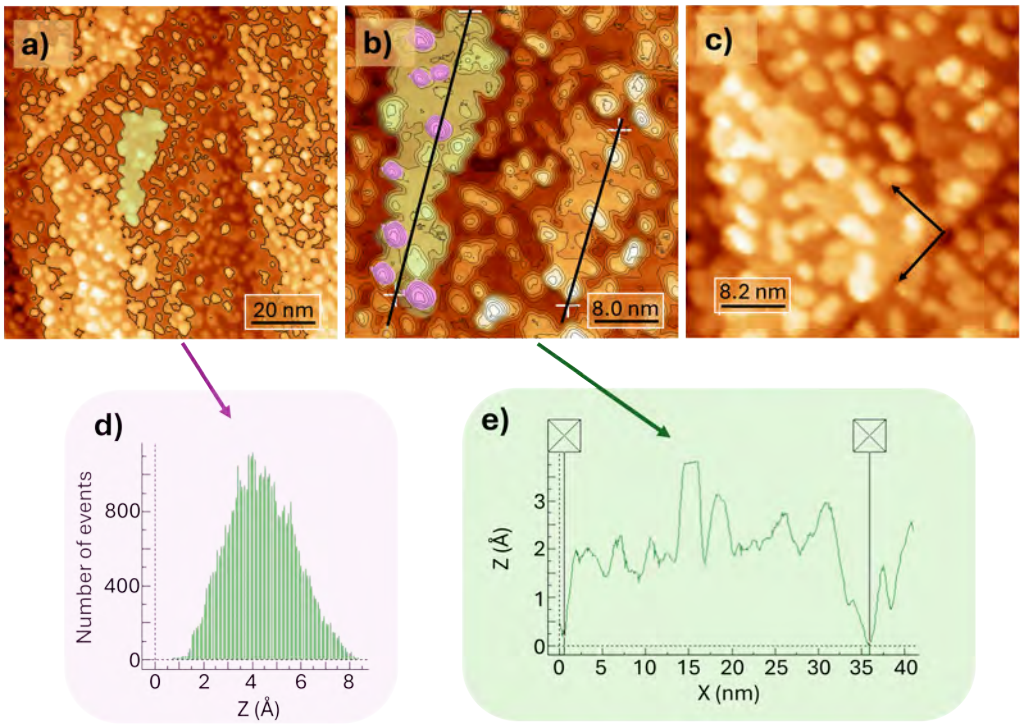

Figure 6.8: STM images of ultrathin MnO film on Ag(001) acquired at 2 V, 10-30 nA with different sizes: a) 100 x 100 nm^2, b) Close up of the island marked in (a) being 40 x 40 nm^2, and c) 41 x 41 nm^2. d) Profiles of the number of items present in a). e) Height profile of the island highlighted in green in b). The STM images were processed with the WSxM software [298].

Moreover, Figure 6.8c depicts what seems to be square Ag(001) terraces, highlighted with black arrows, where the bi-dimensional layer tends to nucleate and grow, indicating possible growth with its edges along the <110> directions of the Ag(001) substrate.

Figure 6.9 showcases the initial stage of Mn_3O_4 film growth. In Fig. 6.9, two distinct phases are observed: (i) a predominant two-dimensional phase in the form of quasi-rectangular strips, acting as a wetting layer (outlined in black), and (ii) a disordered three-dimensional phase. Upon analyzing the number of items the average height of the observed three-dimensional islands is approximately 6 Å(see Fig. 6.9c), which aligns with the expected value for bulk Mn_3O_4, where the crystallographic parameter $a_{Mn_3O_4}$=5.76 Å.

A magnified image within the previous region, presented in Fig. 6.9b, reveals that the ordered wetting layer forms large islands with sharp, square edges, as indicated by the arrows, and rectangular shapes. A second set of three-dimensional islands is also observed, displaying varied shapes: triangular (highlighted in pink) and rectangular (highlighted in blue). The profile for the triangular island is shown in Fig. 6.9d, revealing a height of around 4 Åand a length of 6 nm.

It is noteworthy that the growth of MnOx begins with a two-dimensional premonolayer that acts as a wetting layer in both phases. For MnO, well-defined

and consistent three-dimensional islands dominate the sample, typically exhibiting square shapes and lattice parameters closely matching those of bulk MnO. In the case of Mn_3O_4, the two-dimensional layer predominates, characterized by square edges and rectangular shapes, while the three-dimensional islands observed show no distinct or well-defined shapes.

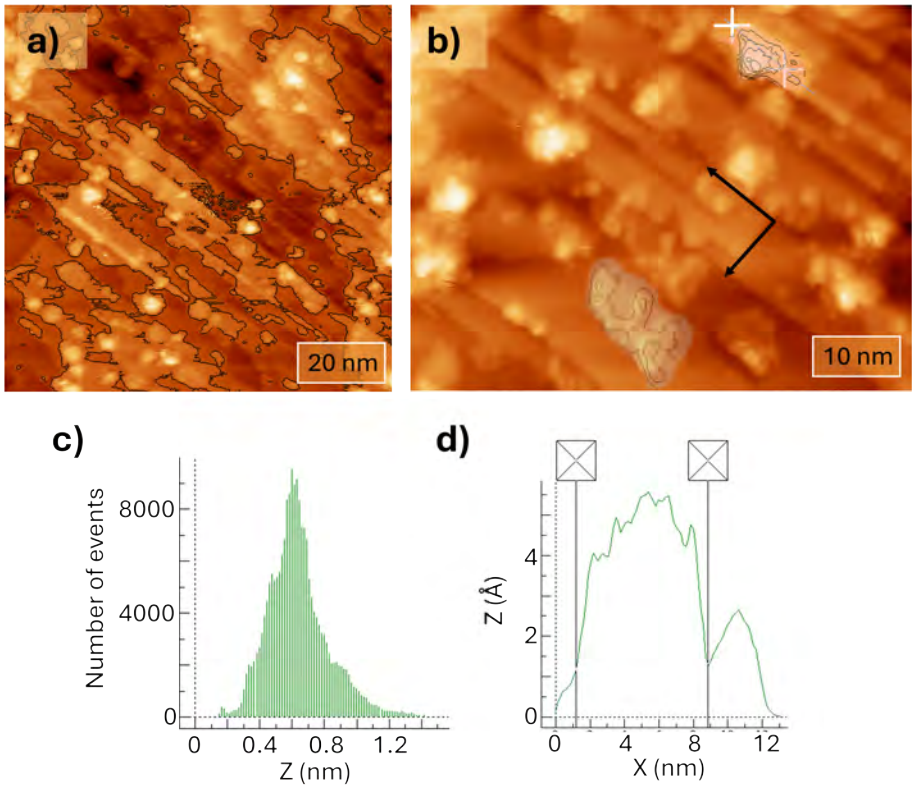

Figure 6.9: STM images of ultrathin Mn_3O_4 film on Ag(001) acquired at 2 V, 10-30 nA with different sizes: a) 100 x 100 nm^2, b) Close up of the island marked in (a) being 50 x 50 nm^2. c) Profile of the number of items present in a). d) Height profile of the island highlighted in pink in b). STM images were analyzed by using the WSxM software [298].

The morphology of multilayer-thick MnOx phases was characterized by AFM under ambient conditions (in air at room temperature). Figure 6.10 presents representative AFM images of MnO (top) and Mn_3O_4 (bottom) multilayer structures on an Ag(001) substrate, grown at $1 \cdot 10^{-8}$ mbar and $1 \cdot 10^{-6}$ mbar, respectively.

MnO (Fig. 6.10a) reveals distinct crystalline islands formed on the Ag(001) substrate, with a noticeable preference for edge terrace locations. A closer examination via a 2 x 2 μm^2 image (Fig. 6.10b) shows a homogeneous distribution of these islands. The height profile, measured along the marked green line and presented in Fig. 6.10, indicates consistent island heights, each measuring approximately 4 Å, consistent with previous observations from LT-STM.

AFM images of Mn_3O_4 phases within the same thickness range are shown in Fig. 6.10c and d. Large-scale images reveal relatively smooth layers composed of small crystals, as confirmed by the zoomed-in image in Fig. 6.10d and the green inset.

The observed morphology closely aligns with the predominance of a two-dimensional layer rather than three-dimensional islands.

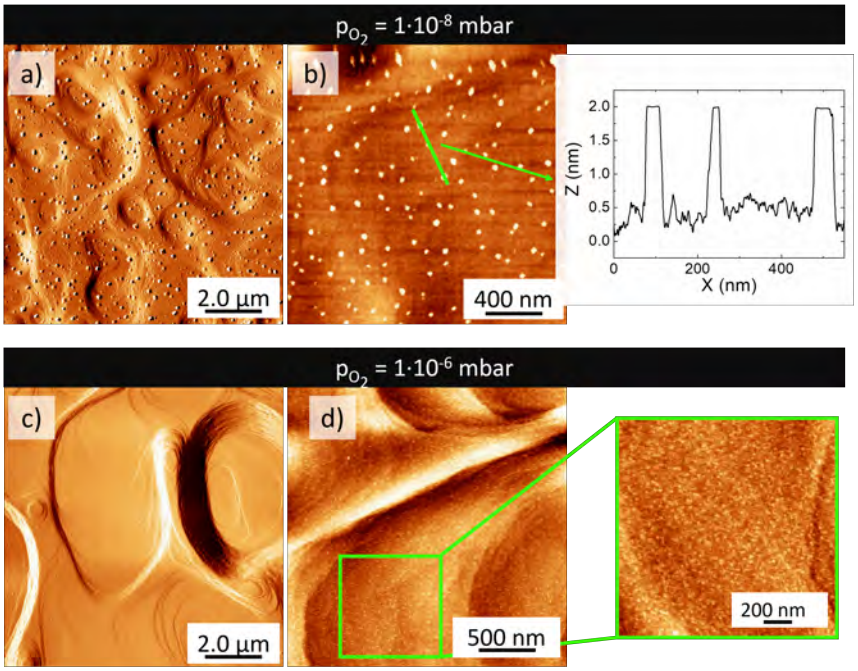

Figure 6.10: AFM images of multilayer-thick MnO (top) and Mn_3O_4 (bottom) phases on an Ag(001) substrate. (a) 10 x 10 μm^2 and (b) 2 x 2 μm^2 images, with an inset showing the height profile measured along the marked line for MnO islands. (c) 10 x 10 μm^2 and (d) 2.5 x 2.5 μm^2 images, with an inset corresponding to a 1 x 1 μm^2 area to highlight the surface roughness of the Mn_3O_4 sample. The AFM images were processed using WSxM software [298].

In summary, the surface structure analysis performed on thick layers confirmed a preferred growth in a three-dimensional islands for the MnO phase, with a higher surface/area ratio, while Mn_3O_4 grows in a preferred two-dimensional form with ordered and homogeneous layers.

6.2.4 Electronic structure of manganese oxides phases

Following the comprehensive characterization of surface structure and morphology, we now turn to electronic structure investigations using XPS with synchrotron radiation. Our goal is to analyze the surface valence band (VB) of both MnOx phases, MnO and Mn_3O_4, across two distinct thickness ranges: sub-monolayer and multilayer, using the same samples previously discussed.

Figure 6.11 presents the surface VB spectra of the samples measured with a photon energy of 200 eV. We compare the clean Ag(001) substrate (black), the Mn/Ag(001) sample (grey), and both sub-monolayer (dashed line) and multilayer (solid line) thicknesses for the MnO (red) and Mn_3O_4 (blue) phases.

The VB spectra unveil distinct electronic signatures for the clean Ag(001) substrate and Mn/Ag(001) sample. In the case of the Ag substrate, represented by the

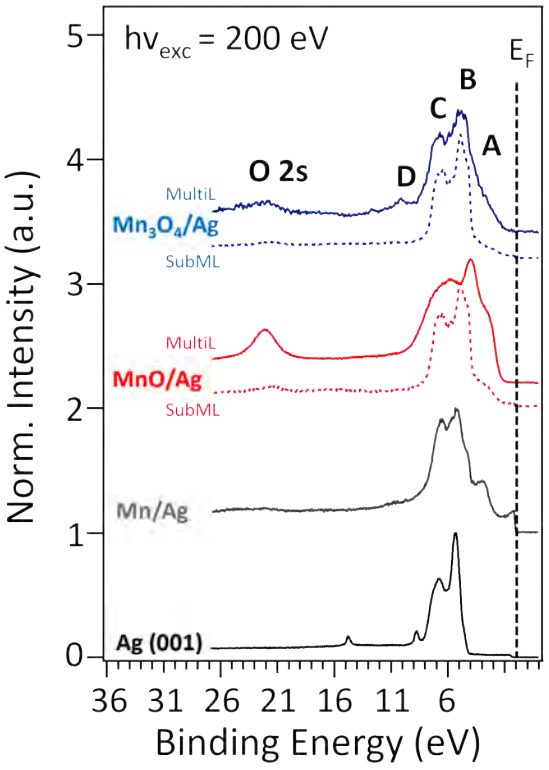

Figure 6.11: Valence band spectra of the clean Ag(001) substrate (black), the Mn/Ag(001) layer (grey) and both manganese oxide structures, MnO (red) and Mn_3O_4 (blue), in two different thickness range, sub-monolayer (dashed line) and multi-layer (continuous line). The binding energy of spectras can be precisely aligned with the Fermi edge of the silver substrate.

black line, two prominent features within the Ag 4d-band region are observed, with maxima located around 5.3 (B) and 6.8 eV (C). Transitioning to the Mn/Ag(001) sample, the VB spectrum manifests notable alterations. A sharp peak labeled B emerges at approximately 5.3 eV, accompanied by a lower-energy shoulder labeled A at 3.5 eV. Additionally, a second peak labeled C arises at around 6.8 eV, along with a small high-binding energy satellite, D, positioned above the Ag 4d band at 11.1 eV. These shifts in peak locations and the presence of satellite bands denote electronic changes induced by the presence of Mn, resulting in a discernible upward shift in the full d-band center compared to pure Ag. Notably, there is no discernible influence of residual oxygen in the O 2s region.

Moving to the discussion on MnOx phases, one anticipates the spectrum to mirror the reduction in the number of Mn 3d electrons involved in bonding, transitioning from Mn^{+2} (formally d^5) to Mn^{+3} (formally d^4). One also expects the outer-valence band region (2-10 eV) to exhibit predominantly O 2p features at higher binding energy and Mn 3d features at lower binding energy. However, direct observation of valence band changes in ultrathin MnOx phases via XPS is challenging due to the masking effect of Ag 4d maxima bands, especially at very low film thicknesses (indicated by dashed lines). Moreover, in the sub-monolayer regime, the silver's Fermi

level is observable, suggesting that the manganese oxide layer is thin enough for the electronic properties of silver to dominate or blend with those of the manganese oxide. Conversely, in the multilayer regime, the Fermi level of silver is not visible, indicating that the manganese oxide has reached a sufficient thickness to obscure the underlying silver's properties.

Assessing the impact of manganese oxidation on the valence band involves comparing the multilayer thickness regime of MnO/Ag and Mn_3O_4/Ag. Within the 3d multiplet structure, overlapping with O 2p states between 2 and 12 eV below the Fermi level (E_f), a noticeable redistribution of intensity is observed among MnOx-based layers, correlating with the degree of oxidation. This redistribution coincides with an escalation in the intensity of feature D, often linked to Mn vacancies at the MnOx surface or non-local contributions [299]. Non-local contributions stem from charge transfers between the coordinating ligand sphere and the metal atom or more extensive charge redistributions, potentially more pronounced in defect-free films or films with larger ordering domains. Furthermore, alterations in the O 2s photoemission line, typically noted around 22.3 eV, display variations in both shape and intensity, particularly evident in Mn_3O_4/Ag samples. These findings are consistent with previous investigations into MnO and Mn_3O_4 [300][268][259], underscoring the reliability of our results.

6.3 Manganese oxide growth on Au(111) substrate

As outlined in the introduction of this chapter, thin MnOx layers catalysts have demonstrated superior efficiency compared to bulk materials. Hence, the primary objective of this study was to evaluate the electrochemical macroscopic response of different MnOx thin films phases on Ag(001) against OER reaction. However, contrary to our preliminary assumptions, MnOx phases do not grow homogeneously exposing the substrate to applied electrochemical conditions. Despite the extensive use of silver electrodes in various electrochemical investigations, this substrate is not a good catalyst for OER[301]. Specifically, silver is thermodynamically unstable at potentials exceeding 0.4 V across the entire pH spectrum, as elucidated by its Pourbaix diagram[77]. Therefore, Ag undergoes oxidation at potentials lower than the anticipated onset of MnOx catalytic activity.[301] This leads to the occurrence of two competitive processes, complicating the accurate analysis of catalyst activity and hindering proper attributions of surface chemical composition. Consequently, a new substrate must be explored to overcome the issue of silver oxidation influence on the OER mechanism.

Au(111) stands out as a promising alternative to Ag(001) due to its noble nature and relative inactivity until relatively high anodic potentials, specifically in the range of 1.8 - 2.1 V in acidic media, as previously elucidated in Chapter 5. This inherent resistance of gold to oxidation up to 1.8 V under the performed study suggests its potential utility as a substrate for the deposition of more catalytically active MnOx layers. Moreover, employing this MnOx/Au(111) as catalyst could potentially reduce the overpotential associated with OER on Au(111) substrates. Because of that our attention shifts to investigating the growth of MnOx phases on Au(111)

surfaces.

To transfer the growth of MnOx phases from the Ag(001) substrate onto Au(111), we used the same methodology described in the previous section, which led to successful growth in terms of different chemical, structural and electronic properties. We focused on phases generated under molecular oxygen atmosphere.

6.3.1 MnOx/Au(111) composition

In order to probe whether the substrate nature influences the chemical composition of deposited layers, various MnOx phases were examined using XPS analysis. Before delving into the results, it is important to note that there is a significant overlap between the most prominent gold core level region, Au 4f (typically found between 84 – 88 eV), and the Mn 3s core level peak (previously detected within the range of 78 – 92 eV), making the precise assessment of the Mn 3s multiplet distance challenging. As a result, only the Mn 2p region will be utilized in this instance to ascertain the primary oxidation state of the freshly prepared thin film. Additionally, it's worth mentioning the faint $Au4p_{1/2}$ core level peak (approximately at 643 eV), coinciding with the Mn 2p region which influence will not be presented.

Figure 6.12 shows the convoluted Mn 2p and O 1s core levels acquired via XPS for different Mn evaporation conditions: under UHV, under molecular oxygen pressure of $1 \cdot 10^{-8}$ mbar, and $1 \cdot 10^{-6}$ mbar. The O 1s lines were normalized to Mn levels.

The upper spectrum of Fig. 6.12 displays the Mn 2p core level spectra for Mn deposited under UHV conditions. The main contribution to the Mn 2p core level originates from the Mn^0 component, centered at 639.4 eV, consistent with the previously characterized metallic state in Ag(001) growth (see Fig. 6.5). For samples prepared under $1 \cdot 10^{-8}$ mbar, the full Mn 2p peak shifts by 1.8 eV towards higher binding energy, with an even more pronunced shift of 2.2 eV at $1 \cdot 10^{-6}$ mbar. Fitting both Mn 2p peaks reveals same two main contributions previously obtained in Ag(001) substrate: one at 640.6 eV, attributed to Mn^{+2}, and another at 642.5 eV, attributed to Mn^{+3}. Notably, the contribution of Au to the Mn 2p core level is negligible.

In the O 1s spectra, clear peaks are observed for both oxidized structures, centered at similar BE (530.1 eV and 530.0 eV), regardless of the deposition pressure. These peaks are fitted using the same components: from lower to higher BE - $O-Mn^{+3}$, $O-Mn^{+2}$, and chemisorbed oxygen. This indicates a comparable chemical assignment for MnOx phases grown on Au(111) to that reported for Ag(001) (see Fig. 6.5): Mn in UHV, MnO at $1 \cdot 10^{-8}$ mbar, and Mn_3O_4 under $1 \cdot 10^{-6}$ mbar. The results highlight the critical role of oxidizing pressure in determining the chemical composition of MnOx structures, rather than the substrate material.

The similarities in the chemical composition of manganese oxide phases grown on different substrates (Ag(001) and Au(111)) suggest that these oxide phases form in the gas phase, further supporting an "in-flight" oxidation mechanism prior to substrate deposition. Therefore, the substrate surface does not play an active role in O_2 dissociation; this process occurs entirely in the gas phase.

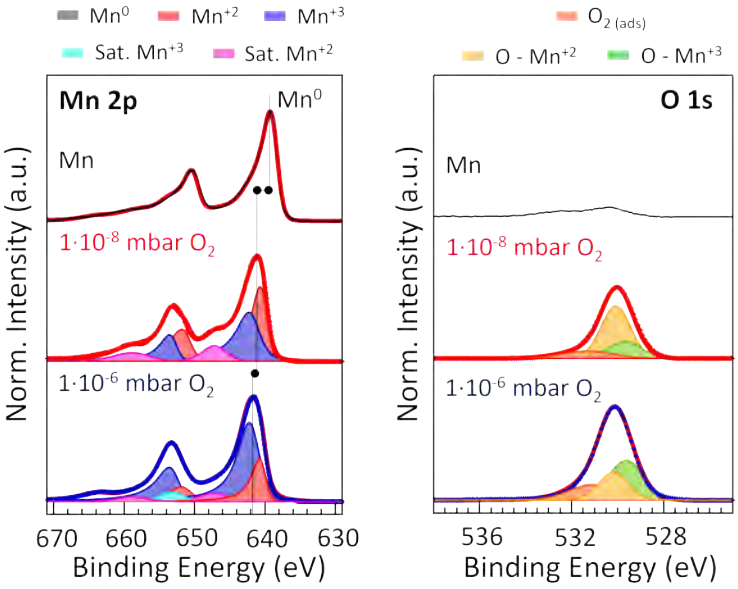

Figure 6.12: XPS spectra and fitting components at the energies of (left) Mn 2p and (right) O 1s core levels for different manganese-based oxides grown at room temperature under different oxygen partial pressure as well as oxidizing agent: (black) in absence of oxidizing agent, (red) under 10^{-8} mbar and (blue) 10^{-6} mbar molecular oxygen partial pressure.

6.3.2 Surface structure of MnOx/Au(111) phases

Now that it has been confirmed that the chemical composition of the grown oxides does not change upon substrate nature, the impact of the substrate orientation in the morphology as well as surface and electronic structure of MnOx phases needs to be checked.

To study the possible surface structural differences in the MnOx phases on Au(111), LEED and LT-STM were carried out. In Fig. 6.13, LEED patterns of Au(111) (a), Mn/Au(111) (b) and MnOx structures grown at $1 \cdot 10^8$ (c) and $1 \cdot 10^6$ mbar (d) are shown at different energies being 77 and 125 eV.

As we saw in preceding chapter, Chapter 5, an hexagonal pattern is obtained for a clean Au(111) surface which nominal unit cell is 2.87 Å. An inset of the characteristic herring-bone reconstruction is displayed in Figure 6.13a. After evaporation of Mn on the Au(111), the LEED pattern (Fig. 6.13b) reveals a diffusive hexagonal reconstruction, comprising a (1×1) structure with a unit cell approximately 15 % larger than Au(111) (as indicated in Fig. 6.13b). For the MnOx phase prepared at $1 \cdot 10^8$ mbar, two separated 12-spot rings are observable at 125 eV (see Fig. 6.13c). At a lower energy, 77 eV, the first-order located inside become prominent. A relatively diffuse pattern emerges, suggesting the formation of a discontinuous layer, such as dispersed layers on the surface or coexisting different structures. Three distinct square domains have been identified, highlighted in red, as expected from the sueprposition of a square or rectangular-based structure into a three-fold crystalline substrate as the Au(111) with three preferential directions. The film exhibits the formation of three domains rotated by 60^{o} (denoted by three squares), aligned with

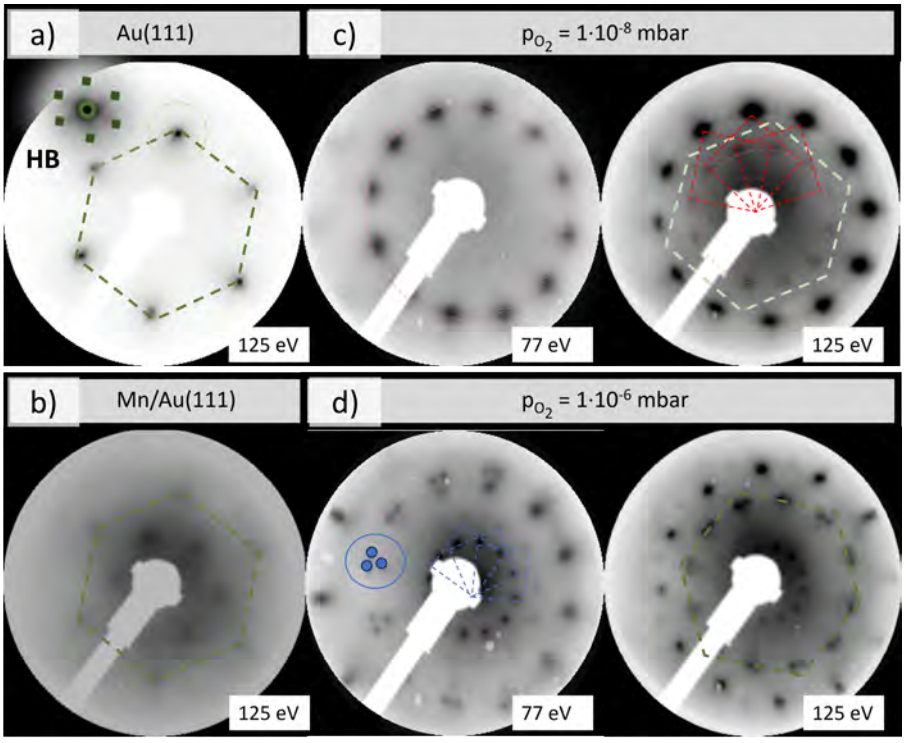

Figure 6.13: LEED patterns measured at 125 eV of a) pristine Au(111), b) Mn/Au(111), c) MnO/Au(111) and d)Mn_3O_4/Au(111). c) and d) also includes images taken at 77 eV for clarification.

the three principal hexagonal Au(111) directions. This arrangement reflects the mismatch between the film's square symmetry and the hexagonal symmetry of the substrate, allowing only this adaptable configuration. The LEED pattern confirms the diffraction pattern obtained for a MnO(001) film with a lattice parameter of approximately 0.290 nm, compared to literature values of 0.315 nm [283].

In the subsequent scenario, Mn deposition under an oxygen pressure of $1 \cdot 10^{-6}$ mbar depicted in Fig. 6.13d reveals two inner rings, clearly visible at 77 eV, comprising twelve spots divided into a three-square pattern due to the threefold domain structure typically found in a c(2×2) layer. The c(2×2) LEED pattern has been widely attributed to Mn_3O_4 (001) grown on different substrates [263, 302, 303]. In this case, this structure adapts to a (111) orientation, resulting in three different domains rotated by 60º (indicated by three blue squares), aligned with the three principal hexagonal Au(111) directions.

Further characterization of film structures was performed using LT-STM. For MnO, a uniform coverage is revealed all over the sample with a calculated coverage of around 0.6 ML. A representative image of the MnO/Au(111) is shown in Figure 6.14a. Free Au(111) surface areas, showcasing the herringbone (HB) structure ($\sqrt{3} \times 22$))-Au(111), can be observed. The islands tend to decorate the steps of the surface, as indicated by the arrow. In Fig. 6.14b, the sample exhibits macroscopic order, with preferential growth starting on the kinks of the HB reconstruction, indicated by dashed lines. The island marked with the profile line is constructed from consecutive

HB kinks, which are not visible, confirming the preferred growth mode on HB kinks and the coalescence of different islands. This island has a length of about 50 nm and a uniform height of around 4 Åwith spiked islands up to 8 Å, as depicted in the profile. The homogeneous part of the island presents the same height characterized for MnO islands grown on Ag(001) characteristic for MnO unit cell, which suggests the same oxide structure.

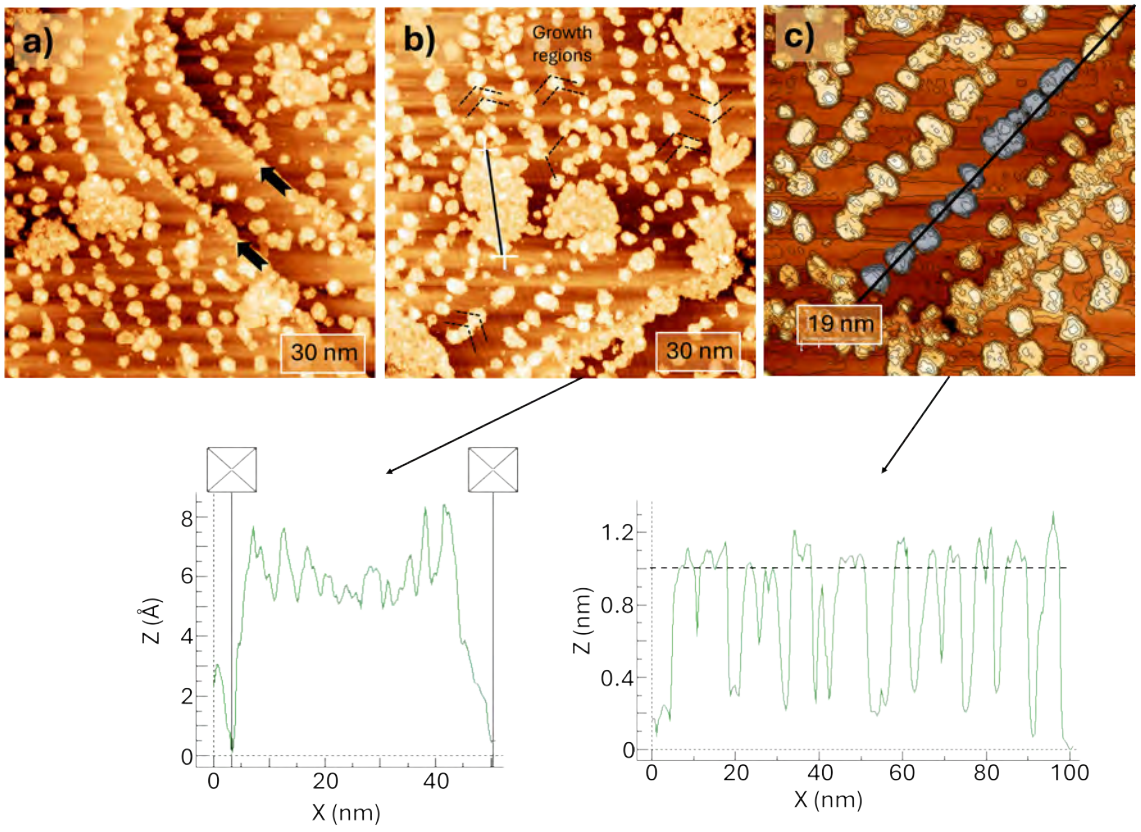

Figure 6.14: STM characterization of ultrathin MnO phase on Au(111) grown under 10^8 mbar oxygen partial pressure. a) and b) 150 x 150 nm^2 size image, 1 V, 50 - 150 pA. c) Close up image of b) being 95 x 95 nm^2. STM images were analyzed by using the WSxM software [298].

A deeper analysis of the islands was conducted in a zone with aligned islands (highlighted in blue), shown in Figure 6.14c. Here, a preferred square shape is observed with an average height of 1 nm and a length of 5 Å, as depicted in the obtained profile. Despite efforts to achieve atomic resolution, it was not accomplished.

A representative STM image for Mn_3O_4, displayed in Figure 6.15a, reveals a layer-by-layer growth as indicated the contour plot, differentiating two layers: the wetting layer or first layer (indicated in green) and the second layer (indicated in blue). A high coverage is observed, being computed around 0.8 ML, and this impedes to see the Au(111) substrate clearly to distinguish whether it growth on the edge of the terraces. The analysis of number of items height, Fig. 6.15a.i, suggests an average height about 2 - 4 Å.

To a better analysis of the growth and characteristics of the islands, a close-up

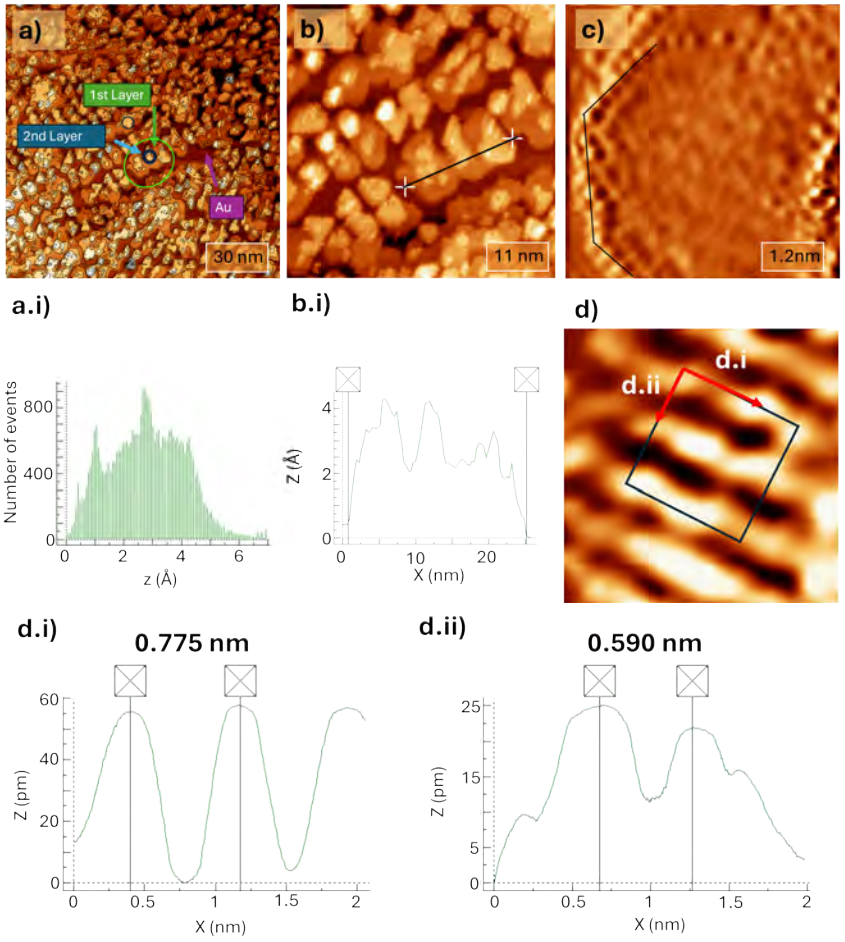

Figure 6.15: STM characterization of ultrathin Mn_3O_4 phase on Au(111) grown under $1 \cdot 10^6$ mbar oxygen partial pressure. a) 150 x 150 nm^2, b) 55 x 55 nm^2 and c) 6 x 6 nm^2 size images and d) atomic resolution image, 1 V, 50 - 150 pA. a.i) Profile obtained in the number of events analysis made in a. b.1) Height profile of the islands indicated in b. d.i and d.ii indicated the unit cell distances. The STM images were processed with the WSxM software [298].

image is presented in Figure 6.15b. Triangular shape islands are identified growing in two different layers where the wetting layer is perceived to be more ordered (as we will see later) and the upper layer is partially disordered. The profile obtained and shown in Fig. 6.15b.i the second layer presents around 10 nm of length and the wetting layer coalesce forming up to 25 nm length islands, each with an average height of 2 Å. Here, we have zoom in in a representative island and is depicted in Figure 6.15c. It can be appreciated three different growth domains indicated by black lines, confirming the growth on the three directions.

In Figure 6.15d it is presented the obtained image where we can appreciate the different atomic rows. With a further analysis, we can appreciate an square net which profile analysis in Fig. 6.15d.i and d.ii points out an stripped pattern with distances of 0.775 and 0.590 nm, respectively. These atomic-scale features observed by STM can be elucidated by an ideal bulk-truncated Mn_3O_4 with parameters of

a=0.576 nm and b=0.949 nm.

6.3.3 Electronic structure of MnOx/Au(111) phases

After STM characterization, we now check electronic structure. Figure 6.16 presents VB spectra of clean Au(111) substrate (black), Mn/Au(111) sample (grey), and sub-monolayer (dashed line) as well as multilayer (solid line) thickness samples of MnO (red) and Mn_3O_4 (blue) phases. A photon energy of 200 eV was used.

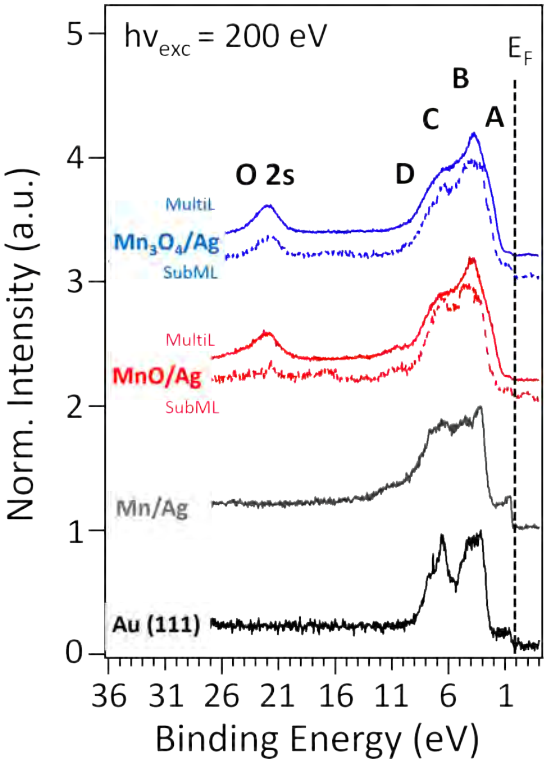

Figure 6.16: Valence band spectra of the clean Au(111) substrate (black), the Mn/Au(111) layer (grey) and both manganese oxide structures, MnO (red) and Mn_3O_4 (blue), in two different thickness range, sub-monolayer (dashed line) and multi-layer (continuous line). The binding energy of spectras can be precisely aligned with the Fermi edge of the gold substrate.

The VB spectra of the clean Au(111) substrate is the typical one obtained for bulk gold [304], showing the typical 5d states with two prominent peaks at 3.35 eV and 6.50 eV. However, after Mn deposition (grey line) only slight changes are observed with a redistribution in the valence band indicating an overlapping between Mn and Au VB spectra. The same situation happens for MnOx phases with a sub-monolayer thickness being challenge to prove differences among them with XPS. However, following the same approach than with sampels grown on top of silver, we have subtracted a scaled valence band reference spectrum of the Au(111) surface from that of Mn/Ag(001) and MnOx thin films and are presented in Figure 6.16-*Right*. The resultant difference spectra exhibit consistent differences between gold spectra and Mn-based layers. Three main contributions are identified at 2.3 eV (A),

5.25 eV (C) and 8.8 eV (E) in the d-band. Notably, a full d-band shift is observed for the Mn-based structures in comparison to Au one, denoting changes in the electronic structure like we have seen before. In this regimen, subML comparable spectra are obtained for both structures probing that in this case the starting structure is MnO. When we move to thicker layer, only differences in the O 2p band and D shoulder is observed. This later is observed in a more prominent manner for MnO/Au sample suggesting potential variations in defect densities.

In this section it has been proven that chemical composition of manganese oxide phases does not change among substrate nature. Instead, structurally those phases adapted its square crystal structure independently of substrate orientation. In the case of Au(111) three different domains along the principal directions of Au(111).

6.4 Mechanistic aspects behind OER on MnOx/Au(111) structures

This section focuses on the systematic study of MnOx structures as model catalysts for the OER. The primary objective is to elucidate the structural and chemical characteristics of MnOx catalysts both before and after OER operation. This will be accomplished through a synergistic approach combining surface science techniques, such as quasi-*in situ* XPS and LEED analyses on exposed surfaces, with electrochemical methods. By establishing correlations between meso- and nanoscopic properties and macroscopic electrochemical responses, we aim to evaluate the structure-function relationship of different manganese oxide phases. This approach will help us uncover electrochemical features, catalytic activity, and the surface structural and chemical states of MnOx. Specifically, we will address questions such as identifying the actual active phase for OER and determining when it is produced.

To this end and after confirming that similar structures are obtained on both substrates, Ag(001) and Au(111), we chose Au(111) as the support for catalyst characterization due to its extensive study in the preceding chapter. Thus, before electrochemically characterizing the MnOx catalysts, we first assess the potential oxidation of the Au(111) substrate in alkaline media at potentials near those required for OER. Alkaline media, specifically NaOH, is chosen because, as discussed in the introduction (**??**), this is the pH range where all stoichiometric phases are stable according to the Pourbaix diagram. This investigation also aims to uncover the role of counter ions and electrolyte concentration on the electro-oxidation mechanism of Au(111).

6.4.1 Au(111) electro-oxidation in alkaline media

As aforesaid, we first delve into the Au(111) electrode surface dynamics in alkaline conditions to identify potential-dependent species that may emerge when the surface is used as a supporting substrate for a more realistic catalyst, such as MnOx structures. Our aim is to gain precise control over any potential undesired species and (electro)chemical reactions that might occur on the Au(111) surface during the

electrochemical characterization of MnOx-based catalysts. This includes subsequent structural and compositional analysis of emerging phases to avoid erroneous assignments. At the same time, by compering the electro-oxidation mechanism obtained in NaOH in conjunction with the previous unveiled dynamic in H_2SO_4 (see chapter 5) we investigate the role of ions contained in the electrolyte.

The surface is examined following same methodology established in the previous chapter for the study of Au(111) surface electro-oxidation in H_2SO_4. We begin by investigating the electrochemical features within its electrochemical window by CV followed by chemical composition characterization by XPS.

Au(111) electrochemical window in NaOH

Figure 6.17 shows the CV obtained in an Ar-purged 0.05 M NaOH solution within the potential window spanning from the OCP, -0.5 V in this case, to 1.1 V vs Ag/AgCl/KCl(sat) - leakless. The scan rate of this experiment is set to 50 mV/s. The characteristic profile obtained resembles to those reported in the literature under alkaline conditions.[152, 305, 306]

In the double-layer region, from -0.5 to approximately 0.2 V, no current transients are observed, indicating no adsorption and resulting in a mere charge/discharge region. In the second potential range, from 0.2 to 0.4 V, a charge transfer peak is discernible at 0.3 V, previously ascribed to the chemical adsorption of OH on the surface.[152, 307] With a subsequent potential increase up to 1.1 V, a potential peak at 0.6 V indicates a phase transition triggered by additional OH adsorption.[152, 307] A broad peak follows this transient, attributed to oxide formation, and before a continuous increase in current due to OER, two additional peaks appear at 0.6 and 0.9 V. Both are attributed to the oxidation of the surface, leading to gold oxide formation.[152, 307] A prominent hysteresis is observed between oxidation and reduction processes, reducing the formed layer at E = 0.1 V.

The thickness of the potential-induced species during the anodic branch can be calculated through the area integrated under CV transients (extracted following Fig. 2.12) and employing Faraday's Law). The charge under the anodic peaks computed to a maximum of 19.3 $\mu C \cdot cm^2$ in the most prominent peak (at 0.6 V), indicating that the thickness of all species that arose is $<$ 0.1 ML. Following the same process, the charge ascribed to the reduction process is calculated. A charge of $\mu C \cdot cm^2$, around 2 ML, is obtained. This suggests that the prominent hysteresis is ascribed to post-electrochemical processes, as previously seen in sulfuric acid. This implies that, in this case, it is also necessary to overcome the kinetic sluggishness by increasing the overpotential or polarization time at E $>$ 1.1 V, where the continuous increasing current trend precluding the OER occurs.

After characterizing the electrokinetics through CV analysis and comparing the results with those obtained in acidic media, we suggest that the electro-oxidation kinetics rate is lower. Given that in sulfuric acid no notable chemical changes were detected within the electrochemical window (even with a further increase in potential), we decided to proceed directly to chronoamperometry polarization for 5 minutes to elucidate any chemical and structural changes.

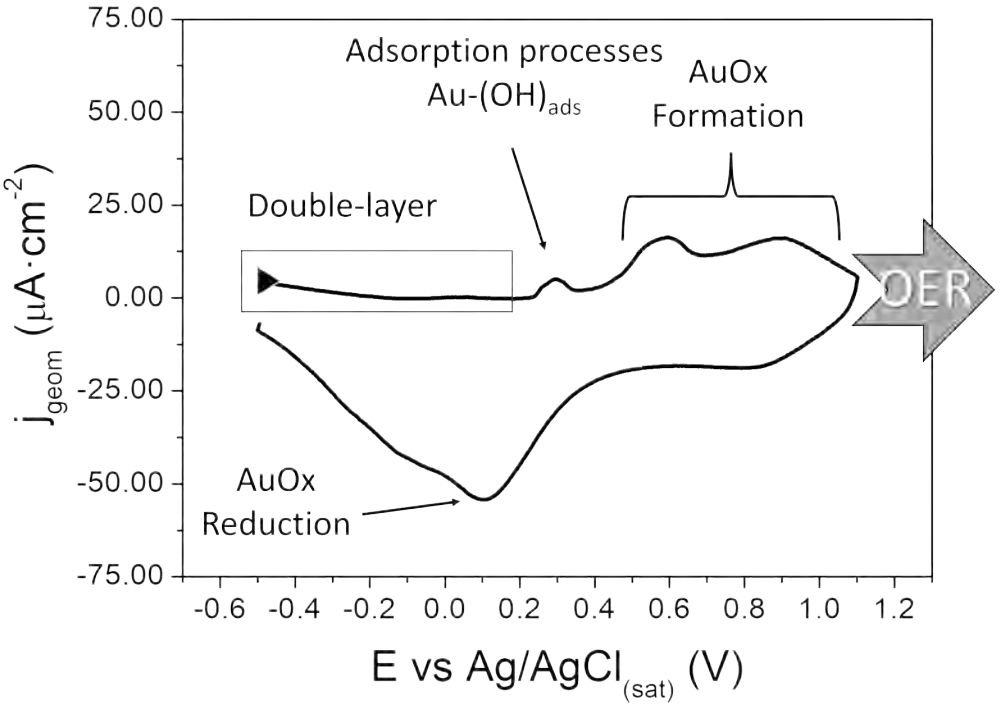

Figure 6.17: Cyclic voltammogram of Au(111) in a deaerated 0.05 M NaOH solution, capturing the oxidation/reduction dynamics of the surface at a scan rate of 50 mV/s. The data presented correspond to the first cycle with tilt ohmic drop corrected.

Chemical composition of emerged phases in NaOH

Our exploration involved studying the chemical variances arising at potentials ranging from 1.0 to 2.1 V through polarization for 5-minute intervals in a 0.05 M NaOH electrolyte following the methodology state din section 4.3. Subsequently, we analyzed the emersed samples by XPS means. Notably, negligible changes were observed from 1 to 1.4 V, prompting us to focus our analysis on polarization values from 1.4 to 2.1 V. The acquired XPS spectra for the Au 4f, O 1s, and Na 1s core levels are depicted in Figure 6.18. The intensity of Au 4f spectra has been resized to equal height, and O 1s in conjunction with Na 1s are referenced to it.

Following 5 minutes CA line at 1.4 V, the Au 4f core level (Fig. 6.18a) spectra exhibits two components corresponding to the two spin-orbit splitting components of the 4f core level for metallic gold (Au^0), centered at 84.1 eV and 87.8 eV for $Au4f_{7/2}$ and $Au4f_{5/2}$, respectively. As the potential was increased to 1.6 V, a feature at 85.7 eV emerged, indicative of Au^{+3} oxidation state. This observation aligns with previous findings in acidic electrolytes, suggesting a similar oxidation state transition in alkaline electrolytes. Notably, the Au^{+3} signal remained relatively stable until 2.0 V and then significantly intensified at 2.1 V. When comparing the analysis in NaOH with results obtained in H_2SO_4 media, we can point out that the emerged layer at 2.1 V in NaOH presents a similar component height to the sample polarized at 1.8 V for 5 minutes in acidic media (see Fig. 5.13), suggesting a sluggish electro-oxidation rate.

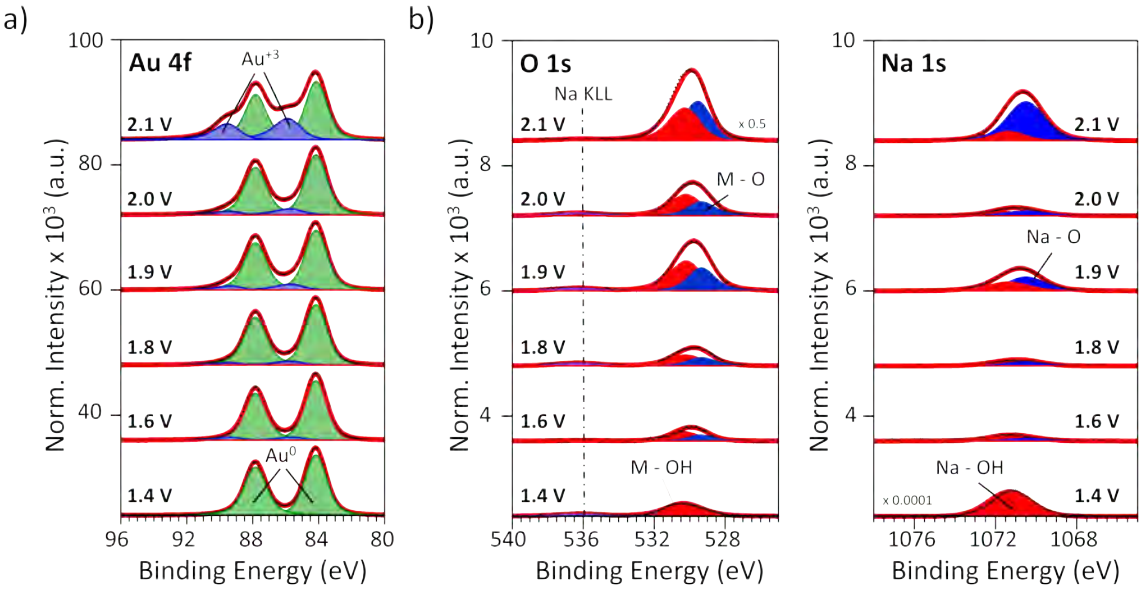

Figure 6.18: XPS spectra and fitting components at the energies of a) Au 4f, b) O 1s and c) Na 1s core levels after 5 minutes of polarization at different potentials ranged from 1.5 to 2.1V in dearated 0.05 M NaOH solution.

To gain insight into the emerging oxide component's chemical stoichiometry, we further analyzed O 1s and Na 1s together, as illustrated in Figure 6.18b. The O 1s spectra exhibited a dramatic increase in peak contribution with increasing potential. At 1.4 V, two distinct contributions corresponding to OH groups anchored at the gold surface (530.3 eV) and Na KLL Auger overlapping with O 1s at ≈536 eV were observed. In this case, the binding energy of Au-OH appears at a lower BE than the component ascribed to Au-H_2O in acidic media (531.7 eV, in section 5.4). This fact further confirms the interfacial adsorption of H_2O on the Au(111) surface as part of the hydration sphere in the emerged layer in acidic media. In contrast, this is not observed in alkaline media, indicating a different chemical structure and arrangement in the emersed layer.

As the potential increased from 1.6 up to 2.0 V, a small peak attributed to Au-O formation appeared in the photoemission spectra (blue component in O 1s panel) positioned at 529.4 eV, same binding energy observed for the Au-O component in sulfuric acid. Au-O component maintains same proportion along potentials, and becomes prominent at 2.1 V. This observation suggests that Au oxidation initiates with the adsorption of OH, facilitating the transformation into O, coinciding with the emergence of the Au^{+3} component. Gold is bound to oxygen in a Au^{+3} state. The O:Au ratio after 5 minutes polarization at 2.1 V using Equation 5.13 is approximately 1.46 for O-Au, closely resembling the expected value for the stoichiometry of Au_2O_3. Thus, it can be inferred that the same stoichiometric oxide is formed during the electro-oxidation of Au(111) in both alkaline and acidic environments.

In the Na 1s spectra (Fig. 6.18b), two different chemical states for sodium were observed during electro-oxidation. At 1.4 V, a predominant contribution at 1071.5 eV was attributed to NaOH adsorbed on the gold surface, red component. With increasing potential and the formation of the oxide layer, a new component in blue

at 1070.5 eV emerged. The concurrent increase in O 1s and Na 1s contributions with increasing potential suggests the involvement of Na^+ cations in the resulting oxide formation.

Our experiments confirmed partial oxidation of Au(111) at 2.1 V, a potential near OER, albeit only adsorbed oxygen-rich layers were observed between 1.6 and 2.0 V. This investigation provides valuable insights into utilizing this surface as a supporting catalyst substrate within the specified potential range, with foreknowledge of potential catalyst-altering components.

Furthermore, the experiments conducted in this section, in conjunction with those in Section 5.4, raise an unresolved question regarding the role of anions and cations present in the electrolyte for Au(111) electro-oxidation. The observed mechanism in alkaline media appears to differ from that found in sulfuric acid. In alkaline media, Na^+ ions do not adsorb on the Au(111) surface; instead, they act as counter ions for the oxygen-based layers formed upon potential application and are retained in the emersed layer. In contrast, in sulfuric acid, anions like sulfate are adsorbed through an S-O bond. The interaction of the sulfate layer forms peroxydisulfate, which acts as a promoter of the oxide and desorbs when oxygen-based species evolve. Despite these differences, the repelling effect between the positively charged Na^+ ions and the Au surface with the same charge could explain this mechanism.

To address this question, a third electrolyte, $HClO_4$, was tested during this PhD thesis, containing anions with lower affinity to gold similar to sodium. However, despite the acquisition of data during the PhD tenure, the investigation into the role of perchloric acid electrolyte and the effect of electrolyte concentration will not be included in this manuscript for consistency with the focus of the thesis.

6.4.2 Which is the actual OER active phase?

In this subsection, we assess the impact of various manganese oxide stoichiometries, including Mn, MnO, and Mn_3O_4, with oxidation states of 0, +2, and +2,+3, on OER activity (overpotential) and stability by probing these structures at potentials close to and above the OER onset. The tunability of the chemical and structural surface composition of manganese oxides allows for the evaluation of the evolution of the catalyst surface towards more oxidative states both precluding and during OER, unveiling structure-function relationship. This investigation aims to determine whether the Mn-based oxide family presents a unique active phase for OER or if different active phases are observed depending on the initial state of the catalyst. This will facilitate the development of active and stable MnOx catalysts for use as anodes in electrolyzers.

For the purpose of this investigation, we first evaluate the electrochemical characteristics and double-layer capacitance (DLC or C_{dl}) of each MnOx phase. This study allows us to analyze the chemical composition as a function of the applied potential, unveiling characteristic electrochemical features attributed to each oxide. Additionally, since each phase presents a different electrochemically active surface area, evaluating the EDLC helps avoid confounding conclusions in terms of current density activity. Subsequently, we investigate the OER catalytic activity by analyzing the overpotential at the same current density production among them. Finally,

we measure the stability of anodic oxygen evolution catalysts through chronoamperometry experiments at two different constant potentials (1.6 V, precluding OER onset, and 2.1 V, during OER). The dominant catalytic process at 2.1 V is confirmed to be OER through Tafel slope analysis. In this final experiment, we aim to evaluate the chemical composition of the resulting phases as a function of the applied potential, utilizing XPS and LEED surface-sensitive techniques to ascertain the resultant phase.

The electrochemically examined layers discussed herein are multilayer manganese oxide films deposited onto Au(111) surfaces. This approach helps mitigate potential substrate-induced effects, ensuring that the characterization exclusively captures the electrochemical attributes arising from the MnOx catalyst, as intended.

Electrochemical behavior of as-grown MnOx structures

To establish meaningful comparisons among different catalysts in terms of electrochemical response, precise methodologies must be defined. Two primary methods are typically employed: normalizing current to geometric surface area, as done previously, or to the catalyst loading. However, relying solely on the geometric-based method can lead to erroneous activity comparisons due to the inherent correlation between higher loading and increased activity, making accurate estimation challenging. One strategy to address this challenge is to calculate the electrochemically active area (ECSA). A larger ECSA indicates greater catalyst loading, contributing to higher current density when normalized to geometric area (J_{geom}) and consequently, enhanced electrochemical activity. Therefore, prior to further electrochemical investigations, the ECSA of each phase was estimated.

One approach to estimate the ECSA of MnOx samples is by determining the Helmholtz DLC and deduce the ECSA, supposing ideal flat surfaces. DLC can be obtained using electrochemical impedance spectroscopy (EIS) or capacitance measurements. Given the absence of EIS module in the potentiostat, capacitance measurements were adopted. Hence, DLC measurements in a narrow potential range with varying scan rates were conducted. It is crucial to select a potential window devoid of Faradaic reactions to accurately determine the resultant capacitance, which equals the double layer capacitance (C_{dl})[308]. Consequently, the range was chosen near the OCP.

Mn/Au(111), MnO/Au(111), and Mn_3O_4/Au(111) samples were studied with CV in argon-purged 0.05 M NaOH electrolyte at different scan rates ranging from 5 to 100 mV/s prior to any electrochemical measurements. Three scans were performed under each condition, and the resulting third scan CV curves are presented in Figure 6.19. These scans for the three Mn-based phases were measured around OCP, value indicated by dashed lines.

For the calculation of the differential capacitance, two approaches were considered: utilizing the charge or current density differences as a function of scan rate. In this study, the latter approach was chosen. As previously seen in chapter 2 with the Randless-Sevick equation, the current is proportional to the square root of scan rate. Thus, the differences in current density between the anodic and cathodic values at OCP, along with the corresponding scanning rates, are plotted in the inset

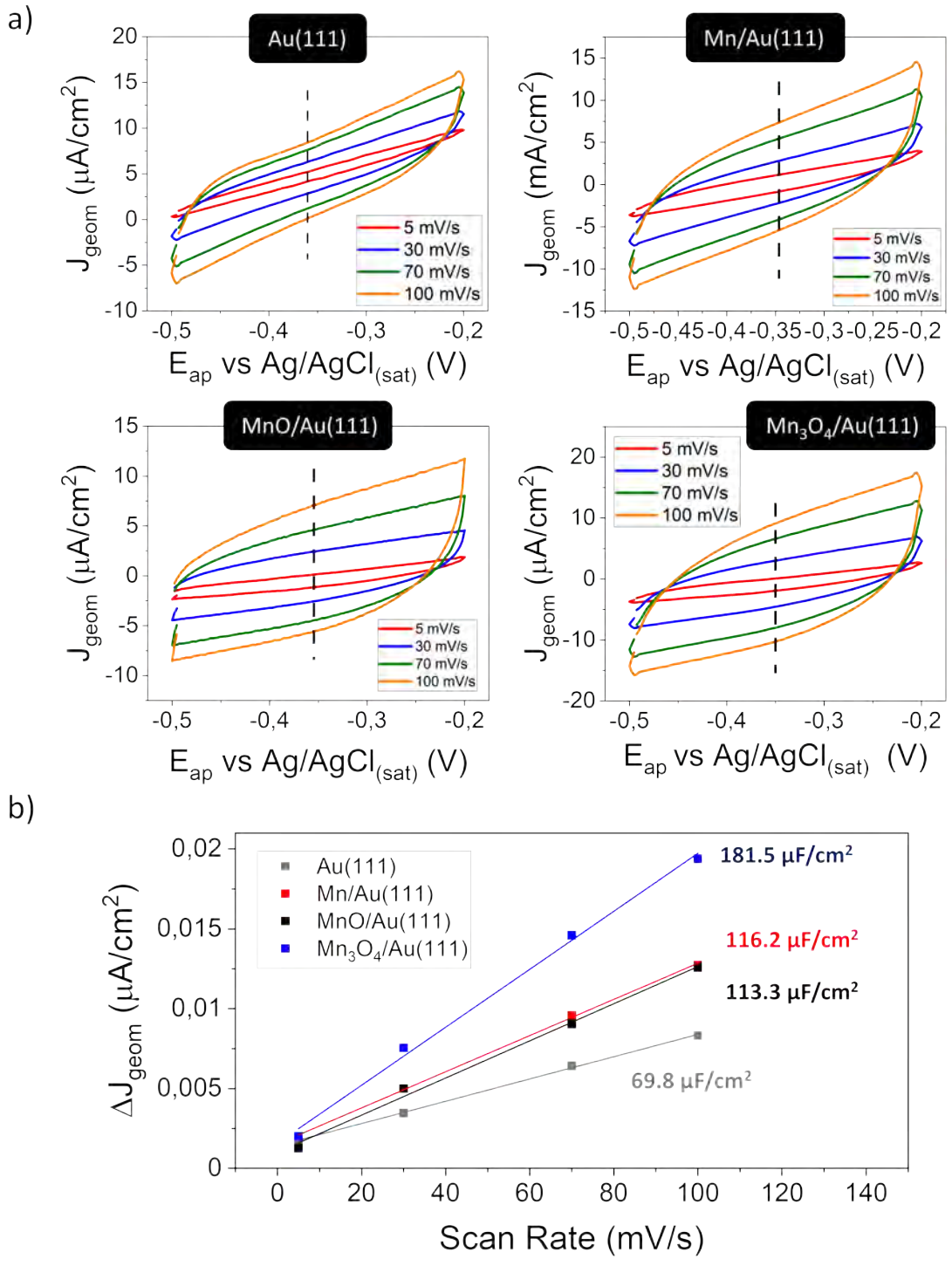

Figure 6.19: a) Cyclic voltammograms obtained in an Ar-purged 0.05 M NaOH around the OCP at different scan rate values: 5, 30, 70, 100 mV/s, for Au(111), Mn/Au(111), MnO/Au(111) and Mn_3O_4/Au(111) samples. It shows the third scan. b) Anodic charging current densities measured at the OCP value as a function of the scan rate for each sample: (grey) Au(111), (black) Mn/Au(111), (red) MnO/Au(111) and (blue) Mn_3O_4/Au(111).

of Figure 6.19 and used to calculate the DLC value, which is half the slope of the observed trend [309]. The obtained DLC values, which are indicative of the electrochemically active area, were estimated and are summarized in Table 6.3. A larger DLC may contribute to higher electrochemical activity and current density in CV characterization when current is normalized to geometric area.

Table 6.3: Calculated double-layer capacitance for Mn-based phases.

Phase	C_{dl} / $\mu F/cm^2$
Au(111)	34.9
Mn/Au(111)	56.7
MnO/Au(111)	58.1
Mn_3O_4/Au(111)	90.8

Once we know in advance a prediction of the ECSA among MnOx phases, we can evaluate their electrochemical features by CV studies. In order to elucidate the redox characteristics of MnOx phases in an Ar-purged solution, a series of CV experiments were conducted over two different potential range: from OCP, -0.5 V, to 1.1 V (precluding electro-oxidation and subsequent OER, in the Au(111) potential window) and from OCP to 1.7 V,in the OER onset at a scan rate of 50 mV/s. The lower limit of the potential scan range was carefully chosen near the OCP to minimize any significant alterations in electrode structure or composition upon immersion in the electrolyte, thus ensuring consistency across all samples for comparative analysis. Figure 6.20 illustrates the voltammograms obtained in the third scan for Au(111), Mn/Au(111), MnO/Au(111), and Mn_3O_4/Au(111) in the Au(111) electrochemical window range (Fig.6.20a) and precluding OER (Fig. 6.20b).

To interpret the intricate CV profiles of MnOx, the behavior of the Au(111) substrate was initially explored to delineate its redox pathway, as discussed previously (see Fig. 6.17). When comparing current density with MnOx phases, the gold features are notably masked, indicating a higher ECSA for the MnOx layer.

For Mn-based samples studied within the Au(111) potential window (Fig. 6.20a), we can distinguish three different potential regions. As the potential is swept in the anodic branch, the $OH_{(ads)}$ region is observed in all three cases, with electrochemical features at approximately 0.1 V and 0.3 V for Mn and MnO, while for Mn_3O_4, these appear at -0.05 V and 0.25 V. This confirms that the features completely change from those in Au(111). With an increase in potential, only in Mn_3O_4 is the onset of electro-oxidation observed, indicated by a continuous increase in current (marked with an asterisk). When the potential is reversed, only a reduction peak is visible for Mn_3O_4 around 0.2 V, confirming the onset of oxidation and pointing to a more active phase compared to Mn and MnO.

When the potential is extended up to 1.7 V, different anodic features for the three phases in the oxidation region are observed (Fig. 6.20b). Mn and MnO present a single broad anodic feature at 1.4 V, while Mn_3O_4 exhibits three different transitions at 1.1 V, 1.3 V, and 1.4 V. This observation points to the same ET at 1.4 V, which may evolve into the actual active phase. Moreover, the final current is the same in all three cases, indicated by a black point, further suggesting that the mechanism

progresses from electro-oxidation to the formation of the actual active phase, which activates the continuous current trend (the onset of OER).

These transitions exhibit reversibility, as evidenced by corresponding cathodic branches that exhibit two small features, almost invisible, proving the irreversibility of the system. Table 6.4 summarizes the electrode reactions involved in the cyclic voltammogram shown in Fig. 6.20 [294, 310], indicating the formation of either Mn_2O_3 or MnO_2 phases as the active ones.

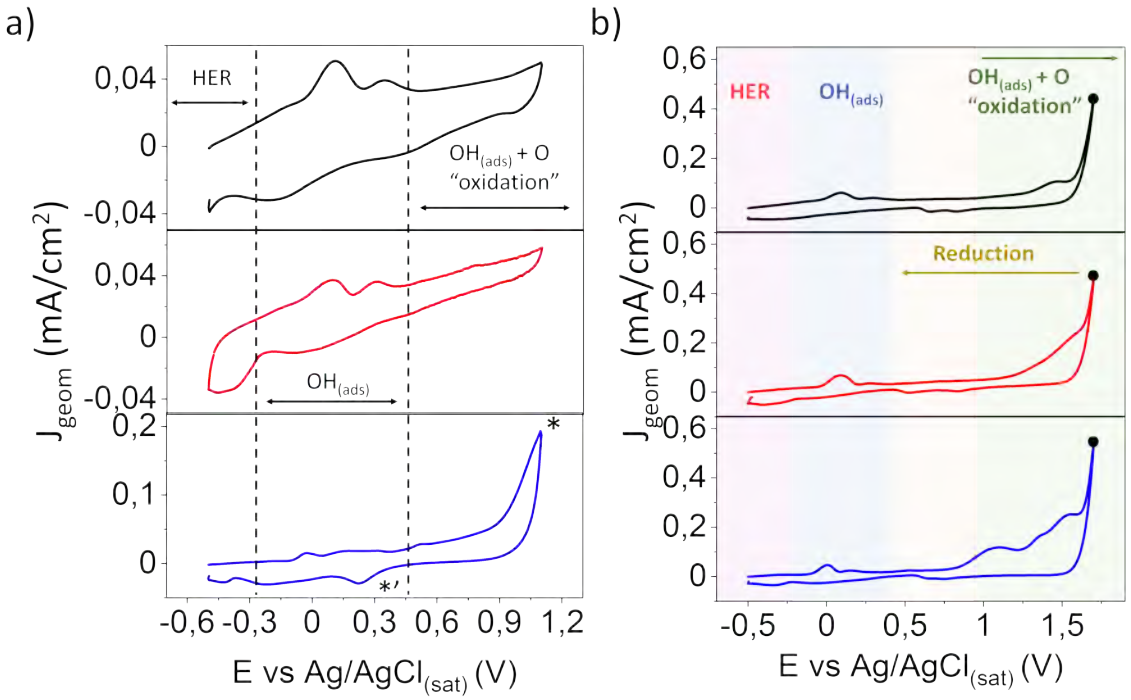

Figure 6.20: Cyclic voltammograms obtained in an Ar-purged 0.05 M NaOH at 50 mV/s in two different potential ranges: a) from OCP to 1.1 V and b) from OCP to 1.7 V for different samples, (black) Mn/Au(111), (blue) MnO/Au(111) and (red) Mn_3O_4/Au(111).

Table 6.4: Redox transitions of Mn and H_2O relevant to the surface processes in Figure 6.20 with calculated expected Ep from [310].

Label	Redox Transition	Ep expected (V vs SHE)
OH_{ads}	$Mn + 2OH^- \leftrightharpoons Mn(OH)_2 + 2e^-$	-1,495
$A/A^{'}$	$2Mn_3O_4 + 2OH^- \leftrightharpoons 3Mn_2O_3 + H_2O + 2e^-$	-0.079
$B/B^{'}$	$3Mn_2O_3 + 2OH^- \leftrightharpoons 2MnO_2 + H_2O + 2e^-$	0.245

In summary, by CV assessment we can confirm that the j-E curve indicates to same electro-oxidation mechanism evolving a similar phase in terms of potential and current. Even though, further characterization is needed

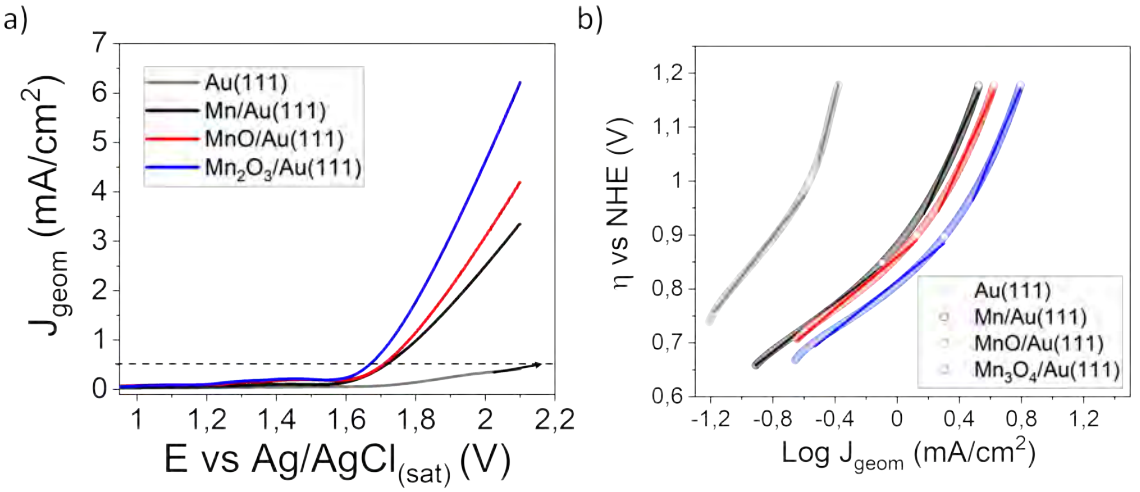

Figure 6.21: a) Current density (j) as a function of E vs Ag/AgCl of Au(111), Mn/Au(111), MnO/Au(111) and Mn_3O_4/Au(111) in dearated 0.05 M NaOH solution at 50 mV/s. b) Tafel slope analysis of linear sweep voltammetry response obtained in a).

Electrocatalytic activity of the MnOx/Au(111) towards OER

To ensure the relevance of deposited layers in terms of activity and to discern dependence on phase-activity correlation, the catalytic activity towards OER of various Mn-based catalysts and the Au(111) substrate was investigated using CV.

Figure 6.21a presents the results from CV, depicting the anodic branch obtained during cycling from OCP to 2.1 V, visible within the range of 1 to 2.1 V. The initial linear sweep in the anodic direction for each material reveals the superior activity of Mn-based catalysts compared to Au(111). Identifying the onset potential for the OER poses challenges due to pre-catalytic events, including the masking effect of pseudo-capacitance, contaminants, surface electro-oxidation, and other electrochemical processes. In this study, a pre-catalytic event, specifically attributed to the electro-oxidation of surfaces and latter on investigated, obstructs the direct estimation of the onset potential. Hence, the potential required to drive 0.5 mA/cm^2 was used to define the onset potential of OER, and thus the overpotential (η), indicated by the dashed line.

In assessing catalyst activities among grown MnOx phases, the focus lies on the effect of Mn-based composition on activity trends (η_{OER} and electrochemical kinetics mechanism). Consequently, the comparison of samples at a specific potential, namely 2.1 V, considering the enhanced activity at the same potential and the η_{OER}, yields the following activity order trend: Mn_3O_4/Au(111) > MnO/Au(111) > Mn/Au(111) > Au(111). These findings align with the anticipated enhancement of electrocatalytic activities due to an increase in the overall oxidative state in the structure [276]. Table 6.5 provides a quantitative comparison of η_{OER} between MnOx films and the metal substrate Au(111).

The investigation into the RDS in the water oxidation mechanism among samples utilized Tafel plots, which offer insights into the kinetics of the reaction [311]. The Tafel plots, derived from the anodic current density region of the CVs, are il-

Table 6.5: Potentials required to reach the current density of 0.4 $mAcm^{-2}$ with Au(111), and grown structures of Mn, MnO and Mn_3O_4 on top of Au(111) substrate; and the corresponding Tafel slopes at low and high current density range.

Sample	$\eta_{OER(0.5mA/cm^2)}$ (V vs Ag/AgCl)	Tafel slope at low / high j ($mVdec^{-1}$)
Au(111)	2.195	37.1 / 111.0
Mn/Au(111)	1.714	22.4 / 64.6
MnO/Au(111)	1.705	24.0 / 62.5
Mn_3O_4/Au(111)	1.665	23.0 / 67.5

lustrated in Figure 6.21b and have been analyzed in both the low current density range (attributed to the electro-oxidation mechanism) and the high current density range (attributed to the OER operation). Tafel slope assessments were conducted for both ranges, with the resulting values summarized in Table 6.5.

At low current density, the Tafel slope consistently remains around 30 mV/dec, suggesting that the rate-determining step preceding the activation of OER involves the chemical O-O coupling step via proton-coupled electron transfer from the resting state [312, 313]. This gives support to the notion of an electro-oxidation step preceding OER. Conversely, the high current density range reveals a faster reaction mechanism for Mn-based samples, with Tafel slopes measuring 64.6 mV/dec, 62.5 mV/dec, and 67.5 mV/dec for Mn, MnO, and Mn_3O_4, respectively. These values significantly undercut the 111 mV/dec of the Au(111) surface, indicating a marked improvement in reaction kinetics when Mn-based catalysts are employed. The Tafel slope is directly linked to the kinetics of the rate-limiting step rather than the total number of available sites [95]. Mn-based catalysts exhibit similar values, averaging around 64.9 mV/decade, indicating the same rate-limiting step with minimal deviation from the anticipated 59 mV/decade. A Tafel slope close to 59 mV/decade suggests a one-electron pre-equilibrium preceding a turnover-limiting chemical step [62]. In contrast, Au(111) demonstrates a Tafel slope near 120 mV, signifying a distinct mechanism for oxygen gas turnover, with the first electron transfer being the rate-determining step. Thus, two disparate mechanisms towards OER are delineated, emphasizing the superior activity of Mn-based catalysts.

In summary, the results obtained in this section suggest that the electro-oxidation mechanism occurs on all anode catalytic surfaces, including Au(111) and MnOx phases, albeit with different mechanistic aspects. In the case of MnOx, each as-synthesized manganese oxide appears to electrochemically evolve into the same pre-catalyst phase. Despite these findings, further characterization is necessary to corroborate this assumption and to unveil the actual chemical composition and surface structure. Therefore, it is imperative to study this through our EC-UHV constructed system to avoid uncontrollable surface modifications.

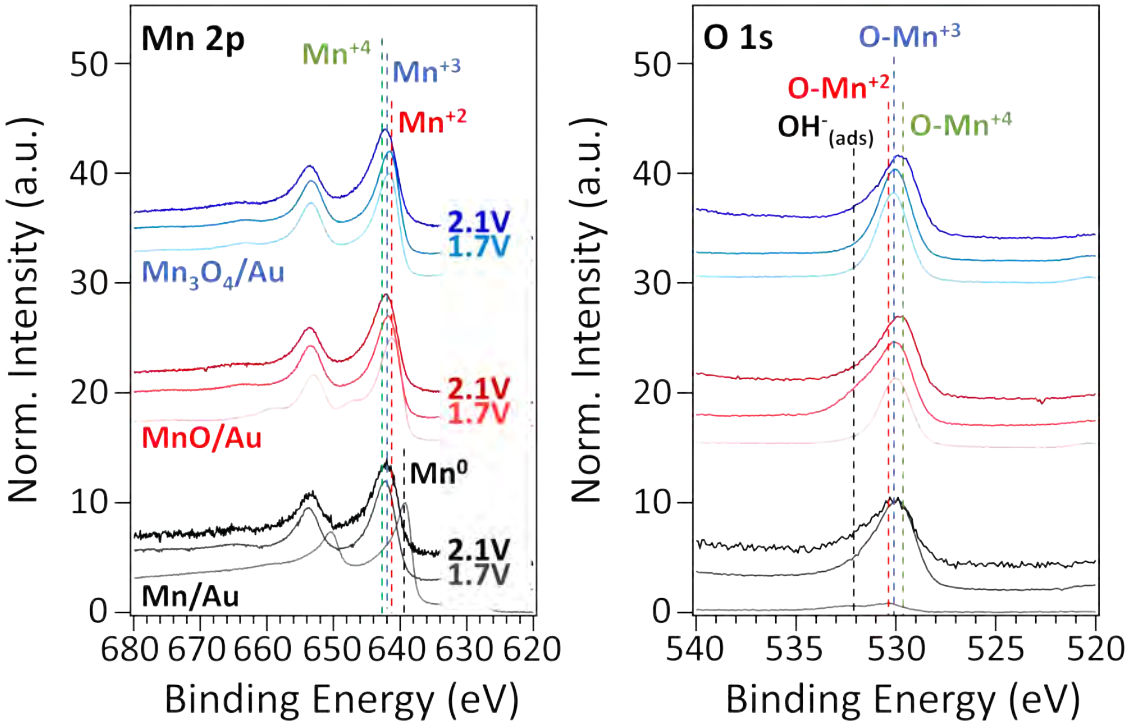

Figure 6.22: XPS spectra at the energies of Mn 2p and O 1s acquired for Mn/Au(111) (black), MnO/Au(111) (red) and Mn_3O_4/Au(111) (blue) after 5 minutes of polarization at 1.7 and 2.1V in dearated 0.05 M NaOH solution.

Quasi-*in situ* XPS characterization of chemical-structural changes at OER potentials

Having confirmed the existence of the same RDS in MnOx catalysts, precluding the OER, the forthcoming subsection focuses on investigating the chemical and structural evolution of the MnOx surface upon anodic polarizations at potentials pertinent to the OER catalysis using quasi-*in situ* XPS and LEED. The objective is to discern the structure that really evolves the OER as a result of the rate-limiting step, unveiling chemical and structural changes on the MnOx surface.

Initially, the samples are subjected to cycling within a non-faradaic regime to stabilize the electrode-electrolyte interface, essential for determining the ECDL. Subsequent to stabilization, the films undergo cycling from OCP (≈ -0.5 V) to a vertex potential of either 1.7 V, precluding OER region, or 2.1 V, where OER is induced, maintained at this potential for a duration of 5 minutes, and then emersed from the electrochemical cell.

As previously elucidated, the oxidation state of manganese-based layers on top of gold substrates is discerned via the Mn 2p multiplet's position and its satellite. To identify a change in the oxidation state between surfaces, the $Mn2p_{1/2}$ position previously discussed for each relevant sate are indicated by dashed lines in red and blue for Mn^{+2} and Mn^{+3}, respectively; in conjunction with the green dashed line ascribed to the Mn^{+4} state.

The spectra of Mn/Au(111) samples obtained post-polarization at 1.7 V (light

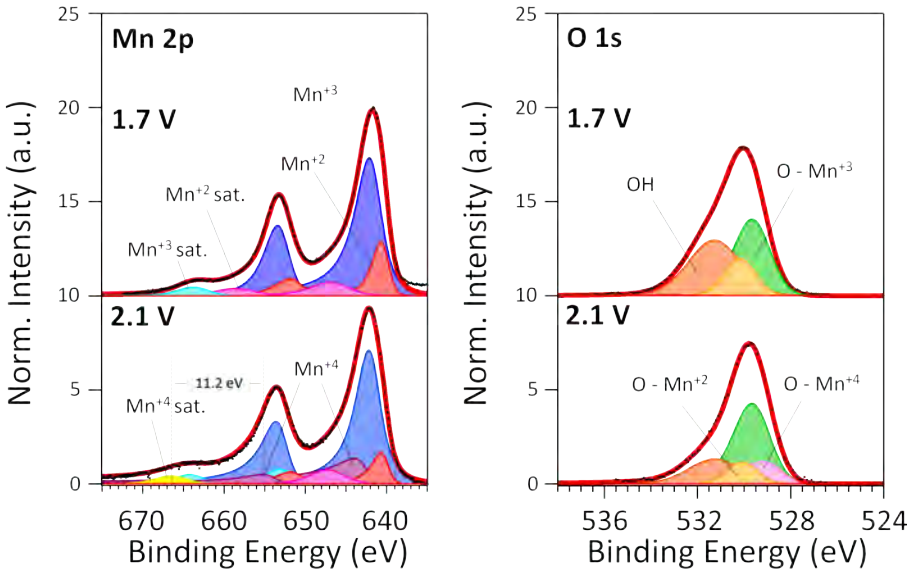

Figure 6.23: XPS spectra and fitting components at the energies of Mn 2p and O 1s core levels after 5 minutes of polarization at 2.1V in dearated 0.05 M NaOH solution. It is the deconvolution representing all emersed Mn-based structures layers with same conditions. This example is from Mn/Au(111) sample.

color) and 2.1 V (dark color), as presented in Figure 6.22, show a shift of the entire Mn 2p spectrum by approximately 3 eV, positioning Mn $2p_{3/2}$ at 642.2 eV. This shift indicates the oxidation of the surface to an enriched Mn^{+3} oxide. This is consistent with the appearance of an O 1s peak located at 529.9 eV, suggesting the formation of an oxide, most likely with a Mn^{+3} oxidation state. Upon further potential increase to 2.1 V, no significant positional changes are noted, although broadening of the peak occurs, attributed to a new component corresponding to Mn^{+4}. The O 1s spectra for both samples exhibit a similar trend, positioned at 529.9 eV, with decreased intensity at higher potentials, likely due to the conversion of adsorbed oxygen at 1.7 V to molecular oxygen at 2.1 V, precluding OER.

For both MnO/Au(111) and Mn_3O_4/Au(111) samples, the Mn 2p peak position at 1.7 V is located at 641.6 eV. This position closely matches the Mn^{+3} state, indicating an enriched Mn^{+3} phase. With further potential increase during polarization, a new peak emerges at 0.5 eV higher binding energy, attributed to a newly formed component of the Mn^{+4} state. In the O 1s spectra, a similar trend is observed with increasing potential, except for the region at higher binding energies attributed to OH^- adsorption, where unpredictable changes occur. The O 1s peak shifts towards lower binding energy with increasing potential, in alignment with the Mn 2p peak, indicating the evolution of a higher oxidative layer with potential.

Hence, XPS analysis reveals a consistent trend across samples, showing a transition from an initial Mn^{+2} and Mn^{+3} state to an enriched Mn^{+3} phase at 1.7 V, and further to a newly emerged Mn^{+4} component at 2.1 V. This observation is supported by changes in the O 1s profile, where similar transitions are observed. Thus, the surface dynamics appear consistent across different MnOx catalyst phases.

To confirm this assumption, it is essential to resolve the actual composition through XPS deconvolution. Our findings indicate that, within the margins of experimental error, the fitting results for the three different Mn-based phases are quite similar at each potential. Therefore, for simplicity, we will present exemplary fitting details from the MnO/Au(111) phase for both polarization potentials, 1.7 V and 2.1 V. The results for Mn and Mn_3O_4 phases are consistent with those for MnO. Figure 6.23 illustrates the XPS spectra along with the resolved components at the Mn 2p and O 1s core levels after polarization.

After 5 minutes at 1.7 V, the Mn 2p core level, centered at 642.2 eV, exhibits features similar to those observed in the Mn_3O_4 phase. This spectrum is composed of two principal components corresponding to Mn^{+2} and Mn^{+3}, as previously stated. Additional components are needed for a complete fit, including the Mn^{+2} and Mn^{+3} satellite peaks. A similar pattern is observed in the O 1s spectrum, which requires three components for fitting: two assigned to $O - Mn^{+2}$ and $O - Mn^{+3}$, and a third peak at higher binding energy, associated with either chemisorbed oxygen or OH groups, which cannot be distinctly resolved. In this case, it is attributed to OH species attached to the Au(111) substrate, as observed in its electro-oxidation mechanism in NaOH electrolyte. This confirms the presence of an enriched Mn^{+3} phase, likely due to the formation of a preferred Mn_2O_3 phase.

Further analysis of the surface chemical composition after OER, performed with polarization at 2.1 V for 5 minutes (where OER occurs), reveals a new component emerging at 643.6 eV, attributed to the Mn^{+4} state. Additionally, a new satellite peak, arising from shake-up processes of the Mn^{+4} state, is detected 11.2 eV from the main component, consistent with previously reported values [272]. In the O 1s core level, a new component emerges at 528.9 eV, coinciding with the changes observed in the Mn 2p spectrum. This new peak signifies oxygen bonded to manganese in the Mn^{+4} state, likely indicating the formation of MnO_2.

In summary, this study provides a comprehensive understanding of the chemical composition and behavior of MnOx catalysts across varying potentials, independent of the catalyst surface. XPS analysis reveals a clear transition in the MnOx phases from Mn^0 and Mn^{+2} states to an enriched Mn^{+3} state at potentials preceding the OER. This suggests that the Mn^{+3} phase, likely corresponding to Mn_2O_3 stoichiometry, is the actual active phase. During OER operation at higher potentials, the surface further oxidizes to a Mn^{+4} state, indicating the formation of MnO_2. These findings underscore that the overpotential required for effective OER catalysis is related to the dynamic surface transformations necessary to achieve the active phase. Consequently, the catalytic activity is enhanced when the surface composition closely resembles the active phase, as the overpotential reflects the degree of surface conversion required to achieve optimal catalytic performance.

6.5 Summary

In this chapter, the growth of model catalysts relevant to the OER was accomplished using surface science tools. The versatility of manganese, with its wide

range of stoichiometries and geometries, facilitated the growth of various stoichiometric phases of oxides, establishing manganese as a model catalyst for investigating the correlation between the number of active centers and their activity toward OER. Multidisciplinary research in surface physics and electrochemistry enabled the exploration of the structure-function relationship of these oxides through a quasi-in situ combined EC-UHV approach. By employing UHV-based growth techniques under controlled conditions, in conjunction with surface-sensitive techniques like XPS, LEED, LT-STM, and AFM, alongside macroscopic characterization using electrochemical techniques, we evaluated the electrochemical reaction mechanisms of various structures both before and during the OER, with a focus on the actual active phase.

Here, we summarize the key aspects and findings of the chapter:

- **Growth of MnOx**: The research clarified that the growth of manganese oxide can be tuned by the oxygen pressure used in reactive deposition in an oxygen atmosphere or by the nature of the oxidizing agent (molecular oxygen or atomic oxygen). The oxidation state achieved depends on both the pressure and the oxidizing agent. High pressures of molecular oxygen result in a higher oxidative structure, saturating in a mixed phase with +2 and +3 states. When atomic oxygen is used, a structure with a completely transitioned oxidation state to +3 is achieved, indicating that the absence of the rate-limiting step in oxide growth, considered to be the dissociation of oxygen, accelerates the oxidation reaction of metals.

  In terms of structure, the use of different substrate orientations with distinct crystallographic parameters (Ag(001) and Au(111)) revealed that the final structure obtained depends on the lattice and orientation mismatch between the oxide crystal bulk and the metallic substrate. Additionally, it was observed that oxidation does not occur on the surface. Instead, manganese is oxidized in air followed by its subsequent deposition on the substrate, maintaining the chemical composition of oxides across different substrates.

- **Catalyst Oxide Phases**: We successfully grew different oxide structures as a function of oxygen pressure: MnO(001) with (1×1)-Ag(001) and $3R30^o(1\times1)$-Au(111) structures at low pressure ($1\cdot10^{-8}$ mbar), $Mn_3O_4(001)$ with a $p(2\times1)$-Ag(001) and $c(2\times2)$-Au(111) supperlatices at higher pressures ($1\cdot10^{-6}$ < p < $1\cdot10^{-4}$ mbars), and an α-Mn_3O_4 phase using atomic oxygen.

- **Structure (oxidation state)-function (OER activity) relationship**: The catalytic activity of MnOx phases on Au(111) surfaces was analyzed through kinetics studies, revealing that the activity of catalysts follows this trend: Au(111) < Mn/Au(111) (0) < MnO/Au(111) (+2) < Mn_3O_4/Au(111) (+2,+3). This confirms that the oxidation state is directly related to the activity of MnOx catalysts and the performance of general catalysts.

- **Actual active phase**: CA polarizations were combined with quasi-in situ XPS and LEED characterization to elucidate the actual active phase. Each

structure was polarized for 5 minutes at two distinct potentials: 1.7 V, precluding OER, and 2.1 V, where OER occurs. Our findings revealed that in the pre-OER state, all different Mn-based phase electrodes evolve to a +3 oxidation state, forming the actual active phase. Surfaces evolved at 2.1 V present a new component evolving to a +4 oxidation state.

In summary, through the synergistic study between surface science and electrochemistry, we elucidated the electrochemical mechanism of MnOx in the OER. The study confirmed that the actual active phase of the OER catalyst does not depend on the former oxide structure; instead, it is the same for all. The precluding phase only influences the overpotential, requiring different energy levels to transform into the actual active phase, which translates to lower efficiency and activity toward OER. These results emphasize the importance of combining surface-sensitive techniques and macroscopic electrochemical tests to gain a comprehensive understanding of real catalysts.

Chapter 7
Concluding remarks

As aforementioned, in view of the growing worldwide demand for energy and climate change, the transition towards more sustainable energy alternatives is mandatory. The efficiency and reaction selectivity of electrolyzers and fuel cell devices depend heavily on the chemical and structural composition of catalyst surfaces. Thus, novel catalytic materials with lower overpotential and higher stability and activity for applications in green chemical fuel production and energy conversion are needed. To develop these materials, a comprehensive understanding and monitoring of the electrochemical interface is essential. This requires detailed insights into the processes occurring at the electrode-electrolyte interface from a micro- and nanoscale perspective during operation and their relationship to macroscopic catalytic performance. For that purpose, surface science techniques combined with electrochemistry can concurrently probe the electrochemical interface occurring during catalytic and electrochemical processes, using chemical and structural surface-sensitive techniques on the same sample. However, progress has been hindered by the complexity of real catalytic systems and the lack of experimental techniques capable of providing detailed information on surface dynamics from molecular interactions to operando conditions.

This thesis establishes a link between surface science and electrochemistry, emphasizing the importance of correlating the electrochemical response of electrodes and catalysts (macroscopic activity) with their structure and chemical composition (microscopic properties) at the meso- and nanoscale. Throughout this thesis, the pressure gap between UHV and electrochemistry has been addressed with a novel UHV-EC system, offering an innovative experimental approach to comprehensively understand the molecular aspects of the electrochemical interface. By developing and implementing a novel quasi-in situ electrochemical characterization method combined with UHV characterization techniques through a clean and controlled transfer atmosphere, the operational potential-induced changes at the electrochemical interface can be characterized using chemical (XPS) and surface (LEED) sensitive techniques on a single sample.

In this manuscript, before describing the adopted approach, we briefly introduced the most relevant aspects of electrochemistry and surface science. We explored why

the electrochemical interface is at the core of electrocatalysis and how to simplify the complexity of catalyst surfaces using well-defined surfaces. We also reviewed thermodynamics and kinetics theory, experimental insights on the OER reaction, and some of the electrochemical experimental techniques employed. Additionally, the surface science perspective on preparing and growing model catalytic surfaces and the principles of surface-sensitive techniques were discussed.

Following a thorough examination of cutting-edge EC-UHV developments in the literature, an emersed or quasi-in situ methodology was selected and implemented. The construction process of the modular UHV-EC system used in this thesis was explained in detail to help readers anticipate the relevant considerations when designing an experimental setup that combines UHV and electrochemistry. The configuration of the isolated EC-UHV transfer chamber, the importance of the electrochemical cell, and the need to work in a meniscus configuration, allowing immersion in electrolyte with a clean atmosphere and controlled perspective, were detailed. The methodology employed for each experiment was comprehensively explained, ensuring clarity and reproducibility in experimental protocols. By removing the sample under potential control and rinsing it with MilliQ, our quasi-in situ method retains irreversible chemical and structural changes induced by the potential in the emersed layer, mimicking the electrochemical interface.

To test the applicability of the quasi-in situ EC-UHV methodology, the model Au(111) surface was used as a testbed. This investigation demonstrated that we could obtain the characteristic electrochemical features of Au(111) in H_2SO_4 solution. Furthermore, surface-sensitive techniques (XPS and LEED) confirmed that certain highly relevant chemical and structural characteristics, such as non-reversible chemisorbed species and phases of the double-layer interface, are preserved in the emersed layer (after losing potential during UHV transfer). Thus, our setup was deemed suitable for unraveling the stable chemical and structural dynamics of electrode surfaces during electrochemical processes.

Having established the suitability of our approach, we investigated potential-induced changes at the Au(111) electrode/electrolyte interface at potentials relevant for electro-oxidation and OER, uncovering the reaction mechanism through surface composition, the role of electrolyte ions, and the actual OER active phase. The study highlighted the crucial role of anions in the electro-oxidation of gold, promoting a surface stoichiometry attributed to Au_2O_3 via a peroxydisulfate intermediate. Additionally, it confirmed that the active phase for OER on gold surfaces is AuOOH.

Building on the success with Au(111), we extended the research to more complex systems, particularly different MnOx phases as model catalysts. Using UHV-based growth techniques and surface-sensitive techniques (XPS, LEED, LT-STM, and AFM), we characterized MnO(001), Mn_3O_4(001), and α-Mn_2O_3 catalysts. This study revealed that the overpotential for oxygen evolution decreases with the oxidation state present in the oxide phase and confirmed that the actual active phase for OER does not depend on the initial oxide structure. The precluding phase only influences the overpotential required to transform into the active phase, impacting efficiency and activity.

In short, throughout this thesis, the dynamic chemical and structural changes that occur on model electrodes during electrochemical processes relevant for sustain-

able energy and catalysis, such as electro-oxidation and OER, have been uncovered. The studies presented in this thesis emphasized the power of performing synergistic studies between UHV and EC to gain a comprehensive understanding of electrochemical processes and surface catalyst changes. This approach has demonstrated its power for revealing, among other possibilities, the surface-potential-dependent reaction dynamics and the role of electrolyte ions in specifically targeting the actual active phase. By covering these target roles, key prerequisites for designing new surfaces with specific catalytic properties can be identified.

Appendix A
List of Publications

Publications closely related to this thesis:

1. M. Peña-Díaz, J. Redondo, P. Kumar, S. Auras, G. Harlow, E. Lundgren, B. Šmíd, S. Ju, J. Mysliveček, C. Rogero, S. Barja **Revisiting Au(111) electrooxidation in H_2SO_4: a combined electrochemistry and surface science approach** *In preparation.*

2. M. Peña-Díaz, Andrea Aguirre, J.F. Vélez-Santa, Maxim Ilyn, Sara Barja, Celia Rogero **Chemical, strcutural and catalytic properties of manganese oxide-based anodes for oxygen evolution reaction: a quasi-*in situ* UHV-EC approach** *In preparation.*

Other relevant publications:

1. A. Aguirre, A. Pinar, C. González-Orellana, J. Ortuzar, O. Stesovych, M. Peña-Díaz, J. Dreiser, M. Muntwiler, C. Rogero, J.I. Pascual, P. Jelínek, M. Ilyn and M. Corso. **Tunable ferromagnetic order in 2D layers of Transition Metal Dichlorides.** *Adv. Mater. 2402723, Abr 2024*

2. SE. Hadjadj, C. González-Orellana, J. Lawrence, D. Bikaljevic, M. Peña-Díaz, P. Gargiani, L. Aballe, J. Naumann, M.A. Niño, M. Foerster, S. Ruíz-Gómez, S. Thakur, I. Kumberg, J. Taylor, J. Hayes, J. Torres, C. Luo, F. Radu, D.G. de Oteyza, W. Kuch, J.I. Pascual, C. Rogero and M. Ilyn. Epitaxial monolayers of magnetic 2D semiconductor $FeBr_2$ grown on Au(111). *ACS Chem. Mater. 35(23), 9847-9856, Nov 2023*

3. J. Yu, F.A. Garcés-Pineda, J.González-Cobos, M. Peña-Díaz, C. Rogero, S. Giménez, M.C. Spadaro, J. Arbiol, S. Barja, J.R. Galán-Mascarós. **Sustainable oxygen evolution electrocatalysis in aqueous 1M H_2SO_4 with earth abundant nanostructured Co_3O_4.***Nature Comm. 13, 4637, Jul 2022*

4. D. Bikaljević, C. González-Orellana, M. Peña-Díaz, D. Steiner, J. Dreiser, P. Gargiani, M. Foerster, M.A. Niño, L. Aballe, S. Ruiz-Gomez, N.s Friedrich,

J. Hieulle, L. Jingcheng, M.Ilyn, C. Rogero, and J.I. Pascual **Noncollinear Magnetic Order in Two-Dimensional $NiBr_2$ Films Grown on Au(111).** *ACS Nano. 15(9), 14985–14995, Sep 2021*

5. A.O. Fumega, M. Gobbi, P. Dreher, W. Wan, C. González-Orellana, M. Peña-Díaz, C. Rogero, J. Herrero-Martín, P. Gargiani, M. Ilin, M.M. Ugeda, V. Pardo and S. Blanco-Canosa. **Absence of ferromagnetism in VSe caused by its charge density wave phase.** *Journal of Physical Chemistry C 2019, 123, 45, 27802–27810, July 2019*

Appendix B
Curriculum Vitae

Marina Peña Díaz

PERSONAL DATA

mpena056@ikasle.ehu.eus

July 18th, 1995

SKILLS

- Electrochemistry
- Research & Innovation
- Process Implementation
- Responsible, organized and highly committed person
- Great communication skills
- Excellent teamwork
- Resolute
- Capacity to work independently

ACADEMIC BACKGROUND

University of the Basque Country (UPV/EHU), Gipuzkoa | **2018 - now**

Ph.D.'s:
Physics of Nanostructures and Advanced Materials.
Short-term stay (1 month) in Alicante University (UA)

Autonomus University of Barcelona (UAB), Barcelona | **2017 - 2018**

Master's:
Electrochemistry. Science and Technology.
Short-term stay (2 months) in Alicante University (UA)

Autonomous University of Barcelona (UAB), Barcelona | **2013 - 2017**

Bachelor's:
Chemistry
Specialization in Green Chemistry and Industrial Chemistry.

R&D EXPERIENCE

Tecnalia Research and Innovation - **Researcher**
Gipuzkoa | **06/2021 - now**

Materials Physics Center (CFM-CSIC-UPV/EHU) - **Predoctoral Researcher**
Gipuzkoa | **10/2018 - now**
"Synergistic Study of Surface Science and Electrochemistry: Unraveling the Mechanisms of Oxygen Evolution Reaction" (PH.D. Thesis).

Catalan Insitute of Nanoscience and Nanotechnology (ICN2) - **Master's degree Internship**
Barcelona | 09/2017 - 08/2018
"Three-dimensional graphene-based microelectrode arrays for neural interfaces" (MSc Thesis).

Universitat Autònoma de Barcelona (UAB) - **Final Degree Internship**
Barcelona | 09/2016 - 08/2017
"Surface modification. An electrochemical approach" (BSc Thesis)

LENGUAGES

Spanish, Catalan : Native
English :B2

Bibliography

[1]S. Shafiee et al., "When will fossil fuel reserves be diminished?", Energy Policy **37**, 181–189 (2009).

[2]V. Ramanathan et al., "Air pollution, greenhouse gases and climate change: global and regional perspectives", Atmospheric Environment **43**, Atmospheric Environment - Fifty Years of Endeavour, 37–50 (2009).

[3]S. E. Hosseini et al., "Hydrogen production from renewable and sustainable energy resources: promising green energy carrier for clean development", Renewable and Sustainable Energy Reviews **57**, 850–866 (2016).

[4]K. Devi Renuka et al., "Unitized regenerative fuel cells: future of renewable energy research", in *Renewable energy technologies* (John Wiley Sons, Ltd, 2022) Chap. 11, pp. 375–402.

[5]N. Sasikala et al., "Bifunctional electrocatalyst for oxygen/air electrodes", Energy Conversion and Management **77**, 545–549 (2014).

[6]B. Paul et al., "Pem unitised reversible/regenerative hydrogen fuel cell systems: state of the art and technical challenges", Renewable and Sustainable Energy Reviews **79**, 585–599 (2017).

[7]G. Milazzo et al., "Tables of standard electrode potentials", Journal of The Electrochemical Society **125**, 261C (1978).

[8]E. Fabbri et al., "Developments and perspectives of oxide-based catalysts for the oxygen evolution reaction", Catalysis Science and Technology **4**, 3800–3821 (2014).

[9]Q. Shi et al., "Robust noble metal-based electrocatalysts for oxygen evolution reaction", Chem. Soc. Rev. **48**, 3181–3192 (2019).

[10]I. C. Man et al., "Universality in oxygen evolution electrocatalysis on oxide surfaces", ChemCatChem **3**, 1159–1165 (2011).

[11]Z. W. Seh et al., "Combining theory and experiment in electrocatalysis: insights into materials design", Science **355**, eaad4998 (2017).

[12]N. Danilovic et al., "Activity-stability trends for the oxygen evolution reaction on monometallic oxides in acidic environments", Journal of Physical Chemistry Letters **5**, 2474–2478 (2014).

[13]C. C. L. McCrory et al., "Benchmarking hydrogen evolving reaction and oxygen evolving reaction electrocatalysts for solar water splitting devices", Journal of the American Chemical Society **137**, PMID: 25668483, 4347–4357 (2015).

[14]Y. Lin et al., "Electrocatalysts for the oxygen evolution reaction in acidic media", Advanced Materials **35**, 2210565 (2023).

[15]R. Subbaraman et al., "Trends in activity for the water electrolyser reactions on 3 d m (ni, co, fe, mn) hydr (oxy) oxide catalysts", Nature materials **11**, 550–557 (2012).

[16]M. S. Burke et al., "Revised oxygen evolution reaction activity trends for first-row transition-metal (oxy)hydroxides in alkaline media", The Journal of Physical Chemistry Letters **6**, PMID: 26722749, 3737–3742 (2015).

[17]M. Bajdich et al., "Theoretical investigation of the activity of cobalt oxides for the electrochemical oxidation of water", Journal of the American Chemical Society **135**, PMID: 23944254, 13521–13530 (2013).

[18]R. Frydendal et al., "Toward an active and stable catalyst for oxygen evolution in acidic media: ti-stabilized MnO_2", Advanced Energy Materials **5**, 1500991 (2015).

[19]Y. Gorlin et al., "A bifunctional nonprecious metal catalyst for oxygen reduction and water oxidation", Journal of the American Chemical Society **132**, PMID: 20839797, 13612–13614 (2010).

[20]P. Rüetschi et al., "Influence of Electrode Material on Oxygen Overvoltage: A Theoretical Analysis", The Journal of Chemical Physics **23**, 556–560 (1955).

[21]S. Trasatti, "Electrocatalysis by oxides — attempt at a unifying approach", Journal of Electroanalytical Chemistry and Interfacial Electrochemistry **111**, 125–131 (1980).

[22]M. T. Koper, "Thermodynamic theory of multi-electron transfer reactions: implications for electrocatalysis", Journal of Electroanalytical Chemistry **660**, Physics and Chemistry of Charge Transfer in Condensed Media, 254–260 (2011).

[23]J. Rossmeisl et al., "Electrolysis of water on (oxidized) metal surfaces", Chemical Physics **319**, Molecular Charge Transfer in Condensed Media - from Physics and Chemistry to Biology and Nanoengineering in honour of Alexander M. Kuznetsov on his 65th birthday, 178–184 (2005).

[24]J. Rossmeisl et al., "Electrolysis of water on oxide surfaces", Journal of Electroanalytical Chemistry **607**, Theoretical and Computational Electrochemistry, 83–89 (2007).

[25]P. P. Lopes et al., "Relationships between atomic level surface structure and stability/activity of platinum surface atoms in aqueous environments", ACS Catalysis **6**, 2536–2544 (2016).

[26]R. Li et al., "Insights into correlation among surface-structure-activity of cobalt-derived pre-catalyst for oxygen evolution reaction", Advanced Science **7**, 1902830 (2020).

[27]Y. Chida et al., "Experimental study platform for electrocatalysis of atomic-level controlled high-entropy alloy surfaces", Nature Communications **14**, 4492 (2023).

[28]C. Reece et al., "Moving from fundamental knowledge of kinetics and mechanisms on surfaces to prediction of catalyst performance in reactors", ACS Catalysis **11**, 3048–3066 (2021).

[29]G. A. Somorjai et al., *Introduction to surface chemistry and catalysis* (John Wiley & Sons, 2010).

[30]G. Ertl, "Reactions at surfaces: from atoms to complexity (nobel lecture)", Angewandte Chemie International Edition **47**, 3524–3535 (2008).

[31]D. J. O'Connor et al., *Surface analysis methods in materials science*, Vol. 23 (Springer Science & Business Media, 2013).

[32]S. Maier et al., "Unveiling the mechanism of water partial dissociation on ru(0001)", Phys. Rev. Lett. **112**, 126101 (2014).

[33]S. Maier et al., "Growth and structure of the first layers of ice on ru(0001) and pt(111)", Journal of the American Chemical Society **138**, PMID: 26844953, 3145–3151 (2016).

[34]J. Gong et al., "Surface science investigations of oxidative chemistry on gold", Accounts of Chemical Research **42**, PMID: 19588952, 1063–1073 (2009).

[35]O. Brummel et al., "Electrifying oxide model catalysis: complex electrodes based on atomically-defined oxide films", Catalysis Letters **150**, 1546–1560 (2020).

[36]J. Matthiesen et al., "Observation of all the intermediate steps of a chemical reaction on an oxide surface by scanning tunneling microscopy", ACS Nano **3**, PMID: 19309169, 517–526 (2009).

[37]J. Fester et al., "Edge reactivity and water-assisted dissociation on cobalt oxide nanoislands", Nature Communications **8**, 14169 (2017).

[38]R. Mu et al., "Structural motifs of water on metal oxide surfaces", Chemical Society Reviews **46**, 1785–1806 (2017).

[39]S. Trasatti, "Surface science and electrochemistry: concepts and problems", Surface Science **335**, Proceedings of the IUVSTA Workshop on Surface Science and Electrochemistry, 1–9 (1995).

[40]D. M. Kolb, "Electrochemical surface science: past, present and future", Journal of Solid State Electrochemistry **15**, 1391–1399 (2011).

[41]M. P. Mercer et al., "Ultrahigh vacuum and electrocatalysis – the powers of quantitative surface imaging", Nano Energy **29**, Electrocatalysis, 394–413 (2016).

[42]E. Pastor et al., "Complementary probes for the electrochemical interface", Nature Reviews Chemistry **8**, 159–178 (2024).

[43]M. P. Soriaga, "Ultra-high vacuum techniques in the study of single-crystal electrode surfaces", Progress in Surface Science **39**, 325–443 (1992).

[44]M. P. Soriaga, "Surface analysis for electrochemistry: ultrahigh vacuum techniques", in *Encyclopedia of analytical chemistry* (John Wiley Sons, Ltd, 2006).

[45]H.-H. Strehblow et al., "Corrosion mechanisms in theory and practice", New York, USA **221** (1995).

[46]W. Hansen et al., "An esca study on emersed electrodes", Journal of Electroanalytical Chemistry and Interfacial Electrochemistry **110**, 369–373 (1980).

[47]L.-W. H. Leung et al., "A new combined ultrahigh vacuum and electrochemical apparatus", Review of Scientific Instruments **62**, 1857–1858 (1991).

[48]F. Reniers, "The development of a transfer mechanism between uhv and electrochemistry environments", Journal of Physics D: Applied Physics **35**, R169 (2002).

[49]J. Kelber et al., "Adsorbate-catalyzed anodic dissolution and oxidation at surfaces in aqueous solutions", Surface and Interface Analysis **31**, 431–441 (2001).

[50]R. A. Wong et al., "Bridging electrochemistry and ultrahigh vacuum: "unburying" the electrode–electrolyte interface", Accounts of Chemical Research **56**, PMID: 37384820, 2015–2025 (2023).

[51]R. A. Wong et al., "Probing consequences of anion-dictated electrochemistry on the electrode/monolayer/electrolyte interfacial properties", Nature Communications **11**, 4194 (2020).

[52]M. D. Lay et al., "Formation of sulfur atomic layers on gold from aqueous solutions of sulfide and thiosulfate: studies using ec-stm, uhv-ec, and tlec", Langmuir **19**, 8416–8427 (2003).

[53]Y. Gründer et al., "Potential-dependent surface compression of gold and its link to electrocatalytic reactivity", Surface Science **680**, 113–118 (2019).

[54]Y. Miura et al., "Nondestructive and repeatable capacitance - voltage and current - voltage measurements across the oxide/electrolyte interface by uhv-electrochemistry approach", Applied Physics Express **7**, 095802 (2014).

[55]J. Wisniak, "Jöns jacob berzelius a guide to the perplexed chemist", The chemical educator **5**, 343–350 (2000).

[56]P. van Leeuwen, *Homogeneous catalysis: understanding the art* (Springer Netherlands, 2004).

[57]E. Santos et al., "Fundamental aspects of electrocatalysis", Chemical Physics **332**, 39–47 (2007).

[58]M. J. Hülsey et al., "Promoting heterogeneous catalysis beyond catalyst design", Chemical science **11**, 1456–1468 (2020).

[59]D. Pletcher et al., *Instrumental methods in electrochemistry* (Elsevier, 2001).

[60]A. Fisher, "Electrode dynamics vol. 34", Oxford Chemistry Primers (1996).

[61]E. Santos et al., "Electrochemical electron transfer: from marcus theory to electrocatalysis", in *Fuel cell catalysis* (John Wiley Sons, Ltd, 2009) Chap. 2, pp. 31–55.

[62]N. Eliaz et al., *Physical electrochemistry: fundamentals, techniques, and applications* (John Wiley Sons, 2019).

[63]E. Herrero et al., *Encyclopedia electrochemistry interfacial kinetics and mass transport*, 2003.

[64]A. Bard et al., *Encyclopedia of electrochemistry, index*, Encyclopedia of Electrochemistry (Wiley, 2007).

[65]D. M. Kolb, "Electrochemical surface science", Angewandte Chemie International Edition **40**, 1162–1181 (2001).

[66]U. Stimming et al., "Solid-state electrochemistry", Fundam. Electrochem., 2nd ed., John Wiley & Sons Ltd., Hoboken, 419–447 (2006).

[67]D. C. Grahame, "The electrical double layer and the theory of electrocapillarity.", Chemical Reviews **41**, PMID: 18895519, 441–501 (1947).

[68]S. N. Steinmann et al., "Understanding electrified interfaces", Nature Reviews Materials **6**, 289–291 (2021).

[69]C. H. Wu et al., "Probing electrode/electrolyte interfaces in situ by x-ray spectroscopies: old methods, new tricks", Physical Chemistry Chemical Physics **17**, 30229–30239 (2015).

[70]R. I. Masel, *Principles of adsorption and reaction on solid surfaces*, Vol. 3 (John Wiley & Sons, 1996).

[71]W. Schmickler et al., *Interfacial electrochemistry* (Springer Berlin Heidelberg, 2010).

[72]D. Kolb, "Reconstruction phenomena at metal-electrolyte interfaces", Progress in Surface Science **51**, 109–173 (1996).

[73]S. Narasimhan et al., "Elastic stress domains and the herringbone reconstruction on au(111)", Phys. Rev. Lett. **69**, 1564–1567 (1992).

[74]D. Abernathy et al., "Reconstruction of the (111) and (001) surfaces of au and pt: thermal behavior", Surface science **283**, 260–276 (1993).

[75]H. Melle et al., Zeitschrift für Naturforschung A **33**, 282–289 (1978).

[76]A. Dakkouri, "Reconstruction phenomena at gold/electrolyte interfaces: an in-situ stm study of au(100)", Solid State Ionics **94**, Papers from the International Workshop, 99–114 (1997).

[77]M. Pourbaix, "Atlas of electrochemical equilibria in aqueous solutions", NACE (1966).

[78]K. S. Exner et al., "Ligand effects and their impact on electrocatalytic processes exemplified with the oxygen evolution reaction (oer) on ruo2(110)", ChemElectroChem **2**, 707–713 (2015).

[79]H. Dau et al., "The mechanism of water oxidation: from electrolysis via homogeneous to biological catalysis", ChemCatChem **2**, 724–761 (2010).

[80]P. Rüetschi et al., "Influence of Electrode Material on Oxygen Overvoltage: A Theoretical Analysis", The Journal of Chemical Physics **23**, 556–560 (1955).

[81]A. J. Medford et al., "From the sabatier principle to a predictive theory of transition-metal heterogeneous catalysis", Journal of Catalysis **328**, Special Issue: The Impact of Haldor Topsøe on Catalysis, 36–42 (2015).

[82]G. Ertl et al., *Handbook of heterogeneous catalysis*, Vol. 2 (VCH Weinheim, 1997).

[83]J. Tafel, Zeitschrift für Physikalische Chemie **50U**, 641–712 (1905).

[84]A. Hickling et al., "Oxygen overvoltage. part i. the inffluence of electrode material, current density, and time in aqueous solution", Discussions of the Faraday Society **1**, 3800–3821 (1947).

[85]P. Rüetschi et al., "Influence of Electrode Material on Oxygen Overvoltage: A Theoretical Analysis", The Journal of Chemical Physics **23**, 556–560 (2004).

[86]J. O. Bockris et al., "The mechanism of the electrolytic evolution of oxygen on platinum", Proceedings of the Royal Society of London. Series A, Mathematical and Physical Sciences **237**, 277–296 (1956).

[87]S. Trasatti, "Reaction mechanism and rate determining steps", in *Handbook of fuel cells* (John Wiley Sons, Ltd, 2010).

[88]P. Cavaliere, *Water electrolysis for hydrogen production* (Springer Nature, 2023).

[89]Y.-H. Fang et al., "Tafel kinetics of electrocatalytic reactions: from experiment to first-principles", ACS Catalysis **4**, 4364–4376 (2014).

[90]B. Conway et al., "Electrochemical reaction orders: applications to the hydrogen- and oxygen-evolution reactions", Electrochimica Acta **9**, 1599–1615 (1964).

[91]S. Trasatti, "Reaction mechanism and rate determining steps", in *Handbook of fuel cells* (John Wiley Sons, Ltd, 2010).

[92]C. C. L. McCrory et al., "Benchmarking heterogeneous electrocatalysts for the oxygen evolution reaction", Journal of the American Chemical Society **135**, PMID: 24171402, 16977–16987 (2013).

[93]J. Yu et al., "Sustainable oxygen evolution electrocatalysis in aqueous 1 m H_2SO_4 with earth abundant nanostructured Co_3O_4", Nature communications **13**, 4341 (2022).

[94]M. Huynh et al., "Nature of activated manganese oxide for oxygen evolution", Journal of the American Chemical Society **137**, PMID: 26574923, 14887–14904 (2015).

[95]T. Shinagawa et al., "Insight on tafel slopes from a microkinetic analysis of aqueous electrocatalysis for energy conversion", Scientific reports **5**, 13801 (2015).

[96]A. Damjanovic et al., "Kinetics of oxygen evolution and dissolution on platinum electrodes", Electrochimica Acta **11**, 791–814 (1966).

[97]M. Gong et al., "An advanced ni–fe layered double hydroxide electrocatalyst for water oxidation", Journal of the American Chemical Society **135**, PMID: 23701670, 8452–8455 (2013).

[98]P. Vanysek, "Electrochemical series", CRC handbook of chemistry and physics **8**, 8–33 (2000).

[99]J.-M. Savéant, *Elements of molecular and biomolecular electrochemistry: an electrochemical approach to electron transfer chemistry* (John Wiley & Sons, 2006).

[100]N. Elgrishi et al., "A practical beginner's guide to cyclic voltammetry", Journal of Chemical Education **95**, 197–206 (2018).

[101]A. J. Bard et al., "Fundamentals and applications", Electrochemical methods **2**, 580–632 (2001).

[102]K. S. Harsha, *Principles of vapor deposition of thin films* (Elsevier, 2005).

[103]S. Rossnagel, "Thin film deposition with physical vapor deposition and related technologies", Journal of Vacuum Science & Technology A: Vacuum, Surfaces, and Films **21**, S74–S87 (2003).

[104]H. Hertz, "Ueber einen einfluss des ultravioletten lichtes auf die electrische entladung", Annalen der Physik **267**, 983–1000 (1887).

[105]A. Einstein, "Über einen die erzeugung und verwandlung des lichtes betreffenden heuristischen gesichtspunkt", Annalen der Physik **322**, 132–148 (1905).

[106]K. Siegbahn, "Esca: atomic, molecular and solid state structure studies by means of electron spectroscopy", Nova Acta Regiae Societatis Scientiarum Upsaliensis (1967).

[107]S. Hüfner, "Valence orbitals in simple molecules and insulating solids", in *Photoelectron spectroscopy: principles and applications* (Springer Berlin Heidelberg, Berlin, Heidelberg, 2003), pp. 211–345.

[108]J. F. Watts et al., *An introduction to surface analysis by xps and aes* (John Wiley & Sons, 2019).

[109]D. A. Shirley, "High-resolution x-ray photoemission spectrum of the valence bands of gold", Phys. Rev. B **5**, 4709–4714 (1972).

[110]C. Fadley, "Basic concepts of x-ray photoelectron spectroscopy", Electron spectroscopy: theory, techniques and applications **2**, 1–156 (1978).

[111]K. Bomben et al., "Handbook of x-ray photoelectron spectroscopy: a reference book of standard spectra for identification and interpretation of xps data", Eden Prairie, MN (USA): Physical electronics (1995).

[112]F. Jona et al., "Low-energy electron diffraction for surface structure analysis", Reports on Progress in Physics **45**, 527 (1982).

[113]P. Worsfold et al., *Encyclopedia of analytical science* (Elsevier, 2019).

[114]G. Binnig et al., "Surface studies by scanning tunneling microscopy", Phys. Rev. Lett. **49**, 57–61 (1982).

[115]C. J. Chen, *Introduction to scanning tunneling microscopy third edition*, Vol. 69 (Oxford University Press, USA, 2021).

[116]S. M, "Sketch of a scanning tunneling microscope",

[117]M. Peuckert et al., "On the surface oxidation of a gold electrode in 1n H_2S0_4 electrolyte", Surface Science **141**, 515–532 (1984).

[118]K. Juodkazis et al., "Xps studies on the gold oxide surface layer formation", Electrochemistry Communications **2**, 503–507 (2000).

[119]F. J. Rodríguez Nieto et al., "Scanning tunneling microscopy, voltammetry, and x-ray photoelectron spectroscopy study of the early stages of electrochemical faceting of au(111) in aqueous sulfuric and perchloric acid", The Journal of Physical Chemistry B **107**, 11452–11466 (2003).

[120]Ž. Petrović et al., "A multi-technique study of gold oxidation and semiconducting properties of the compact -oxide layer", Journal of Electroanalytical Chemistry **629**, 43–49 (2009).

[121]U. Zhumaev et al., "Electro-oxidation of au(111) in contact with aqueous electrolytes: new insight from in situ vibration spectroscopy", Electrochimica Acta **112**, 853–863 (2013).

[122]S. Axnanda et al., "Using "tender" x-ray ambient pressure x-ray photoelectron spectroscopy as a direct probe of solid-liquid interface", Scientific reports **5**, 9788 (2015).

[123]O. Brummel et al., "A versatile approach to electrochemical in situ ambient-pressure x-ray photoelectron spectroscopy: application to a complex model catalyst", The Journal of Physical Chemistry Letters **13**, 11015–11022 (2022).

[124]J.-J. Velasco-Vélez et al., "A comparative study of electrochemical cells for in situ x-ray spectroscopies in the soft and tender x-ray range", Journal of Physics D: Applied Physics **54**, 124003 (2021).

[125]M. Favaro et al., "Spectroscopic analysis with tender x-rays: spantex, a new ap-haxpes end-station at bessy ii", Surface Science **713**, 121903 (2021).

[126]S. Nappini et al., "Soft x-ray spectroscopies in liquids and at solid–liquid interface at BACH beamline at Elettra", Review of Scientific Instruments **92**, 015115 (2021).

[127]S. Zhu et al., "Hippie: a new platform for ambient-pressure x-ray photoelectron spectroscopy at the max iv laboratory", Journal of synchrotron radiation **28**, 624–636 (2021).

[128]Z. Novotny et al., "Probing the solid–liquid interface with tender x rays: A new ambient-pressure x-ray photoelectron spectroscopy endstation at the Swiss Light Source", Review of Scientific Instruments **91**, 023103 (2020).

[129]M. Favaro et al., "Unravelling the electrochemical double layer by direct probing of the solid/liquid interface", Nature communications **7**, 12695 (2016).

[130]T. Masuda et al., "In situ x-ray photoelectron spectroscopy for electrochemical reactions in ordinary solvents", Applied Physics Letters **103** (2013).

[131]L. Haug et al., "A laboratory-based multifunctional near ambient pressure X-ray photoelectron spectroscopy system for electrochemical, catalytic, and cryogenic studies", Review of Scientific Instruments **94**, 065104 (2023).

[132]C. Arble et al., "Lab-based ambient pressure x-ray photoelectron spectroscopy from past to present", Surface Science Reports **73**, 37–57 (2018).

[133]C. Griesser et al., "Lab-based electrochemical x-ray photoelectron spectroscopy for in-situ probing of redox processes at the electrified solid/liquid interface", Electrochemical Science Advances **n/a**, e2300007.

[134]J. J. V. Vélez et al., "The rise of electrochemical napxps operated in the soft x-ray regime exemplified by the oxygen evolution reaction on iro x electrocatalysts", Faraday discussions **236**, 103–125 (2022).

[135]J. Hammond et al., "Xps spectroscopic study of potentiostatic and galvanostatic oxidation of pt electrodes in H_2SO_4 and $HClO_4$", Journal of Electroanalytical Chemistry and Interfacial Electrochemistry **78**, 55–69 (1977).

[136]R. Ansell et al., "X-ray photoelectron spectroscopic studies of electrode surfaces using a new controlled transfer technique: part i. description of apparatus and preliminary studies", Journal of Electroanalytical Chemistry and Interfacial Electrochemistry **98**, 69–77 (1979).

[137]J. Schnaidt et al., "A combined uhv-stm-flow cell set-up for electrochemical/electrocatalytic studies of structurally well-defined uhv prepared model electrodes", Physical Chemistry Chemical Physics **19**, 4166–4178 (2017).

[138]F. Faisal et al., "Preparation of complex model electrocatalysts in ultra-high vacuum and transfer into the electrolyte for electrochemical IR spectroscopy and other techniques", Review of Scientific Instruments **89**, 114101 (2018).

[139]T. Maagaard et al., "On the possibilities and considerations of interfacing ultra-high vacuum equipment with an electrochemical setup", ChemPhysChem **20**, 3024–3029 (2019).

[140]R. A. Wong et al., "Stepping beyond cyclic voltammetry: obtaining the electronic and structural properties of electrified solid–liquid interfaces", Current Opinion in Electrochemistry **34**, 100964 (2022).

[141]D. Aberdam et al., "Structural changes of a pt(111) electrode induced by electrosorption of oxygen in acidic solutions: a coupled voltammetry, leed and aes study", Surface Science **171**, 303–330 (1986).

[142]M. E. Hanson et al., "Low-energy electron diffraction, x-ray photoelectron spectroscopy, and auger electron spectroscopy", in *Electrochemical surface science* () Chap. 10, pp. 141–153.

[143]T. Solomun et al., "Electrochemical reactivity of ordered and disordered n-gaas(110) surfaces. a combined xps, leed and electrochemical study", Berichte der Bunsengesellschaft für physikalische Chemie **91**, 412–416 (1987).

[144]G. Attard et al., "Palladium adsorption on pt(111): a combined electrochemical and ultra-high vacuum study", Electrochimica Acta **39**, 1525–1530 (1994).

[145]A. Wieckowski, *Interfacial electrochemistry: theory: experiment, and applications* (CRC press, 1999).

[146]P. Mrozek et al., "Sulfate adsorption on a au(111) electrode studied by aes, ceels, leed and cyclic voltammetry", Surface Science **319**, 21–33 (1994).

[147]M. Zei et al., "The structure of H_2SO_4 monolayers on au (111)", Journal of Electroanalytical Chemistry and Interfacial Electrochemistry **229**, 99–105 (1987).

[148]W. N. Hansen, "Electrode resistance and the emersed double layer", Surface Science **101**, 109–122 (1980).

[149]W. Hansen et al., "The work function of emersed electrodes", Journal of Electroanalytical Chemistry and Interfacial Electrochemistry **100**, 493–500 (1979).

[150]H. Neff et al., "Photoelectron spectroscopic study of emersed gold electrodes", Journal of Electroanalytical Chemistry and Interfacial Electrochemistry **151**, 305–310 (1983).

[151]B. Wurster, *Two-dimensional metal-organic networks as a new class of electrocatalysts*, tech. rep. (EPFL, 2015).

[152]D. Grumelli et al., "Bio-inspired nanocatalysts for the oxygen reduction reaction", Nature communications **4**, 2904 (2013).

[153]V. Climent et al., "Surface electrochemistry with pt single-crystal electrodes", Advances in Electrochemical Science and Engineering: Nanopatterned and Nanoparticle-Modified Electrodes **17**, 1–57 (2017).

[154]V. Climent et al., "Electrochemical behavior of single crystal electrodes on model processes", in *Springer handbook of surface science*, edited by M. Rocca et al. (Springer International Publishing, Cham, 2020), pp. 1117–1158.

[155]I. Ledezma-Yanez et al., "Interfacial water reorganization as a ph-dependent descriptor of the hydrogen evolution rate on platinum electrodes", Nature Energy **2**, 1–7 (2017).

[156]L. Burke et al., "The electrochemistry of gold: i the redox behaviour of the metal in aqueous media", Gold Bulletin **30**, 43–53 (1997).

[157]M. Schneeweiss et al., "Oxide formation on au(111) an in situ stm study", Solid State Ionics **94**, Papers from the International Workshop, 171–179 (1997).

[158]T. Kondo et al., "Structure of au(111) and au(100) single-crystal electrode surfaces at various potentials in sulfuric acid solution determined by in situ surface x-ray scattering", The Journal of Physical Chemistry C **111**, 13197–13204 (2007).

[159]T. Kondo et al., "In situ real-time study on potential induced structure change at au(111) and au(100) single crystal electrode/sulfuric acid solution interfaces by surface x-ray scattering", Surface Science **631**, Surface Science and Electrochemistry - 20 years later, 96–104 (2015).

[160]W. Linpé et al., "Revisiting optical reflectance from au(111) electrode surfaces with combined high-energy surface x-ray diffraction", Journal of The Electrochemical Society **168**, 096511 (2021).

[161]O. Diaz-Morales et al., "Electrochemical water splitting by gold: evidence for an oxide decomposition mechanism", Chemical Science **4**, 2334–2343 (2013).

[162]B. S. Yeo et al., "Identification of hydroperoxy species as reaction intermediates in the electrochemical evolution of oxygen on gold", ChemPhysChem **11**, 1854–1857 (2010).

[163]S. Yang et al., "Redefinition of the active species and the mechanism of the oxygen evolution reaction on gold oxide", ACS Catalysis **10**, 12582–12589 (2020).

[164]B. E. Conway, "Electrochemical oxide film formation at noble metals as a surface-chemical process", Progress in surface science **49**, 331–452 (1995).

[165]A. Hamelin, "Cyclic voltammetry at gold single-crystal surfaces. part 1. behaviour at low-index faces", Journal of Electroanalytical Chemistry **407**, 1–11 (1996).

[166]W. ZHANG et al., "Passive behavior of gold in sulfuric acid medium", Transactions of Nonferrous Metals Society of China **25**, 2037–2046 (2015).

[167]H. Angerstein-Kozlowska et al., "Elementary steps of electrochemical oxidation of single-crystal planes of au—i. chemical basis of processes involving geometry of anions and the electrode surfaces", Electrochimica Acta **31**, 1051–1061 (1986).

[168]H. Angerstein-Kozlowska et al., "Elementary steps of electrochemical oxidation of single-crystal planes of au part ii. a chemical and structural basis of oxidation of the (111) plane", Journal of Electroanalytical Chemistry and Interfacial Electrochemistry **228**, 429–453 (1987).

[169]N. Cabrera et al., "Theory of the oxidation of metals", Reports on Progress in Physics **12**, 163 (1949).

[170]A. Chen et al., "Electrochemical and spectroscopic studies of hydroxide adsorption at the au(111) electrode", The Journal of Physical Chemistry B **103**, 682–691 (1999).

[171]G. Tremiliosi-Filho et al., "Limit to extent of formation of the quasi-two-dimensional oxide state on au electrodes", Journal of Electroanalytical Chemistry **422**, 149–159 (1997).

[172]J. S. Gordon et al., "Application of an electrochemical quartz crystal microbalance to a study of water adsorption at gold surfaces in acidic media", Journal of Electroanalytical Chemistry **365**, An International Journal Devoted to all Aspects of Electrode Kinetics, Interfacial Structure, Properties of Electrolytes, Colloid and Biological Electrochemistry, 267–274 (1994).

[173]U. Oesch et al., "Electrochemical study of gold electrodes with anodic oxide films—i. formation and reduction behaviour of anodic oxides on gold", Electrochimica Acta **28**, 1237–1246 (1983).

[174]R. Sirohi et al., "Electrochemical ellipsometric study of gold", Journal of the Electrochemical Society **116**, 910 (1969).

[175]S. Barnartt, "The oxygen-evolution reaction at gold anodes: i. accuracy of overpotential measurements", Journal of The Electrochemical Society **106**, 722 (1959).

[176]Z. Shi et al., "Investigations of SO_4^2 adsorption at the au(111) electrode in the presence of underpotentially deposited copper adatoms", Journal of Electroanalytical Chemistry **364**, An International Journal Devoted to All Aspects of Electrode Kinetics, Interfacial Structure Properties of Electrolytes, Colloid and Biological Electrochemistry, 289–294 (1994).

[177]L. A. Kibler et al., "New insights on hydrogen evolution at au single crystal electrodes", Current Opinion in Electrochemistry **9**, 265–270 (2018).

[178]Y. Fang et al., "Revisiting the atomistic structures at the interface of au(111) electrode–sulfuric acid solution", Journal of the American Chemical Society **142**, PMID: 32338907, 9439–9446 (2020).

[179]J. Lipkowski et al., "Ionic adsorption at the au(111) electrode", Electrochimica Acta **43**, 2875–2888 (1998).

[180]O. M. Magnussen, "Ordered anion adlayers on metal electrode surfaces", Chemical Reviews **102**, PMID: 11890754, 679–726 (2002).

[181]C. Köntje et al., "Roughening and long-range nanopatterning of au(111) through potential cycling in aqueous acidic media", Langmuir **29**, PMID: 23855899, 10272–10278 (2013).

[182]G. J. Edens et al., "The adsorption of sulfate on au(111) in acidic aqueous media: adlayer structural inferences from infrared spectroscopy and scanning tunneling microscope", Journal of Electroanalytical Chemistry **375**, 357–366 (1994).

[183]A. Cuesta et al., "The adsorption of sulfate and phosphate on au (111) and au (100) electrodes: an in situ stm study", Physical Chemistry Chemical Physics **2**, 5684–5690 (2000).

[184]B. Braunschweig et al., "Superstructures and orderdisorder transition of sulfate adlayers on pt(111) in sulfuric acid solution", Langmuir **25**, PMID: 19456179, 11112–11120 (2009).

[185]S. Venkatachalam et al., "The au (111) electrolyte interface: a dft investigation", Verhandlungen der Deutschen Physikalischen Gesellschaft **43** (2008).

[186]O. M. Magnussen et al., "In situ scanning tunnelling microscopy observations of a disorder-order phase transition in hydrogensulfate adlayers on au (111)", Faraday Discussions **94**, 329–338 (1992).

[187]R. Frankenthal et al., "The anodic behavior of gold in sulfuric acid solutions: effect of chloride and electrode potential", Journal of The Electrochemical Society **123**, 799 (1976).

[188]X. W. Xiangnan Chen et al., "A review on c1s xps-spectra for some kinds of carbon materials", Fullerenes, Nanotubes and Carbon Nanostructures **28**, 1048–1058 (2020).

[189]W. Luo et al., "XPS Characterization of Metal-free Functionalized Carbons", in *Metal-free Functionalized Carbons in Catalysis: Synthesis, Characterization and Applications* (The Royal Society of Chemistry, May 2018).

[190]J. Hill et al., "Properties of oxidized silicon as determined by angular-dependent x-ray photoelectron spectroscopy", Chemical Physics Letters **44**, 225–231 (1976).

[191]R. O. de la Morena et al., "Shape controlled assembly of carboxylic acids: formation of a binary monolayer by intercalation into molecular nanotunnels", Physical Chemistry Chemical Physics **22**, 4205–4215 (2020).

[192]Z. Zhang et al., "Surface sulfate ion on cds catalyst enhances syngas generation from biopolyols", Journal of the American Chemical Society **143**, PMID: 33904731, 6533–6541 (2021).

[193]X. Duan et al., "Sulfur moiety as a double-edged sword for realizing ultrafine supported metal nanoclusters with a cationic nature", ACS Applied Materials & Interfaces **11**, 11317–11326 (2019).

[194]D.-H. Kim et al., "Bioinspired cocatalysts decorated wo3 nanotube toward unparalleled hydrogen sulfide chemiresistor", ACS Sensors **3**, PMID: 29762012, 1164–1173 (2018).

[195]N. Comini et al., "Factors influencing surface carbon contamination in ambient-pressure x-ray photoelectron spectroscopy experiments", Journal of Vacuum Science & Technology A **39** (2021).

[196]D. Rochefort et al., "Xps investigations of thermally prepared RuO_2 electrodes in reductive conditions", Electrochimica Acta **48**, 4245–4252 (2003).

[197]L. A. Kibler, "Hydrogen electrocatalysis", ChemPhysChem **7**, 985–991 (2006).

[198]T. Dickinson et al., "X-ray photoelectron spectroscopic studies of oxide films on platinum and gold electrodes", Journal of the Chemical Society, Faraday Transactions 1: Physical Chemistry in Condensed Phases **71**, 298–311 (1975).

[199]Z. Wu et al., "Thiolate ligands as a double-edged sword for co oxidation on CeO_2 supported $Au_{25}(SCH_2CH_2Ph)_{18}Nanoclusters$", Journal of the American Chemical Society **136**, PMID: 24702268, 6111–6122 (2014).

[200]Z. Chen et al., "Understanding the selectivity trend of water and sulfate (SO_4^{2-}) oxidation on metal oxides: on-site synthesis of persulfate, h2o2 for wastewater treatment", Chemical Engineering Journal **431**, 134332 (2022).

[201]S. A. Shafiee et al., "Electroreduction of peroxodisulfate: a review of a complicated reaction", Journal of The Electrochemical Society **165**, H785 (2018).

[202]G. Ayyakannu Sundaram et al., "Synthesis, characterization, and enhanced sunlight-active photocatalytic property of single-site octahedral iron(iii) oxide complex – grafted graphene oxide", Journal of Alloys and Compounds **968**, 172068 (2023).

[203]Y. Tu et al., "Fabrication of reduced graphene oxide micro patterns by vacuum-ultraviolet irradiation: from chemical and structural evolution to improving patterning precision by light collimation", Carbon **119**, 82–90 (2017).

[204]D. V. Sivkov et al., "The identification of cu–o–c bond in cu/mwcnts hybrid nanocomposite by xps and nexafs spectroscopy", Nanomaterials **11**, 10.3390/nano11112993 (2021).

[205]Y. Kuang et al., "Photoactivated graphene oxide to enhance photocatalytic reduction of CO_2", ACS Applied Materials & Interfaces **12**, PMID: 31889436, 3580–3591 (2020).

[206]J. Chastain et al., "Handbook of x-ray photoelectron spectroscopy", Perkin-Elmer Corporation **40**, 221 (1992).

[207]M. Wahlqvist et al., "Xps spectra and electronic structure of group ia sulfates", Journal of Electron Spectroscopy and Related Phenomena **156-158**, Electronic Spectroscopy and Structure: ICESS-10, 310–314 (2007).

[208]A. A. Audi et al., "X-ray photoelectron spectroscopic studies of sulfates and bisulfates interpreted by x and band structure calculations", Surface and Interface Analysis **29**, 265–275 (2000).

[209]X. Wang et al., "Probing of photocatalytic surface sites on SO_4^{2-}/TiO_2 solid acids by in situ ft-ir spectroscopy and pyridine adsorption", Journal of Photochemistry and Photobiology A: Chemistry **179**, 339–347 (2006).

[210]S. Americo, "Electronic and catalytic properties of two-dimensional materials and van der waals heterostructures", English, PhD thesis (2023).

[211]F. Gossenberger et al., "Sulfate, bisulfate, and hydrogen co-adsorption on pt(111) and au(111) in an electrochemical environment", Frontiers in Chemistry **8**, 10.3389/fchem.2020.00634 (2020).

[212]K. K. TUREKIAN et al., "Distribution of the Elements in Some Major Units of the Earth's Crust", GSA Bulletin **72**, 175–192 (1961).

[213]J. E. Post, "Manganese oxide minerals: crystal structures and economic and environmental significance", Proceedings of the National Academy of Sciences **96**, 3447–3454 (1999).

[214]I. Zaharieva et al., "Electrosynthesis, functional, and structural characterization of a water-oxidizing manganese oxide", Energy & Environmental Science **5**, 7081–7089 (2012).

[215]Y. Li et al., "Activation of co over ultrathin manganese oxide layers grown on au(111)", ACS Catalysis **11**, 849–857 (2021).

[216]J. Zhang et al., "Catalytic oxidation of formaldehyde over manganese oxides with different crystal structures", Catalysis Science & Technology **5**, 2305–2313 (2015).

[217]H.-Y. Su et al., "Identifying active surface phases for metal oxide electrocatalysts: a study of manganese oxide bi-functional catalysts for oxygen reduction and water oxidation catalysis", Physical Chemistry Chemical Physics **14**, 14010–14022 (2012).

[218]B. Kang et al., "An effective way to improve bifunctional electrocatalyst activity of manganese oxide via control of bond competition", Applied Catalysis B: Environmental **236**, 107–116 (2018).

[219]K. N. Ferreira et al., "Architecture of the photosynthetic oxygen-evolving center", Science **303**, 1831–1838 (2004).

[220]R. J. Debus, "The manganese and calcium ions of photosynthetic oxygen evolution", Biochimica et Biophysica Acta (BBA) - Bioenergetics **1102**, 269–352 (1992).

[221]Ö. Hansson et al., "Current perceptions of photosystem ii", Photosynthesis research **23**, 131–162 (1990).

[222]A. Bergmann et al., "Unified structural motifs of the catalytically active state of co (oxyhydr) oxides during the electrochemical oxygen evolution reaction", Nature Catalysis **1**, 711–719 (2018).

[223]W. Niu et al., "Understanding synergism of cobalt metal and copper oxide toward highly efficient electrocatalytic oxygen evolution", ACS Catalysis **8**, 12030–12040 (2018).

[224]Z. Feng et al., "Catalytic activity and stability of oxides: the role of near-surface atomic structures and compositions", Accounts of Chemical Research **49**, PMID: 27149528, 966–973 (2016).

[225]A. Erbe et al., "Operando studies of mn oxide based electrocatalysts for the oxygen evolution reaction", Physical Chemistry Chemical Physics **25**, 26958–26971 (2023).

[226]H. Radinger et al., "Manganese oxide as an inorganic catalyst for the oxygen evolution reaction studied by x-ray photoelectron and operando raman spectroscopy", ChemCatChem **13**, 1175–1185 (2021).

[227]H. An et al., "An operando-raman study on oxygen evolution of manganese oxides: roles of phase composition and amorphization", Journal of Catalysis **367**, 53–61 (2018).

[228]Y. Gorlin et al., "In situ x-ray absorption spectroscopy investigation of a bifunctional manganese oxide catalyst with high activity for electrochemical water oxidation and oxygen reduction", Journal of the American Chemical Society **135**, PMID: 23758050, 8525–8534 (2013).

[229]S. Sasaki et al., "On the estimation of atomic charges by the x-ray method for some oxides and silicates", Acta Crystallographica Section A: Crystal Physics, Diffraction, Theoretical and General Crystallography **36**, 904–915 (1980).

[230]K. Satomi, "Oxygen positional parameters of tetragonal Mn_3O_4", Journal of the Physical Society of Japan **16**, 258–266 (1961).

[231]S. Geller, "Structure of α-Mn_2O_3,(mn0. 983fe0. 017) 2o3 and (mn0. 37fe0. 63) 2o3 and relation to magnetic ordering", Acta Crystallographica Section B: Structural Crystallography and Crystal Chemistry **27**, 821–828 (1971).

[232]W. H. Baur, "Rutile-type compounds. v. refinement of mno2 and mgf2", Acta Crystallographica Section B: Structural Crystallography and Crystal Chemistry **32**, 2200–2204 (1976).

[233]S. Buller et al., "Nanostructure in energy conversion", Journal of Energy Chemistry **25**, 171–190 (2016).

[234]D. M. Robinson et al., "Photochemical water oxidation by crystalline polymorphs of manganese oxides: structural requirements for catalysis", Journal of the American Chemical Society **135**, PMID: 23391134, 3494–3501 (2013).

[235]S. Mitra et al., "Novel p-type wide bandgap manganese oxide quantum dots operating at deep uv range for optoelectronic devices", Advanced Optical Materials **7**, 1900801 (2019).

[236]A. Hirohata et al., "Review on spintronics: principles and device applications", Journal of Magnetism and Magnetic Materials **509**, 166711 (2020).

[237]J. Wang et al., "Manganese oxide-based catalysts for sustainable synthesis of value-added chemicals through oxidation process: a critical review and perspective for future", Green Chemistry (2024).

[238]V. Anisimov et al., "Band-structure description of mott insulators (nio, mno, feo, coo)", Journal of Physics: Condensed Matter **2**, 3973 (1990).

[239]W. Feng-Ping et al., "Canted antiferromagnetic and optical properties of nanostructures of Mn_2O_3 prepared by hydrothermal synthesis", Chinese Physics B **21**, 117311 (2012).

[240]L. Narayani et al., "Mechanism of high temperature induced phase transformation and magnetic properties of Mn_3O_4 crystallites", Journal of Magnetism and Magnetic Materials **476**, 268–273 (2019).

[241]J. Melder et al., Zeitschrift für Physikalische Chemie **234**, 925–978 (2020).

[242]W. Wei et al., "Manganese oxide-based materials as electrochemical supercapacitor electrodes", Chemical society reviews **40**, 1697–1721 (2011).

[243]M. Ren et al., "Advances on manganese-oxide-based cathodes for na-ion batteries", Energy & Fuels **34**, 13412–13426 (2020).

[244]M. Langell et al., "Thermally induced surface reconstruction of mno(100)", Surface Science **185**, 105–119 (1987).

[245]V. S. Kumbhar et al., "Recent advances in water-splitting electrocatalysts based on manganese oxide", Carbon Resources Conversion **2**, 242–255 (2019).

[246]N. Baig et al., "Nanomaterials: a review of synthesis methods, properties, recent progress, and challenges", Materials Advances **2**, 1821–1871 (2021).

[247]F. Zaera, "Nanostructured materials for applications in heterogeneous catalysis", Chemical Society Reviews **42**, 2746–2762 (2013).

[248]D. M. Mattox, *Handbook of physical vapor deposition (pvd) processing* (William Andrew, 2010).

[249]C. E. Frey et al., "Evaporated manganese films as a starting point for the preparation of thin-layer mno x water-oxidation anodes", Sustainable Energy & Fuels **1**, 1162–1170 (2017).

[250]F. Müller et al., "Epitaxial growth of mno/ag(001) films", Surface Science **520**, 158–172 (2002).

[251]K. Gillmeister et al., "Surface reconstructions on $Mn_3O_4(001)$ films", Phys. Rev. B **105**, 195415 (2022).

[252]A. K. Kundu et al., "Stabilization of polar $Mn_3O_4(001)$ film on ag(001): interplay between kinetic and structural stability", Surface Science **664**, 207–215 (2017).

[253]D. H. Olson et al., "Structural and electrical characterization of amorphous and crystalline manganese oxide thin films deposited by dc magnetron sputtering", MRS Advances **1**, 3929–3934 (2016).

[254]F. Li et al., "Two-dimensional manganese oxide nanolayers on pd (100): the surface phase diagram", Journal of Physics: Condensed Matter **21**, 134008 (2009).

[255]C. Franchini et al., "Structural and vibrational properties of two-dimensional Mn_xO_y layers on pd(100): experiments and density functional theory calculations", Phys. Rev. B **79**, 035420 (2009).

[256]C. Franchini et al., "Interplay between magnetic, electronic, and vibrational effects in monolayer Mn_3O_4 grown on Pd(100)", The Journal of Chemical Physics **130**, 124707 (2009).

[257]A. K. Kundu et al., "Growth and characterization of ultrathin epitaxial mno film on ag(001)", Journal of Crystal Growth **446**, 85–91 (2016).

[258]A. Chassé et al., "Growth and structure of thin mno films on ag(001) in dependence on film thickness", Surface Science **602**, 597–606 (2008).

[259]M. Nagel et al., "Interface properties and electronic structure of ultrathin manganese oxide films on ag(001)", Surface Science **601**, ECOSS-24, 4484–4487 (2007).

[260]E. A. Soares et al., "Quantitative low-energy electron diffraction analysis of MnO(100) films grown on Ag(100)", Phys. Rev. B **73**, 035419 (2006).

[261]L. Zhang et al., "Growth and vibrational properties of mnox thin films on rh(111)", Surface Science **606**, 1507–1511 (2012).

[262]K. Liu et al., "An hreels investigation of mnox/rh(100) model catalyst", Surface Science **641**, 78–81 (2015).

[263]P. Chen et al., "Scanning tunneling microscopy of mnox ultrathin films on au(111)", Surface Science **730**, 122248 (2023).

[264]Y. Liu et al., "Dynamic structural evolution of mn–au alloy and mnox nanostructures on au(111) under different atmospheres", The Journal of Physical Chemistry C **125**, 15335–15342 (2021).

[265]G. Rizzi et al., "An x-ray photoelectron diffraction structural characterization of an epitaxial mno ultrathin film on pt(111)", Surface Science **482-485**, 1474–1480 (2001).

[266]C. Hagendorf et al., "Growth, atomic structure, and vibrational properties of mno ultrathin films on pt(111)", Phys. Rev. B **77**, 075406 (2008).

[267]S. Sachert et al., "Thickness dependent vibrational and electronic properties of mno(100) thin films grown on pt(111)", Phys. Rev. B **81**, 195424 (2010).

[268]V. Bayer et al., "Formation of Mn_3O_4(001) on mno(001): surface and interface structural stability", Phys. Rev. B **76**, 165428 (2007).

[269]E. Annese et al., "Mn_3O_4 Thin film on cu(111): modulating electronic structure through film–substrate interaction", The Journal of Physical Chemistry C **124**, 15162–15170 (2020).

[270]H. Nesbitt et al., American Mineralogist **83**, 305–315 (1998).

[271]E. S. Ilton et al., "Xps determination of mn oxidation states in mn (hydr)oxides", Applied Surface Science **366**, 475–485 (2016).

[272]V. Di Castro et al., "Xps study of mno oxidation", Journal of Electron Spectroscopy and Related Phenomena **48**, 117–123 (1989).

[273]J. H. Van Vleck, "The dirac vector model in complex spectra", Phys. Rev. **45**, 405–419 (1934).

[274]J. Foord et al., "An x-ray photoelectron spectroscopic investigation of the oxidation of manganese", Philosophical Magazine A **49**, 657–663 (1984).

[275]A. Bergmann et al., "Electrochemical water splitting by layered and 3d cross-linked manganese oxides: correlating structural motifs and catalytic activity", Energy & Environmental Science **6**, 2745–2755 (2013).

[276]A. Ramírez et al., "Evaluation of mnox, Mn_2O_3, and Mn_3O_4 electrodeposited films for the oxygen evolution reaction of water", The Journal of Physical Chemistry C **118**, 14073–14081 (2014).

[277]A. Indra et al., "Uncovering structure–activity relationships in manganese-oxide-based heterogeneous catalysts for efficient water oxidation", ChemSusChem **8**, 776–785 (2015).

[278]M. Morita et al., "The anodic characteristics of massive manganese oxide electrode", Electrochimica Acta **24**, 357–362 (1979).

[279]T. Takashima et al., "Inhibition of charge disproportionation of mno2 electrocatalysts for efficient water oxidation under neutral conditions", Journal of the American Chemical Society **134**, PMID: 23088413, 18153–18156 (2012).

[280]T. Takashima et al., "Mechanisms of ph-dependent activity for water oxidation to molecular oxygen by MnO_2 electrocatalysts", Journal of the American Chemical Society **134**, PMID: 22206433, 1519–1527 (2012).

[281]C. E. Frey et al., "Water oxidation catalysis by synthetic manganese oxides with different structural motifs: a comparative study", Chemistry–A European Journal **21**, 14958–14968 (2015).

[282]Y. Gorlin et al., "Investigation of surface oxidation processes on manganese oxide electrocatalysts using electrochemical methods and ex situ x-ray photoelectron spectroscopy", Journal of the Electrochemical Society **159**, H782 (2012).

[283]W. B. Pearson, *A handbook of lattice spacings and structures of metals and alloys: international series of monographs on metal physics and physical metallurgy, vol. 4*, Vol. 4 (Elsevier, 2013).

[284]K. Takayanagi et al., "Roles of lattice fitting in epitaxy", Thin Solid Films **48**, 137–152 (1978).

[285]G. Schön et al., "Esca studies of ag, Ag_2O and ago", Acta Chem. Scand **27**, 2623 (1973).

[286]P. Schieffer et al., "Initial growth and structure of mn on ag(100): formation of a superficial alloy", Solid State Communications **97**, 757–761 (1996).

[287]M. E. Keal et al., "Redox electrochemistry of mn(ii) via carbon black nanoparticle impacts", The Journal of Physical Chemistry C **127**, 13380–13388 (2023).

[288]P. Schieffer et al., "The early stages of growth of mn deposited at room temperature on ag (001) studied by mn k-edge sexafs and mn l2, l3-edges xas", Journal of Synchrotron Radiation **6**, 784–786 (1999).

[289]H. Poppa, "Model studies in catalysis with uhv-deposited metal particles and clusters", Vacuum **34**, 1081–1095 (1984).

[290]K. Reuter, "Nanometer and subnanometer thin oxide films at surfaces of late transition metals", in *Nanocatalysis*, edited by U. Heiz et al. (Springer Berlin Heidelberg, Berlin, Heidelberg, 2007), pp. 343–376.

[291]J. Uddin et al., "Phase tunable nickel doped Mn_3O_4 nanoparticle synthesis by chemical precipitation: kinetic study on dye degradation", Nanoscale Advances **6**, 902–909 (2024).

[292]X. Jiang et al., "Integral structured co-mn composite oxides grown on interconnected ni foam for catalytic toluene oxidation", RSC advances **9**, 6533–6541 (2019).

[293]Y.-F. Han et al., "Controlled synthesis, characterization, and catalytic properties of Mn_2O_3 and Mn_3O_4 nanoparticles supported on mesoporous silica sba-15", The Journal of Physical Chemistry B **110**, PMID: 17134200, 24450–24456 (2006).

[294]Y. Pei et al., "Insights into the electrochemical behavior of manganese oxides as catalysts for the oxygen reduction and evolution reactions: monometallic core-shell mn/mn3o4", Small **19**, 2204585 (2023).

[295]N. Yu et al., "High-performance fiber-shaped all-solid-state asymmetric supercapacitors based on ultrathin mno2 nanosheet/carbon fiber cathodes for wearable electronics", Advanced Energy Materials **6**, 1501458 (2016).

[296]M. Li et al., "Morphology change of oxygen-restructured TiO_2(110) surfaces by uhv annealing: formation of a low-temperature (1×2) structure", Phys. Rev. B **61**, 4926–4933 (2000).

[297]B. Gilbert et al., "Multiple scattering calculations of bonding and x-ray absorption spectroscopy of manganese oxides", The Journal of Physical Chemistry A **107**, 2839–2847 (2003).

[298]I. Horcas et al., "WSXM: A software for scanning probe microscopy and a tool for nanotechnology", Review of Scientific Instruments **78**, 013705 (2007).

[299]F. Parmigiani et al., "Fine structures in the x-ray photoemission spectra of mno, feo, coo, and nio single crystals", Journal of Electron Spectroscopy and Related Phenomena **98-99**, 287–302 (1999).

[300]A. A. Audi et al., "Valence-band x-ray photoelectron spectroscopic studies of manganese and its oxides interpreted by cluster and band structure calculations", Surface and Interface Analysis **33**, 274–282 (2002).

[301]R. C. Salvarezza et al., "Kinetics and mechanism of the silver (i) oxide to silver (ii) oxide layer electrooxidation reaction", Electrochimica acta **33**, 1753–1759 (1988).

[302]R. Caetano et al., "The structure of mn3o4 (110) thin films", Surface Science **720**, 122062 (2022).

[303]J. Barreto et al., "Core-level binding energy shifts between interior, terrace and edge atoms in mno(001) thin films", Surface Science **725**, 122159 (2022).

[304]L. Guczi et al., "Gold nanoparticles deposited on SiO_2/si(100): correlation between size, electron structure, and activity in co oxidation", Journal of the American Chemical Society **125**, PMID: 12670256, 4332–4337 (2003).

[305]A. Hamelin et al., "Cyclic voltammetric characterization of oriented monocrystalline gold surfaces in aqueous alkaline solution", Journal of Electroanalytical Chemistry and Interfacial Electrochemistry **295**, 291–300 (1990).

[306]P. Rodriguez et al., "Electrocatalysis on gold", Physical Chemistry Chemical Physics **16**, 13583–13594 (2014).

[307]M. Gallagher et al., "Structure sensitivity of co oxidation on gold single crystal surfaces in alkaline solution: surface x-ray scattering and rotating disk measurements", Surface science **582**, 215–226 (2005).

[308]S. Trasatti et al., "Real surface area measurements in electrochemistry", Pure and Applied Chemistry **63**, 711–734 (1991).

[309]D. M. Morales et al., "Seven steps to reliable cyclic voltammetry measurements for the determination of double layer capacitance", Journal of Physics: Energy **3**, 034013 (2021).

[310]F. D. Speck et al., "Mechanisms of manganese oxide electrocatalysts degradation during oxygen reduction and oxygen evolution reactions", The Journal of Physical Chemistry C **123**, 25267–25277 (2019).

[311]H. Over, "Surface chemistry of ruthenium dioxide in heterogeneous catalysis and electrocatalysis: from fundamental to applied research", Chemical Reviews **112**, PMID: 22423981, 3356–3426 (2012).

[312]S. Anantharaj et al., "Precision and correctness in the evaluation of electrocatalytic water splitting: revisiting activity parameters with a critical assessment", Energy & Environmental Science **11**, 744–771 (2018).

[313]R. Miao et al., "Mesoporous iron sulfide for highly efficient electrocatalytic hydrogen evolution", Journal of the American Chemical Society **139**, PMID: 28871790, 13604–13607 (2017).